PROCESS PARAMETER EXPERIMENTATION FOR THE HOLISTIC OPTIMIZATION OF SURFACE QUALITY IN DIRECT METAL LASER SINTERING

A Thesis

Submitted to the Graduate Faculty

in Partial Fulfilment of the Requirements

for the Degree of Master of Science

in Sustainable Design Engineering

Faculty of Sustainable Design Engineering

University of Prince Edward Island

Lucas G. Gallant

Charlottetown, Prince Edward Island

2022

ABSTRACT

Direct metal laser sintering (DMLS) is an established technology in metal additive manufacturing, where metal AM is rapidly rising in industrial use, research and development, and academic research. Continued research is needed to better understand the process and print properties to control and improve build parameters and as-built part quality. Characteristic defects in as-built parts of porosity, residual stress, and surface roughness, namely for overhang geometries with downward-facing surfaces, can lead to part failures and reduced mechanical or related performance. Improving as-built roughness through informed process parameter selection and optimization, without compromising density, can reduce post-processing time and support material while improving part quality and performance. This thesis presents the experimental development of process parameters for the holistic minimization of as-built surface roughness of 316L stainless steel DMLS prints and subsequent verification through application to a developed complex design. An initial benchmarking study of DMLS printers using a novel test artifact is included, followed by surface roughness-focused experiments of N_2 and Ar shielding gas, two powder sizes, and optimization of main laser exposure parameters using design of experiments tools. Characterization includes profilometry, 3D scanning, mechanical property measurement, optical microscopy, and residual stress deflection. The resulting optimized down-facing surface (‘downskin’) arithmetical average height roughness (Ra) was measured and found to be reduced by 28%. An upward-facing surface (‘upskin’) Ra below 5 µm is achieved for limited surfaces. The DMLS print parameters were used to improve the downskin roughness and pressure drop characteristics of a novel graded cell-size gyroid heat exchanger design.

ACKNOWLEDGMENTS

All those who have supported me throughout this research deserve an emphasized acknowledgement. The global conditions and restrictions that have run their course over the duration of my studies have surely added difficulty to all who helped with this project. For this, I am extremely grateful for all levels of contribution. Though difficult at times, this work has led me to gain experience and knowledge in experimentation and utilizing available characterization techniques, manuscript writing, presentation of research, and the academic research process. I will especially benefit from personal development in managing long-term independent work and setbacks heightened by all the closures and uncertainty of the past years.

To my supervisors, Dr. Amy Hsiao and Dr. Grant McSorley, thank you for the continuous positivity in support of the project and growth as an academic from the very start of my introduction to research, as well as encouragement and support towards scholarship applications. I would also like to thank my committee members, Dr. Ali Ahmadi and Dr. Sheldon White, for their insight and questions.

Thank you to the great employees at MDS Coating Technologies, whom I had the opportunity to interact with during my time at their facility, namely Ed Bonjokian, Jason Lee, and Steve Gauthier. As well, thank you to FSDE technician Jeff Bowser for all the manufacturing help and DMLS training.

Special thank you to my wonderfully kind girlfriend for her patience and support during extended work hours and to the rest of my loving family.

In loving memory of my grandparents,

George and Fanny Gallant

TABLE OF CONTENTS

LIST OF FIGURES

LIST OF TABLES

LIST OF ABBREVIATIONS

AFM – Abrasive Flow Machining

AM – Additive Manufacturing

BR – Build Rate

CAD – Computer-Aided Design

CAM – Computer-Aided Manufacturing

DAE – Dross Area Error

DfAM – Design for Additive Manufacturing

DMLS – Direct Metal Laser Sintering

DOE – Design of Experiments

EBSD – Electron Backscatter Diffraction

HB – Brinell Hardness

HCAF – Hydrodynamic Cavitation Abrasive Finishing

h_d – Hatch Distance

HX – Heat Exchanger

IPF – Inverse Pole Figure

LED – Linear Energy Density

LOF – Lack of Fusion

L-PBF – Laser Powder Bed Fusion

MP – Melt Pool

OM – Optical Microscopy

P – Laser Power

PAR – Parallel [to the build direction]

PERP – Perpendicular [to the build direction]

Ra – Arithmetic Average Height Roughness

RPc – Peak Count Roughness

RSm – Mean Profile Element Width Roughness

Rz – Average Peak to Valley Height Roughness

SA/V – Surface Area to Volume Ratio

SEM – Scanning Electron Microscopy

SLM – Selective Laser Melting

SS – Stainless Steel

t – Layer Thickness

TEM – Transmission Electron Microscopy

TPMS – Triply Periodic Minimal Surfaces

U – Overall Heat Transfer Coefficient

UTS – Ultimate Tensile Strength

v – Laser Scan Speed

VED – Volumetric Energy Density

YS – Yield Strength

CHAPTER 1

Introduction

1.1 Metal Additive Manufacturing

Additive manufacturing (AM) is the process of building a 3D part layer-by-layer in computer-aided manufacturing (CAM)-enabled machines to realize complex designs with minimal material waste, as opposed to traditional subtractive machining or other forming processes. Although publicly popularized with commodity plastic filament printers, the materials portfolio across available AM processes is extensive and rapidly expanding. Not limited to this list is the manufacturing capability of fully dense metal parts, suitable for rapid prototyping and complex end-use designs. Laser-based AM has found strong ground in the aerospace and medical fields, where AM systems have been at the proven operation readiness level since 2015 [1]. For example, the medical industry benefits through the application of improved and custom conformal implants [2].

The development of modern AM was enabled in the early 1960s with the onset of commercial lasers and CAD/CAM [2]. However, the evolution of additive processes can date back over 100 years with processes such as weld build-up. Processes patents describing the first 3D printing technology, stereolithography, were eventually filed in the early 1980s [1]. The powder-based Direct Metal Laser Sintering (DMLS) technology was first marketed by Electro Optical Systems GmbH in 1995; this process is the focus of this thesis [3]. Other established forms of metal AM include Electron Beam Melting, Direct Energy Deposition, Binder-Jet, Wire-Arc Additive Manufacturing, Sheet Lamination, Bound Metal Deposition, and Cold Spray Additive Manufacturing [4-6].

DMLS is a metal laser powder-bed fusion (L-PBF) printing technology used to produce complex 3D metal parts. In the same manner as other 3D printing methods, DMLS parts are built from layers using slices generated from computer-aided design (CAD) geometry. As shown in Figure 1, the DMLS process uses an ytterbium (Yb)-fibre laser to melt scan lines in metal powder, which is deposited for each layer using a recoater blade system. Though it can be used to fabricate sintered porous materials, the full melting consolidation capability of the DMLS printers allows for highly dense parts to be printed without the need for post-sintering [7, 8].

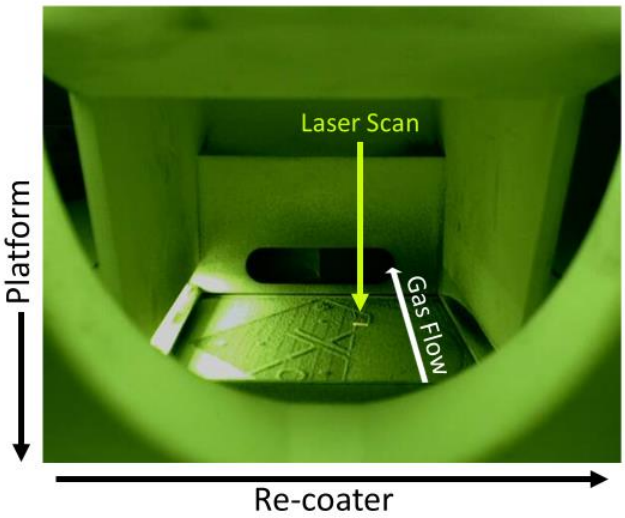

Figure 1: The DMLS process captured in an EOS M100, showing the scan stripe exposure

Processable materials through DMLS include aluminum alloys, titanium alloys, iron alloys, nickel superalloys, and high entropy alloys [9, 10]. In this thesis, experimental studies are conducted using 316L Stainless Steel (SS), a low-carbon austenitic SS alloy, with additions of Mo [11]. The 316L alloy has temperature-robust strength and exceptional corrosion resistance, contributing to its wide use in applications for industries such as medical, marine, food processing, and aerospace [9, 12].

Design for Additive Manufacturing (DfAM) is a process methodology for considering design goals and AM process constraints to achieve optimal print time, cost, and quality. The DMLS process is limited by accuracy, overhang printability, and variable properties but also creativity barriers imparted on designers from traditional manufacturing constraints. Design freedoms include complex internal features (notably for fluid and cooling channel performance), topology optimization (structural or thermal), conformal surfaces, lattices, and functional grading (material or lattices). The layered process also allows for part consolidation and printed assemblies [2].

Despite advancements in metal AM, its application is inhibited by part accuracy, surface properties, porosity, and control and characterization of anisotropic mechanical properties [13]. As such, the research field for AM has also grown exponentially, with the most heavily researched process being DMLS. Popular research activities include process monitoring and feedback control, data management, simulation and feed-forward control, materials expansion, and post-treatments [1].

1.1.1 Sustainability in Metal AM

The use of DMLS in the production of metal parts has massive potential to improve sustainability. Material usage is greatly reduced, with the additive process and powder recycling resulting in much lower ratios of material in versus material out compared to subtractive milling [2, 14]. Another benefit of metal AM is reduced supply chain vulnerability; just-in-time manufacturing is enabled, benefitting both the manufacturer and customer [2].

The costs associated with DMLS depend on materials, production, and labour. More specifically, non-recycled powder, support structures, print time, and post-processing increase manufacturing costs. On the other hand, increased batch sizes and part complexity positively influence cost savings. Even for less-complex parts, DMLS enables cost-effective production of low-volume production runs. Production costs per part for full build volumes are unchanging, so there is an eventual breakeven point where AM is not cost-effective for parts that can be traditionally manufactured [15]. However, the capabilities of AM often result in part designs with intricate geometries unsuitable for these methods.

In contrast, the processing and manufacturing phases of the metal AM part life cycle are not improved from traditional manufacturing processes and may have higher specific energy consumption [14]. Most of the environmental impact is in process energy consumption, particularly for idle machines, followed by powder production, ranging from roughly 100-2000 MJ/part depending on machine use [16]. However, the most significant environmental and economic impacts of DMLS are achieved with functional improvements for the use life phase. For example, AM components for lighter and more efficient passenger aircraft are estimated to have potential energy savings in the order of 100×10^6 GJ/year in the U.S. alone [17]. Energy consumption and productivity in DMLS can also be optimized as a function of process parameters [18]. Another major consideration is the energy and material consumption in post-processing; heat treatment, chemicals in surface treatments, and even part removal using EDM can have significant contributions to environmental impacts [17].

1.1.2 DMLS Process Parameters

Various process parameters can be adjusted in the DMLS process for changes to performance and properties. Parameters include exposure parameters, scan strategies, layer thickness (t), feedstock material and powder characteristics, support structures, and shielding gas. Exposure parameters are mainly the laser power (P), laser scan speed (v), and hatch distance (h_d) between scan lines. Settings can be adjusted for downward-facing surfaces ('downskins') and upward-facing surfaces ('upskins') as well as for contours, which follow the perimeters of layer exposures. Different scan strategies are often used in DMLS to lower unwanted properties such as residual stress, such as with a chessboard laser scan pattern [19]. The EOS printers use a commonly adopted stripe scanning strategy, with default rotation of the scan lines 67° for each layer. An optimal combination of build settings is required to mitigate the defects affecting part properties.

Volumetric energy density (VED) is a calculated parameter used to characterize the energy input of a given exposure; it is calculated from P, v, h_d, and t, as shown in equation (1). For single contour lines (no spacing/h_d), linear energy density (LED) is often used (calculated as P/v). However, energy density is not a sufficient parameter for property prediction or optimization, as there are complex interactions between process parameters [20]. The VED parameter is generally assumed to be correlated to porosity and some mechanical properties to an extent [21-23]. However, this assumption is often inaccurate, as was the case for Parikh et al. [24] with Vickers microhardness. VED does not properly account for the interactions of exposure parameters and other process parameter differences between machines or builds. Miranda et al. [25] effectively show the limit of VED in their DOE

ANOVA of relative density, hardness, and shear strength. They found non-linear response regressions for the same parameters that make up VED, with interactions not captured by VED. Unaccounted process parameters in the VED equation include powder size, material-specific properties, pre-heating temperature, build volume or build platform size, and inter-layer recoating time. Laser beam size is also not included, which directly influences the energy input and has a notable effect on melt pool (MP) width [25]. As shown by Bertoli et al. [26] in Figure 2, the simplicity of the VED/LED equations makes them unable to describe the mechanisms that govern the size and stability of laser MPs, resulting in major differences in scan track morphology. Processing regions of VED are also proven to not transfer between machines for the same feedstock material [27]. Oliveira et al. [20] recently proposed the addition of a dimensionless parameter of powder size over beam diameter to the VED equation, which is described further in Section 3.1.2; it would be used where the material in question is consistent.

$$VED = \frac{P}{v \cdot h_d \cdot t} \qquad \left[\frac{J}{mm^3}\right] \tag{1}$$

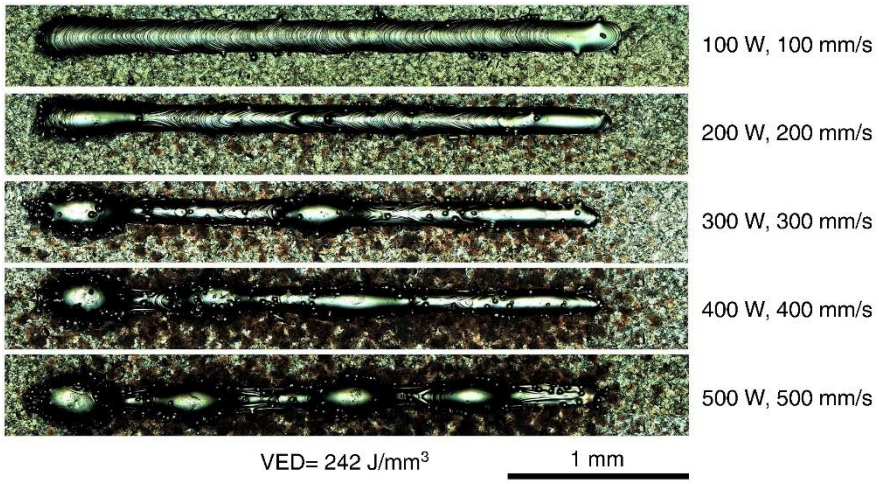

Figure 2: Single scan tracks deposited with the same VED. Reprinted from **[26]**, with permission from Elsevier

1.1.3 Benchmarking and Test Artifacts for AM

General metal L-PBF design rules are not suitable for use with varying machines. Instead, benchmark specimens are used to develop local rules, develop parameters, or compare processes [2]. Benchmarking is necessary for equivalent or transferrable results between prints. For the same EOS DMLS printer models used in this thesis, Steinlechner [28] showed that the processing windows of low-alloy steels varied between machines and that optimization of parameters would be required from one machine to the other.

There remains a lack of standards for AM, including DMLS prints; therefore, benchmark specimens are used to gain information about specific machine abilities and print quality characteristics [29]. Moylan [13] constructed a generalized list of eight key print criteria to test in an AM test artifact to assess a machine or process. They suggested an AM process should be capable of printing:

- straight features,
- parallel and perpendicular features,
- circular and arced features,
- fine features of minimum attainable size,
- freeform features,
- holes and bosses,
- in XY and Z directions, and
- features in the correct locations and orientation.

Further ‘rules’ established by Richter and Jacobs [30] include that a test artifact is large enough to test the edges and center of a build area, print time is minimized, minimal

material is used, and it includes a variety of sized features that are easy to measure and found in functional parts. Scaravetti [31] added that a test artifact should be made of simple shapes for defining geometry and require no manual intervention or support material.

Several widely referenced benchmark parts for AM have followed the above rules to varying extents and are applicable to DMLS printing [13, 32-34]. Kruth [33] presented an artifact that included flat surfaces for surface roughness measurements, with small holes, small cylinders, and thin walls for dimensional analysis. Other design features included sharp corners for investigating overheating, a sloping plane for investigating the stair effect of layers, and a thin plane to indicate warping. The artifact also allowed for pieces to be cut out for mechanical testing. A test specimen used by Castillo [32] included a feature of multiple planes at different angles, tall extrudes, and a hemisphere. For their comparison of prints from different machine vendors, Yasa [34] developed a modified version of Kruth's design by incorporating overhanging angle features, similar to Castillo, and a pipe extrusion. Moylan [13] proposed a standard specimen, shown in Figure 3, in compliance with the eight previously mentioned criteria. Many test specimens have also been developed to investigate specific print properties, such as roughness and dross formation on unsupported overhanging features [18, 35].

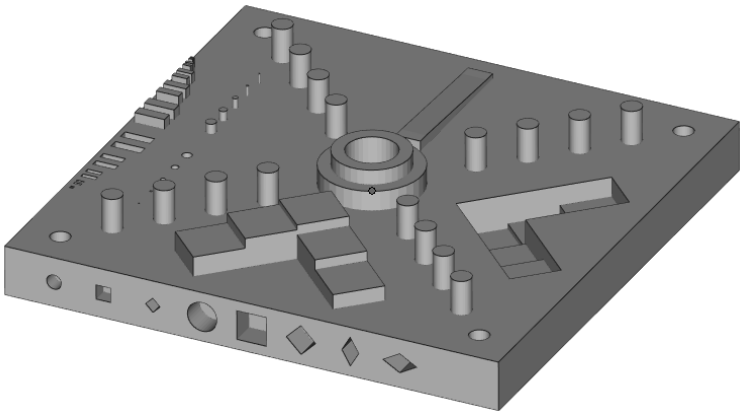

Figure 3: The NIST Standard Test Artifact model, as proposed by Moylan et al. **[13]**

ISO and ASTM International [36] recently published a standard containing a suite of benchmarking test artifacts for individual geometry-type evaluations in AM machines: linear rails, circular artifacts, pins, holes, ribs, slots, and surface roughness. They are said to serve quantitative and qualitative geometric performances but do not specify measurement procedures to strictly follow. The test pieces can be consolidated to some extent, but the large size of the artifacts and the need to print multiple orientations would require many separate and distinct builds for statistical comparison of all geometry types. This same method of individual geometry assessment is what Thomas [37] used to develop their suite of general design guides for selecting laser melting (SLM), analogous to DMLS.

Further, the complex MP dynamics and defects of DMLS that govern the mechanical properties result in large variations between machines and laser exposure strategies, as is discussed in Section 1.2. Thus, the need to include characterization of mechanical performance in benchmark studies of metal AM printers is clear. For efficient testing, this would be done in tandem with the characterization of feature printability, as enabled by current AM test artifacts. In this way, the test artifact can be used to understand differences

in the build performance of standard machines or to conduct a holistic performance test of a parameter set developed for improved performance of an individual property. However, a microstructural characterization is also needed to get insight into the origins of mechanical performance.

1.2 Properties of DMLS Parts

This section will discuss the various process characteristics and properties of DMLS. Given differences in the specific behaviours of feedstock material, the emphasis will be on reports regarding 316L. This SS alloy is a low-carbon austenitic SS designed for extreme temperatures and corrosive environments through additions of Mo, Ni, and Mn; the standard chemical composition can be seen in Table 1.

Table 1: Standard Chemical Composition of 316L SS **[38]**

Chemical Composition (wt.%)								
C	Si	Mn	P	S	Cr	Ni	Mo	Fe
< 0.030	< 1.00	< 2.00	< 0.045	< 0.030	16.00 – 18.00	10.00 – 14.00	2.00 – 3.00	Balance

1.2.1 Mechanical Properties and Performance of DMLS Prints

DMLS builds are found to have intrinsically anisotropic as-built mechanical properties, owing not simply to the fusion of layers and related defects but also to microstructural characteristics [39]. These microstructural characteristics can also give rise to mechanical properties that are much improved from cast or wrought metals. The DMLS process offers the best mechanical performance over other forms of metal AM [1]. The DMLS process also results in innately rough surfaces and some porosity. Porosity of increasing size

significantly impacts strength and ductility, though a relative density of 99.9% is usually achievable [21]. These characteristic roughness and porosity defects are further discussed in Sections 1.3.2 and 1.3.3, respectively.

For low-porosity DMLS or SLM 316L, yield strength (YS) perpendicular to the build direction (PERP), or in the XY direction, is around 550 MPa, with reports as high as 590 MPa—much greater than the 220 MPa of wrought annealed 316L [12, 27]. The difference in ultimate tensile strength (UTS) is less pronounced: around 650 MPa and up to 750 MPa for DMLS 316L, as opposed to 480 MPa for wrought [12, 27, 40]. One reason for this not being as improved is the presence of porosity in DMLS prints. The degree of anisotropy varies for reported strength, though strength parallel to the build direction (PAR), in the Z direction, remains higher than wrought at around 500 MPa for YS and 600 MPa for UTS [12].

Hardness is another principal mechanical property, often characterized using Vicker's microhardness [41]. Like strength, microhardness can be much improved from the standard 223 HV of wrought 316L [42]. Microhardness as high as 325 HV is reported for DMLS 316L [43]. However, hardness is generally reported to be more comparable at around 230 HV [12]. It has been reported to be anisotropic, with the hardness of PERP surfaces (XY plane) being around 10 HV less than the hardness of PAR surfaces (XZ plane), though others report comparable hardness values [27, 44].

Ductility has a wide reported range of around 20 to 60%, where wrought elongation at failure is 40% [12, 21]. The lower end of this range can be attributed to high porosity or similar defects [45]. Many authors report that for high-density parts, a unique

microstructure allows for improved ductility and heightened strength [25, 39, 46]. This mechanical performance includes a more stable plastic strain hardening rate in DMLS parts [39]. Without significant defects, builds are generally more ductile in the Z direction than in the XY direction [12].

1.2.1.1 Residual Stress of As-Built DMLS Parts

Residual stress in DMLS parts occurs in three levels: macroscopic, intergranular, and intragranular [4]. Macroscopic tensile residual stress has been measured in DMLS 316L to be near the yield stress [44]. As such, permanent deformations can occur as a part is removed from the build platform [47]. This deflection may also occur to delaminated or unsupported features within the build, which can cause contact failure with the recoater, as shown in Figure 4 [13]. This deflection occurs even for supported overhanging geometries, depending on the incline and thickness [48]. Residual stress built up in layers may also result in part cracking, though this is much more likely to occur in Ni or Ti alloys [49].

Figure 4: Deflection of DMLS part from support material with the resulting recoater contact indicated by the red arrow

The Temperature Gradient Model explains the residual stress formation through large local thermal gradients in the heat-affected zones. Material strength decreases from temperature

rise, and the expanding melted material then plastically compresses surrounding solid material. Upon cooling, MP shrinkage induces deflection or residual tensile stress in the deposited layers. A second mechanism for residual stress is the cooling and shrinking of melted layers, which are restricted by solidified part layers, forming tensile stress in the top layers. This residual stress grows with successively deposited layers as shrinkage is further restricted. As such, stresses increase in the build platform, which can also deform [50].

The residual stress in solidified layers is biaxial, with the major component aligned with the scanning directions [51]. Measurement of this residual stress may be completed using X-ray diffraction, but a more practical assessment of residual stress in builds can be completed by analyzing the curved deflection of test specimens [52]. Applying measured deflections to an FEA model can give an inverse value for the residual stress in MPa, which has been shown to be comparable [51]. However, the measured deflection value is equally useful for relative comparisons [50].

Residual stress in as-built parts is shown to be a function of the energy input from P, v, and h_d, as it increases with VED [50]. The current popular method of reducing residual stress in as-built parts is to reduce the thermal gradients by preheating the build platform [53]. Using shorter scan vectors may also accomplish this goal [52]. Post-processing methods of reducing residual stress include shot-peening to induce compressive stresses and stress-relief annealing [53].

1.2.2 DMLS Microstructure

The distinct differences in mechanical properties of DMLS materials from their cast and wrought counterparts are determined by uniquely intricate microstructures. These microstructures result from complex laser exposure heating that governs the solidification mechanics.

1.2.2.1 DMLS vs. Cast Microstructures

Conventional production of wrought austenitic SS yields equiaxed microstructures with symmetrical twins contributing to around half of all boundaries; an example is shown in Figure 5b [54]. Similar microstructures are formed in powder pressing processes but with higher porosity [55]. In contrast, Figure 5a and Figure 6 show examples of a 316L microstructure resulting from DMLS, which produces a hierarchical structure with irregular columnar grains in the build direction and, in many cases, a higher degree of texture [54]. These grains are made up of columnar cell structures of dense dislocation entanglements, as in Figure 6, whereas dislocations are seldom in wrought-annealed 316L [39]. Most as-built microstructures are fine-grained due to the rapid solidification from local heating of small volumes. The complex microstructure of the builds owes to the cyclic heating and melting of multiple scan passes [56]. Moreover, MP superstructures are often visible after etching [57]. The microstructural differences of anisotropic grains, grain boundary density, texture, and other phenomena of DMLS solidification all contribute to the effects on performance, as described in Section 1.2.1 above.

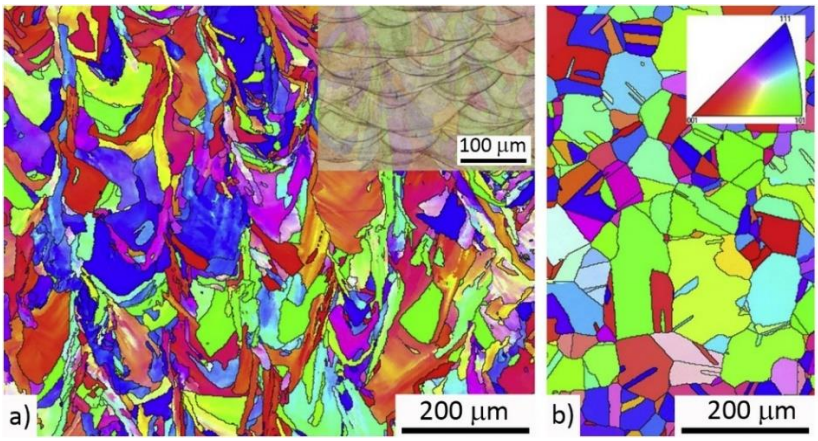

Figure 5: Electron backscatter diffraction (EBSD) inverse pole figure (IPF) maps of processed 316L SS samples: a) DMLS, b) forged. Reprinted from **[54]**, with permission from Elsevier

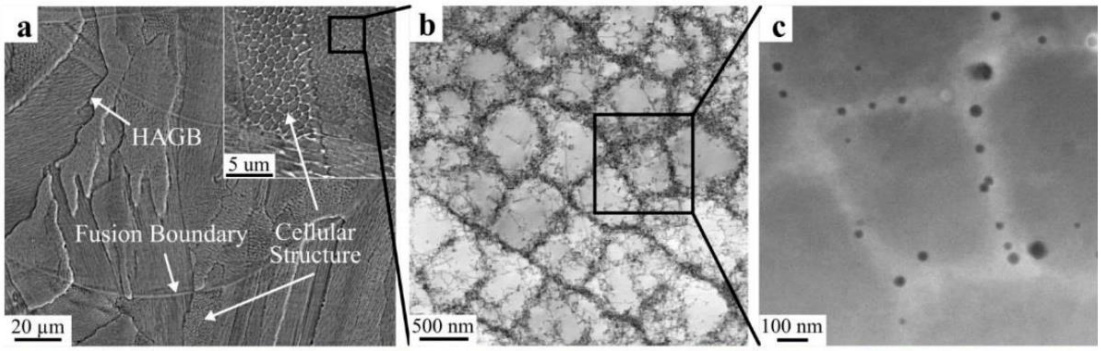

Figure 6: Typical hierarchical microstructure of an SLM produced 316L SS: a) scanning electron microscopy (SEM) image of MP fusion boundaries, high-angle boundaries (HAGBs), and columnar cell structures, b) bright-field transmission electron microscopy (TEM) image of the dislocation cell network, c) dark-field scanning TEM image of the cells. Reprinted by permission from Springer Nature: Nature Materials **[25]**

It should be noted that the microstructures of as-cast steels are normally not fully equiaxed. Instead, columnar, mixed, and equiaxed zones solidify along the ingot or slab cross-section [58]; large dendrites may solidify throughout the cross-section in smaller moulds [54]. Austenitic SS, such as 316L, cannot be heat treated for grain refinement without added dislocations [59]. Refinement in metal castings can be achieved through stirring or inoculation techniques [60]. More typically, the metal is formed followed by solution annealing, resulting in completely equiaxed microstructures with the observed crystal

twins and no precipitates [61]. DMLS alloys, on the other hand, exhibit their improved strength in the as-built state [62].

1.2.2.2 Solidification Theory

To further understand the microstructural differences and, therefore, the differences in applying classic microstructural characterization, the unique solidification kinetics of DMLS samples must be recognized.

The kinetics of crystal nucleation and growth is governed by the minimization of free energy in the liquid—a function of enthalpy, temperature, and entropy. Fundamentally, the elements diffuse to cluster together as the molten metal is cooled. They solidify locally in the more stable structure of densely ordered arrays. More specifically, the free energy of these solidifying clusters is derived as a function of two terms: the free energy between phases and the surface free energy of the clusters as it relates to surface tension [61]. In homogeneous nucleation, the nuclei are uniformly distributed throughout the liquid. The surface free energy term dominates for small nuclei, so only clusters that reach a certain critical size are thermodynamically favourable and continue growth as equiaxed dendrites of the solid phase. This nucleation in a material occurs for a solution at a range of temperatures much below the given melting temperature, known as supercooling (or undercooling). The degree of supercooling has a direct effect on grain size. However, supercooling for homogeneous nucleation is only at these large local temperature differences [61, 63].

Heterogeneous nucleation is the more likely phenomenon in most processes. In this case, nuclei form at existing surfaces due to lowered surface free energy from wetting. A smaller

degree of supercooling is thus required, so dendrites preferably grow from these sites, as shown in Figure 7 for the surfaces in a casting process [61]. Transition to equiaxed nucleation will still occur where the local supercooling ahead of the growth boundary is sufficiently large [64]. Supercooling can also involve constitutional, attachment, or curvature supercooling [9]. In DMLS, constitutional supercooling is generally found to dominate [65]. The differences in diffusion rates of alloy elements determine the extent of non-equilibrium phases or concentrated solutes formed at the solid-liquid interfaces and as microsegregation between dendrites. These solute layers result in constitutional supercooling [61, 63]. The temperature gradient and the solid growth rate, as they relate to diffusion coefficients and total supercooling, govern the grain growth size and whether it is planar, cellular, columnar dendritic, or equiaxed dendritic. This relationship is represented in Figure 8. Precipitates may also form more commonly in the solute regions [9].

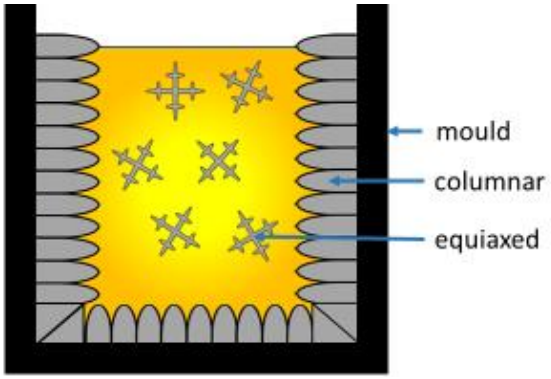

Figure 7: Dendrite growth from heterogenous nucleation on cast mould surfaces and equiaxed nucleation zone (recreated based on **[66]**)

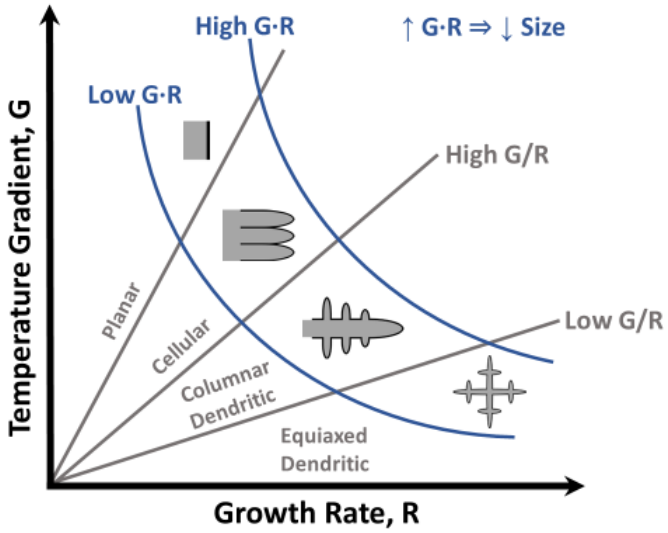

Figure 8: Solidification growth transitions for different G and R (recreated based on **[63]**)

In 316L SS, the dominating crystal structure phase for iron is face-centred cubic (FCC) γ-austenite due to stabilization from alloys such as Mn, preventing the retained transformation of body-centred cubic (BCC) allotrope phases upon cooling [59, 61]. Crystal lattices grow until they eventually meet and form misaligning high-angle grain boundaries (HAGBs). Grain boundaries hinder dislocation motion, so the nature of grains forms the basis of the mechanical properties of a material, along with composition, phases, and precipitates [59, 61]. Though the time spent at high temperatures—related to the cooling rate—governs the grain size, the MPs of DMLS involve additional mechanisms.

1.2.2.3 Solidification of DMLS: 316L SS and Other Alloys

Solidification in DMLS is understood as a more complicated version of fusion welding kinetics [20]. Heterogeneous nucleation occurs at the tail end of the laser MP solid-liquid boundary [65]. The grain morphology is thus heavily dependent on the geometry of the individual MPs from laser scan tracks. Long MPs with low depth-to-width ratios from slower cooling result in coarse and elongated grains with strong texture in the build

direction [9, 56, 67]. The cooling rates in DMLS can be in the order of 10^7 K/s [68]. Therefore, evidence of microsegregation and constitutional supercooling is often observed [45].

For DMLS 316L, this solidification mostly yields fine cellular growth of γ-austenite in colonies that make up the larger fine grains of 10 – 100 μm [68]. Intragranular structures also include columnar cells with honeycomb-shaped walls of tangled dislocations [11, 23]. This dislocation network impedes dislocation motion and is stabilized through the pinning effects of segregations [39]. These structures are the main contributor to the desirable high strength and ductility [25, 39]. Cell size is usually around 500 nm and roughly homogeneous among a cell colony, with uniform width along the solidification orientation [43]. However, average cell sizes of colonies originating from the bottom of the MP are smaller than those on the sides, as the cooling rate and thermal gradient are highest in this zone [46]. In some cases, these cellular networks are only observed in as low as half of the grains [25], but they can also be present in the entire volume [54].

Austenite is maintained as the primary phase in DMLS 316L, with most authors reporting fully austenitic microstructures [11]. Some authors have shown small amounts of BCC phases from the rapid cooling: δ-ferrite needles or α'-martensite laths [23, 27, 43, 68, 69]. Additionally, spherical nano-inclusions (up to 200 nm) of amorphous silicate containing Cr or Mn are found throughout the microstructure and at cell interfaces, which also strengthen the DMLS 316L [11, 46, 54, 68-70]. Some, but not all, authors report sub-grain boundaries that are enriched in Mo, Si, and O [57]; others also note depleted Fe and higher contents of Cr and Ni [39, 54, 71]. These segregations can reinforce DMLS 316L against

crack propagation [72]. MP boundaries have also been reported to be depleted of Mo and Cr due to rapid solidification [54]. It is these variations in composition, as well as the dense dislocations, that result in improved intergranular corrosion resistance for DMLS 316L in comparison to the non-enriched boundaries of commercial 316L [73]. This resistance allows cell structures and MPs to be visible through an optical microscope after etching [74, 75]. The MPs themselves do not have a significant impact on tensile behaviour [62]. Corrosion in commercial 316L occurs along the non-enriched grain boundaries for a higher sensitization than DMLS 316L [44].

Other feedstock metals yield meta-stable microstructures that can vary along a part geometry due to complex thermal cycling and rapid cooling [4, 56]. These include secondary phases at cell walls, which can enable cracking during prints [76]. As such, 316L SS has exceptional relative printability despite its susceptibility to thermal strain, lack of fusion (LOF), and alloy vaporization of lighter alloy elements (e.g., Mn) [77].

1.2.2.4 Grain Growth in DMLS

Columnar grains nucleate at the solidification boundary of the MP. These grains take on the crystallographic orientation of the local solid, demonstrating epitaxial growth of the previous layer [23, 78]. Grains then solidify from roughly normal to the MP surface: towards the MP center and the scanning direction [9]. This directed growth typically results in build-direction-oriented grains along the center of MPs, originating at the base [23, 79]. Growth higher on the MP boundary is more XY-oriented than growth near the bottom. The higher growth also has an increased potential for equiaxed growth due to a lower temperature-gradient-to-growth-rate ratio (G/R), especially along the top centerline of an

MP [11, 65, 79]. The growth is cellular from rapid cooling, and cellular colonies that make up the grain structure grow in the same orientation [11, 23, 78]. However, minor misorientations occur among solidifying dendrites and form low-angle boundaries, seen in Figure 9 as orientation gradients within a grain [11, 54]. Marangoni flows in the MP from temperature-driven surface tension gradients affect local heat fluxes and thus contribute to the orientation gradients or non-orthogonal changes in growth direction [45].

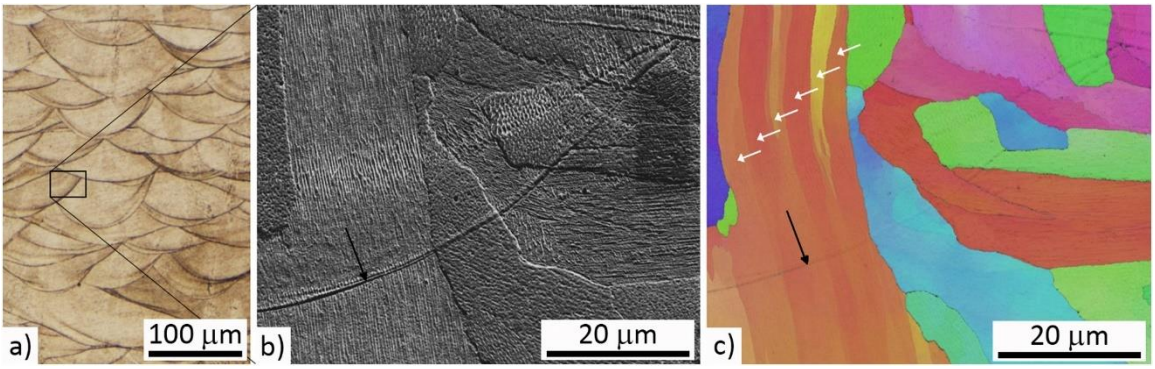

Figure 9: Micrographs of DMLS 316L: a) OM image of MP structure, b) SEM image with MP boundary indicated, c) EBSD band contrast image, with orientation gradients indicated for a single grain. Reprinted from **[54]**, with permission from Elsevier

Cells of the FCC Fe grow along the <100> direction, the preferred crystallographic orientation for growth in the direction of the highest thermal gradient [63]. Therefore, the cellular dendrite orientation in epitaxial growth is not always normal to the MP boundary, as a maintained orthogonal growth in one of the <100> orientations is preferred. If the intersection of a grain and a new MP is not near perpendicular, the cellular growth of the grain in the new MP is changed to an orthogonal direction (~90°) to the previous cells to better align with the heat flux [10, 45]. This phenomenon further contributes to the observed feature of cellular structures oriented in various directions, which is not fully represented by EBSD analysis [46]. Nonetheless, grains aligned with the thermal gradient

will outgrow slower misaligned grains in a competitive growth that results in mostly columnar grains [9, 11].

The degree and size of the cellular growth in DMLS depend on the MP geometry, as it relates to the thermal gradient and growth rate [9]. In some cases, the increased temperature gradient at the MP bottom is very high, so much so that Wang et al. [45] observed planar growth in some of these zones (no visible cells or misorientation), changing to cellular growth at the subsequent MP boundary. MP characteristics such as cooling rates and temperature distribution also vary throughout a geometry, so the microstructure also varies [68].

1.2.2.5 Dislocation Cell Formation

It is well-accepted that dislocations build up in DMLS prints due to thermal strain [70]. The constraint to thermal expansion on the printed material influences the number of dislocations formed [80]. This buildup leads to cellular dislocation structures with high thicknesses of up to 300 nm [11]. However, there has been disagreement in recent years over the formation mechanism of the dislocation structure [79]. Some authors have explained the formation of the dislocation cells as being driven by misplaced Mo, inducing dislocation tangling [68, 72]. However, this mechanism does not account for dislocation networks observed without microsegregation, as in Qiu et al. [46]. Likewise, the dislocation cells are not strictly found to overlap with cellular dendrites; it just happens that the nanometer-scale cellular growth of DMLS 316L matches the stable dislocation cell size to facilitate the organization of dislocations and consistently overlap [80].

Others have instead adopted the explanation of dislocations piling up to reach equilibrium structures, for which cell boundaries help shape the cells and the dislocations trap heavier element diffusion to form the precipitates [23]. Additionally, Birnbaum et al. [74] showed in single scan prints that zones of grains not containing noticeable cellular structures share a continuous line of grain boundaries. Since the dislocation structures were influenced by existing HAGBs, this proved that both the segregation of solutes and the formation of dislocations occur after solidification due to thermal stresses and not significantly by temperature variations during growth. They also label these grains as planar growth on account of no segregation from constitutional supercooling, despite usually being thermally unlikely [76]. A recent review by Liu et al. [81] has also rested upon the conclusion of thermal stress dislocation-driven post-solidification structures. There is still further elucidation to be done in this area, including the exact development, interactions, and planar growth: the true frequency of occurrence, if homogenization of segregation occurs, and if fully formed dislocation structures can build in these grains. Nonetheless, the general takeaway is that the dislocation cells and segregated solutes are primarily post-solidification structures from thermal stresses, where both can originate during solidification and can facilitate the development of the other.

1.2.2.6 Effects of DMLS Parameters on Solidification and Performance

The anisotropic as-built microstructures in DMLS prints, in addition to the stress-raising defects of microsegregation, oxidation, inclusions, and porosity along layer boundaries, all contribute to the anisotropic mechanical properties outlined in Section 1.2.1 above, including potential premature and brittle failure [78]. Even so, ensuring a proper selection

of laser scan exposure parameters and strategies can help to partially control epitaxial growth and texture to overcome defects and achieve high elongation while maintaining strength. Sun et al. [82] mitigated high texture using a high-P high-v build with 67° layer-to-layer rotations. Still, this result is paired with anisotropic lowered strength in the build direction.

As previously described, the epitaxial cellular growth, and thus the dislocation cells, have been shown to redirect roughly orthogonally with the new MP temperature gradient [10]. Using this grain growth theory, Krakhmalev et al. [11] employed and analyzed the microstructure from a layer-by-layer scan strategy of alternating between X and Y-oriented hatching vectors. They found that the solidification texture was modified to follow layer-wise zig-zagging orientations, meant to induce successive misorientations at fusion lines and allow better-aligned colonies to outgrow epitaxial grains. However, the inspection of the resulting grains was for an orthogonal plane of the build direction, but the expected trajectory of the grain growth would not be orthogonal. Thus, the true resulting texture was not fully analyzed. This logic of a potentially realized net epitaxial grain growth direction could partially explain why some authors present even lower strengths in 45°-printed specimens than in PAR-oriented specimens, whereas others report higher strengths [83-85].

In comparison, builds with no scan rotation can exhibit high degrees of texture in the build direction from long epitaxial grains, as shown in Figure 10 [86]. Limited texture for a 67° scan strategy is noted by Casati et al. [78]. Leicht et al. [87] found this strategy to produce the lowest PAR strength and ductility compared to other standard scan rotations that

produced a higher <110> texture in the build direction. Neindorf et al. [88] found that a highly <100> textured elongated-grain structure yielded lower YS and slightly lower UTS of PAR specimens compared to the weakly-textured fine-grain samples, though still with better ductility and elasticity. However, in the case of Sun et al. [82], these scan rotations and suitably high power were used to yield a finer grain structure and a preferred <110> texture. They attributed the improved strength and ductility to nano-twinning in the <110> cells. As previously discussed, this difference in build direction texture is related to the MP shape and is useful in tailoring or understanding the anisotropic properties of DMLS prints.

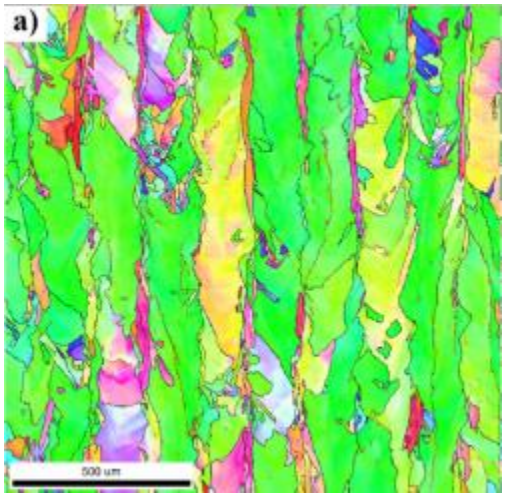

Figure 10: Strong texture shown in an IPF map of L-PBF 316L SS with constant layer-to-layer laser scanning directions (parallel to the gas flow). Reprinted from **[86]**, with permission from Elsevier

The complex nature of the DMLS microstructure in 316L SS has made it difficult for researchers to fit a relationship for accurate predictions using the different sizes of hierarchical features and mechanical properties [87]. Although Hall-Petch relationships using cell spacing are found to better account for increased strength, proving this dimension dominates, it does not sufficiently account for the full strengthening of DMLS microstructures [25]. Some of this Hall-Petch strengthening is also partially accounted for

by HAGBs, such that Zuback and DebRoy [41] showed both reported Vickers microhardness and YS to follow Hall-Petch relations, but they did not discuss prediction accuracy. Wang et al. [25] used a finite element polycrystal model to investigate mechanical properties. They found that strength and hardening are instead governed by some effective length that combines HAGBs and cell structure features, though not a simple superposition of the two sizes. Plastic deformation of the γ microstructure occurs through slipping and twinning. Dislocation blocking at HAGB occurs in addition to dislocation cell mechanisms [25]. Substantially fine-grain structures would have an increased impact on dislocation motion and the activation of twinning [82]. Twinning occurs across individual grains and as nano-twinning among cells due to the dislocation walls and slight misorientations [39, 89]. This twinning compensates for defects to achieve high ductility with heightened strength [25, 46]. These reported findings give an indication of the interplay between the hierarchical cell morphology and the resulting mechanical properties.

Further, the grain size, intragranular cell size, dislocation wall thickness, and degree of elemental segregation are all influenced by laser exposure parameters (P, v, beam size, etc.) as they relate to heating and cooling [11, 25, 39, 78]. Qiu et al. [46] found that by increasing power, the grain size increases. Larimian et al. [67] had the same result from increased VED by adjusting v and h_d. They added that a re-melting strategy coarsened grain size and related it to an inverse VED trend for microhardness. Liu et al. [39] and Yadroitsev et al. [90] both found that by decreasing speed, the cell size increases. Bertoli et al. [76, 91] furthered the connection to cell size through studies using experimental and computational

methods; clear relationships were fit for changes to LED and the resulting temperature gradient (G), growth rate (R), and cooling rate (G·R). Leicht et al. [21] further showed that by increasing VED through lowering v and h_d, the grain size, cell size, and degree of <110> texture increased for lower strength with higher ductility.

Although an even deeper knowledge of hierarchical morphology and defects is required to explain the resulting mechanical properties, grain size is one influence that is interconnected with other microstructure measures and may give an initial insight into these differences between prints, especially for tensile strength, where plastic deformation mechanisms apply.

The specific microstructure will depend on MP dimensions, temperatures, and cooling rates, where both are functions of exposure parameters and scan vectors (speed and strategy) and are affected by surrounding geometry [56]. For example, increased scan speed results in elongated and shallow MPs, leading to increased epitaxy and build direction texture of cellular growth [67, 79, 82, 90]. However, in a low-P high-v exposure for shallow MPs with a low thermal gradient and high growth rate, supercooling can cause a transition to equiaxed growth [65, 67, 79]. Scan lines parallel to shielding gas flow have been shown to exhibit shallower MPs and increased texture [86]. Time in between layers is also shown to impact heat accumulation effects of slower cooling and deeper MPs. Consequently, sub-grain size (high and low-angle boundaries) is found to increase with shorter inter-layer time, as well as with laser input energy [92]. Similarly, a high pre-heating of the build lowers the thermal gradient and thus increases the probability of equiaxed grains [76].

These compounded dependencies result in the wide variations of as-built microstructures and related properties throughout the reported literature depending on process parameters. Though rooted in complex solidification processes, the growing knowledge of microstructural behaviour to process parameters improves the ability to interpret metallographic examination. It also has the potential to allow some degree of microstructure customization for design performance. However, parameter constraints from low-porosity process regimes may limit the ability to tailor microstructural features.

1.2.3 Heat Treatment

Heat treating a DMLS part is one of the post-processing steps often conducted. One main objective of this treatment is to relieve the accumulated residual stress, and the other can be to achieve isotropic mechanical performance. As mentioned in 1.2.1 above, recrystallization of the as-built austenite through solution annealing is achievable in DMLS 316L parts without requiring a cold working step; this is enabled by the strain energy of the existing dislocation structure [43, 61, 93]. This processing characteristic offers a significant advantage over casting for fabricating intricate 316L parts with traditional and predictable 316L mechanical properties. Removal of residual stress is completed while the part is still on the build platform to avoid part deformation upon removal leading to unacceptable dimensional deviation. Un-relieved part stresses can also cause premature fatigue cracking [49]. This stress relief of DMLS 316L for parts held at around 600-800 °C for 3-5 hours can result in the complete removal of residual stress [27, 51].

Heat treatment temperatures of DMLS 316L are roughly divided into recovery from 600-1100 °C and recrystallization achieved at 1100-1400 °C [43, 94, 95]. In recovery heat

treatments, atomic diffusion leads to the thinning of cellular walls and MP boundaries, both disappearing around 900 °C [43, 95]. Some dislocations are removed, whereas others distribute from the tangled cell walls and reorganize as larger sub-grains along low-angle boundaries. At 1100 °C, the grain HAGBs are no longer stable, and recrystallization occurs, increasing dramatically at higher temperatures. The dislocation density drops as grains are recrystallized [95]. Additionally, trace amounts of ferrite may act to nucleate ferrite phases in the recrystallized microstructure [43].

The removal of cell boundaries at temperatures around 900 °C leads to a pronounced reduction in hardness and YS [11]. Stress-relieving at temperatures below this point (600 °C) may result in improved hardness but with a drop in elongation [94]. Though the grain boundaries are maintained up to 1050 °C, the hardness is lowered within the range of conventional 316L. Moreover, precipitate oxide particles interacting with dislocations are thermally stable in the solid solution but do not maintain additional hardness after cooling [11]. Recrystallization results in the removal of any as-built texture. Annealing twins are formed in the newly recrystallized grain structures, as is in wrought 316L, for partial rehardening [42, 43]. Riabov et al. [62] found a 50% reduction in YS for a partially recrystallized sample, though no reduction in UTS. Liverani et al. [57] noted a 25% increase in ductility and a reduced YS comparable to wrought 316L, with only slightly lower UTS.

Hot Isostatic Pressing (HIP) is a high-temperature, high-pressure treatment used for similar heat treatment effects as normal annealing but with added densification of pores and cracks [55]. Although YS is found to lower further than regular annealing, ductility can be doubled

to high elongation values (70%) and unchanged UTS as opposed to non-HIPed annealing. Enlarged Mn silicates also form throughout the matrix [57].

A high-pressure HIP treatment of 316L parts built in nitrogen environments results in reduced porosity, as decreasing volume drives the soluble nitrogen within pores to dissolve through the steel matrix. HIPing above 1050 bar has been demonstrated to achieve a near 100% relative density for samples with less than 1% initial porosity. Parts with higher initial porosity experience variable reduction in pore sizes [57]. For 316L samples built in an argon environment, internal argon pores are not removed as argon is effectively insoluble in steel. In fact, argon pores re-expand after annealing to an increased net porosity [55]. Surface roughness is not impacted through the HIPing of parts with high relative density [96].

Overall, the high-strength mechanical properties of DMLS materials, such as 316L, are affected by part defects but depend on the complex microstructure. The governing microstructural characteristics include hierarchical grains of epitaxial cellular colonies with inner dendrites, dislocation cells, and segregated elements that grow in the scan direction of each track [54]. The resulting degree of hierarchical grain sizes, grain orientations, texture, and induced thermal stress, determine the bulk mechanical performance. These microstructural properties depend on most build parameters, including geometry [9]. Unlike cast 316L, DMLS 316L can be heat treated to varying temperatures to accomplish stress relief, dislocation removal, solubilization, and recrystallization. However, heat treatment may lower hardness and tensile properties. Modelling of DMLS solidification kinetics, such as the approaches of Liu et al. [79], has provided insight into

grain growth mechanisms. Their models correlate well with the microstructures of cubic builds for control or post-treatment planning. However, this area of DMLS research is still far from achieving an effective tool for coupled scan track morphology, defect, and microstructure modelling for part geometries.

1.3 Consolidation Mechanism and Defects of DMLS

Characteristic rough surfaces and porosity in DMLS parts arise from the layer-based nature of the process, as well as the scan track exposures and their complex and variable physical MP dynamics.

1.3.1 Melt Pool Phenomena

Intensive vaporization of metal from the laser causes a depressed MP zone from resulting recoil pressures [97]. This phenomenon results in different melting modes shown in Figure 11 that can occur with increasing energy input: conduction, transition, and keyhole [98, 99]. Conduction mode forms shallow or circular MPs, whereas keyhole mode forms a deep vapour cavity from multiple reflection ‘drilling’ and convection heat transfer dominates. Transition to keyhole mode depends on the vaporization depth. The threshold depth is less in highly reflective and conductive materials, such as Al alloys, than in alloys with lower reflectivity and conductivity, such as 316L SS. Keyhole melting is generally undesirable as it can cause large pores from collapsing MPs, as in Figure 11c, though shallow conduction melting can result in LOF voids [99]. Smaller gas pores are formed in both melting modes. In re-melting from subsequent scan tracks, some gas pores escape through the depression zone while others circulate in the solidifying MP [100].

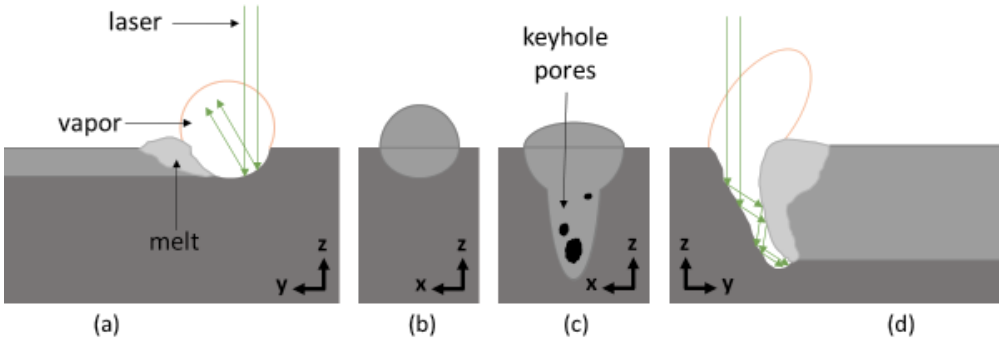

Figure 11: Representation of conduction (a, b) and keyhole (c, d) mode melting (based on **[99]** and **[101]**)

Spatter occurs as powder particles or agglomerates are entrained in the vapour plume and melted by the laser, ejecting them onto the layer surface; this generally increases with energy input [97, 102]. Low laser power leads to a vapour jet directed more forwards (in front of the laser scan), which can impede the laser beam [103]. A proper shielding gas crossflow helps to limit the vapour plume and ejections but cannot extract high-momentum particles [103, 104]. Similarly, the denudation phenomenon is driven by the vapour flow. As shown in Figure 12, denudation is an effect in which powder surrounding the scan tracks is cleared away [104]. This effect occurs as surrounding particles are entrained toward the melt. At higher powers, denudation is further increased as a backwards plume forces additional powder away from the scan track. Denudation thus depends on the laser energy and shielding gas flow, though it also depends on layer thickness and the underlying roughness [103, 104].

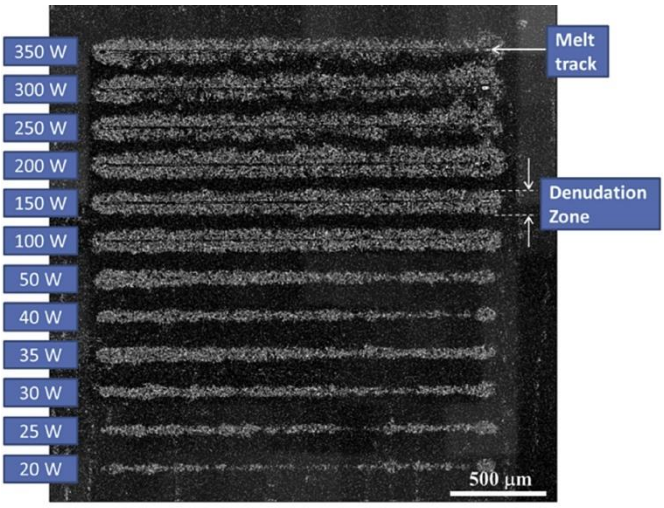

Figure 12: Denuded zones around single melt tracks created by L-PBF as a function of laser power. Taken from **[104]** / CC BY

Balling is observed in DMLS as both beading and rough surfaces of laser scan tracks, as in Figure 2 [105]. Two different types of balling occur in laser melting scan tracks. The first type is due to insufficient melting of a powder layer, and the second type is due to melt-pool instabilities [7, 106]. Generally, higher-VED melting produces scan tracks with less balling, avoiding ellipsoidal balling from insufficient melting [7, 106]. At these high energy inputs, a large thermal gradient and, thus, surface tension gradient along the MP causes outward thermocapillary Marangoni flows that flatten the MP for continuous scan tracks [8, 107]. However, excessively high power or low scan speed elongates the length-to-width ratio of the MP and weld bead during scanning. As such, Plateau – Rayleigh instabilities from high surface energy induce melt track width fluctuations or complete balling [104, 107]. Surface energy is also released as melt splashes in this regime [7]. Overly wide MPs result in poor weldability and balling due to the large thermal gradient along the width and resulting localized flows [19, 105]. In multi-track builds with short scan vectors, instability balling is lowered as the MP width is enlarged from previous solidifying scan tracks [8].

The balling phenomena can also be pronounced from increased oxygen content in the build chamber, as oxidation of the melt interface reduces wetting ability [106]. Moreover, oxygen dissolution in the MP can affect the Marangoni flow and increase balling [105]. Balling behaviour for a scanned layer can result in a rough surface, thus impeding melt track wetting in the next layer [7].

Overhanging geometries experience unique MP behaviour that requires special consideration. As shown in Figure 13, dross formation and sagging occur as the powder bed is unable to support or dissipate heat effectively from the MP [108]. MPs are deeper than the nominal part contours for low angles due to the low powder conductivity, so agglomeration occurs with the supporting powder and the MP sinks [109, 110]. For shorter straight overhangs, DePond et al. [111] showed that while low VED caused traditional balling of the unsupported track, increasing power can similarly form a string of beaded dross that coalesces with parallel scans to form ridges perpendicular to the scans. Throughout all angles, the adhesion of surrounding powder is the dominant contributor to the surface roughness, though the phenomenon is enhanced by sinking and dross formation at low angles; warp also plays a larger role below 40° [112]. Insufficient support and heat dissipation can result in the degradation of the surface and warping of scan layers, which compounds in subsequent layers [40]. However, supported overhangs are not without surface defects, as support connections are fused to the surfaces and leave scarring and fragments after removal [110].

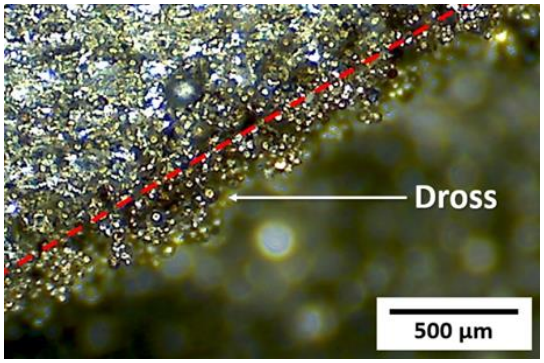

Figure 13: Dross formation and adhered powder on a downskin incline surface

Charles et al. [113] used a discrete element model coupled with computational fluid dynamics (CFD) to simulate overhang dross. They found scan tracks perpendicular to overhangs to initiate dross formation at the onset of the lack of support. The MP overheats and is depressed to a keyhole melting mode with pronounced drilling, forming deep grooves for each layer and sub-surface porosity along the downskin area. Lower LED was found to reduce this dross error by lowering the recoil pressure and flow from overheating.

Contrarily, Le et al. [114] performed a full multi-layered simulation procedure, alternating between deposition through discrete element modelling and laser scanning through CFD, to investigate different overhang scan track conditions. Their finding was that overhanging melt tracks displayed characteristic discontinuity, where resulting defects include surface roughness and poor fusion of layered tracks. Thus, the relation to Plateau-Rayleigh instabilities meant that simulations and experiments with higher P and low v reduced these defects for overhang incline contours, despite the popular belief that this consistently leads to increased dross. It was deduced that large temperature gradients lead to high Marangoni flows for molten spreading over a longer period, thus smoothing defects. However, when paired with low powder absorption, the laser may penetrate the powder bed and reflect,

deepening the melt. There was also no analysis completed for warp-related effects in the study.

Montgomery [115] found in their experiments with large straight overhanging surfaces that the MP length-to-depth ratio, as it relates to P and v, is an important characteristic for successful prints. For example, high v results in an elongated MP that will bead up and cause LOF failures. However, high LED scanning from a higher power is more susceptible to dross formation, so low v and low P were found to perform best.

Many other studies are available that report exposure parameter effects on these mechanisms. Matthews et al. [104] found that denudation increases with energy input. Koutiri et al. [116] found melt spatters to increase with high P and low v, leading to more incrusted powder melts on the surface. Balling of melt tracks is shown by Gu [7] to be heightened from low power limiting melting and high scan speed causing capillary instability; stability generally improved with increased VED. Both warping and dross formation are shown by Wang et al. [117] to grow with an increase in energy input and a decrease in overhang angle. The same author found warping to also increase from longer scanning vectors [40]. Fathi et al. [118] found that reduced hatch distance may result in cyclically large and small scan tracks, where the smaller MP is formed from the increased overlap and conduction with the previous large MP, causing subsequently less overlap and the large MP. This periodic MP structure results in variable microstructure sizes and a smoothed surface.

1.3.2 Density in DMLS

As previously noted, the porosity of successfully printed parts in DMLS machines can be significant due to LOF, gas pores, or keyhole voids. Voids spanning multiple layers can also be formed from residual stress-induced cracking and MP separation in rapid cooling [84]. Printable builds with a relative density as low as 68% have been reported [119]. Any porosity can be detrimental to mechanical properties such as tensile strength and ductility. However, it is generally found that these defects have less of an impact and that fracture is ductile when porosity is kept below 1% [12]. Nonetheless, porosity in DMLS prints results in lower fatigue strength [120]. Trapped particles of unmelted powder serve as crack initiation sites for tensile specimens and are more prevalent with increases in layer thickness [121].

A proper laser input energy is required to form MPs with reliable fusion and stability [67]. Parikh et al. [24] found good correlations between VED and porosity, with some variability from specific parameter levels. Cherry et al. [122] similarly used VED to determine a range of values for minimum porosity based on the exposure parameters adjusted. Qiu et al. [46] found that porosity could be tuned by varying laser power alone. These VED correlations are useful for distinguishing between low-density (relative density < 99%) and high-density parts for porosity control but not fine-tuning [24, 46, 122]. Furthermore, for a selected VED with high-density prints, Sun et al. [69] showed that experiments with changes to specific parameters (v and h_d) for the same VED can lead to further porosity tuning. Fine-tuning porosity is important for mechanical performance, notably fatigue strength, which usually suffers in DMLS parts [120]. Conversely, Ilie et al. [123]

demonstrated that controlling parameter sets of the same VED for porosities in specific layers can be used to design specified tensile failure zones while maintaining strength and only slightly reducing elongation.

Di et al. [124] found that P and v could effectively separate scan track morphology into regions where thickness and irregularity generally increase with speed. In subsequent one-factor experiments of volume prints, they found that relative density increases with both decreasing hatch distance and decreasing velocity, up to a point where they have more deleterious effects approaching their smallest values. They concluded that thin and regular scan tracks are desirable and that staggering the scan lines improves fusion and the bonding strength of layers.

1.3.3 Surface Roughness of DMLS Part Geometries

Although the DMLS 316L material can be less susceptible to corrosion than wrought, the rough surfaces generated in the DMLS process are highly susceptible to pitting corrosion and thus must first be addressed [125]. A standard measured parameter for surface roughness is arithmetic average height (Ra). An Ra of ~10 µm for top surfaces, ~10 µm for sides, and 10 to over 20 µm for downskins of high incline angles is generally considered good for DMLS 316L, but surface roughness can be much worse for certain low-angle geometries [12, 125, 126].

The discrete layers of DMLS make inclined surfaces subject to a higher roughness due to what is known as stair-stepping, shown in Figure 14, which combines with the ‘edge effect’ (elevated perimeters of scanned areas). The edge effect is limited to low inclines where stair widths are large [127]. The staircase effect is observable for both upskins and

downskins [128]. Adhered powder is pronounced for side and angled surfaces as the surrounding powder will adhere to MP edges [19]. This surface-adhered powder is also more pronounced for geometries with lower spacing than other geometries, as heat accumulation favours partial melting of the powder [129].

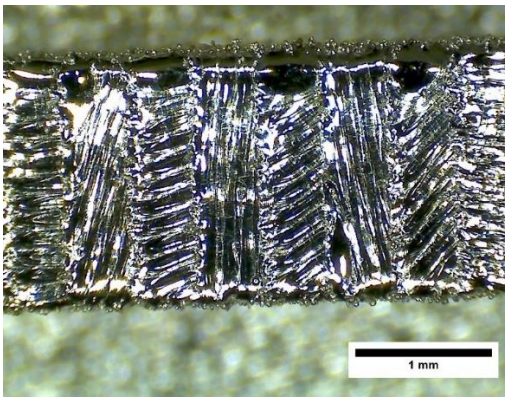

Figure 14: Top-down view of upskin staircasing, exaggerated by a ~2° incline

Fatigue life is improved by reducing surface roughness, which can be necessary for biomedical implants [96, 120]. Decreased surface roughness with less adhered powder is found to have reduced pathogen biofilm for implant test coupons without compromising cell viability and attachment [130]. The surface quality of DMLS 316L is also shown to directly influence the resulting roughness of γ-alumina coatings and their hydrophobic nature and corrosion resistance [131]. The high surface roughness of DMLS worsens corrosion resistance, and while shot peening and polishing processes increase resistance, sandblasting worsens it [118, 132].

1.4 Build Parameter Effects on Surface Roughness and Other Part Properties

The effects of DMLS process parameters concerning MP mechanics, microstructure, and mechanical properties of metal parts, have been previously mentioned in Section 1.2. Though some general effects of process adjustments have been stated, accurately

correlating these changes to final part properties for robust control is complicated. This section describes the understanding and unknowns in relating process parameters and part properties, with an emphasis on how they impact surface roughness.

1.4.1 Process Parameter Trends

Given the range of defects to part and surface quality that can occur from changes in process parameters, managing the trade-offs of these changes is complicated. For top surfaces, roughness and porosity are generally correlated as they are both heavily influenced by the control of balling, and the surface roughness of each layer directly impacts the porosity. Therefore, they can be concurrently optimized well [133]. However, improvements to downskin surface roughness are at the expense of part density and vice versa. Chen et al. [134] observe this trade-off for changing VED; they also found that surface roughness and relative density are compromised at excessively high or low energy inputs. However, using VED as the sole parameter to control surface roughness is limited. VED does not account for parameter interactions that affect MPs and thus surface roughness; a wide range of roughness values is possible for the same VED from different parameter levels [86, 116]. Still, higher energy input generally relates to a lower upskin Ra until balling becomes an issue [122].

Trends are usually found for top-surface roughness with VED or its constituent parameters. Attarzadeh et al. [135] found that increasing VED would rapidly reduce top-surface roughness up to a VED where defects such as spattering and entrapped gas would increase. Slower scan speeds were required for increased laser power to compensate for the MP temperature gradients and maintain relative density. Calignano et al. [136] conducted a

Taguchi DOE for top-surface roughness for aluminum alloy prints and found scan speed to have the highest impact. Dursun et al. [137] also showed that higher VED to increase MP overlap would decrease top-surface roughness, but Tian et al. [138] found that small hatch distances with large overlapping MPs would promote adhered powder for other surfaces.

Maamoun et al. [139] similarly found through a DOE of P, v, and h_d that top-surface roughness can be modelled with a 2^{nd}-order polynomial function of VED, showing that excessive increase leads to defects. Although, in their case, the scatter of the corresponding relative density for VED did not yield an accurate relationship, and surface flatness conversely decreased with VED. Instead, by using overlaid contour plots of P and v, the authors determined optimal process windows for minimum top surface Ra, maximum relative density, and minimum dimensional error for the two Al alloys. In the case of Al6061, a reasonable tolerance range (±0.03 mm) limited the maximum relative density to the experimental range tested.

It is thus clear that optimization of all surfaces from a single set of exposure parameter levels is not possible without trade-offs. The EOSPRINT build preparation software addresses this issue by allowing separate exposure parameters for upskins and downskins, as shown in Figure 15. Charles et al. [140] showed that changing the parameters of downskin layers only, with otherwise default parameters, does allow for significant improvements and optimization of downskin surface roughness. The shape of the downskins can also affect surface quality, as shown by Piscopo [141], where overhang length, curvature, and angle were all significant factors.

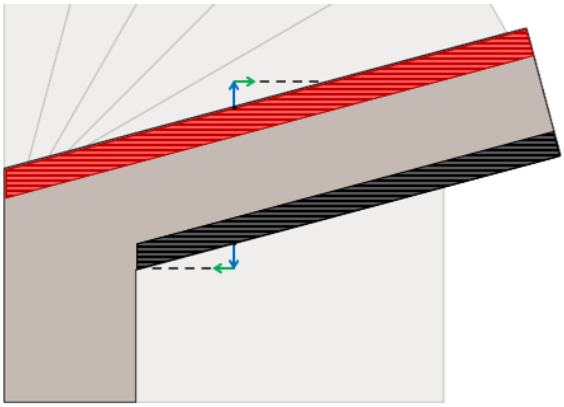

Figure 15: Upskin (red) and downskin (black) exposure regions for a 15° feature (regions are shown at 5x relative thickness to the default settings for visualization)

Deng et al. [133] effectively used combined optimization for minimal top-surface roughness and maximal relative density by implementing response surface DOE ANOVA and multi-objective optimization. This work displays the need and ability to conduct more holistic improvements of DMLS by applying statistical optimization techniques. However, their optimization weighted density and roughness equally, whereas it may be necessary to ensure a high relative density for part performance.

1.4.2 Shielding Gas

In the DMLS process, shielding gas replaces the build chamber air with inert or nearly inert gas and removes the process by-product from laser melting. The uniform flow of shielding gas is a key parameter in ensuring a desirable density and roughness of a build [142]. Vapour plume obstructions of the laser in areas of low gas flow can result in LOF and balling from lower penetration levels [143]. Shielding gas composition can significantly impact the effective thermal conductivity of the powder bed, as the gas of a given thermal conductivity infiltrates the gaps in the bulk powder [144]. Increasing this conductivity with a sufficiently conductive gas could improve overhang defects such as dross formation.

Nitrogen is a standard and cheap shielding gas with a lower thermal conductivity than the process-standard argon; it also adds the benefit of soluble gas pores that can be removed through a HIPing process for porosities < 1% [57].

Montgomery et al. [145] reported using nitrogen and argon gas for angled upskins. They found no apparent differences as the conductivity of the solidified layers is orders of magnitude higher than the gas. However, Nezhadfar et al. [146] found that for 17-PH SS, the higher cooling rate of a nitrogen environment produced a finer microstructure and resulted in slightly higher strength and ductility than in argon. Pauzon et al. [147] observed no difference between side surface roughness or mechanical properties of Ar and N_2 prints of the same purity. However, they did find that prints using a nitrogen generator (~99.8% purity) increased oxygen pick-up by 100 ppm O_2 for more oxidation and powder degradation but no difference in mechanical properties. Dai and Gu [148] found in their simulations of keyhole melting in Al and Ti alloys that using N_2 versus Ar shielding gas flow resulted in a less stable depression zone; this caused fluctuations of material stacking that would result in a rough layer surface. The effect was validated by observing a lower relative density in printed specimens. Other reported gas options include a 50-50 Ar-He mixture used by Mendoza [149] to produce thin-walled overhanging features. The use of pure helium was attempted by Montgomery et al. [145], but the low molecular weight gas had issues pumping to establish proper chamber partial pressure.

1.4.3 Powder Size

Powders for DMLS are produced by either gas, plasma, or water atomization. Although water-atomized powder is a low-cost and simple option and has been shown to produce

high-density parts for some powders [22], it is currently avoided by most manufacturers due to irregular particles and increased oxygen content [56]. Continued powder recycling can also result in a coarse powder, resulting in an increased overhang surface roughness [150]. Powder compaction increases thermal conductivity, though still orders of magnitude below that of a bulk material [151].

Due to the extensive potential distributions of metal powders and environmental interaction, effects from different powder sizes are not entirely predictable. An increased amount of fine powder can have the positive effects of increased powder bed packing density [152], lower energy melting [153], increased density, better layer surface quality, and higher mechanical strength [154]. However, too many small particles can give rise to the negative impacts of increased particle agglomerates impeding flow [152], increased powder bed reflectivity reducing laser energy absorption for consolidation [155], increased powder spatter and vaporization leading to lower density at high energy input [79, 152], and sensitivity to humidity impeding flow characteristics [156]. Additionally, wider PSDs allow for increased packing, higher density, and smoother side surfaces, whereas narrow PSDs result in better flowability, higher tensile strength, and higher hardness [79]. When the effective layer thickness is much less than the powder size, the recoating removes larger particles and thus changes the PSD and powder packing [155].

1.5 Strategies and Current Limits of DMLS Roughness Reduction

Methods to address the high surface roughness of DMLS prints include process parameters, post-processing technologies, and pre-processing of the build layout or exposure. Supports are the first-line approach for maintaining downskin surface integrity while reducing

warping, though manual removal increases the risk of part bending, and support connections leave residual fragments [108]. Contactless supports, such as in Figure 16, have been used to allow heat conduction and avoid the warping of specimens while allowing for improved downskin surface quality, as dross effects from heat accumulation are reduced without fused connections to the surface [110, 157]. However, these supports would be limited to accessible geometry and increase material usage. Lefky et al. [158] developed a process using carburization and chemical etching to achieve self-terminating support removal. Like other chemical-based post-processing, the use of applicable chemicals inflicts a high amount of chemical waste; they may also be restricted for a given application. Another method of support removal may involve hybrid manufacturing, where CNC milling makes surface-conforming cuts. However, the bending of solid supports induces stresses in the surface layers [159].

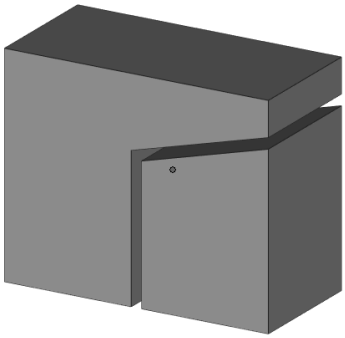

Figure 16: A 15° overhang specimen with the general contactless support type used by Cooper et al. **[157]**

Selective Laser Erosion and Laser Surface Re-melting can be applied within the build process after any number of layers to improve densification, reduce step size, or smooth the final surface layer [18]. Re-melting layers can be performed in some SLM machines of capable adjustability; direct rescans of scan vectors, rotated vectors, or vectors shifted by a half h_d are potential re-scan strategies [11]. The re-melting procedure can also be

conducted post-build on part surfaces to improve the roughness of different angled surfaces by up to 80% and leave a fully dense surface [160]. However, this treatment can only address certain visible or accessible surfaces.

Chemical-based post-processing includes chemical polishing or "chempolishing," electropolishing, "dry" electropolishing, and chemical-abrasive flow machining [161-163]. Other non-chemical post-processing methods include hydrodynamic cavitation abrasive finishing (HCAF) [164], abrasive fluidized bed machining [165], abrasive flow machining (AFM) [166], stream finishing [167], or the more accessible and commonly used sandblasting, grinding, and CNC machining. These post-processes improve surface roughness for varying degrees of part complexity. Time, consumables, cost, and material loss are common issues for all current post-processing methods in varying capacities.

Shot peening compresses a surface by cold working with high-velocity ceramic beads; at high pressures, this can significantly reduce roughness, though the surfaces must have an open line-of-sight for the projectile media, and the process requires manual labour [136].

Abrasive flow machining is a material removal process by passing a polymeric fluid with abrasives through or over a part. Bouland et al. [166] showed AFM to be capable of lowering the surface roughness of DMLS Ti-6Al-4V to as low as 0.2 µm Ra for angled upskins (Ra = 22 µm @ 45°) and just below 0.8 µm for angled downskins (Ra = 26 µm @ 45°); the effectiveness of AFM would increase for the softer 316L. However, the roughness reduction and material removal rates level off at an increased number of passes, and the effectiveness is diminished for the rougher surfaces. As such, heterogeneous part surface roughness and a high maximum Ra would cause non-homogeneous material removal and

lower feasibility of smooth surfaces below 1 µm Ra. The effectiveness of AFM processing on internal channels depends on the relationship between design complexity and fluid viscosity [163].

Nagalingam et al. [168] presented the novel process of HCAF for surface treatment of DMLS parts; a closed loop hydrodynamic system of water and concentrations of abrasives generates cavitation bubbles that implode and project the abrasives to erode the rough surfaces. In subsequent works, the authors showed the capability to achieve an Ra of 0.5µm from an initial Ra of up to 19 µm even complex internal channels, a potentially improved polishing ability than AFM [164, 169]. However, they show how the process efficiency is improved for lower initial surface roughness due to long processing time, converging roughness reduction, and increasing material removal rates with time [170].

Electropolishing uses strong acids as electrolytes and cathodes to remove metal ions from the rough surface [162]. This process requires conformal electrodes that limit the processing to only accessible surfaces and is, therefore, not applicable to complex geometries or internal channels [163]. Dry electropolishing is a newer technique that addresses this issue and the excessive use of chemicals by introducing micro-powder as electrodes with small amounts of acid electrolyte. Though still with some limitations in applicable part complexity, this process has so far been shown to achieve low roughness below 0.8 µm Ra from initial Ra up to 12 µm [162, 171]. Mohammadian et al. [162] tested a combined chemical-abrasive flow polishing to remove adhered particles and reduce surface roughness more effectively than either individual treatment. However, the process took numerous hours and was less effective for unsupported overhangs of 17 µm Ra (20%

reduction versus 45% for 7 µm). They concluded that a large increase in fluid velocity might improve the performance.

Post-processes such as electropolishing prove that polished surfaces for select DMLS-printed geometries are attainable. The material removal post-processing methods of AFM and HCAF are in ongoing process optimization, but they both display potential in achieving polished surfaces in complex DMLS parts without the wastes of chemical solutions. Nonetheless, lowering surface roughness is key for ensuring attainable final Ra values and process efficiency.

Pre-processing methods include part orientation optimization for minimal overhangs [172]. Rott et al. [173] developed an orientation process that maximized surfaces with the laser incidence angled into the part to ensure proper heat conduction, as surfaces facing away from the laser source accumulate adhered powder and dross [174]. However, not all surfaces in complex parts are improvable through orientation. These approaches only improve the average part roughness or specific area roughness, not the maximum roughness. Yeung [175] implemented a geometric conductance factor to the laser exposure, which variably adjusts the power level based on the heat conduction potential. Effectively, the energy input near edges and overhangs is reduced, which may require additional control for porosity. Objectively, these methods of feed-forward power control have great potential and can be combined with feedback from process monitoring, such as the melt track height monitoring of DePond et al. [111] for in-situ improvements to the models. However, implementing these approaches is not possible for many existing industrial machines, pending integration by the manufacturer due to software and hardware limitations.

At the design level, methods may involve compensating the CAD model for geometric defects, such as with an analytical model for residual stress-induced overhang warp prediction, to improve the accuracy of overhanging channels [176]. However, compensation methods are most effective for discrete geometries and not complex parts. Topology optimization can be constrained to maximum overhang angles for AM-printable generated designs [177]. Designers also implement printable geometries such as the channel shape shown in Figure 17 [37]. Despite these approaches to printable designs in DMLS, the low printability of unsupported overhangs limits the efficiency of designs and constrains the freedom of complexity that AM processes aim to achieve.

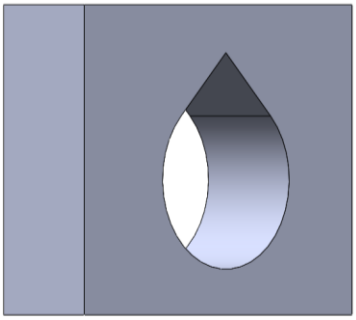

Figure 17: Teardrop channel geometry with printable 45° overhangs, as proposed by Thomas et al. **[37]**

Overall, most pre-processing design and build orientation approaches to lowering high as-built surface roughness do not address the maximum roughness for overhanging geometries. These solutions either focus on minimizing overhang areas, designing geometry compensations, or are not universal for existing machines. Other in-process methods, such as re-melting and optimized supports, are limited to accessible geometries and may reduce process efficiency and add waste. On the other hand, post-processing can effectively lower surface roughness down to polished levels depending on the process used and part complexity. However, post-processing efforts should be minimized as they are

costly and require excess time, labour, energy, and consumables that may include amounts of harsh chemicals. A desire is thus to achieve the lowest possible surface roughness within the build process through exposure and build settings. Lowering as-built surface roughness can mitigate post-processing requirements, such as time, and allow for lower final surface roughness. As presented in Section 1.4.1, generalized trends for low-roughness processing regions are limited and differ based on part geometry. Approaches to lowering roughness in the literature have included optimization techniques, although many of these works focus only on top or side surfaces. However, to lower the surface roughness in as-built parts, lowering the maximum roughness in overhang downskins is most relevant and can lead to reduced support material [178].

1.5.1 Multiple Post-Contours

One exposure type available in EOSPRINT is contour exposures; these are scanned along the perimeter of a layer, mainly to re-melt and smooth the layer edges [138]. Tian et al. [138] found their lowest downskin surface roughness for a single contour print to be achieved with a lower P and the highest tested v; they noted that it is ideal to have an MP depth that does not exceed the powder size. However, contour exposures and infill exposures are interdependent, as shown by Patel [179], where side surface roughness improvement from a high VED infill was said to be caused by the larger denuded zones of the edges, improving the contour scan melting mode. Yang et al. [180] experimented with infill and contour exposure parameters for the overhang surfaces in AlSi10Mg printing using a Taguchi DOE. They found that a reduced infill VED and increased contour energy resulted in lowered surface roughness for the experimented range of P and v. This result

was explained by less powder adhesion from the infill and improved wettability of the contour to suppress MP sinking while having sufficient MP depth for proper melting/re-melting of adhered powder. In contrast, Feng et al. [112] found that higher-energy contours from increased P (more so than v) with consistent infill parameters led to an increased sinking of the MP and adhered powder, increasing overhang Ra. They also showed that at lower overhang angles, layered contours lack overlap and thus form a wavy contour. Therefore, overhang surface roughness improvement appears to involve optimizing VED-related parameters and properly matching the contour and infill energies.

The number of contours scanned can be increased, which has been shown to increase higher-angled upskin quality and reduce the edge effect [127]. Artzt et al. [181] found an in-to-out exposure of multiple low-P high-v post-contours that replace the infill areas to reduce surface roughness. However, it was also shown that the tested contour parameters resulted in inverse relationships for roughness and residual stress; low-energy contours had the best side surface roughness but the worst residual stress. A similar shell-core strategy using multiple contours was tested by Cloots et al. [182] for downskin angled overhangs; the use of contours was based on the finding that scan angles parallel to the overhangs were best for surface roughness due to the transverse conduction into the part. They found that the strategy could lower the critical overhang angle, and the success of the multiple contours was improved for an optimized infill exposure. However, the ‘shell’ of contours was required to be millimetres thick for angles below 35° and had a local porosity of around 5%.

1.6 Literature Review Summary

The DMLS process allows for the low-waste fabrication of high-density, high-performing 316L prints of intricate and innovative designs. Issues that limit process expansion include porosity, complex microstructures and anisotropy, residual stress, and high surface roughness. Limited functional knowledge of the relationships between these performance characteristics and process parameters has made it difficult for researchers to relate results between machines. Process mapping using analytical models is limited for process optimization and does not account for the variability of AM parts. Likewise, simulation methods are not currently at a level for application to builds other than for general insight.

Dynamic microstructural and powder consolidation phenomena are ascribable to the MP and scan track characteristics. These mechanics yield the intrinsically complex physical and mechanical properties in DMLS and make for parameter interactions and property trade-offs that are challenging to model. Microstructures in DMLS include hierarchical structures of sub-grain cellular dislocation networks and competitive epitaxial grain growth. Scan track phenomena related to MP instability, vaporized material, adhered powder, and dross formation result in defects that compromise surface quality and mechanical performance. The main process parameters of P, v, h_d, and t—often oversimplified as VED—, laser beam focus, shielding gas, and powder characteristics, have varying effects on build performance. Post-processing of parts includes heat treatment for stress relief or recrystallization, build platform and support removal, and mechanical or chemical surface treatments. Though some post-processes are more effective than others, all are limited by part complexity and initial roughness. These processes require long

processing times, induce excess costs in labour and consumables, and produce material wastes—including harsh chemicals. Thus, high as-built surface roughness must be addressed to reduce post-processing efforts for desirable roughness. Existing literature towards this goal mainly focuses on surfaces other than downskins, which pose the greatest process limitation. Increased experimental knowledge of the build parameter effects on these surfaces is required, including the potential of multiple post-contour strategies that have shown promise for reduced surface roughness but are incompletely tested for their applicability to overhanging geometry.

1.7 Thesis Overview and Objective

In powder-bed fusion-based metal AM, there are difficulties with part surface roughness and support structures, which require costly post-processing and limit design. Furthermore, a trade-off with part porosity limits the ability to improve down-facing surface roughness by only reducing laser energy; a more methodical approach is required. In this thesis, part roughness is reduced in the DMLS process through parameter experimentation and DOE methods to understand and optimize surface roughness with constrained density and characterization of other part properties. Improvements to build performance and capabilities are verified through application to an AM design with complex geometry. Experimental surface roughness optimization by modifying process parameters improves as-built surface quality for complex designs while maintaining high part density.

The objectives of this research are regarding experiments in DMLS and are as follows:

- Develop and apply a novel and accessible benchmarking methodology to compare a full suite of print performance characterizations in metal AM/DMLS processes.

- Investigate the effectiveness and potential of using multiple contour strategies to decrease overhang roughness.
- Determine the effect of a finer powder PSD and nitrogen shielding gas on the surface roughness of DMLS with respect to relative density, residual stress, and mechanical properties.
- Analyze and optimize the primary exposure parameters of DMLS for minimal surface roughness with maintained porosity below 1%; validate process settings through application to a complex DMLS part design.

This thesis is organized into chapters to detail the characterization methods and discussion or results in separate sections of combined experimental studies. Following this introduction and literature review, CHAPTER 2 describes the characterization techniques used throughout all experiments. CHAPTER 3 explains the experimental methods for each benchmarking and surface roughness investigation objective. CHAPTER 4 presents the results of characterization techniques used in the benchmarking and surface roughness experiments. This chapter also includes a discussion and analysis of the results and their limitations. CHAPTER 5 provides a case study of applying developed parameters to a complex AM heat exchanger design geometry, along with a developed consideration for a potential industrial application and the required next steps toward this purpose. CHAPTER 6 concludes the research project with a final examination of findings and recommendations for future work toward process understanding and surface roughness reduction in DMLS.

CHAPTER 2

Characterization Techniques

2.1 Benchmark Test Artifact

An innovative test artifact was developed for the benchmarking of metal AM processes. In this case, two DMLS machines were tested using the benchmark artifact: EOS M290 (build envelope of 250 x 250 x 325 mm) and EOS M100 (build envelope of Ø100 x 95 mm). The artifact aims to compare builds on the two printers to identify variations in build quality between the machines, as well as the impact of specific XY and Z orientations of features. Several specific requirements not addressed previously drive the need for a novel test artifact. First, the benchmarking benefits from the evaluation of as-built mechanical properties, so features must be designed and located in such a way as to require minimal post-processing, including cutting or machining, before conducting tensile and hardness tests. The new test specimen was also developed to include a measure for residual stress. Finally, it was adapted for the geometry of the M100 build envelope (Ø100 x 95 mm), which would not be possible through simple scaling of previously developed artifacts. Such a test artifact allows for a simple yet comprehensive qualitative and quantitative assessment of print performance.

2.1.1 Design

The model for the newly presented test artifact is shown in Figure 18 and Figure 19. The artifact is modified after the proposed artifact of Moylan [13]. The overall dimensions for the build are 70 mm x 70 mm to reach the outer regions of the M100 build envelope. The artifacts are printed in a diamond with respect to the recoater blade to mitigate issues from

sudden increases in cross-sectional area. The design includes small PAR (2) and PERP (6) features, steps for Z-axis error measurements (7), straight surfaces of various orientations (3), a ramp for analyzing the stair effect (13), and tower features for testing the printable aspect ratio (12) for which the general rule has been cited as 7:1 [183]. The artifact also includes unsupported circular (1), angled (5), and bridge-type overhangs (11). The bridge-type overhangs allow for examining an increased severity of overheating effects, which can be attributed to the poor conductivity of the supporting powder [184]. A description of all feature types and their means of measurement is seen in Table 2. Simple overhang measurements are used to capture dross effects with easily available tools for performance characterization of downskin quality.

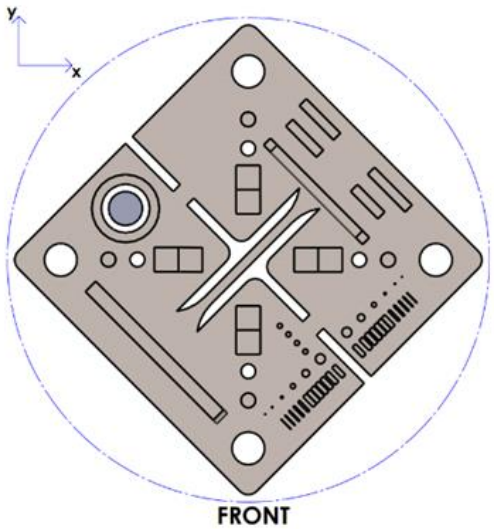

Figure 18: Top view of the test artifact placement on an M100 build platform

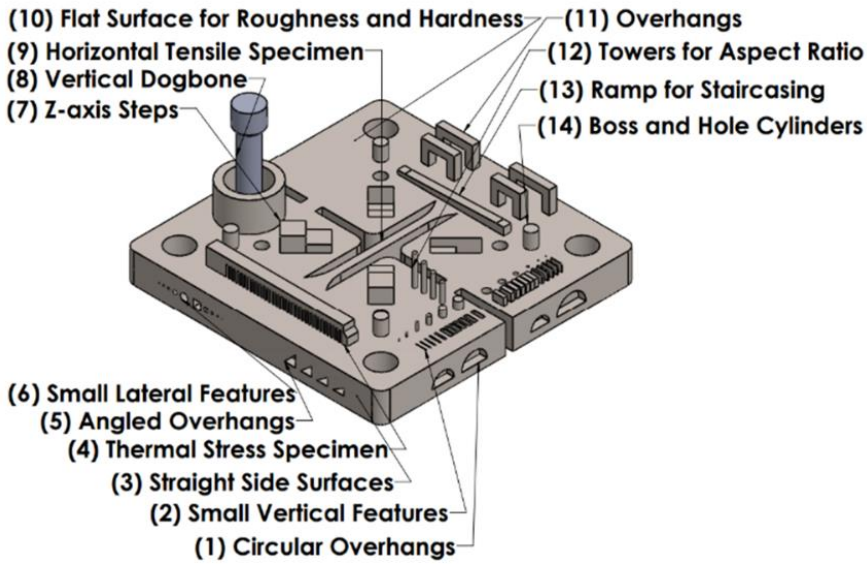

Figure 19: Novel test artifact design with feature labels

Table 2: Test artifact feature types, dimensions, and characterization tools

Feature No.	Type of Feature	Dimensions	Inspection Method
1	Circular overhangs	5 – 8 mm diameter	ISM Digital Analyzer
2	Small PAR features	0.1 – 2 mm	ISM Digital Analyzer
3	Straight side surfaces	70 mm	Calipers, indicator
4	Thermal stress specimen	38.5 mm length	Height gauge
5	Angled overhangs	30 – 45 degrees	ISM Digital Analyzer
6	Small PERP features	0.1 – 2 mm	ISM Digital Analyzer
7	Z-axis steps	2 mm	Height gauge
8	PAR-oriented tensile specimen	5 mm diameter	TQ SM1002 Bench Top Tensile Testing Machine
9	PERP-oriented tensile specimen	2 mm x 8 mm	TQ SM1002 Bench Top Tensile Testing Machine
10	Flat surface for roughness and hardness	n/a	Starrett SR300 Surface Roughness Tester, TQ SM1002 Bench Top Tensile Testing Machine, and ISM Digital Analyzer
11	Overhangs	4 – 7 mm	ISM Digital Analyzer
12	Towers for aspect ratio	5 – 8 mm length, 1 mm diameter	ISM Digital Analyzer
13	Ramp for staircasing	1 mm rise, 25 mm run	Starrett SR300 Surface Roughness Tester
14	Boss and hole cylinders	3 mm diameter	Calipers

Test prints of previous artifact iterations led to changes in the final design. The PAR tensile specimen was adjusted and shortened as insufficient powder feeding near build heights of 50 mm was identified as an issue on the M100 due to the powder hopper volume. An additional cone volume support pattern was developed for the outer edges of the part to prevent the corners from lifting due to thermal stresses.

2.1.2 Features and Characterization

A cantilever beam 38.5 mm in length is included to assess the magnitude of residual stresses created during manufacturing. The inclusion of this feature on the test artifact (4), shown in Figure 20, allows for a relative measure of residual thermal stresses in the artifact. The percent deflection at the tip of the feature is measured after an incision is made to remove the supporting legs of the cantilever piece (see Section 2.5).

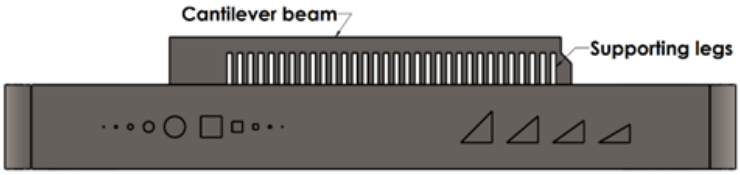

Figure 20: Side view of residual stress deflection specimen

The test artifact included specified areas on both the top surface and the sides for Ra and average peak-to-valley height roughness (Rz) measurements to be taken using a Starrett SR300 Surface Roughness Tester. Three measurements are taken and averaged for specified directions on the top and side surface areas.

Designated areas are also defined on both the top (or PERP) and side (or PAR) surfaces of the test specimen for Brinell Hardness (HB) testing following ASTM E10 [185]. The top surface area used is noted in Figure 19 (10) and allows for three indents with sufficient

spacing (3 x diameter). The side indents were made near the circular overhangs. Indent surfaces were ground using 120-grit abrasive paper before the indents were taken to reduce optical measurement error from the rough surfaces; no intensive polishing procedure is required. HB values from the indents on each surface were taken and averaged for comparisons. Using a TQ SM1002 Bench Top Tensile Testing Machine and a digital microscope, the diameter of the indentation resulting from a 1500 kgf load and 10-mm steel indenter is measured.

The artifact includes two specimens for tensile strength testing. The specimens are oriented orthogonally, as it has been shown that the build orientation of parts printed through DMLS processes impacts their strength properties greatly [85]. The specimens will identify how these variations may be different between machines. One specimen is a PAR-oriented round dog bone to test strength in the Z direction (see Section 2.6). The other specimen is a PERP-oriented plate-type dog bone designed into the test artifact base in the XY direction. The specimen has a nominal cross-section of 2 mm x 8 mm with 10 mm corner radii. The PERP specimen was designed as part of the main body for spatial efficiency; it also allows for direct measurement of the test artifact strength as it will conduct thermal energy through the artifact. This tensile testing requires a custom gripper to ensure the applied force is axially loaded. Both specimens are tested as-built to simulate the mechanical behaviour of a part printed with minimal post-processing, including any effects from the surface quality.

Two methods of characterizing the dimensional capabilities of the printers are considered: minimum feature size and overall accuracy of dimensional features. The minimum feature

size is assessed by a qualitative observation of the print success for PAR rectangular and circular bosses and holes and PERP square and circular holes. Overall accuracy is determined using the dimensional errors of the boss and hole features, step features, and artifact boundaries. Maximum and minimum errors make up the tolerance range for the printers.

2.1.2.1 Overhang Features

Three different unsupported overhanging features are assessed through the test artifact: straight overhangs, circular overhangs, and angled overhangs. All three overhang types require different evaluation measures to efficiently quantify their print success and dross defects.

Four unsupported straight overhang bridges were included in the test artifact at lengths from 4-7 mm to test the limits of unsupported overhangs. Though there is observed overheating and burning, the surface morphology of the straight overhangs is dominated by dross formation and sagging. Dross formation in metal AM is primarily due to the sintering of supporting powder as the heat dissipation through the powder is restricted, providing lower conductivity than support structures, so more energy is absorbed, and the MP sinks due to gravity and capillary forces. The related sagging occurs when there is insufficient support for the large melt structure [186, 187]. As such, this accumulation is characterized by its 2D area. The area of the additional dross is determined by taking five equally spaced measurements of the bridge thickness with a digital microscope; the area can then be calculated using the Midpoint Rule. The error of the bridge area from the CAD

model can then be calculated to find what will be labelled as dross area error (DAE). Figure 21 shows an example of the dross formation observed.

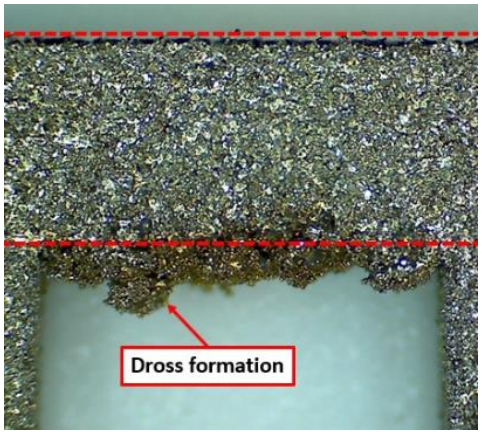

Figure 21: Excess dross formation of a 4-mm straight overhang (M100) for DAE measurement, with the nominal 2-mm thickness shown by the dashed lines

The circular overhangs are characterized by the theoretical eccentricity of the half-circle. Eccentricity has been used to characterize metal L-PBF features [188, 189]. For the arc overhangs, eccentricity is essentially used as a measure of the extent to which the rough dross defects of unsupported arcs impact the accuracy of the circular geometry. Measurements are taken of the major axis (the base length, d_M) and the minor axis (the maximum arc height, r_m). The resulting eccentricity, e, is calculated with equation (2).

$$e = \sqrt{1 - \frac{(2r_m)^2}{d_M^2}} \quad \textbf{(2)}$$

The dross on the angle overhangs is characterized by the error of the height dimension (opposite the orientation angle) measured by a digital microscope, as shown in Figure 22.

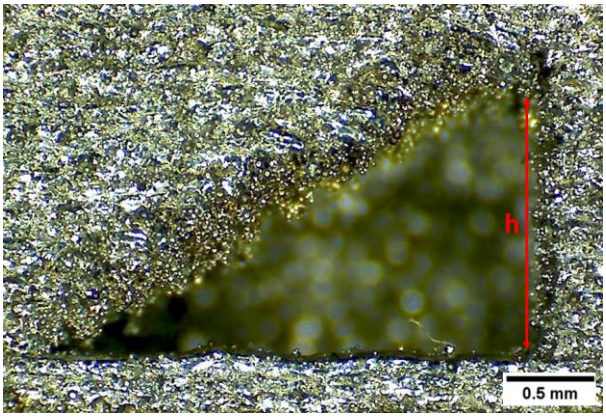

Figure 22: Measured dimension for the simple angle overhang characterization

2.1.3 Small Specimens

The small specimen used in addition to the test artifact in this study is shown in Figure 23. The design includes key features designed for physical and mechanical investigation. Features included in this condensed design are small PAR features (1), angled overhangs (2), a flat top surface for hardness measurements (3), flat surfaces for roughness measurements (3 & 4), major dimensions (5), and a designated cross-section location for longitudinal microstructural and density inspections (6). All measurement techniques are the same as for the test artifact, where calipers are used to measure the major dimensions.

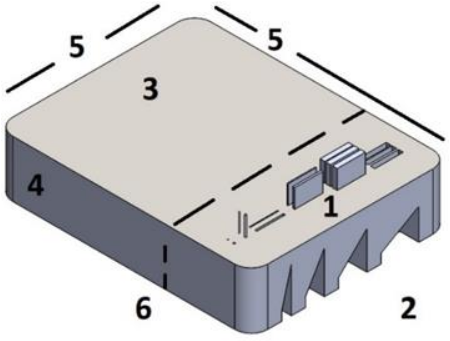

Figure 23: Labelled design of the smaller test specimen

2.2 Surface Specimen Layout

Surface test artifacts were required to assess the effect of process parameters on the quality of DMLS surfaces. The primary goal of these specimens is to compare surface profiles of unsupported geometries for different build conditions to ultimately compare the quality of overhangs. A review of surface artifacts in the literature was used to develop specific specimen design criteria to support the desired suite of surface quality evaluations [35, 140, 161, 175, 186]. The specimens were to:

- include unsupported geometries from 30° to 90°,
- allow cross-sectioning for microscopy,
- allow for hardness and tensile strength testing,
- allow for 3D scanning and stylus profilometry of upskins and downskins,
- test concave, convex, and flat overhang geometries, and
- test support structure success and effects (qualitative/visual).

The selected surface artifact design methodology was similar to Calignano [186] in that individual specimen pieces were designed to inspect each geometry type: curved, angled, and straight ledge overhangs. The different geometries allow for comparison of surface performance in a range of part geometry scenarios, which may vary for dross formation and warping from different build conditions. The ‘angle specimen’ in Figure 24a includes angled fingers with top and bottom surfaces angled from 15° to 90° in 15° increments. Support structures are applied to the 15° strut to serve as a qualitative assessment of any defects for these surfaces. The angled fingers can be cut from the specimen for confocal microscope profilometry. The curved specimen is shown in Figure 24b; it has both convex

and concave overhangs with 5-mm radii. The ledge specimen is shown in Figure 24c; three ledge lengths are included: 0.25 mm, 0.5 mm, and 1 mm.

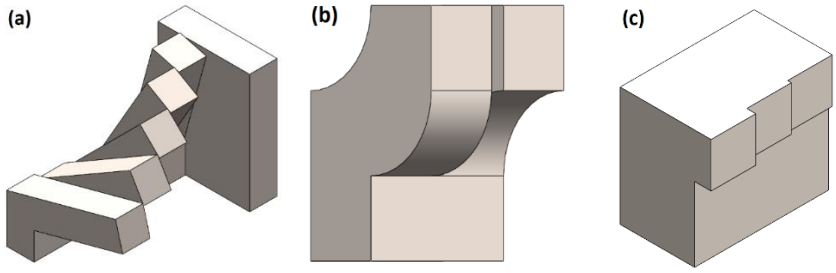

Figure 24: Overhang geometry specimens for surface inspection: a) angles, b) curves, c) ledges

The build layout for the M100 prints can be seen in Figure 25. There are three of each overhang test specimen for statistical comparison for each surface type between prints. Also included in the builds are dogbones for tensile testing and deflection specimens for a relative measure of residual stress. All parts are angled by 5° to reduce abrupt changes in the contact area with the recoater (travelling left to right). The parts are also staggered to minimize potential collateral damage from poor surface quality. Overhanging geometries are positioned to face towards the right so that angles slope in the recoating direction. All M100 builds are printed at 20 µm layer thickness as opposed to 40 µm for the M290 builds.

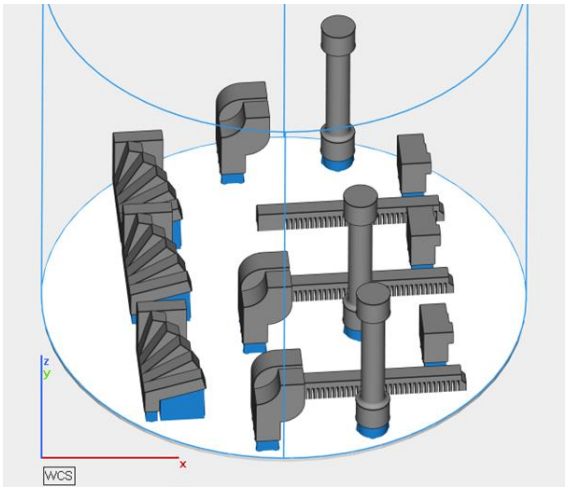

Figure 25: Surface inspection build layout for the M100 experiment runs

2.3 Roughness Parameter Measurement

The two main roughness parameters calculated in this study are arithmetic mean deviation (Ra) and average peak-to-valley height (Rz). These parameters are calculated using a profile of deviations (y) and sampling points (n) as shown in equations (3) and (4), where both are calculated for each sampling length of a total evaluation length and averaged [190].

$$Ra = \frac{1}{n}\sum_{i=1}^{n}|y_i| \quad \textbf{(3)}$$

$$Rz = Rp\ (max.peak\ height) + Rv\ (max.valley\ depth) \quad \textbf{(4)}$$

2.3.1 Contact Profilometry

Ra and Rz roughness parameters were collected using a Mitutoyo SJ-410 contact profilometer with a 5-µm stylus. A 2.5 mm cut-off length wavelength was selected based on recommendations from Triantaphyllou et al. [191] and a short-wave cut-off of 8 µm; the total evaluation length was 7.5 mm for each measured surface. Other roughness parameters of mean profile element width (RSm) and peak count (RPc) were also measured but were not the focus of the characterization for surface roughness reduction. These parameters can indicate transitions from surfaces dominated by adhered powder particles (low RSm, high RPc) to those dominated by melt track formations (high RSm, low RPc) [192]. Plots for the additional roughness parameters are found in **Appendix D.**

2.3.2 Non-Contact Optical Profilometry

Optical profilometry was conducted using a Nanovea ST-400 chromatic confocal microscope profilometer. Optimized and default downskins were characterized. A 400-micron-range probe was used, with the scan parameters set to a 100 Hz frequency and a spacing of 5 µm in the X and Y axes. Scans of 2.5 mm x 5 mm were collected for one 30° downskin surface from each exposure type. Any non-measured points were automatically filled. Colour maps of the roughness surface heights were generated in addition to the areal arithmetic mean height parameter (Sa).

2.3.3 Optical Microscope Method

Optical microscopy (OM) images of polished cross-sections are used to calculate the roughness parameters of inaccessible surfaces; the direct method is described and applied in Section 5.4. This technique also allows for the observation of re-entrant features, visible in Figure 26, that are not captured by profilometry methods [193]. That said, the calculations of Ra in this work do not include values for re-entrant features; they are filtered out to imitate profilometry inspection.

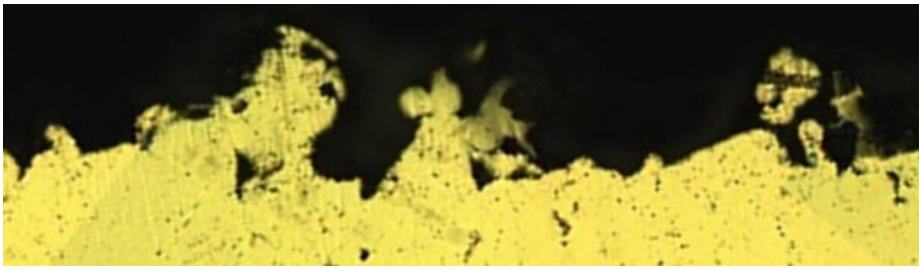

Figure 26: Cross-section of a DMLS overhang surface with protrusion-formed re-entrant features

2.4 3D Scanning of Dimensional Error

Characterization of geometrical accuracy for the printed downskins is necessary to ensure no significant overhang surface defects, such as large dross formation or warping, that could potentially exceed part tolerances. A measured dimensional error from dross formation is still possible for low-roughness surfaces [140]. For this purpose, 3D part geometry data was acquired using a COMET L3D 5M 3D scanner. The field of view used was 45 x 38 x 30 mm^3 for a 3D point distance of 18 µm. STL files were generated and imported to the GOM Inspect software to extract the surface deviation data. The top surface of each measured overhang feature was aligned with the CAD model for surface comparison of the collected and nominal downskin surface data, as shown in Figure 27. The alignment was completed through an initial 3-point pre-alignment and a local best fit of the top surface. Output deviation measurements from the surface-to-CAD comparison are the maximum distance (max), minimum distance (min), area of valid distance (AVD), and integrated distance (ID), where the mean deviation (m) is the ID divided by AVD.

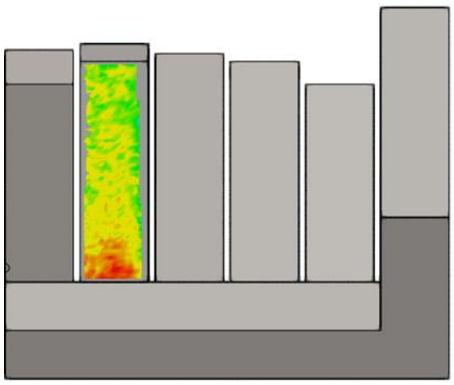

Figure 27: Surface comparison map, shown on the nominal part surface

For the statistical analysis of geometrical surface quality, neither min, max, nor mean deviation is suitable for comparing different surfaces, as none of these measures completely

represent the surface quality. As such, a surface quality index (k) proposed by Piscopo [141] is implemented so that a single parameter containing information about mean deviation and variation range (r = max - min) can be used for simplified analysis. The surface quality index is defined in equation (5), where input values are in millimetres:

$$k = (1 + m^2) \cdot r \quad \textbf{(5)}$$

In general, k decreases with improved surface quality; if the range (r) is low and the mean (m) is high, the mean will largely define k, but when m is near zero, r dominates. Surfaces with $k \geq 0.7$ could be roughly classified as having poor surface quality for a tolerance of ± 0.3 mm, though the parameter is used for relative comparisons and not for part tolerancing.

2.5 Residual Stress Deflection

Residual stress from the AM process is characterized using the deflection of a cantilever beam specimen, as implemented by Buchbinder [194]. The beam, shown in Figure 28, is 38.5 mm long and has supporting legs to hold the beam in place during the build. A relative measure of residual thermal stresses in the specimen is achieved by measuring the percent deflection at the tip of the cantilever piece; an incision is made with a hacksaw to remove the supporting legs. Residual stresses resulting from the large, localized temperature cycling of the layer-by-layer process are built up in the part. The stresses become uneven as the beam supports are removed, and the unstable beam deflects [51].

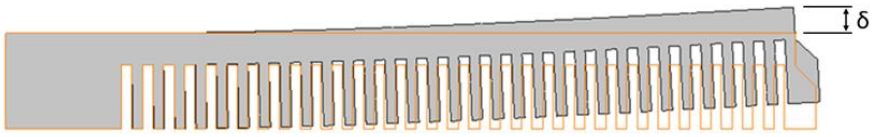

Figure 28: Residual stress specimen design showing the beam deflection (δ)

2.6 Tensile Strength

UTS was measured for all successfully printed dogbones in their as-built condition, with minimal post-processing, to include any influence from surface defects. Specimens used for tensile testing are designed for a TQ SM1002 Bench Top Tensile Testing Machine (5-mm diameter, 22-mm test length, and 1-mm radii).

2.7 Density

The relative density of printed test specimens in this work is determined using microscope image processing, described in Section 2.7.2. Additionally, an initial comparison of density results using Archimedes' method was conducted for a set of printed disks and is described in Section 2.7.1. The comparison is meant to validate image processing estimations of relative density for the test specimens, as they would not be easily measured using Archimedes' method.

2.7.1 Archimedes' Method

The densities of Ø50 x 10 mm disks printed on the EOS machines were measured using Archimedes' method, according to ASTM B962 [195], as well as the previously described image analysis method for comparison. A total of five disks were printed, two on the M100 and three on the M290. These disks were finely ground on all surfaces to reduce error, although no oil impregnation was used as there was no excessive surface porosity.

2.7.2 Optical Microscope Porosity

The relative density of printed specimens is measured through image processing of polished cross-section OM images, such as Figure 29. This method is popular in the literature as Archimedes' fractional density measurements have high standard deviations at

high densities [79, 135]. Specimens are sectioned to capture the plane perpendicular to the build direction, roughly in the middle of the part height. Digital images are taken through an Olympus microscope at 100X magnification. A MATLAB script is used to convert the image to binary using a determined threshold, and then porosity is estimated as the ratio of black pixels to white pixels. Five images are taken along the center of each cross-section, and the calculated densities are averaged.

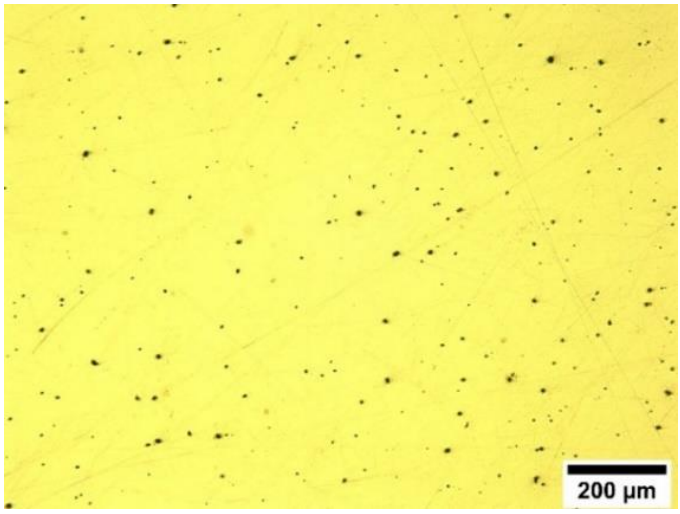

Figure 29: OM image of a polished cross-section (part #2 of the DOE print) before binary conversion, showing the dark spots of distributed gas pores

2.8 Vickers Microhardness

Vickers Microhardness of the polished cross-sections was measured using a MICROMET 1600-6100 microhardness tester following ASTM E92 [196]. A load of 1 kgf was selected, with a dwell time of 15s, for an indent that properly fits the 40X objective lens field-of-view (FOV) to reduce measurement error, as shown in Figure 30. The machine calibration was verified using a Buehler test block of 254 HV1. A minimum of two different indents in different areas of the cross-section were measured for each sample tested.

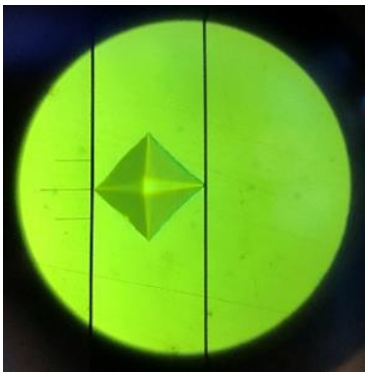

Figure 30: FOV of the 40X lens for Vickers indents

2.9 Microstructure

Specimens were prepared for OM inspection with a final polish of 0.1 µm alumina suspension and a swabbing etch using Kalling's No.2 etchant. The etch duration was less than one minute to reveal the MPs and roughly two minutes for the grain boundaries. OM images of the microstructure are shown throughout the thesis body and in **Appendix B.**

As a tool for the benchmarking procedure, OM inspection offers a widely available and simple technique for an efficient inspection of microstructural features. The other microscopy techniques of increasing magnification, SEM and TEM, also require increasing levels of sample preparation. However, the various-sized features of the benchmark specimen would allow for any desired microstructural characterization to be conducted on available machines. Any observation of hierarchical morphology, phases, or inclusions through OM is qualitative.

2.10 Statistical Analysis

Statistical analysis for comparing build parameter adjustments in the M100 printer was either achieved through one-way ANOVA or individual t-tests using Minitab software. One-way ANOVA was conducted for tests with multiple groups to analyze the significance

of geometry trends and differences between the experimental test conditions. Levene's tests for equal variances were conducted for each one-way ANOVA. When significance was found, a post-hoc Tukey HSD test was performed to determine which groups differed. T-tests performed did not assume equal variances. When applicable, a power analysis with power = 0.8 (20% type II error rate) was conducted to determine the range of which values are shown to be statistically similar. The alpha level for all statistical analyses is $\alpha = 0.05$.

For the response surface analysis, regression models were constructed using a stepwise term removal with a threshold of $p = 0.15$. Models are presented with contour plots for 30° downskins, average upskins, and top (0°) surfaces, as well as for other measurements of relative density, deflection, geometrical deviations, and microhardness. The 30° surface model was used for the optimization objective of downskins as these surfaces have the highest roughness, so optimizing them would result in the greatest improvement to the overall surface roughness of the part. The multi-objective response optimization was constructed in Minitab using the 30° downskin Ra and relative density models. Ra was minimized with a weight and importance of 10, whereas relative density was maximized with a weight and importance of 1, so lowering surface roughness was prioritized. A lower limit of 99.4% was set for relative density.

CHAPTER 3

Experimental Methods

3.1 Benchmarking

3.1.1 Default Parameters

All artifacts were printed using the default parameters of the respective machine. A comparison of the printers for machine specifications and energy density of the default 'stripes' skin exposure parameters is seen in Table 3. The M100 printer has a smaller build volume and build platform, a lower-power laser, a smaller laser focus diameter, and a smaller default layer thickness. The M100 has a higher default VED.

Table 3: Key differences in EOS printers

Machine Specification	EOS M100	EOS M290
Build Envelope	Ø 100 x 95 mm	250 x 250 x 325 mm
Laser Type	200 W Yb fibre laser	400 W Yb fibre laser
Focus Diameter	40 µm	100 µm
Layer Thickness	20 µm	40 µm
Default VED	92.5 J/mm^3	57.7 J/mm^3

In addition to the differences between machines, two 316L SS powders were in use for the benchmarking print jobs: EOS StainlessSteel 316L powder in the M100 printer and Carpenter CT PowderRange 316L in the M290. The particle size distributions of the powders were determined using an optical microscopy (OM) imaging technique for projected area diameter and are shown in Figure 31. The median (D50) powder sizes for the EOS and CT powders are 25.85 and 32.75 µm, respectively; the CT powder size is confirmed to agree with the given range of 32.5 – 34.4 µm [197]. A comparison of the powder compositions is found in Table 4. The difference in powder size should not have a substantial effect on the print properties.

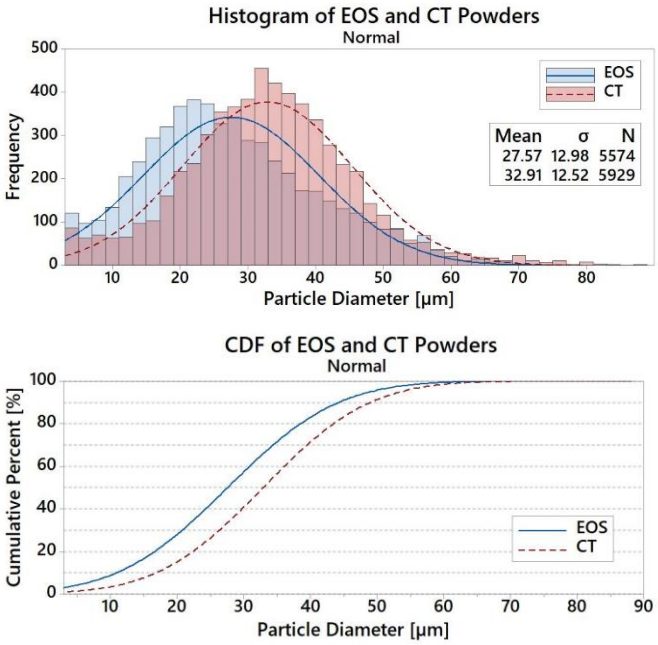

Figure 31: PSD of 316L powders as a histogram (top) and a Cumulative Distribution Function (CDF) plot (bottom)

Table 4: Chemical compositions of the 316L powders

Element	**CT (wt. %)** [197]	**EOS (wt. %)** [126]
Fe	Balance	Balance
Cr	17.0-18.0	17.00-19.00
Ni	12.0-13.0	13.00-15.00
Mo	2.00-2.50	2.25-3.00
Mn	< 2.00	< 2.00
Si	< 0.75	< 0.75
P	< 0.030	< 0.025
C	< 0.030	< 0.030
S	< 0.015	< 0.010
Cu	< 0.75	< 0.5
N	< 0.10	< 0.10
O	< 0.10	-

Due to the difference in build platform size, the default pre-heating of the M290 build platform was kept; the pre-heated M290 build platform is expected to result in a more

similar heat conduction behaviour as the M100. Steinlechner [28] found the pre-heating of 180 °C in the M290 to yield similar hardness as M100 builds than the higher hardness from the M290 starting at room temperature, signifying a reduction in cooling rate.

A combined 12 test artifacts were printed on the M290 and M100 using CT PowderRange 316L and EOS StainlessSteel 316L powders, respectively [126, 197]. Two print jobs were completed on the M290 printer, with four artifacts in each run. The four artifacts were printed in two different orientations, 180 degrees from each other; a print layout on the build platform can be seen in Figure 32. The orientations on the second M290 print were rotated 180 degrees from the first print. The remaining four artifacts were printed individually on the M100, also at 0 and 180-degree orientations.

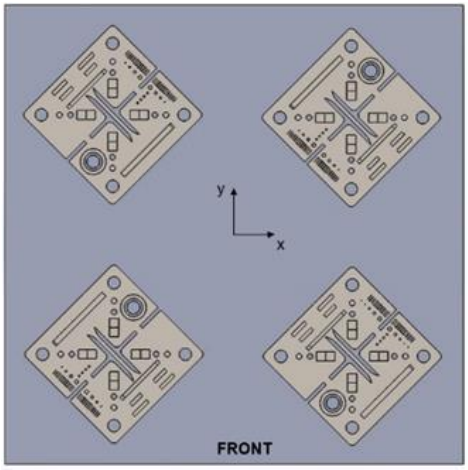

Figure 32: Layout of a test artifact print in the M290

Aside from test artifact prints, solid disks were printed on the M100 (two) and M290 (three) for a baseline Archimedes density measurement. The deflection specimen was included as a part of the test artifact but was first printed directly onto the build platform. Four deflection specimens were printed on the M100, and six on the M290, also printed with default process parameters.

3.1.2 Equalized Energy Density

Though machine-specific optimizations may yield different properties in separate printers, an ideal condition would be for a universal build parameter that can accurately predict print performance for any machine. Riabov and Bengtsson [198] attributed the inability to use their M290-optimized parameters for successful 316L printing on an M100 to the difference in laser spot size.

Oliveira [20] found that the range of energy densities that yield highly dense parts is wide. A dimensionless parameter (β) was proposed to be added to the classic VED equation (6): the ratio of powder grain size (g_s) over laser beam diameter (d_b). The dimensionless parameter was verified to narrow the VED range of reported high-density Ti-6Al-4V parts. They present the new energy density equation for comparing prints of different process conditions. They also note an added potential to help produce replicate experiments. Although only applied to relative density, it is suggested that the β·VED may produce comparable process regions for other properties [20]. This proposed VED equation had the potential to help relate the energy densities of the M100 and M290.

$$\beta \cdot VED = \left(\frac{g_s}{d_b}\right) \cdot \frac{P}{v \cdot t \cdot h_d} \quad \textbf{(6)}$$

Since the reported dimensionless parameter validation is only for Ti-6Al-4V, the same validation was first applied to published relative density values for 316L to see if the VED range is similarly narrowed. Figure 33 shows that the dimensionless parameter narrows the range of the density results, though not to the same extent as with the Ti-6Al-4V alloy. For reference [24], a $d_b >> g_s$ seems to result in an over-correction. Additionally, Figure 34 shows that with the dimensionless parameter applied, there is a more defined relationship

between published 316L densities and VED, where EDs above 40 J/mm^3 mostly produce higher-density parts.

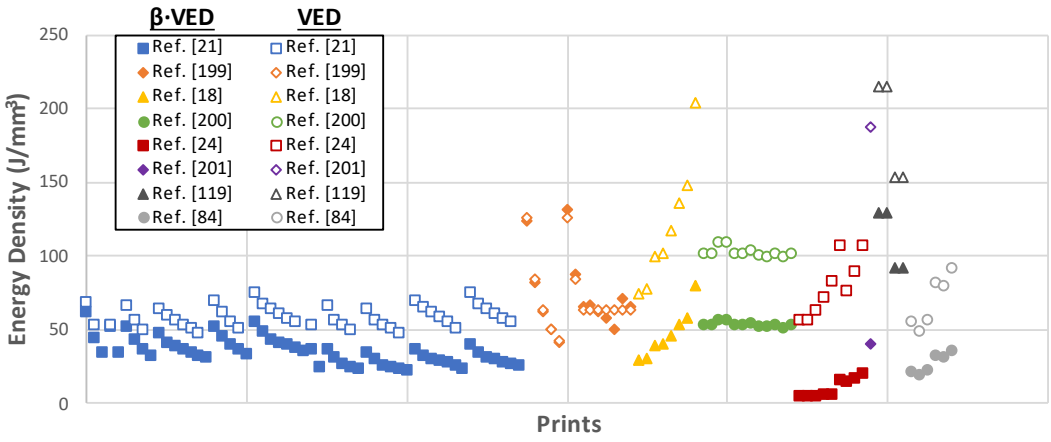

Figure 33: Comparison of VED calculations with (filled symbols) and without (open symbols) the dimensionless parameter for high density (>99%) 316L parts, using the same method as Oliveira et al. used for Ti-6Al-4V **[20]**

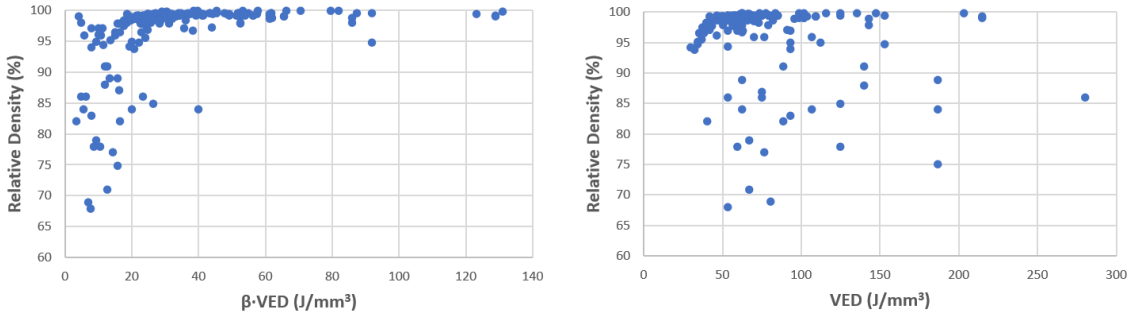

Figure 34: Relative density vs. VED with (left) and without (right) the dimensionless parameter (using references **[18, 21, 24, 69, 84, 119, 199-202]**)

An additional two prints of the test artifact were conducted on the M100 to test printing with similar energy input and process parameters as the M290 default settings. Both print jobs used the same layer thickness and hatch distance, but each print used a different method for equating the energy densities of the printers.

For the first print, the traditional VED equation is used. The M100 is equipped with a different laser than the M290, which is not capable of achieving 214.2 W, the M290 default power. As such, the linear energy density (LED) for this print was equated to that of the M290 default exposure using the maximum power (170 W) for the M100 (v = 736.6 mm/s).

For the second print, the dimensionless parameter proposed by Oliveira [20] is included in the equating of the printer LEDs. The powder grain size was assumed to be the same as in the M290. The laser scan speed was set to be the same as the M290, and the laser power was adjusted accordingly (P = 85.7 W) to equate the energy densities using the new equation. This inclusion of the dimensionless parameter was to test its ability to account for the increased heat localization from a smaller beam diameter when matching machine parameters. A table showing the energy densities for all print jobs using either equation can be seen in Table 5.

Table 5: Energy densities calculated for test artifact prints

	Part			
ED equation	M100	M290	M100_VED	M100_ $\beta \cdot VED$
VED (J/mm^3)	66.6	57.7	57.7	23.1
$\beta \cdot VED$ (J/mm^3)	58.3	20.2	50.5	20.2

3.1.3 Small Specimens

For the follow-up study of adjusting exposure parameters, the designed test artifact was condensed to a smaller specimen that maintains features which, in this case, were determined to be key features for inspection. These small specimens facilitate printing a 2^2 full factorial design with two replicates. This design allows for a low-cost analysis of the effects and interactions, as inputs such as argon shielding gas make running individual print jobs expensive.

Power and scan speed were selected as parameter factors to investigate first-order effects and second-order interactions; P and v make up LED and are the main influential parameters in most cases [203]. The levels for the factors were selected to be on either side of the default settings for both machines and to not result in a low LED that risks LOF print failure. Given that the default settings differ between machines and that the M290 has a higher-power laser, different P and v settings were selected for each printer. A factorial was also printed for the M100 at a 40-micron layer thickness for a comparable BR, which also required different factor settings as the t lowers the input VED. The design table with all factor levels for the stripe exposures can be seen in Table 6. The additional P and v settings for exposure parameter subsets were adjusted proportionally.

Table 6: Laser power and speed setting treatments for the small specimen DOE prints

M290			**M100 (20um)**			**M100 (40um)**		
Treatment	**Power (W)**	**Speed (mm/s)**	**Treatment**	**Power (W)**	**Speed (mm/s)**	**Treatment**	**Power (W)**	**Speed (mm/s)**
1	200	800	1	90	650	4	160	800
4	360	1000	2	160	650	1	140	550
4	360	1000	4	160	950	3	140	800
3	200	1000	3	90	950	1	140	550
1	200	800	1	90	650	2	160	550
3	200	1000	3	90	950	4	160	800
2	360	800	2	160	650	2	160	550
2	360	800	4	160	950	3	140	800

The specimens are designed to fit all treatments on a single M100 build platform, where the treatment positions on the build platform can be randomized. For example, the placements of the corresponding M290 print job specimens are seen in Figure 35.

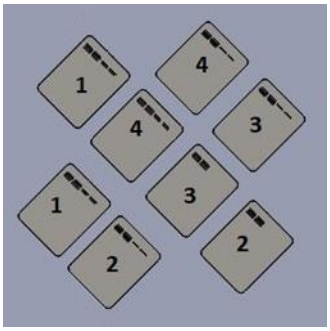

Figure 35: Placement of small specimen treatment parts for the M290 print job (build platform not to scale)

3.2 Surface Roughness Experiments

Both EOS M100 and EOS M290 printers were used for the surface roughness experiments. Following conclusions drawn from the benchmarking of the two machines, the M100 was used for all tests that adjusted build strategies. The M290 is needed for experiments focused on specific exposure parameter levels. Tests on the M100, as described in this section, include a shielding gas performance comparison, a powder size performance comparison, and comparisons of different exposure strategies using multiple contours. On the M290, a DOE response surface design varying main exposure parameters was printed, followed by a verification print. All experiments focus on the quality of DMLS surfaces, namely downskins, with the goal of roughness reduction in as-built printed parts.

3.2.1 Contour Exposure Strategies

The first set of tests on the M100 was to experiment with contour exposure strategies not previously attempted in the literature. The default M290 exposure uses a single contour scan line, though recent papers suggest using multiple contours for improved roughness. Artzt et al. [181] used multiple contours to improve side surface roughness from infill patterns of the same VED, but downskins were not tested. Additionally, multiple contours

with low VED compared to infill exposures were used by Cloots et al. [182] to improve downskin printability, but the resulting contour region had high porosities. Three strategy types or conditions remain for using multiple contours that have not been reported. These contour strategies are uniform contours with constant VED for downskin geometries ('equal VED'), contours with a lower h_d for high VED ('low hatch'), and contours with lowered P in-to-out ('decreasing power'). The three remaining strategies were tested experimentally to probe for potential in using multiple contours for reliably improved downskins.

All contour strategies use four contour scan lines, where the first scanned contour is not offset from the infill scan lines. On the M100, these contour exposures are easily set using the contours exposure tab that allows for four contour exposures. On the M290, an increased number of contours is accomplished by a workaround of having nested exposure parameter sets, each with contour exposure settings, until the desired number of contours is met. The default settings of the M100 do not include a contour scan.

Contour print exposure settings used default infill stripe exposures with the adjusted contours. Firstly, the 'equal VED' contours have similar laser scan speed and power as default infill exposures, with the contour spacing set equal to the infill h_d. Secondly, the 'low hatch' contours have the same laser scan speed and power as the equal VED contours, but the contour spacing is lowered to 35 µm. The intention of lowering the spacing was to increase conduction into the already solidified part (or previously scanned contour), thus reducing the overhang overheating and surface defects. This high VED method would depend on the increased energy input being outweighed by the increased conductivity,

which would also depend on the time allowed for each contour line to dissipate heat. The small part dimensions, such as the angled struts (3 x 3 mm), allow for a test condition with short time intervals between contour scans. Lastly, the ‘decreasing power’ strategy would have the same scan speed as the other contour exposures but with decreasing power, starting from the inner contour and consistently lowering for each subsequent contour. The contour spacing was set using default downskin settings to allow MP overlap of low-P contours. A desirable overlap would avoid the high porosity contour region from the low-VED contours tested by Cloots [182]. A smoothing of the angled-downskin stair-stepping effect through the decreasing MP size was also hypothesized, as represented in Figure 36. Power levels were selected based on the default exposure settings for downskins. The relevant exposure parameters for all contour strategies are shown in Table 7, with a schematic image of the exposure lines from EOSPRINT in Figure 37.

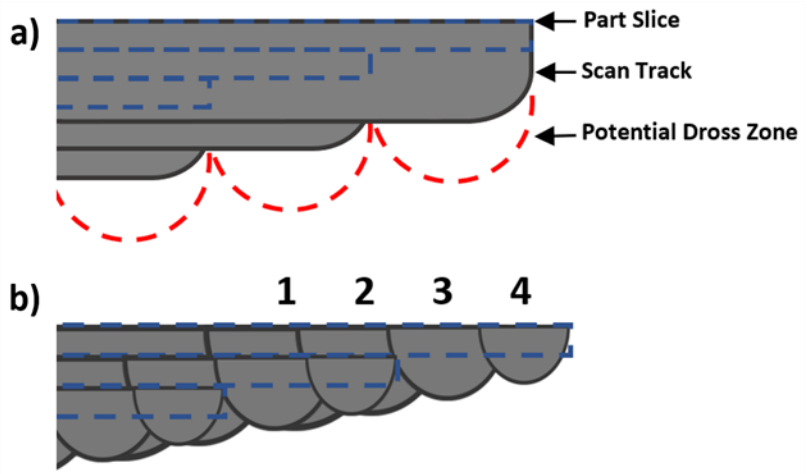

Figure 36: Idealized schematic representation of MP structures for an angled overhang: a) stripe exposure with the scan vectors 90° to the part border, b) decreasing power contour strategy

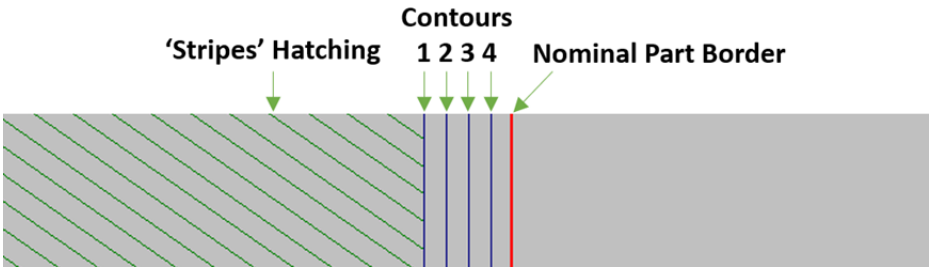

Figure 37: EOSPRINT layer scan lines with four contours

One print of the M100 build layout was completed and inspected for each contour strategy. A print using default exposures was conducted as a benchmark for the contour prints. All prints used EOS StainlessSteel 316L powder and argon shielding gas. The characterization of the parts is focused on surface roughness and dimensional accuracy, especially for downskins, where dross formation and warping are issues.

Table 7: Exposure parameters for the contour strategies

Strategy	Contour	P [W]	v [mm/s]	Spacing [mm]	VED [J/mm^3]
Default	n/a (infill only)	107.1	827	0.07	92.5
Low Hatch	all	100	800	0.035	178.6
Equal VED	all	100	800	0.07	89.3
Decreasing P	1	75	800	.06	--
	2	60			--
	3	45			--
	4	30			--

3.2.2 Shielding Gas

The same M100 build layout is used to compare the performance of two prints: one in an argon environment and one in a nitrogen environment. Default parameters are used for the prints, which have been shown to yield comparable properties to M290 default performance. This test assesses whether nitrogen shielding gas can produce parts with

comparable or better surface roughness than argon. Other properties such as hardness, residual stress, and tensile strength would ideally be maintained or improved. Since nitrogen has a higher thermal conductivity (0.026 W/m-K) than argon (0.018 W/m-K), the increased conduction of the powder bed could result in reduced overheating of overhangs and thus improve downskin surface roughness. Although, these gases have been shown to produce equally rough surfaces in prints with 304 SS [145]. Nitrogen would be advantageous as a shielding gas, even for similar part properties as with argon gas, as porosity from the process could be almost completely removed in a HIPing process [57], and a proper nitrogen generator setup could result in cost savings.

3.2.3 Powder Size

An additional M100 build layout is printed using sieved and unsieved powder to compare the performance of different PSDs. The print is compared to the same default Ar print as the N_2 print. The goal is to assess whether a finer powder feedstock results in parts with improved surface roughness than the current distribution, though the other physical and mechanical properties are also assessed. The reduced average size of the powder would result in a more densely packed powder bed, increasing the effective thermal conductivity of the bed and potentially improving the roughness of downskins; upskin surface roughness could also be improved by a more densely packed bed [152].

3.2.4 Design of Experiments

A DOE approach was implemented to develop a statistical model and select optimal exposure parameter settings for the surface roughness of upskins and downskins. A response surface design is implemented, which includes factors of laser power, h_d, and v,

as they are known to be the most influential parameters on surface roughness [140]. The goal is to minimize and achieve lower surface roughness than default exposure parameters. Though minimum surface roughness is desired, a constraint is applied to the optimization to maintain high density, as there is an inherent trade-off between these two properties [134]. Other assessed properties are hardness and residual stress. The deflection specimen is printed using the same DOE layout.

A 20-part face-centred CCD response surface design was printed on the M290 in a single print job, as shown in Figure 38. The face-centred design was selected to have a well-controlled experimental region. The experiment is set to completely analyze a range of VED reported to not cause print failures for the M290 [204]. The exposure parameter levels are outlined in Table 8, and the placement order of exposure treatments was randomized. All exposure treatments kept the default contour settings constant.

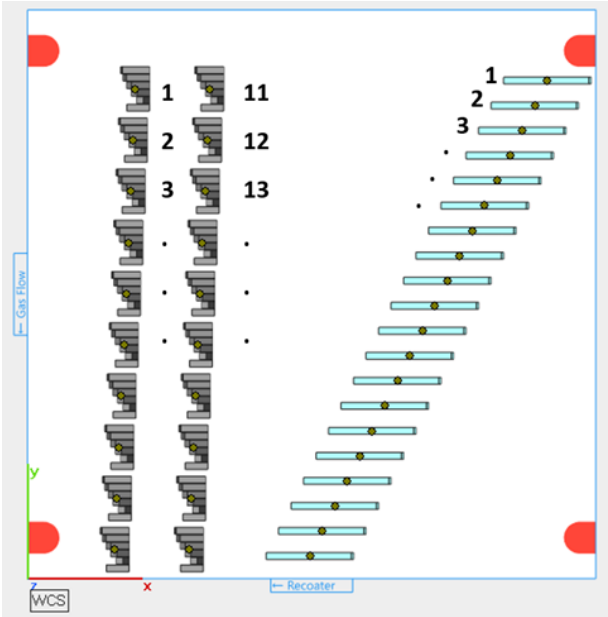

Figure 38: M290 print layout for the DOE print with labelled positions

Table 8: Exposure parameters for the face-centred CCD print

Position	P [W]	v [mm/s]	h_d [mm]	VED [J/mm^3]
1	170	800	80	66.4
2	240	800	60	125.0
3	170	1000	80	53.1
4	170	900	80	59.0
5	170	900	80	59.0
6	170	900	80	59.0
7	170	900	80	59.0
8	170	900	100	47.2
9	100	900	80	34.7
10	170	900	60	78.7
11	100	1000	100	25.0
12	100	800	60	52.1
13	240	900	80	83.3
14	100	800	100	31.3
15	240	800	100	75.0
16	240	1000	100	60.0
17	170	900	80	59.0
18	100	1000	60	41.7
19	240	1000	60	100.0
20	170	900	80	59.0

3.2.5 Verification Prints

After completing statistical analysis and selecting optimal parameter settings, a final build was printed, shown in Figure 39, comprised of both angled specimens and tensile specimens with optimal and default exposures. This print aims to verify the improved surface roughness from optimized exposure parameters and test for any changes to tensile strength. Also included in the build is a test artifact previously used for benchmarking. The artifact includes many features, described in Section 2.1, to investigate the effects of the selected parameters on print quality. The results are compared to the M290 default-printed artifacts from the benchmark testing.

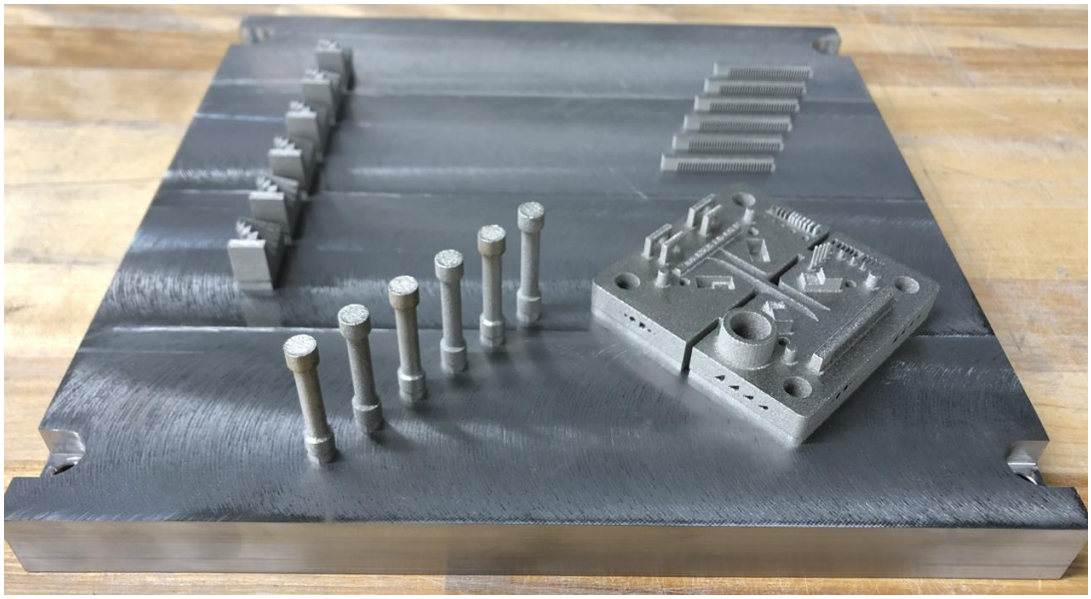

Figure 39: Final verification build printed on the M290

3.2.6 Design Application

An application case is used to analyze the impact of the roughness reduction parameters on DMLS design capabilities. The resulting parameters are applied to a complex channel model for next-generation heat exchanger (HX) designs. The detailed HX design and characterization study, along with the assessment of the DMLS 316L roughness reduction applicability, is found in CHAPTER 5. Analysis of CFD simulations and print characterization of the HX is used to explore complex overhang printability for HX design objectives. AM HXs are proven to have major efficiency improvement capability, serving the most sustainable aspect of DMLS technology [17, 205]. The design feature and as-built surface roughness reduction have the potential to offer design pathways for lower pressure drop and wider applicability of these HXs.

CHAPTER 4

Characterization Results

4.1 Benchmarking

All 12 test artifacts of default parameters were successfully printed on their respective machines for benchmarking purposes, as shown in Figure 40 for the M100.

Figure 40: Successfully printed test artifact on the M100 build platform

For the small specimen investigation, eight specimens were successfully printed on the M290, with no part failures. The differently exposed specimens after being cut off the build platform can be seen in Figure 41. The specimens of higher LED have greater discoloration near the bottom edge on the support-part interface, which corresponds to increased overheating at this interface of high to low heat conductivity.

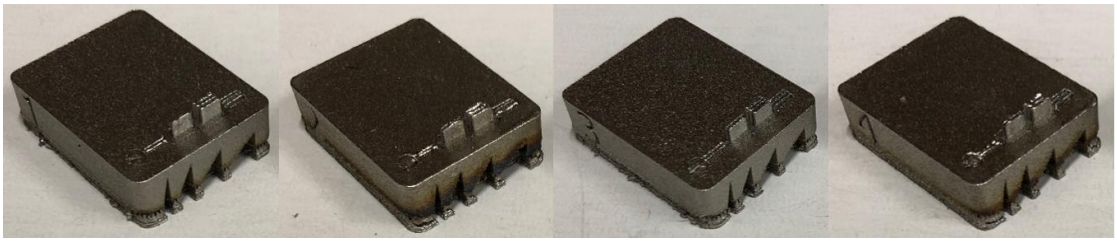

Figure 41: Exposure treatments 1 (left) to 4 (right) of small specimens printed on the M290

The first of the small specimen prints with a 40-micron layer thickness on the M100 did not successfully print all specimens; the two parts to the right of the platform experienced underdosing of powder. The M100 recoating system uses a hopper that drops the required amount of powder in front of the re-coater blade before passing over the build platform, which is different and less versatile than the rising dispenser system in the M290. The hopper system uses a specific dosing cylinder to feed set amounts of 316L powder for 20-micron layers. The number of feedings for a layer is calculated based on the area and placement of the part, a map representation of which is shown in Figure 42 [206]. The system assumes the correct dosing cylinder is installed and therefore does not account for layer thickness in the dosing calculation, which led to the underdosing seen in Figure 43. The test artifact printed with 40-micron layers did not experience this underdosing as its placement included the area with the highest dosing compensation.

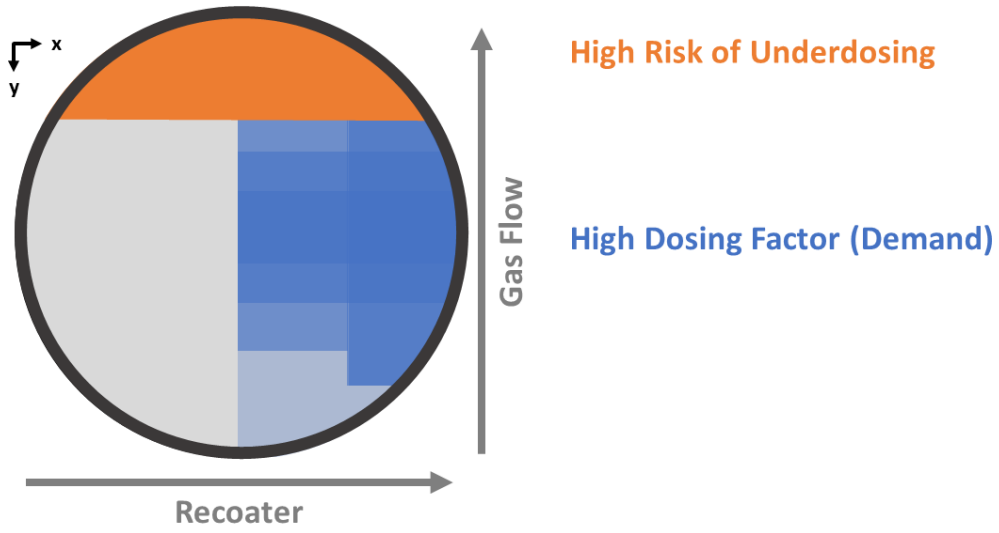

Figure 42: Visualization of the EOS M100 dosing matrix (as in **[206]**)

Figure 43: Underdosing observed for 40 µm print #1 on the M100

A second print job was printed to make up for the underdosed parts. In this print setup, no parts were included on the rightmost side of the platform. As well, the dosing factor was increased to the maximum setting of 200%. Even with the extra dosing factor, the powder was underfed for the small features. The dosing factor is applied to the area calculation and does not automatically double the feedings. Since the small features do not cover much area, the re-coater only makes a single pass, and the layer is not properly coated, as shown in Figure 44.

Figure 44: Underdosing observed for 40 µm print #2 on the M100

All parts from both print jobs had highly rough surfaces with many large balling defects. The maximum top-surface roughness peaks exceeded the 200-micron limit of the Starrett profilometer. Roughness issues can be attributed in part to insufficient scan track fusion in the MP tracks. Results for measured part accuracy, small feature success, and side roughness can be seen in **Appendix A**.

A 20-micron layer thickness factorial print was successful and showed the same overheating with increasing energy density on the bottom edge of the parts, as seen in Figure 45.

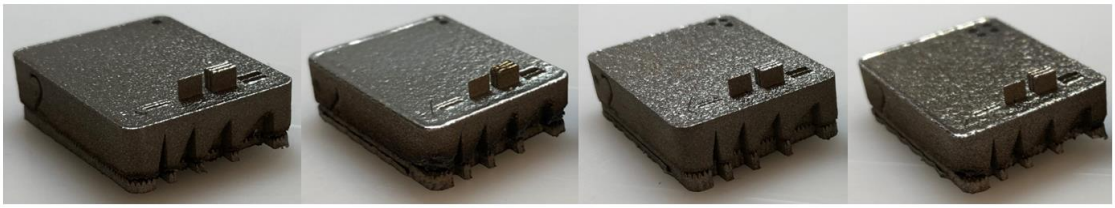

Figure 45: Exposure treatments 1 (left) to 4 (right) of small specimens printed on the M100 at 20 µm layer thickness

4.1.1 Tensile Strength

The mean values of UTS for the two machines and two specimen orientations are calculated in Table 9. The resulting interval plot can be found in Figure 46.

Table 9: Tensile strength results of as-built test artifact specimens

Printer	Build Orientation	UTS (MPa) ± SD
M100	PERP	639 ± 15
M100	PAR	581 ± 6
M290	PERP	662 ± 15
M290	PAR	590 ± 11

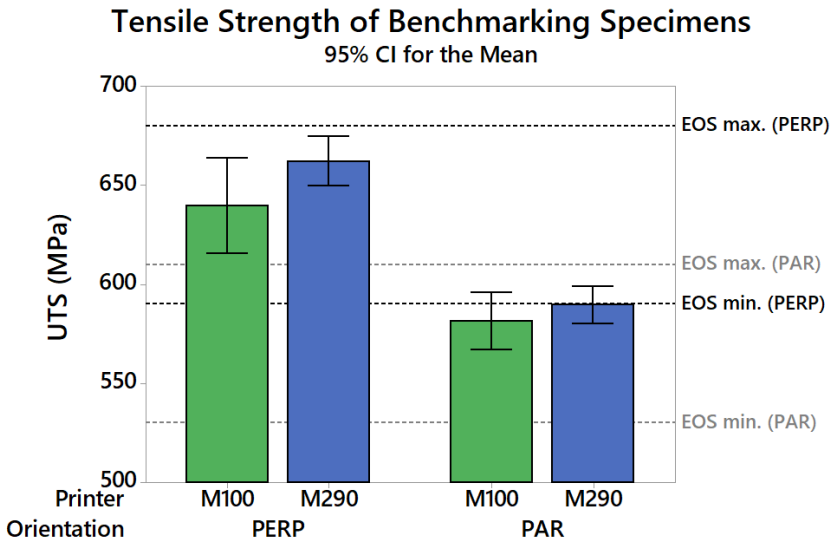

Figure 46: As-built XY-direction (PERP) and Z-direction (PAR) ultimate tensile strength (UTS) of default DMLS prints

Conducting t-tests on the data using Minitab software reveals that both M100 and M290 printers show statistically significant differences between the UTS of PAR and PERP specimens ($p = 0.002$ and $p < 0.001$, respectively), with the stronger orientation being PERP. As such, UTS is observed to be an anisotropic mechanical property for the DMLS process in both machines. The tensile load for the PAR dog bone is orthogonal to the layering of the printed part, therefore increasing the risk of failure. It can also be seen that there is no statistically significant difference between the printers themselves for the printed artifacts. All the data points for the two printers fall within the respective maximum and minimum ranges specified by EOS [126].

4.1.2 Hardness

The mean values of Brinell hardness for the two machines and two indent surfaces are found in Table 10. The resulting interval plot can be found in Figure 47.

Table 10: Brinell hardness results of test artifact surfaces

Printer	Surface Orientation	HB 10/1500 ± SD
M100	PAR	194 ± 3
M100	PERP	206 ± 1
M290	PAR	189 ± 3
M290	PERP	203 ± 3

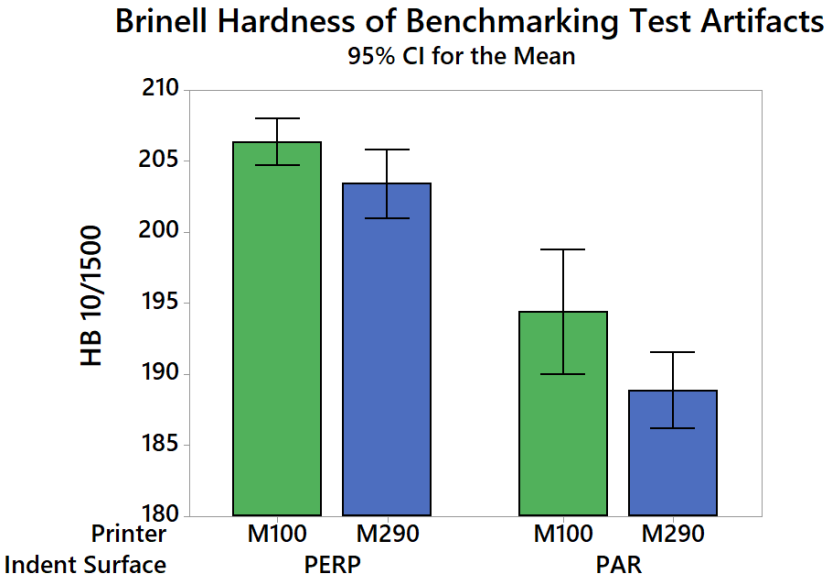

Figure 47: Top (PERP) and side (PAR) surface Brinell hardness (HB) of default DMLS prints

T-tests reveal that both M100 and M290 printers show statistically significant differences between the hardness values of PERP and PAR surfaces ($p = 0.004$ and $p < 0.001$, respectively), with PERP surfaces being harder. As such, macro-hardness is observed to be an anisotropic mechanical property.

Results of HB hardness tests for small specimens are plotted against VED in Figure 48. The hardness of the M290 prints appears to decrease with increasing ED, whereas for the M100, hardness decreases for the same range of VED, then increases. Through ANOVA analysis of the results, power was found to be a significant factor for the M290 ($p = 0.029$), with a negative effect on the hardness. None of the factors or interaction effects were found

to be significant for the M100; individual value plots and interaction plots are shown in **Appendix A**.

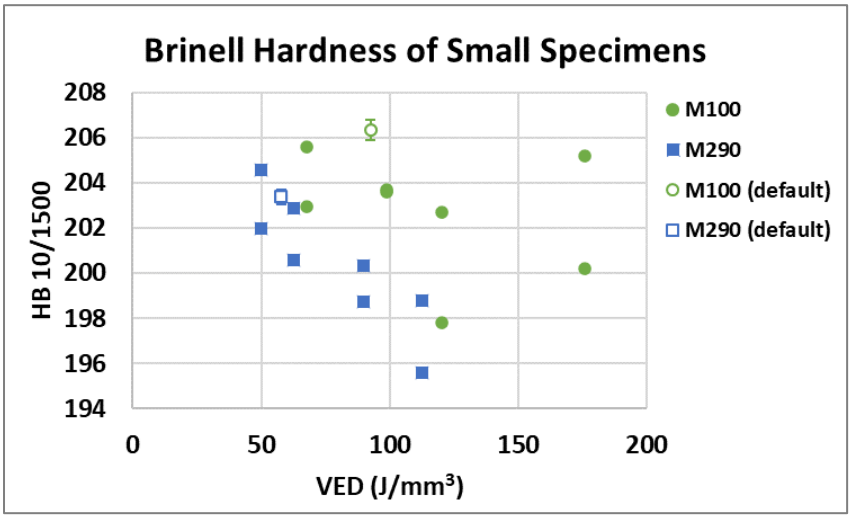

Figure 48: Brinell hardness (HB) of PERP surfaces plotted against VED for DMLS prints with varied P and v

4.1.3 Roughness

The default benchmarking results from the stylus profilometer testing can be found in Table 11 and Figure 49. T-test results show no difference between printers or surfaces for Ra or Rz. All the data falls under the maximum roughness values given by EOS [126].

Table 11: Surface roughness results of default benchmarking

Printer	Surface	Ra (µm) ± SD	Rz (µm) ± SD
M100	Side	9.5 ± 0.3	63.1 ± 1.8
M100	Top	10.2 ± 0.4	64.4 ± 5.9
M290	Side	9.5 ± 1.0	62.8 ± 6.3
M290	Top	10.7 ± 4.1	66.9 ± 18.9

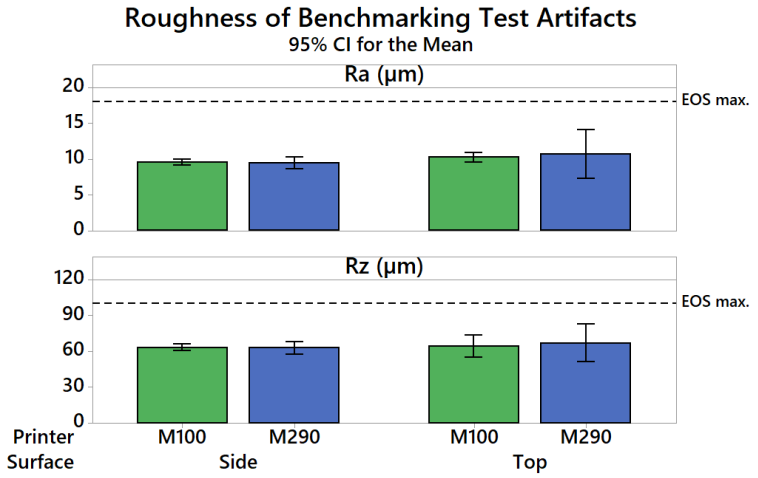

Figure 49: Arithmetic average height and average peak-to-valley height roughness (Ra and Rz) for top and side surfaces of as-built default DMLS prints

Results of top and side surface roughness measurements are seen plotted against VED in Figure 50 and Figure 51. Only results for Ra are shown, as the trends are the same for Rz, though the Rz plots can be found in **Appendix D**. The top-surface roughness of the M290 prints appears to lower with increasing ED, whereas the M100 sees a similar trend for the same range of VED, then decreases. No notable trends are seen for the side roughness plot.

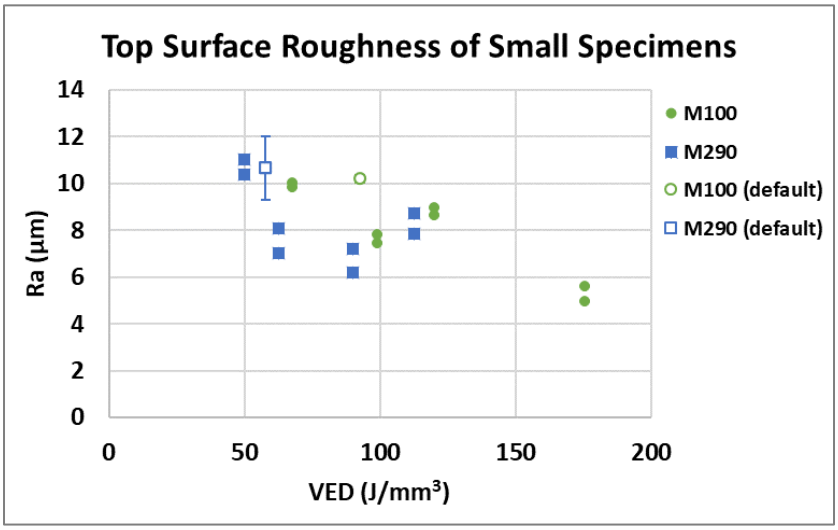

Figure 50: Top surface roughness (Ra) of small specimens plotted against VED, with default artifact data for reference

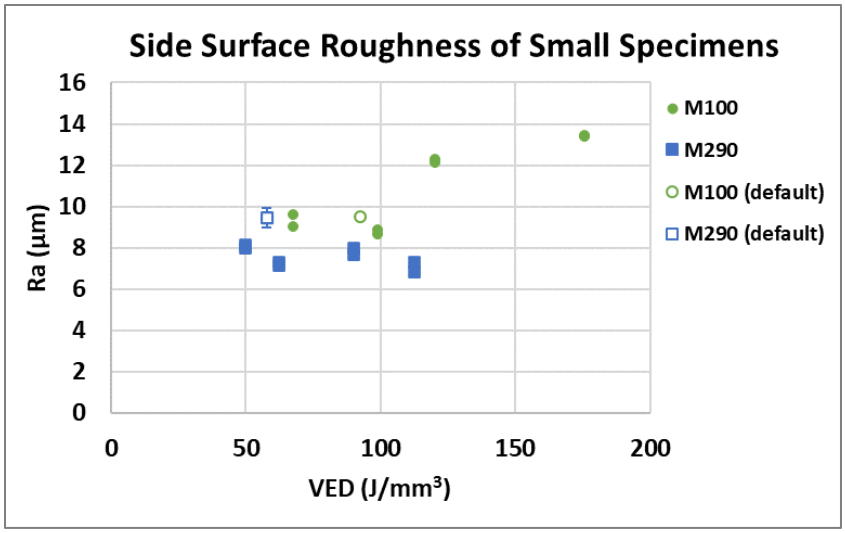

Figure 51: Side surface roughness (Ra) of small specimens plotted against VED, with default artifact data for reference

ANOVA on the top roughness data found power and the interaction of P*v to be significant factors for the M290, with p-values of 0.022 and 0.006, respectively, and power as a positive effect (increases roughness). Speed has a positive effect on the top roughness at high power and a negative effect at low power. For the M100, both factors and their interaction were found to be significant, with $p = 0.001$ for power as a negative effect, $p < 0.001$ for speed as a positive effect, and $p = 0.041$ for the P*v interaction. For the side roughness on the M290, speed was found to have a significant positive effect ($p = 0.008$). Power and the P*v interaction were found to have a significant effect for the M100 ($p < 0.001$ and $p = 0.006$), with power as a positive effect.

4.1.4 Dimensional Accuracy

Dimensional errors for the printers can be seen in Figure 52. The M290 printer appears to have a wider tolerance range than the M100. For the Z-axis, this difference may be attributed to the difference in layer height of the two default parameter sets. Additionally,

the tolerance range in the XY direction appears to be narrower than the tolerance range in the Z-axis for both machines.

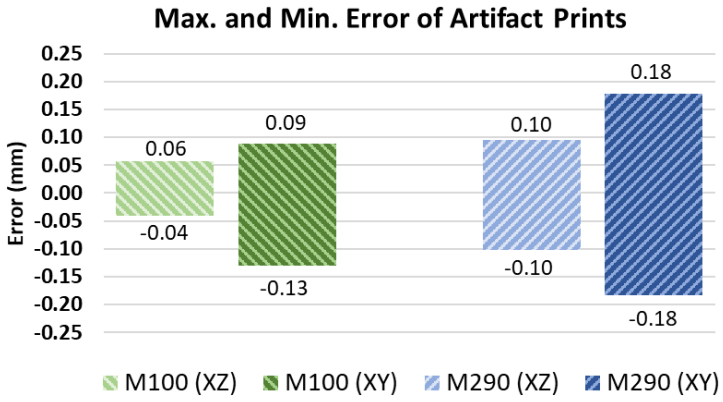

Figure 52: Maximum and minimum XY and Z errors for default test artifact prints

Small feature success is categorized in Table 12 based on observation with a digital microscope. A feature is considered to be failed (F) if there is no formation for the bosses or if there are no open gaps for the holes, partial (P) if there is an incomplete formation for the bosses or if the hole is mostly closed off, and is otherwise considered to have successfully printed (S); examples of each success category are shown in Figure 53. The XY-direction resolution capabilities of the printers vary depending on whether the part is a boss or hole. The M100 is more capable of forming small PAR hole features, while the M290 is more capable of forming small PAR bosses. Figure 54 provides a labelled CAD visual of the small PAR features. Both printers were capable of reliably printing the 8:1 aspect ratio feature. For PERP hole features, the 250-micron features were compared in Table 12, as all 100-micron features failed. In the case that the two sides of the test artifact had different print success, the better-printed holes were listed. There is no apparent difference between the performance of the printers.

Table 12: Small feature print success for default test artifacts (a: Failed, b: Partial, c: Success)

Feature	**M100**				**M290**							
(100 µm)	***1***	***2***	***3***	***4***	***1***	***2***	***3***	***4***	***5***	***6***	***7***	***8***
Rectangular boss	F[a]	F	F	F	P[b]	F	F	F	P	P	P	F
Rectangular walls	F	F	F	F	P	S[c]	S	F	S	P	F	F
Rectangular hole	P	S	P	P	F	F	F	F	F	P	F	F
Rectangular spaces	S	S	S	S	P	P	P	P	P	P	P	P
Circular boss	F	F	F	F	S	S	S	S	S	S	S	S
Circular hole	P	P	P	P	F	F	F	F	F	F	F	F
PERP square holes (250 µm)	F	P	P	P	F	P	P	P	P	P	F	P
PERP circular holes (250 µm)	P	P	P	P	P	P	P	P	F	P	P	P

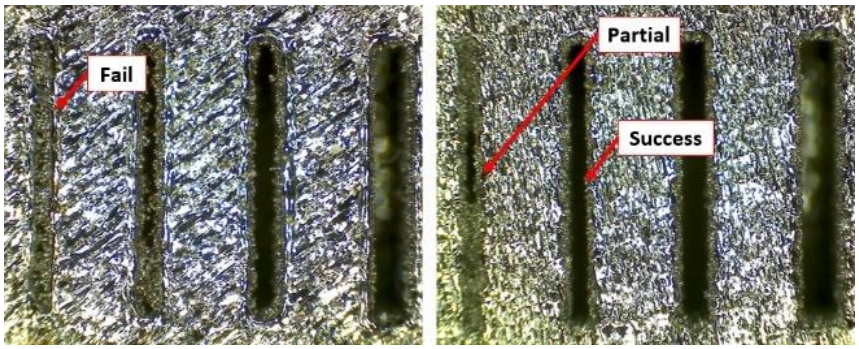

Figure 53: Labeled degrees of success for rectangular holes on the M290 (left) and M100 (right)

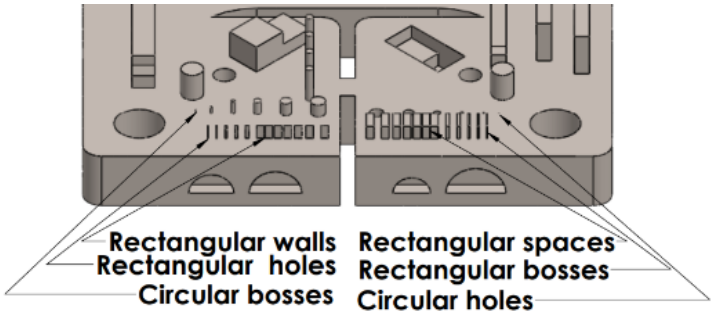

Figure 54: Labeled CAD of small PAR features

Since there was partial small space feature success for M290, the results do not simply point to oversized bosses, but that the larger beam diameter ensured proper 100-micron thickness scanning. The true thickness is measured by the digital microscope to be 93.2 ± 14 µm but is observed to have been formed from unstable melt tracks.

The print success of the small features for the M100 at 20-micron layer thickness and the M290 are shown in Table 13. No clear trends are observed for the success of printing boss features in either printer. However, parts printed at lower power settings were more successful at printing the holes and spaces in both printers.

Table 13: Small feature print success for small specimens (a: Partial, b: Success, c: Failed)

Feature (100 µm)	***M290***								***M100 (20 µm)***							
	1a	***1b***	***2a***	***2b***	***3a***	***3b***	***4a***	***4b***	***1a***	***1b***	***2a***	***2b***	***3a***	***3b***	***4a***	***4b***
Rectangular boss	P[a]	P	S[b]	P	S	S	S	P	F[c]	F	F	F	F	F	F	F
Rectangular walls	S	S	S	S	S	S	S	P	F	F	F	F	F	F	F	F
Rectangular hole	P	P	F	F	P	P	P	P	S	S	P	P	S	S	F	P
Rectangular spaces	P	P	F	F	P	P	F	F	S	S	P	P	S	P	P	P
Circular boss	S	S	S	S	S	S	S	S	F	F	F	F	F	F	F	F
Circular hole	F	F	F	F	F	F	F	F	P	P	F	F	P	P	F	F

Deviations of measured part dimensions from the nominal dimensions are plotted against VED in Figure 55. The average difference of the M290 prints appears to decrease in magnitude first and then increase with VED. The M100 does not show any trend in terms of VED. Through ANOVA analysis of the results, the P*v interaction term was found to be a significant factor for the M290 ($p = 0.007$), where increasing speed decreases the part accuracy at low powers but decreases it at high power. For the M100, both power and speed were found to have significant positive effects with p-values of 0.022 and 0.001, respectively.

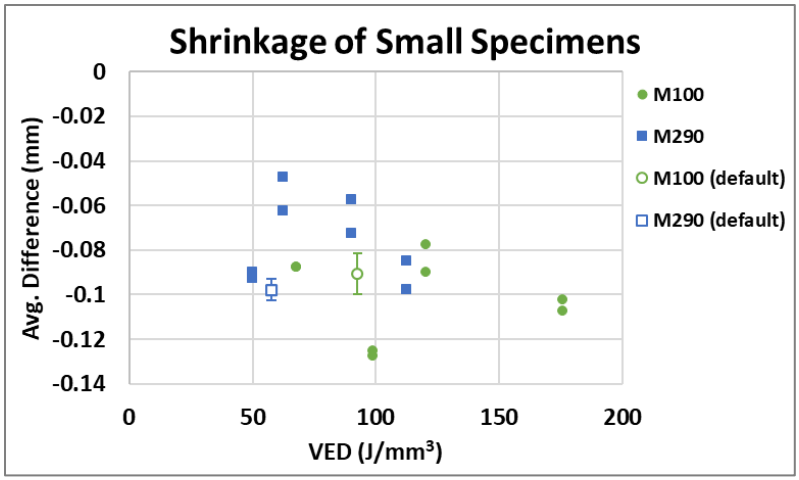

Figure 55: Dimensional error ('shrinkage') of small specimen XY bounding dimensions plotted against VED, with default artifact data for reference

4.1.5 Overhangs

Measures for the success of straight, circular, and angled overhangs are described in Section 2.1.2.1. The resulting mean dross area errors (DAEs) of straight overhangs can be seen in Figure 56. A one-way ANOVA test was used to test for any significant difference between the DAE of the overhang lengths. Levene's test for equal variances was used to confirm the assumption of equal variances for the ANOVA. The tests yielded no statistical difference between any of the overhang lengths ($F(3,44) = 1.36$, $p = 0.269$). As such, the overhang lengths were grouped to compare the DAE of the two printers through a 2-sample t-test. The t-test showed no statistical difference in DAE between the M100 and M290 printers. General recommendations advise that unsupported overhangs not exceed around 2 mm [207]. The lack of a definitive relationship between DAE and length may be due to high instability at such long bridge lengths, causing severe dross and warping of the overhangs. The scan orientations of the initial overhang layers may also result in long and unstable overhang melts.

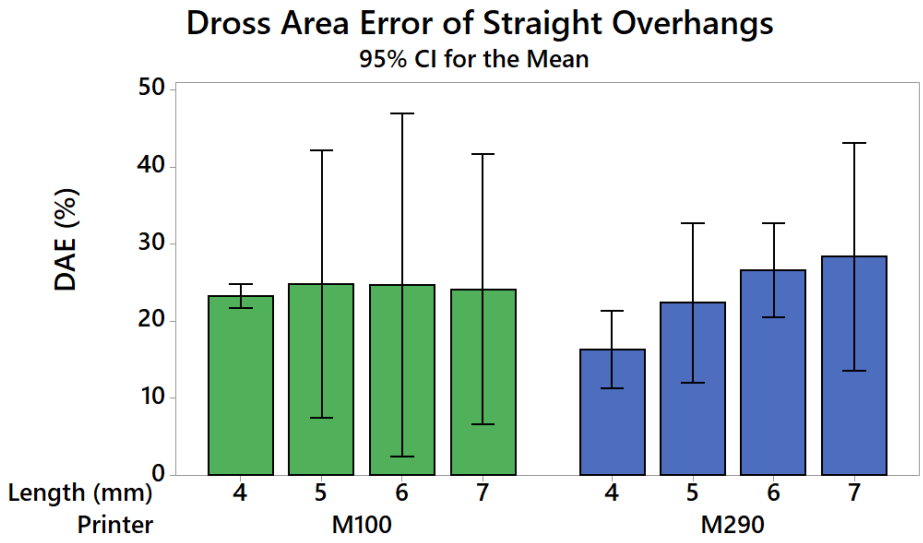

Figure 56: Dross area error (DAE) of default DMLS-printed straight overhang features

For the accuracy of circular overhangs, the resulting mean eccentricities can be seen in Figure 57. The lower the eccentricity, the more accurate the printed semi-circle is to the CAD model. There was a statistically significant difference between groups as determined by one-way ANOVA ($F(3,92) = 5.17$, $p = 0.002$). A post-hoc Tukey test was used to determine which specific groups differed. This multiple comparison test revealed that there are differences between eccentricities from 8 mm to 5 mm, and 7 mm to 5 mm. The trend shows decreasing eccentricity for increasing diameter. This unintuitive result may be explained by the competing phenomena of warping and degradation with dross or sagging [176, 187]. The dross phenomena may dominate at smaller arc diameters but then be increasingly offset by the effects of warping and burning as the diameters increase; this is shown in Figure 58 for a 5-mm and 8-mm diameter overhang.

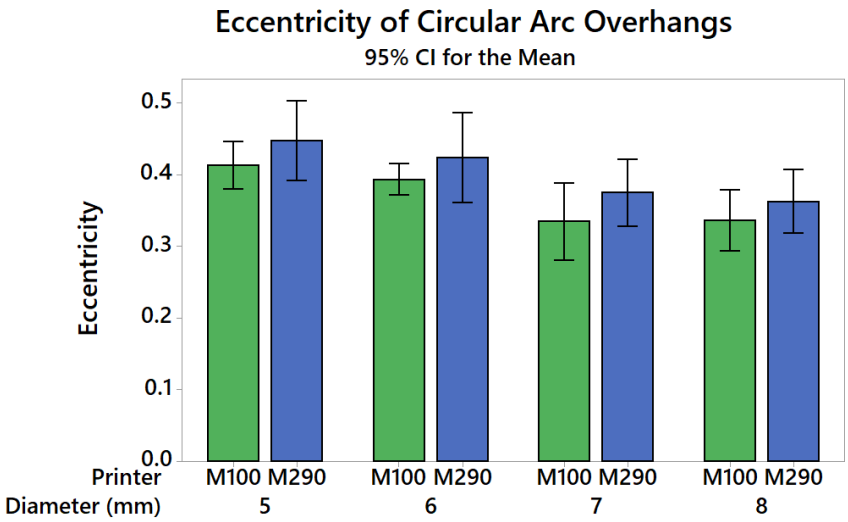

Figure 57: Eccentricity of circular arc overhang features in default DMLS prints

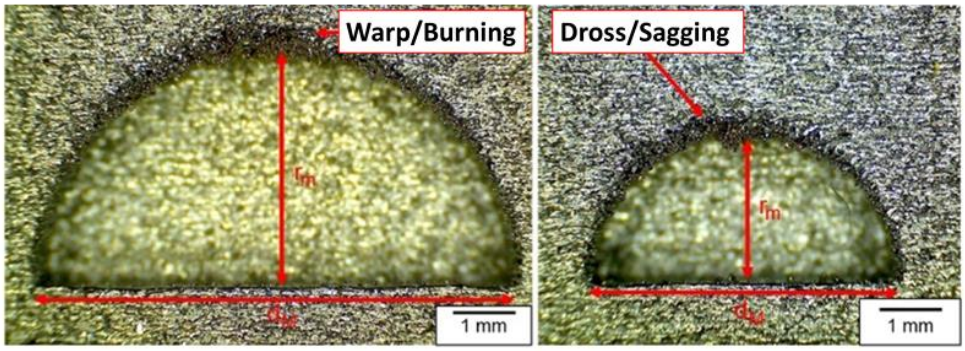

Figure 58: The circular overhangs of 8-mm (left) and 5-mm (right) diameters from the same M290 print; dross formation is visible for both surfaces, with increased burning and warp in the larger radius.

Since the different arc diameters affect the resulting eccentricity, individual t-tests at each diameter were used to confirm there is no significant difference in the eccentricity of unsupported arcs between the two printers.

The resulting mean errors for the angled overhangs can be seen in Figure 59. A one-way ANOVA ($F(3, 92) = 17.74$, $p < 0.001$) and post-hoc Tukey test revealed that all overhang angles differed significantly in dimensional error at $p < 0.05$, with the exceptions of 45 to 40 degrees and 40 to 35 degrees. The trend from this test shows that the error (dross, surface

texture) increases with decreasing angles. This result aligns with the general rule that angled overhangs begin to fail when unsupported at angles below 35 degrees [51, 187]. Individual t-tests at each angle reveal no significant difference in error for unsupported angles between the two printers.

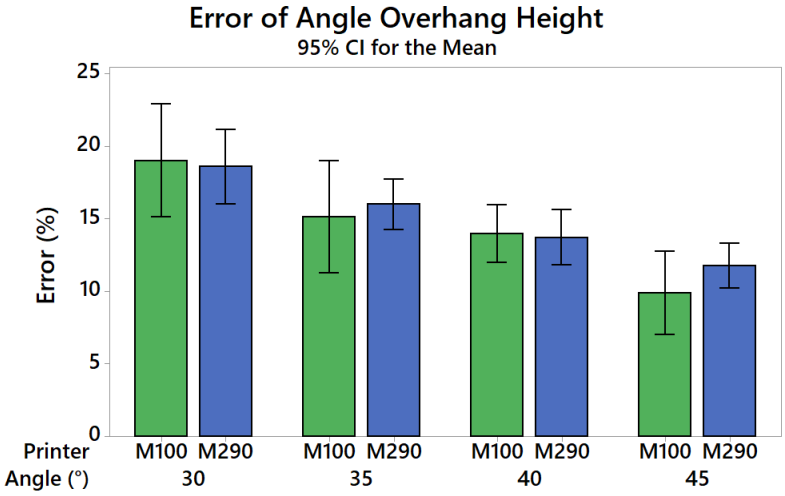

Figure 59: Height dimension error of default DMLS-printed angle overhangs

The effect of VED on the quality of the printed angled overhangs for each printer is visualized in Figure 60; the dimensional error due to dross formation is noted for each part shown. The M290 experienced more overheating on the bottom surface than the M100, despite being printed at lower VEDs. Both printers experience a linear VED-overheating correlation. The tempering colour changes are commonly seen in DMLS-printed SS due to heat accumulation where thermal diffusivity and conduction are limited [92]. The dross formation is less severe on the M100 than the M290 for similar VED, and the overhang quality generally decreases with increasing VED for both printers. The increased overheating effects in the M290 further contribute to the understanding that the VED parameter does not account correctly for actual energy density; the thermal phenomena of

DMLS are impacted by the other process parameter differences, such as layer thickness and beam diameter.

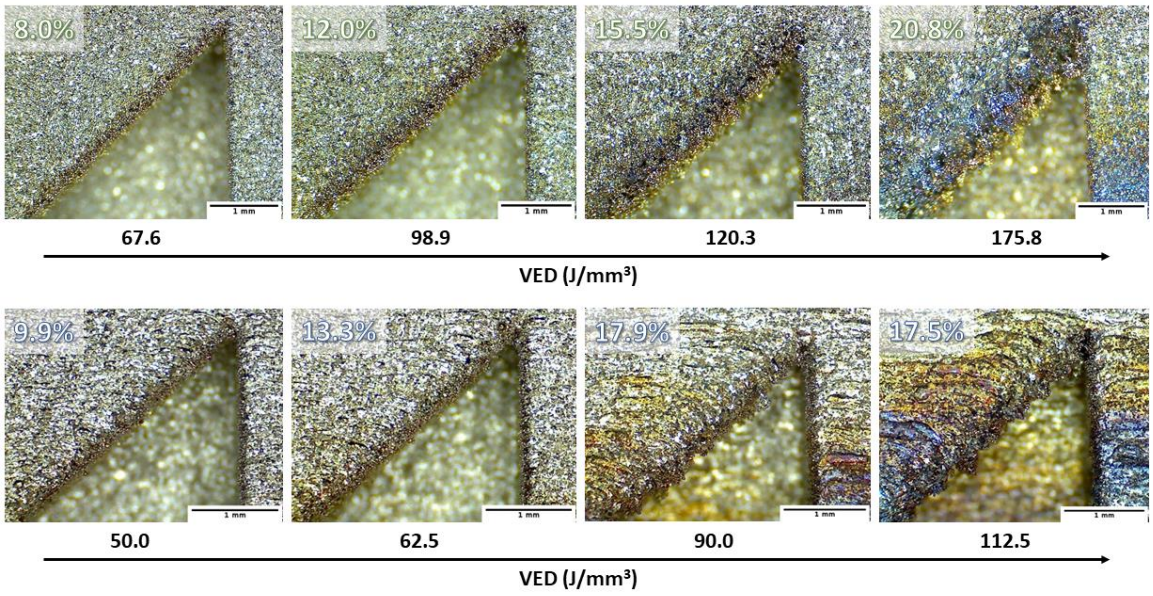

Figure 60: Angled overhang features (45°) of the small specimens printed on the M100 (20 µm, top) and M290 (bottom) prints, ordered by increasing VED and noting height error caused by dross formation

4.1.6 Density

From the Archimedes density tests, all printed disks were found to have densities of 7.99 g/cm^3, which is above the minimum reported density by EOS of 7.97 g/cm^3 [126]. The relative densities of the printed disks determined by the OM method can be seen in Figure 61; the Archimedes density measurement is also plotted and is estimated using a theoretical density of 8 g/cm^3. As can be seen, the OM estimate is consistent as a measure of relative density, though it slightly overestimated the density relative to Archimedes' method, with an average difference of + 0.05%. This overestimation may be attributed to the measurements being taken along the midline of the PAR cross-section, as porosity tends to increase near part walls.

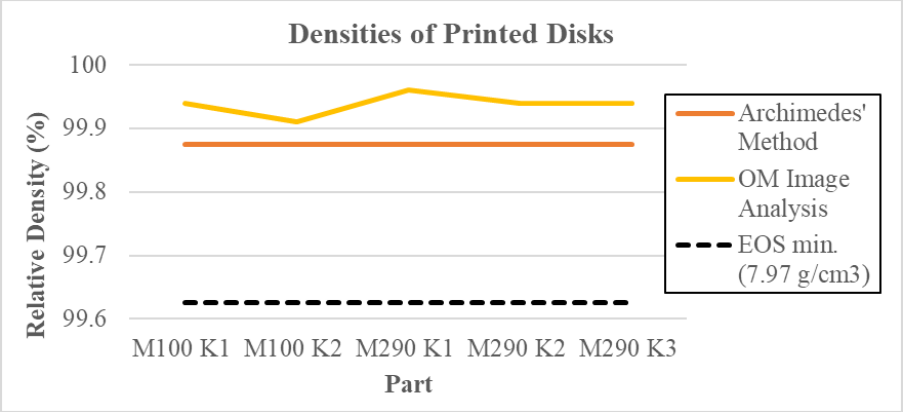

Figure 61: Comparison of relative densities of printed disks determined by Archimedes' method and OM image analysis

This difference in measurement techniques is consistent with other authors, though the trend is not as clear for this comparison since all measurements were for low-porosity parts [208]. It is expected that the Archimedes measurements result in lower values than the true density, with larger errors. On the other hand, the OM density measurements used in the rest of the thesis should be recognized as a slight overestimate.

The resulting average relative densities from OM image processing for the test artifact prints of the two printers are seen in Figure 62. A t-test conducted using Minitab statistical software did not find any significant difference in relative densities between machines (p-value = 0.247).

Results of relative density estimate measurements are seen plotted against VED in Figure 63. The porosity of the M290 prints appears to increase, then decrease with increasing VED, whereas no notable trends are seen for the M100. ANOVA analysis found no significant factors on density for the M290 exposure settings tested. For the M100,

speed was found to have a significant positive effect on the density ($p < 0.001$). The P*v interaction term was also found to have a significant effect ($p = 0.005$).

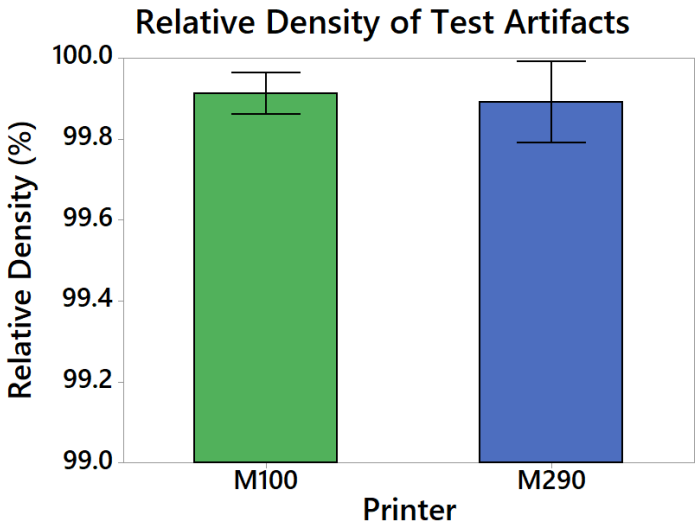

Figure 62: Relative density of default DMLS prints

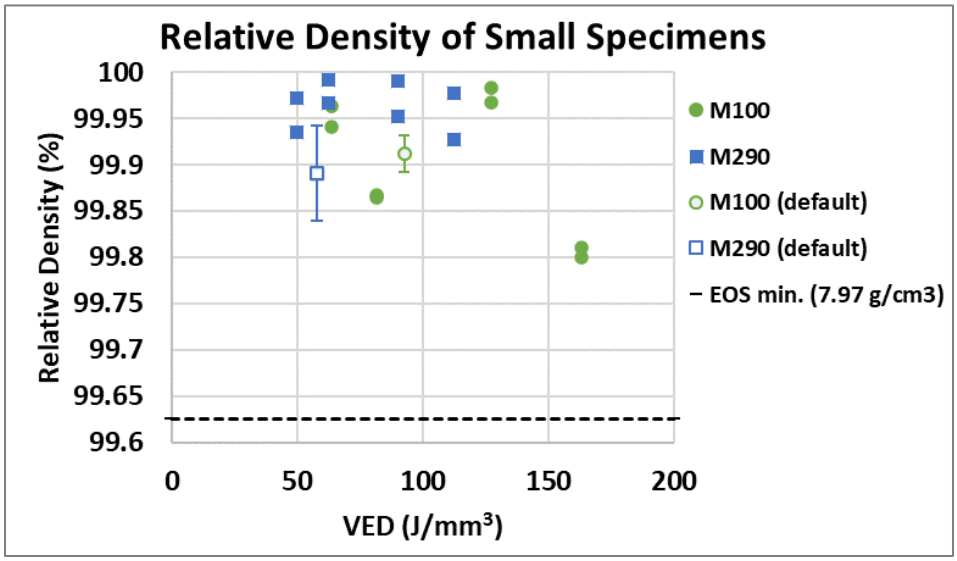

Figure 63: Relative density results for small specimens plotted against VED

4.1.7 Residual Stress

The average deflections from specimens printed as part of and separate from the test artifacts are seen in Figure 64. T-tests determined no significant difference between

deflection in the M100 and M290 printers for both on-platform and on-artifact builds (p-values of 0.412 and 0.278, respectively). However, there was a significant difference in whether the deflection specimen was printed on the test artifact (p-value = 0.022). As such, the increased part volume was seen to increase the deflection and thus indicate higher residual stresses.

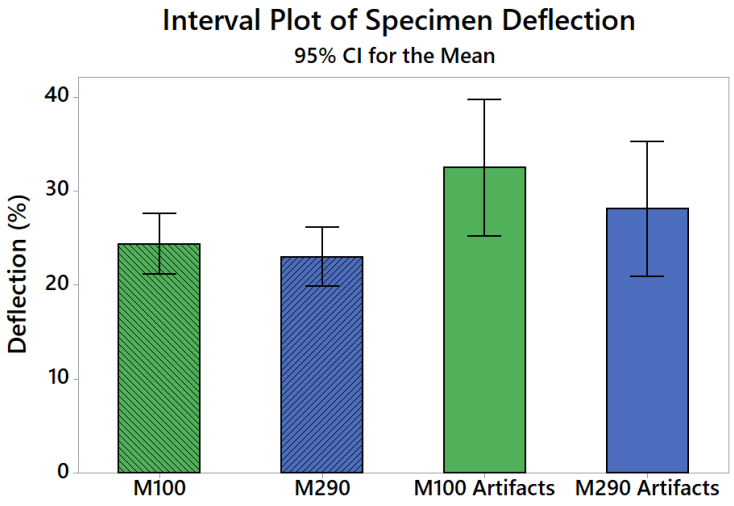

Figure 64: Residual stress feature deflections of default parameter prints

4.1.8 Microstructure

Etching at lower time intervals reveals regions where the MP superstructure of the build process can be clearly observed for both top and sectioned surfaces, as seen in Figure 65. The MP dimensions are w ≈ 75 µm and h ≈ 80 µm for the M100 builds and w ≈ 115 µm and h ≈ 90 µm for the M290 builds. Both printers have default settings where the actual MP width slightly exceeds the hatch distance, forming some overlap.

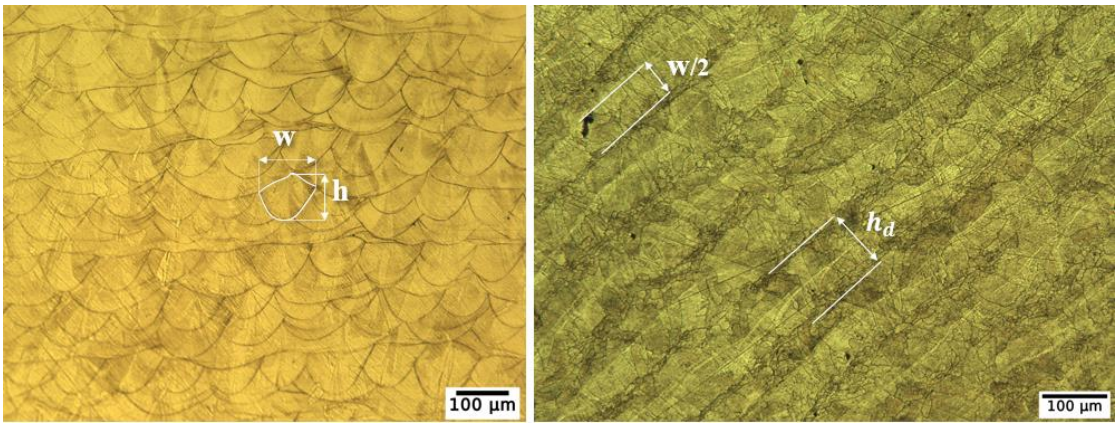

Figure 65: Melt pool structure (left) and melt track structure (right) for M290 prints, with melt track width (w) and height (h) as well as hatch distance (h_d) labelled

The microstructures of the M100 and M290 printers are seen in Figure 66 and Figure 67. Both printers have similar grain structures, with columnar grains in the build direction from epitaxial growth and smaller grains along the centerlines of laser scan tracks. However, the M290 grains are more columnar, and the centerline is less defined and made up of larger grains. Grain measurements following ASTM E112 [209] yield mean intercept lengths in the XY plane to be 19.9 ± 0.4 µm for the M100 and 24.9 ± 0.5 µm for the M290. Elongation ratios for the Z-axis are 1.9 for the M100 and 2.6 for the M290. The wider MPs in the M290 allow for the Z-axis-elongated and XY-equiaxed microstructure due to the relationship between MP dimensions and solidification orientation [9]. Though present, these microstructural differences did not result in a large difference in macro mechanical properties.

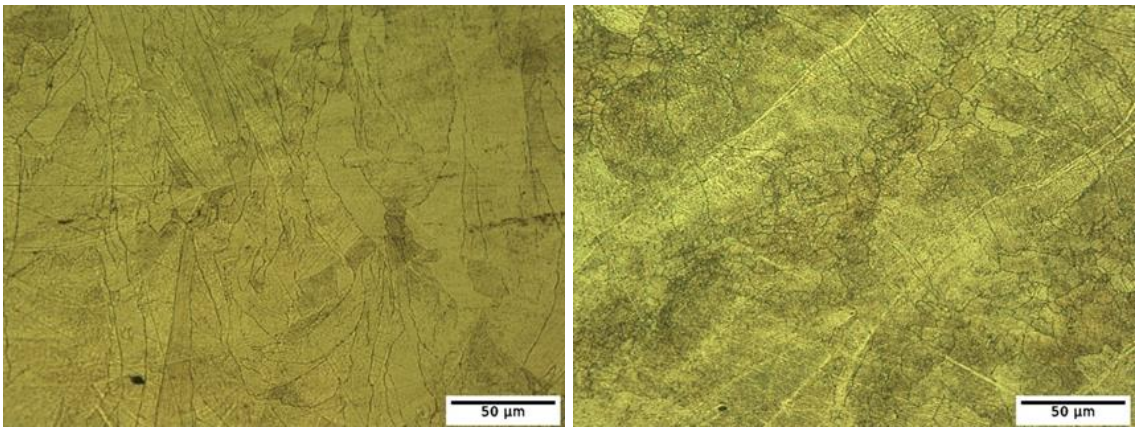

Figure 66: XZ-plane microstructure (left) and XY-plane microstructure (right) for M290 prints

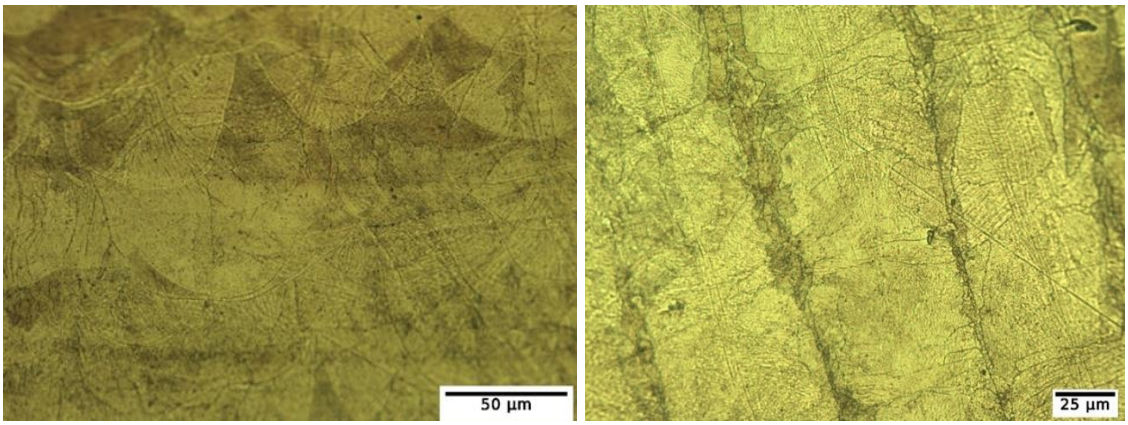

Figure 67: XZ-plane microstructure (left) and XY-plane microstructure (right) for M100 prints

4.1.9 Equalized Energy Density

The first build, where the traditional VED was used, was successfully printed on the M100; it can be seen in Figure 68. One noticeable observation from a visual inspection was that there were more tempered regions of overheating on this artifact than those printed on the M290, notably on the PAR tensile specimen. This result indicates higher energy absorbed than in the M290, despite the intended equal energy density. This discrepancy can not only be attributed to the interaction of power and speed but also to the process parameters unaccounted for in the VED equation, such as the beam diameter included in the proposed dimensionless parameter [20].

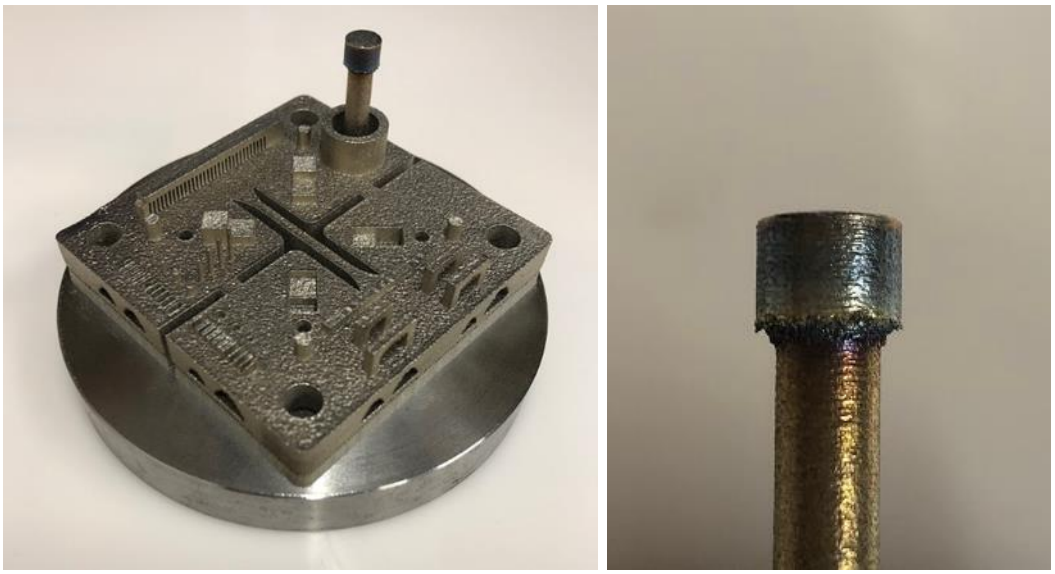

Figure 68: As-built M100 test artifact with adjusted parameters for equalized VED, showing increased discoloration on the dogbone feature (right)

The measured relative density of the part was 99.92%, so it is still a highly dense part, in a similar range as the previous test pieces. The deflection of the cantilever piece was 29.72%, also within the range of previous pieces. However, OM observations of the microstructure are much different from that of the M290. Firstly, the OM images of the XZ-plane cross-section in Figure 69 show deep, elongated MPs ($h > 150$ µm). This large penetration depth again indicates a higher laser energy input than previously printed artifacts. The grain structure is much less columnar and includes thin grains grown perpendicular to the MPs. This observed finer structure likely resulted in a Z-direction UTS of 624 MPa, higher than the previous artifacts. From the parallel plane, the center line of the MP appears to be an interface of inwardly grown grains with no smaller grains. It can also be seen that the melt track width ($w \approx 65$ µm) is much smaller than the hatch distance ($h_d = 100$ µm). This difference should result in large LOF defects; however, the rotating layer scan vectors and

deep laser melt penetration allows for a highly dense part to be built. The melt tracks from the previous layer can be seen between the top MPs at an angle of 67 degrees.

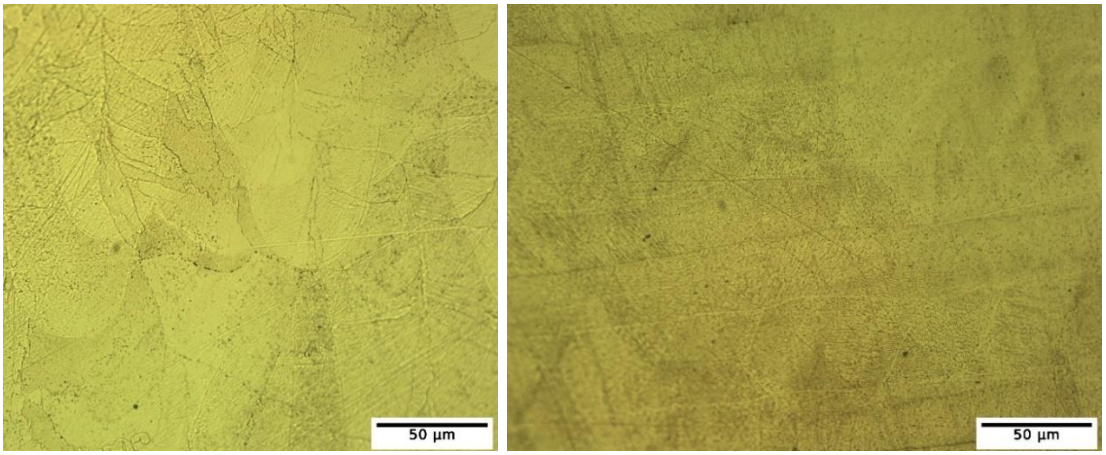

Figure 69: XZ-plane microstructure (left) and XY-plane microstructure (right) for the equalized VED M100 print

Other part properties measured for this part include a PERP surface hardness of 208 HB, which is close to other printed artifacts. Top-surface Ra is 18.47 µm, much higher than previous artifacts. For the side surface, the Ra is 8.5 µm, which is slightly lower but close to previous artifact results. This high top-surface roughness is partly attributed to the lack of MP overlap. Dimensional accuracy in the XY direction is within the range of the M100 default print, but Z-axis accuracy is closer to the range of the M290. The dimensional error values can be seen in Figure 70. This similarity in Z-axis accuracy is likely from the same 40-micron layer thickness. The dross formation on overhangs was also observed to be much worse than in previous prints in either printer.

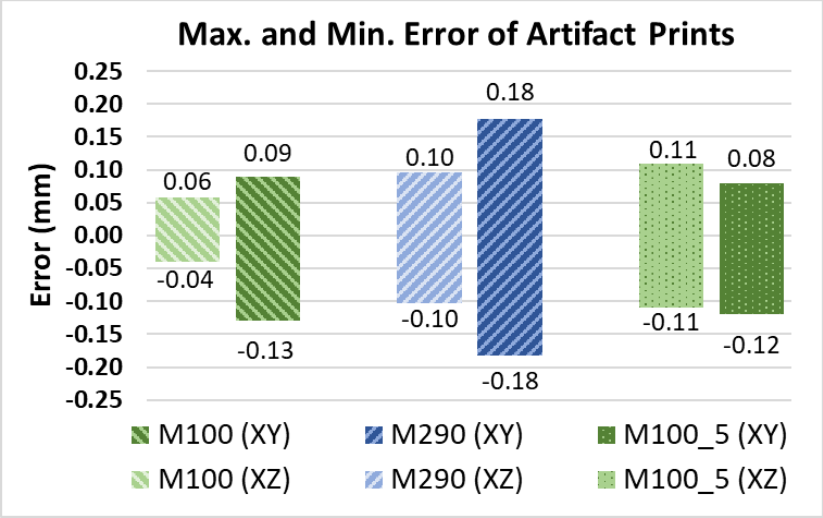

Figure 70: Maximum and minimum errors of test artifacts, including the equalized VED

The second print, which used the proposed dimensionless parameter to attempt to account for the smaller focus diameter of the M100 when transferring process parameters, was not successfully printed. LOF and subsequent contact failure in the early downskin layers prevented the part from being built. The resulting printed part layers are shown in Figure 71. This print failure could be influenced by the hatch distance being too large, though lowering this setting would require the LED to be further reduced to equate the β·VED values.

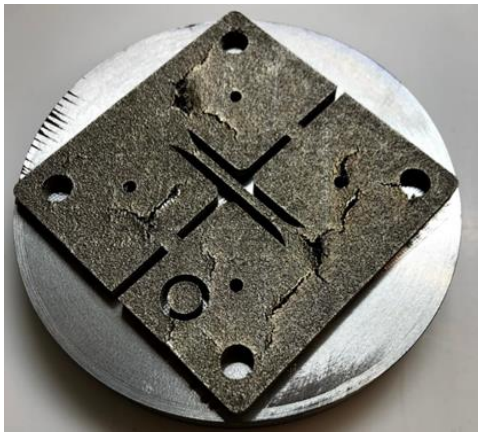

Figure 71: Failed print of the equalized β·VED

4.2 Contour Exposure Strategies

4.2.1 Ledges

The resulting mean surface quality index values for each ledge length can be seen in Figure 72. From the plot, all exposure strategies appear to have the best surface quality for the 0.5-mm ledges, except the decreasing power strategy, for which the 0.25-mm and 0.5-mm ledges seem to have similar quality. This result suggests that both ledges with small and large overhangs are subject to unstable overhang surfaces. As shown in Figure 73, the small ledges have large dross formation, whereas the large ledges are subject to surface degradation due to warping. The decreasing power contour strategy appears to be favourable for the small ledge surfaces, as the low power of the external contours has a greater influence on short overhangs. In this case, the contours account for 0.18 mm of the 0.25 mm overhang. One-way ANOVA tests between exposure parameters at each length yielded no significant differences between prints for any length despite the observed difference: 1 mm ($F(3,11) = 0.18$, $p = 0.904$), 0.5 mm ($F(3,11) = 0.27$, $p = 0.844$), and 0.25 mm ($F(3,11) = 2.19$, $p = 0.167$). However, a two-sample t-test for the 0.25 mm surfaces of default ($\bar{k} = 0.56$, SD = 0.04) and decreasing power contours ($\bar{k} = 0.43$, SD = 0.04) to confirm the lack of significant difference did, in fact, determine that the means were significantly different ($t(4) = 3.96$, $p = 0.029$); the one-way ANOVA gave an overly conservative result.

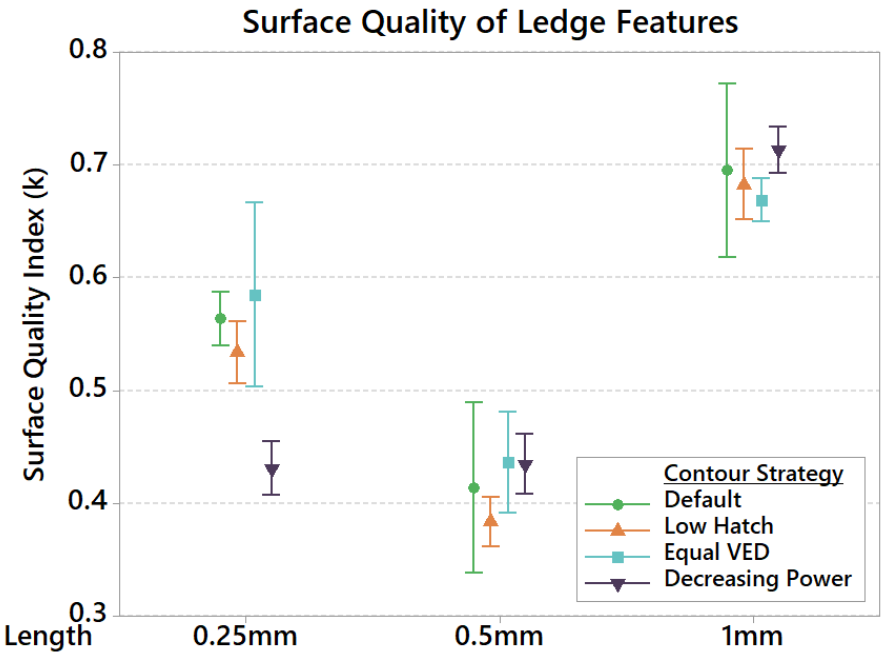

Figure 72: Surface quality of DMLS-printed ledge features using different contour exposures

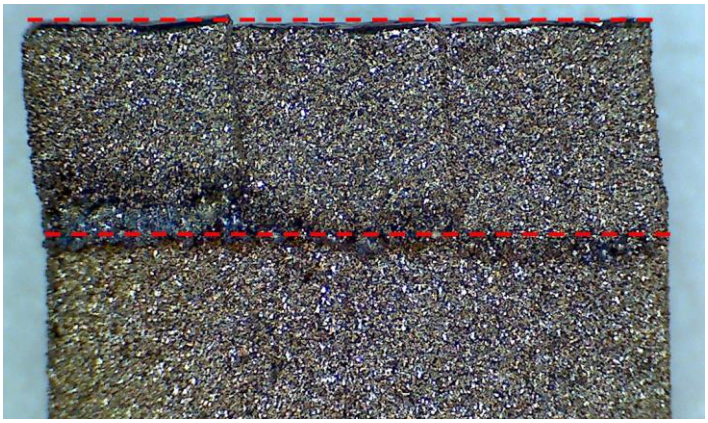

Figure 73: Image of a default-printed with nominal ledge thickness shown by the dashed red lines (ledge overhang length from left: 1 mm, 0.5 mm, and 0.25 mm)

Secondary one-way ANOVA tests and Tukey pairwise comparisons were conducted for each contour strategy to compare the differences between ledge lengths. For the default settings ($F(2,8) = 4.88$, $p = 0.055$), the mean k values of 1-mm and 0.5-mm ledges were significantly different, with a p-value of 0.047. All ledges were significantly different for the low hatch contour strategy ($F(2,8) = 30.45$, $p = 0.001$), with $p < 0.05$. No significance

was found between ledge lengths for the equal VED strategy ($F(2,8) = 4.60$, $p = 0.061$). The decreasing power contours ($F(2,8) = 45.75$, $p < 0.001$) yielded significant differences in k for both the 1 mm – 0.25 mm and 1 mm – 0.5 mm pairs, with both p-values < 0.00. These statistical results generally confirm the trend of k first decreasing and then increasing for longer ledge lengths with both default and low hatch exposures. As well, the poor surface quality of small ledges is shown to be mitigated with the decreasing power strategy, with 0.25-mm and 0.5-mm ledges having comparable dimensional surface quality.

4.2.2 Angled Downskins

Mean surface quality index values for all angled downskins can be seen in Figure 74. All exposure strategies show a decreasing trend in k for increasing angle, with larger differences between strategies at the lowest angle of 30°. One-way ANOVA comparing mean k values of all angles for each print determined that all prints had significant differences between at least two angles, validating the decreasing trends observed: ($F(3,11) = 23.31$, $p < 0.001$) for the default exposure, ($F(3,11) = 132.61$, $p < 0.001$) for low hatch contours, ($F(3,11) = 54.82$, $p < 0.001$) for equal VED contours, and ($F(3,11) = 35.82$, $p < 0.001$) for the decreasing power contours. Tukey's test for multiple comparisons found that the mean k-value was significantly different between 30° and all other angles for all exposure strategies tested, with p-values < 0.00. Additional statistical significance was determined between 60 and 45-degree and 75 and 45-degree surfaces for the low hatch strategy, with $p < 0.00$.

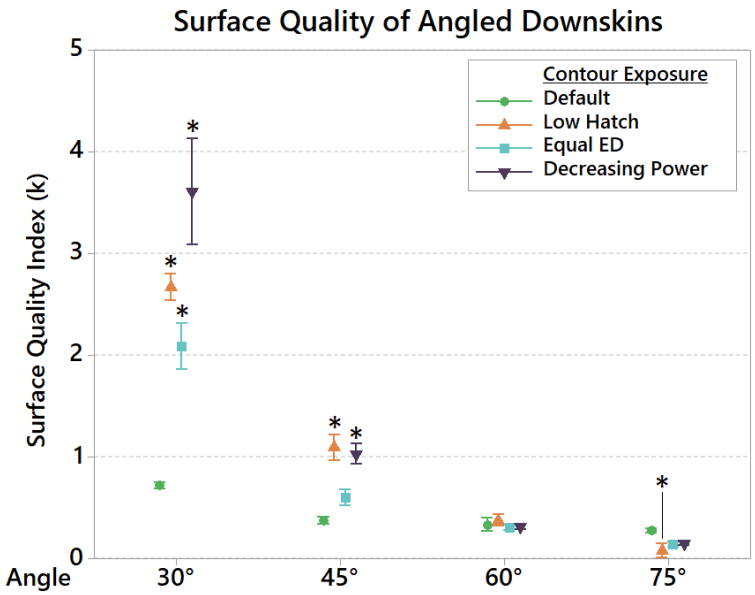

Figure 74: Surface quality of angled downskins in DMLS using different contour exposures (asterisk (*) marks a significant difference to the 'Default' value at $\alpha = 0.05$)

One-way ANOVA was also performed for each angle to compare the differences in mean k between the contour strategy prints. For 30° surfaces, significant differences were found ($F(3,11) = 16.99$, $p = 0.001$). The post-hoc Tukey test revealed that all new contour strategies differed significantly from the default exposure print, with $p < 0.05$. These surfaces had very high form errors, with k above 2. The form error and discoloration are visible to the naked eye, as captured in Figure 75. The low hatch and decreasing power strategies also had significantly different mean k values, with $p = 0.026$. Significant differences were also found for 45° surfaces ($F(3,11) = 15.08$, $p = 0.001$). The significant differences were between low hatch and default, decreasing power and default, equal VED and low hatch, and decreasing power and equal VED, all with $p < 0.05$. No significant differences were found at 60° ($F(3,11) = 0.51$, $p = 0.688$). At 75°, the surface quality of the prints is shown to be improved compared to the default settings. The one-way ANOVA

($F(3,11) = 4.17$, $p = 0.047$) and Tukey test reveal statistical significance in this observation for the low hatch contour strategy ($p = 0.036$).

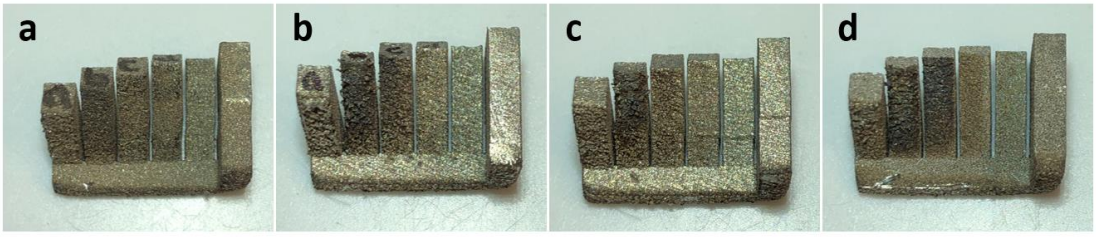

Figure 75: Downskin surfaces of angled specimens for all contour strategy prints: a) default, b) low hatch, c) equal VED, and d) decreasing power

These results suggest that using multiple contours, namely those with higher VED, may be applicable for improving surface quality in surfaces at angles greater than 60°. However, in general, the use of contours appears to have a detrimental effect on downskins, whether through poor geometrical accuracy with the tested strategies or high porosity for contours with low VED, as shown by Cloots et al. [182]. Given that the equal VED contours had much worse surface quality than default exposures without contours, the use of contours does not appear to be a positive factor for overhang printability, as was suggested by their results. Rather, the adjusted 'shell' laser exposure settings for lower VED resulting in high porosity may have had the dominant effect. Based on this initial inspection, it was clear that further parameter optimization of multiple contours for improved downskin quality was not to be pursued, despite the promising results in the literature for non-overhanging geometry [181].

4.2.3 Curved Overhangs

The resulting surface quality index values for the concave and convex overhang specimens can be seen in Figure 76. All printed curves have poor surface quality, with $k > 1$. The

mean k values for the default exposure are the lowest for both convex and concave features. One-way ANOVA was performed on both concave and convex feature results to determine any statistical significance in the differences between prints. There was no significance for concave overhangs ($F(3,11) = 1.26$, $p = 0.352$). The one-way ANOVA for the convex overhangs suggested a significant difference between prints ($F(3,11) = 4.85$, $p = 0.033$). However, the Tukey HSD test did not find any significance; the pair with the lowest p-value was decreasing power and default prints ($p = 0.052$). A two-sample t-test comparing the means of pooled concave and convex geometries from all print conditions found that concave overhangs ($\bar{k} = 1.20$, $SD = 0.15$) have significantly better surface quality than convex overhangs of the same radius ($\bar{k} = 1.48$, $SD = 0.20$); $t(22) = -3.77$, $p = 0.001$, though all curved overhangs were of poor quality. Example side views of each surface for the default exposure can be seen in Figure 77.

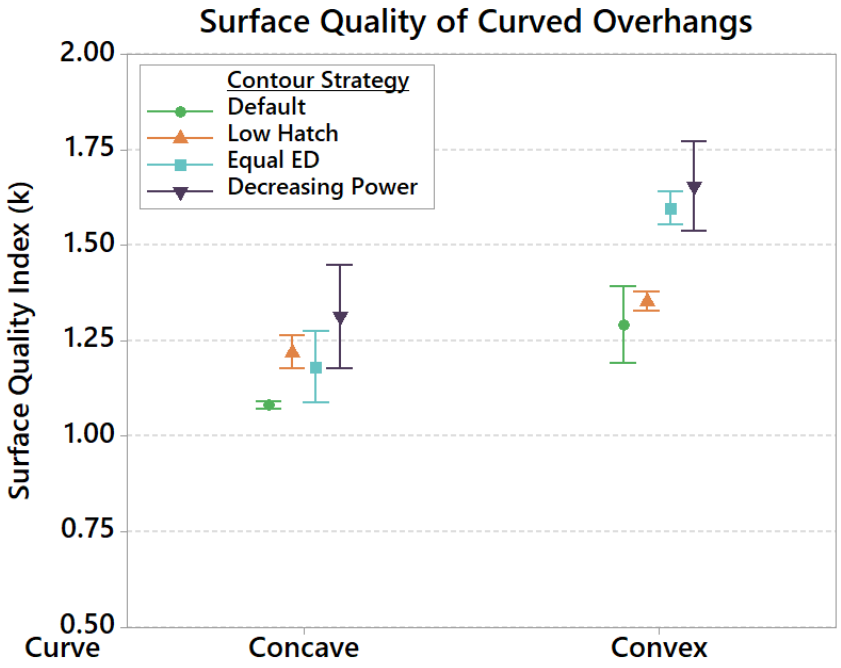

Figure 76: Surface quality of curved overhangs in DMLS using different contour exposures

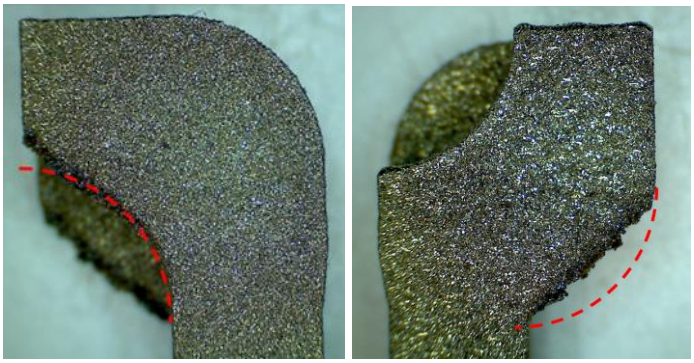

Figure 77: Image showing the surface degradation of default-printed curved overhangs (nominal part contour shown by the dashed red lines)

4.2.4 Upskin Roughness

Since the angled downskins of the contour strategy builds had poor surface quality, which would not have been measurable for roughness parameters, only the upskin and side surfaces were measured.

The mean Ra and Rz values for the angled upskins of all contour prints can be seen in Figure 78. The graph shows that both roughness parameters follow similar trends, with the surface roughness generally decreasing with increases to the incline angle above 30°. It is well known that upskin surface roughness decreases for increasing angles due to the staircase effect, though this characteristic would have less effect on low-angled surfaces, which is observed. Overall, the equal VED contour strategy appears to have the smoothest surfaces. One-way ANOVA and post-hoc Tukey tests were conducted, comparing the mean upskin Ra values of the different exposure strategies for each angle. The difference of the improved equal VED contour upskin Ra compared to the default print was confirmed to be significant for 30° surfaces ($F(3,11) = 6.63$, $p = 0.015$), with an improvement in Ra of 7.37 µm ($p = 0.011$). No other significant differences were determined. The consistently lower surface roughness from equal VED contours shows that using these contours may

improve angled upskins. A reduced edge effect from the contours may have contributed to this improvement [127]. The measured RPc are similar for the default and equal VED contour prints, so the presence of adhered powder is likely similar. Low hatch contours did appear to have systematically lower RPc (**Appendix D)** but no significant effect on the measured Ra. There appears to be a slight improvement in Ra for side surfaces when constant power contours are used; this observation, though not significant, aligns with results from Artzt [181].

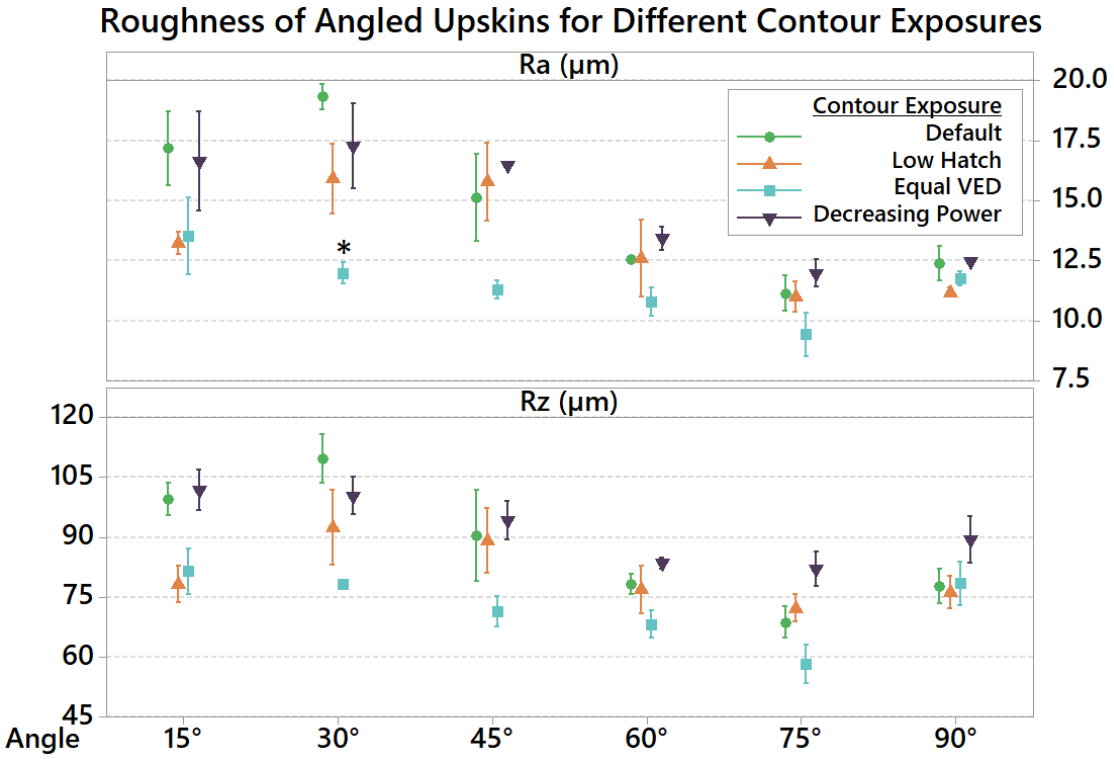

Figure 78: Angled upskin Ra and Rz for contour strategy experiment specimens (asterisk (*) marks a significant difference to the 'Default' Ra value at $\alpha = 0.05$)

4.2.5 Tensile Strength

The tensile specimens were successfully printed in the default and the equal VED contour print jobs. However, the other contour strategies caused the overhanging geometry of the dogbones to deflect upwards. This part curling resulted in recoater contact and the failure

of two dogbones for the low hatch print and one dogbone for the decreasing power print. The deflections could be explained by the increased residual stress in the overhanging region [181]. The resulting mean UTS for each print condition can be seen in Figure 79. The default, low hatch contour, and equal VED contour prints all have UTS values near the maximum reported value from EOS (595 MPa) [126]; all values are listed in Table 14. The decreasing power contour strategy resulted in UTS much lower than the other exposures, though still above the minimum EOS value of 485 MPa [126]. Microscopy of sample cross-sections was used to explore potential causes for this difference and is explored in Section 4.2.7.

Table 14: Tensile strength (UTS) of contour strategy prints

Strategy	N	UTS ± SD [MPa]
Default	3	593 ± 1
Low Hatch	1	591
Equal VED	3	595 ± 9
Decreasing P	2	552 ± 7

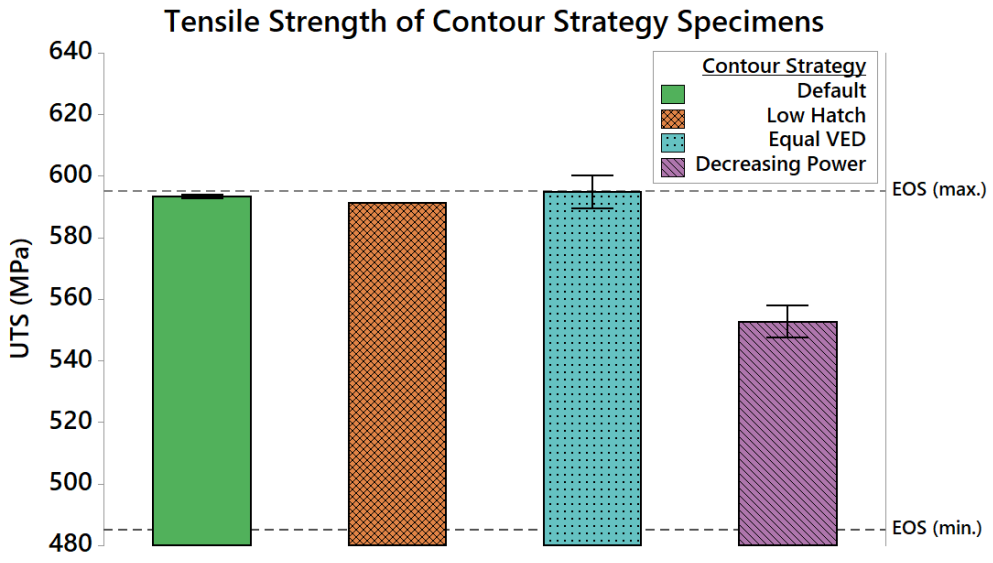

Figure 79: Tensile strength (UTS) of DMLS prints with different contour exposures

4.2.6 Residual Stress

Deflections resulting from residual stress in the cantilever specimens are shown in Figure 80. A one-way ANOVA revealed significant differences between the mean deflections of prints ($F(3,11) = 46.09$, $p < 0.001$). The Tukey test determined that all pairs of exposure strategies had significantly different mean deflections ($p < 0.05$) except for the low hatch equal VED pair. All contour exposure strategies resulted in higher deflections than the default settings. The increased deflections for contour prints align with the observations by Artzt [181] that the use of contours increased the residual stress and that low power exacerbates this effect. These increased residual stresses are also assumed to cause surface cracks, as shown in Figure 81, observed for the contoured prints due to warping and delamination of the contour surface edges [181]. The highest deflections were from the decreasing power contour strategy, which clarifies the cause of the dogbone print failure in this print. However, one potential source of error for these measured deflections is the degradation of the cantilever downskins, as shown in Figure 81. This degradation results in beam sections with reduced thickness, where the beam could more easily deflect.

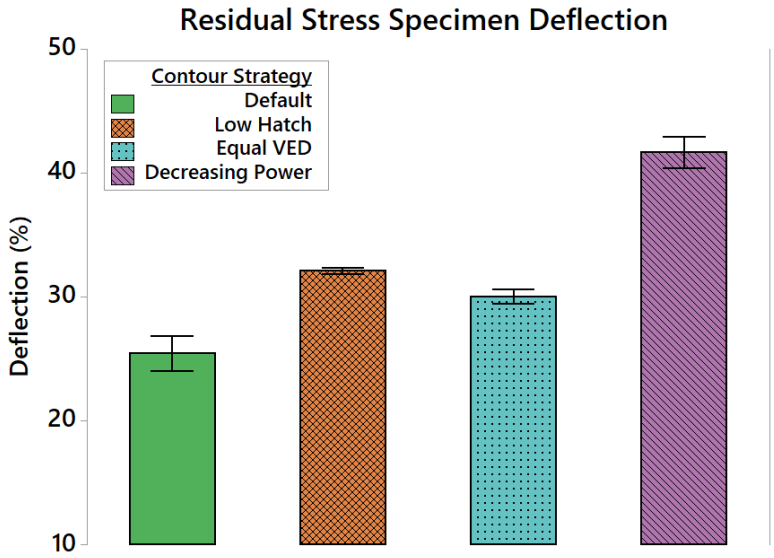

Figure 80: Percent deflection of DMLS-printed cantilever beams using different contour exposures

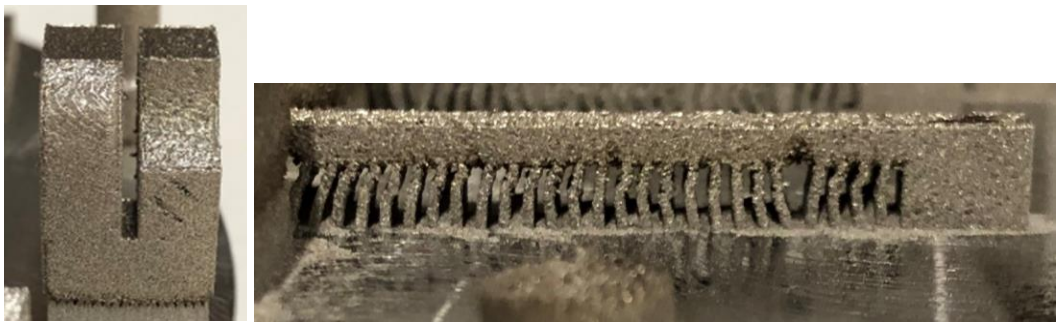

Figure 81: Surface cracks from equal VED contours (left) and downskin degradation for decreasing power print deflection specimen (right)

4.2.7 Microscopy

Single XY-plane cross-sections were prepared and etched for microscopic inspection of each contour strategy print; the images can be seen in Figure 82. The grain structure is visible from the etch, which shows the grains formed from the contour exposures. For the low hatch and equal VED contour samples, the contour lines are visible, with an outer contour effectively smoothing the side surface of the part. The decreasing power contours are not so clearly visible, as the region of contour scan lines has numerous LOF defects.

These defects may not have been significantly detected through stylus profilometry, as many of the irregularities are re-entrant features and sub-surface defects. However, these defects would serve as initiation sites for crack propagation in the tensile specimen, resulting in the lower UTS.

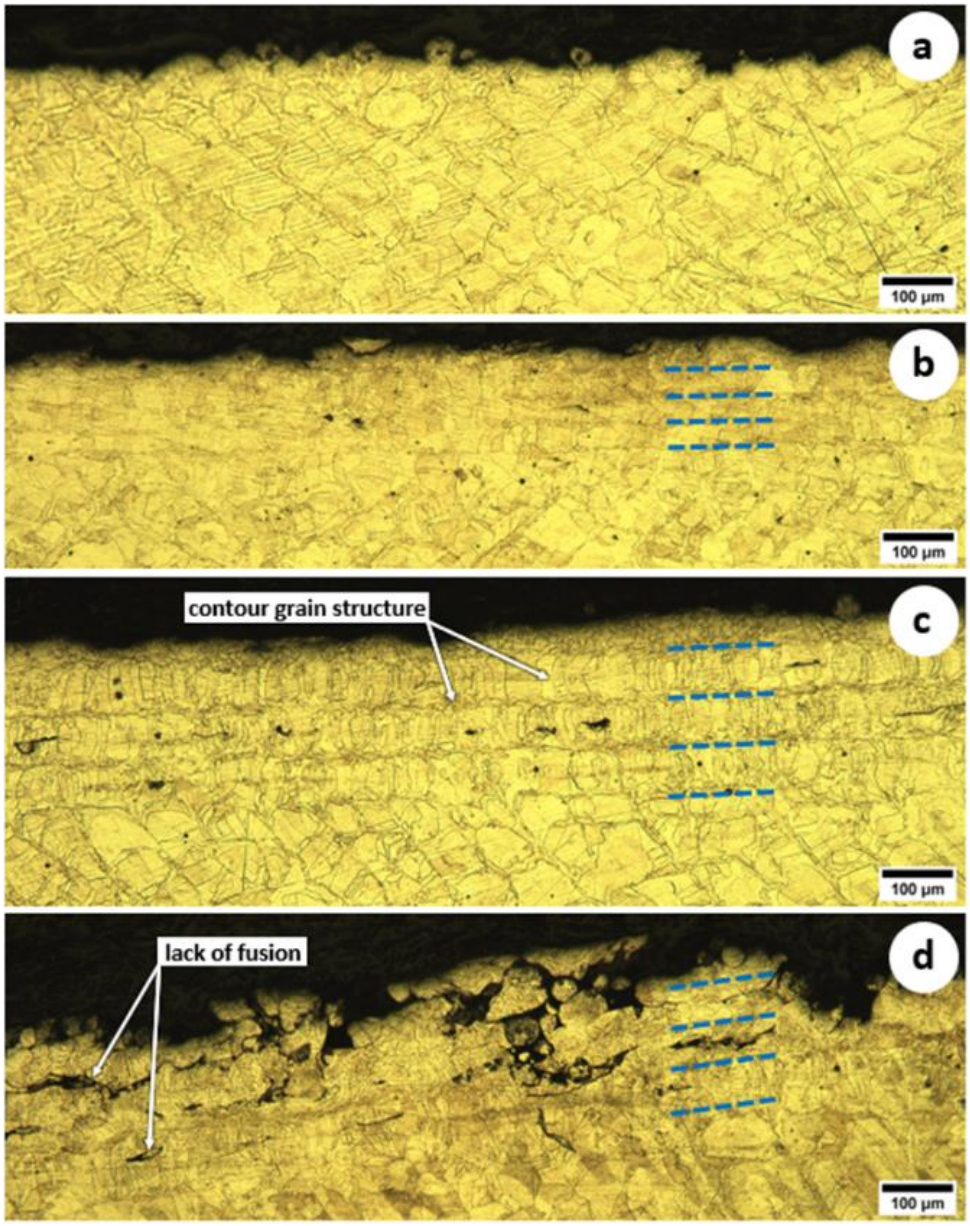

Figure 82: Etched contour print cross-section edges with contour spacing shown by dashed blue lines (a: default, b: low hatch, c: equal VED, d: decreasing power)

4.3 Shielding Gas & Powder Size

Both prints use the CT PowderRange 316L F powder from Carpenter Additive [197]. Shielding gases used in this test are >99.995% purity nitrogen and argon. The CT PowderRange 316L F powder was sieved manually using a 450-mesh sieve. A sample of the sieved powder and as-provided powder was taken, and PSD was measured using backlit OM images captured at 100X. MATLAB image processing was used to estimate each PSD by projected area diameters (d_p), as is used in the literature [210], with approximate sample sizes of 6000 particles. The resulting powder size histograms and cumulative distribution plots for both samples are shown in Figure 83. The D50 powder grain sizes were 22.2 µm for the sieved powder and 32.7 µm for the new powder.

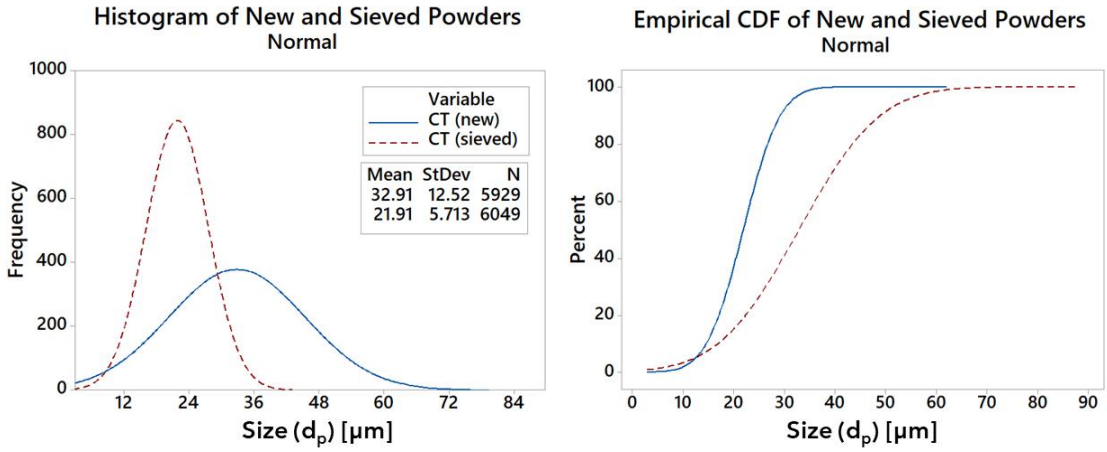

Figure 83: Histogram and cumulative distribution (CDF) plots for sieved and new CT powder

Results from testing the different process parameters of powder PSD and shielding gases are presented and discussed together in this section. The fine CT powder and nitrogen prints are compared to the default CT powder and argon print. Effects of the PSD or shielding gas on powder degradation were not assessed. The test artifacts were printed on an EOS M100.

4.3.1 Roughness

The resulting Ra and Rz for all angled downskin and side surfaces are shown in Figure 84. All build conditions resulted in the same decreasing surface roughness trend for increasing overhang angle for both Ra and Rz, with similar values for all conditions. Individual t-tests for each angle, comparing the fine powder and default and the nitrogen and default prints, were conducted using Ra as the response. No significant difference was found for any comparison. A retrospective power analysis was conducted for the 60° t-tests to determine the similarity between Ra values for a power of 0.8. The analysis determined the fine and standard powder to yield similar downskin Ra within at least 5.82 µm; nitrogen and argon yield similar downskin Ra within at least 6.22 µm. The maximum differences to default downskin Ra were 4.80 µm for the fine powder print and 2.82 µm for the nitrogen print. As such, neither sieved powder nor nitrogen gas was found to have any notable improvement to downskins, despite the theoretical increase in thermal conductivity of the powder bed.

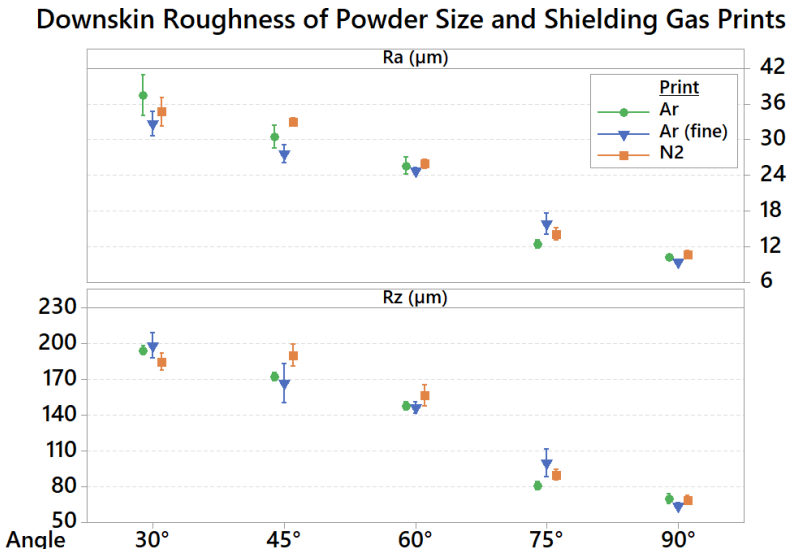

Figure 84: Ra and Rz of angled downskins in DMLS with different gas and powder conditions

The Ra and Rz for angled upskin and top surfaces are shown in Figure 85. All build conditions have the same general Ra and Rz trends, with low roughness for top surfaces (0°) and decreasing surface roughness with increases to the angle above 30°. The fine powder surfaces appear to have the lowest roughness, especially for 30° surfaces, where other conditions have an increased Ra from 15°, but the fine powder results in a decrease. This smoothing could be caused by the improved melting of the fine powder [32]. Individual t-tests for each angle, comparing the fine powder and standard powder (Ar) and the nitrogen and argon prints, were conducted using Ra as the response. There was a significant difference found between the fine powder ($\overline{Ra}$ = 384.30, SD = 23.10) and standard powder ($\overline{Ra}$ = 596.40, SD = 54.50) 30° surfaces (t(2) = 6.21, p = 0.025). There was also a significant difference found between the fine powder ($\overline{Ra}$ = 385.68, SD = 5.47) and standard powder ($\overline{Ra}$= 501.60, SD = 23.9) 45° surfaces (t(2) = 8.20, p = 0.015). No significant differences were found between the nitrogen and argon prints for any upskins. A retrospective power analysis was conducted for the 45° t-tests to determine the similarity between Ra values for a power of 0.8. The analysis determined that nitrogen and argon environments yield similar downskin Ra within at least 3.91 µm. The use of nitrogen yielded similar upskins to argon, where the largest observed difference between the upskin Ra was 2.02 µm. In contrast, the use of sieved powder improved angled upskins by up to 5.39 µm Ra.

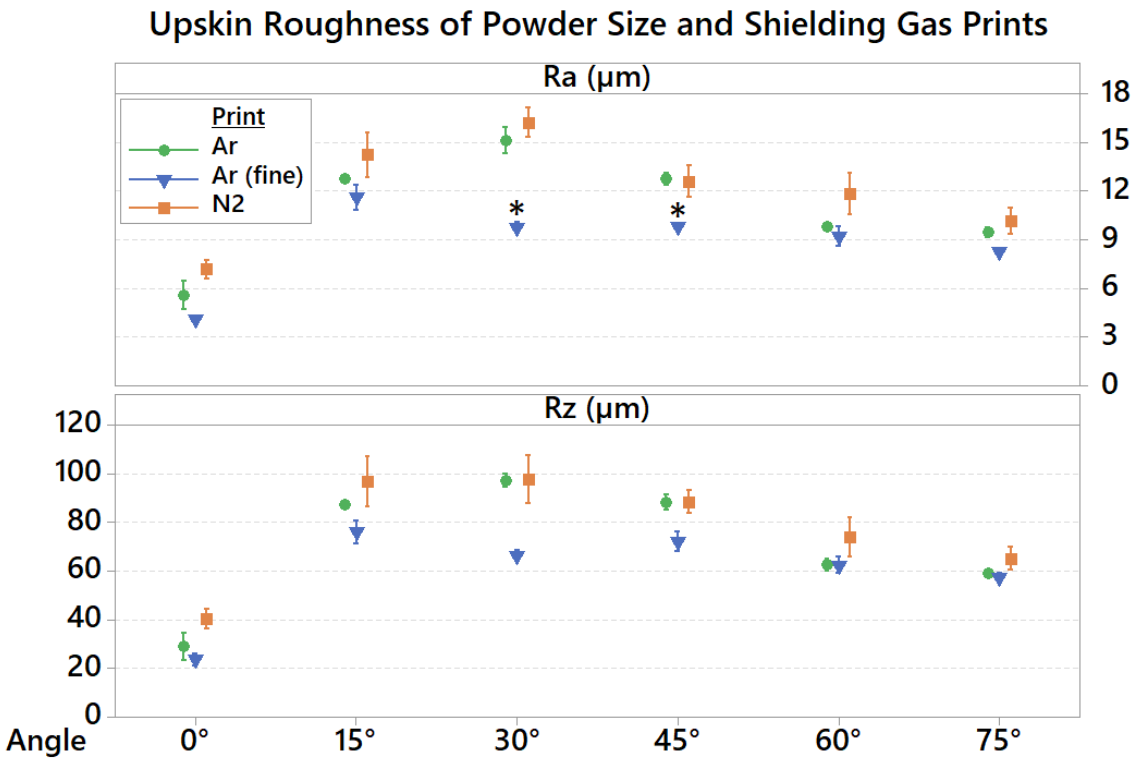

Figure 85: Ra and Rz of gas and powder print angled upskins (asterisk (*) marks a significant difference to the 'Ar' Ra value at α = 0.05)

4.3.2 Density

One sample from each print was cross-sectioned and polished for relative density estimation using the OM image processing method. The resulting relative densities are listed in Table 15. All print conditions resulted in highly dense parts for the default exposure parameters of the M100.

Table 15: Relative density results for shielding gas and powder size prints

Print	Relative Density ± SD [%]
Argon	99.85 ± 0.13
Argon (fine powder)	99.98 ± 0.01
Nitrogen	99.81 ± 0.14

4.3.3 Tensile Strength

The UTS of the printed dogbones for each print condition can be seen in Figure 86, and the values are listed in Table 16; all the dogbones were successfully printed. The results show an increased tensile strength for the nitrogen prints to well above the EOS-reported maximum, whereas the other prints have strengths around this given value. Individual t-tests between the default (Ar) and adjusted build parameter prints determined that the difference between the argon and nitrogen printed samples is statistically significant ($t(3) = 10.15$, $p = 0.002$). This strengthening of the SS could be through microstructural changes from the higher cooling of nitrogen or increased nitrogen in the 316L matrix.

Table 16: Tensile strength (UTS) of shielding gas and powder size prints

Print	UTS ± SD [MPa]
Argon	601 ± 5
Argon (fine powder)	596 ± 4
Nitrogen	634 ± 3

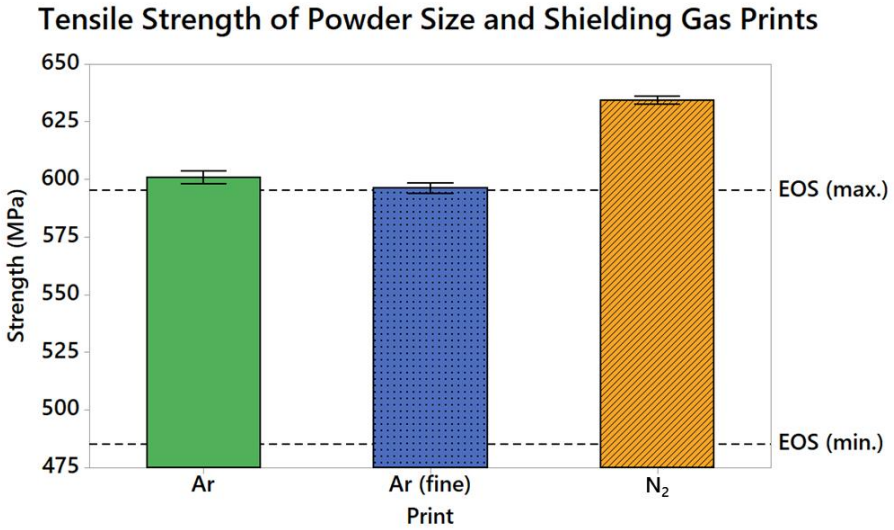

Figure 86: Tensile strength (UTS) of shielding gas and powder size prints

Polished and etched XZ-plane cross-sections were prepared for argon-printed and nitrogen-printed samples to investigate any changes in microstructure. The cross-sections were imaged at 100X for grain size measurements following ASTM E112 [209]. The OM images in Figure 87 show larger and elongated grains for the argon sample. Both samples have an austenitic microstructure with epitaxial growth. The measurements yielded mean intercept lengths in the Z-axis of 63.2 ± 5.4 µm for the argon sample and 30.6 ± 2.8 µm for the nitrogen sample, which would lead to marginal Hall-Petch strengthening in the Z direction. However, the hierarchical microstructure of DMLS 316L makes it unclear exactly to what extent this contributed to the increased strength [54]. The smaller grain size would indicate a higher cooling rate, so a finer cellular growth and dislocation cell size is expected, also contributing to increased strength [21].

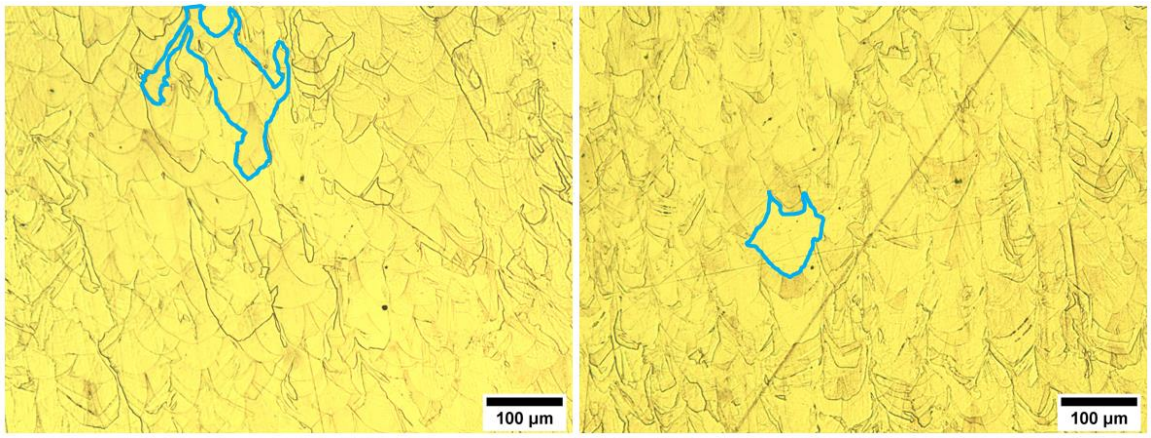

Figure 87: XZ-plane microstructures of Ar (left) and N_2 (right) prints with highlighted grains

It is well known that nitrogen is soluble in the 316L matrix. In the additive process, each layer and each molten scan track are exposed to the shielding gas environment. As such, the nitrogen can readily diffuse into the metal and form interstitials. Valente et al. [211] measured increased nitrogen pick-up in samples printed in a nitrogen environment to be

within the range for AISI 316LN (min. 0.1 wt. %), though this would depend on build and exposure parameters. This increase in nitrogen content has been shown to increase the YS and UTS of 316L [210].

4.3.4 Vickers Microhardness

The Vickers microhardness values can be found in Figure 88 and Table 17. The default (Ar) and N_2 prints have roughly the same hardness values, with slightly lower hardness for the fine powder print. However, no significant differences were found for the fine powder or nitrogen print from individual t-tests. Power analysis for the nitrogen-argon t-test showed that the microhardness of these samples is similar within at least 22 HV1. However, Valente et al. [211] showed that differences in hardness between prints of different shielding gases and nitrogen content are more significant at higher build heights.

Table 17: Vickers microhardness of shielding gas and powder size prints

Print	Hardness ± SD (HV1)
Argon	237 ± 9
Argon (fine powder)	228 ± 9
Nitrogen	238 ± 4

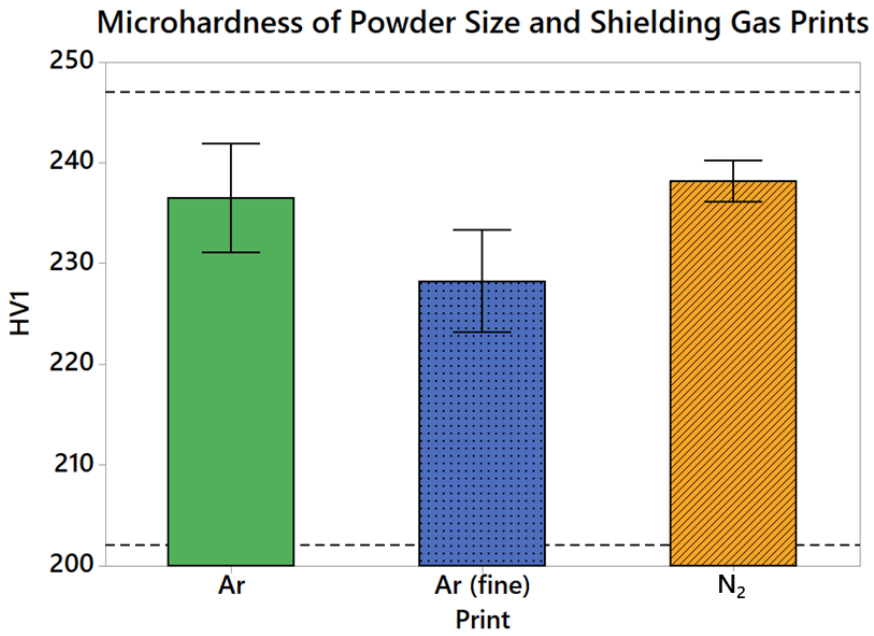

Figure 88: Microhardness of gas and powder prints; dotted lines show the range of HV1 found in the literature for DMLS/SLM 316L **[27, 92]**

4.3.5 Residual Stress

Deflections due to residual stress are shown in Figure 89. The fine powder and nitrogen prints have slightly higher mean deflections, with the nitrogen specimens having the largest deflections. Increased residual stress from nitrogen gas would be due to the higher thermal conductivity of the atmosphere, resulting in more rapid cooling of the top layer for higher residual tension [52]. However, there is no statistical significance found for these differences.

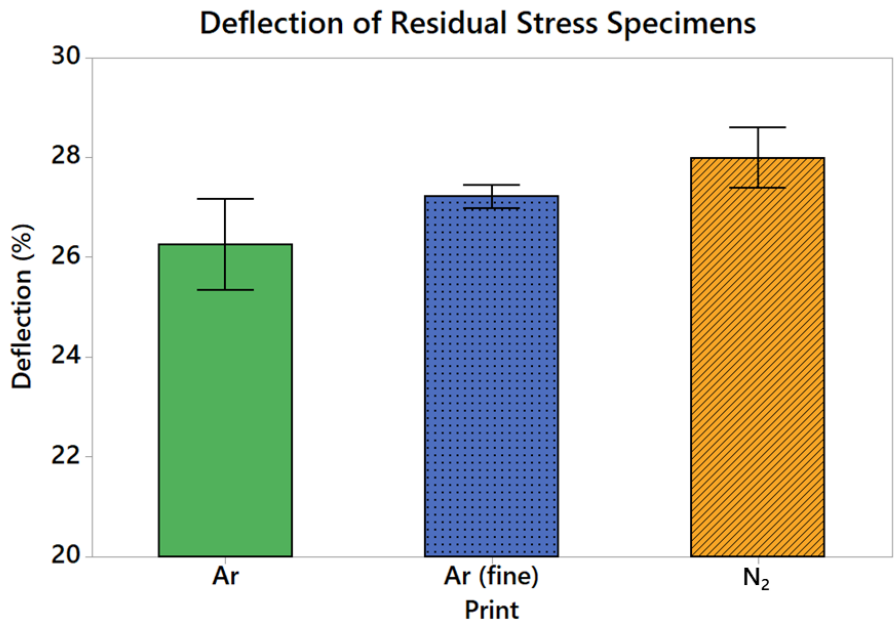

Figure 89: Percent deflection of gas and powder print beams

4.4 Design of Experiments

The ANOVA table for the stepwise model 30° downskin Ra can be seen in Table 18. Power, v, h_d, and the interaction of P*v are significant terms, with $p < 0.05$. The model has adjusted R^2 and predicted R^2 values of 89.35% and 73.99%, respectively, and therefore is well-fitted. Power is found to have the highest F-value and, therefore, the largest effect on surface roughness. Main effect plots and residual plots for this model and all subsequent models discussed are found in **Appendix C**, and the regression equation is shown in equation (7).

$$Ra = 64.8 + 0.743P - 0.0271v - 1.900h_d + 0.00694h_d * h_d - 0.000505P * v - 0.001624P * h_d + 0.000969v * h_d \quad \textbf{(7)}$$

Table 18: ANOVA table for the 30° downskin Ra response surface regression

Source	DF	Adj SS	Adj MS	F-Value	P-Value
Power	1	1226.01	1226.01	119.14	0.000
Speed	1	125.63	125.63	12.21	0.004
Hatch	1	151.03	151.03	14.68	0.002
Hatch*Hatch	1	38.49	38.49	3.74	0.077
Power*Speed	1	100.16	100.16	9.73	0.009
Power*Hatch	1	41.35	41.35	4.02	0.068
Speed*Hatch	1	30.07	30.07	2.92	0.113
Lack-of-Fit	7	90.79	12.97	1.98	0.234
Pure Error	5	32.70	6.54		
Total	19	1836.22			

A contour plot for the power and hatch factors is shown in Figure 90; speed is held to 800 mm/s as v had the lowest effect on the response and 800 mm/s results in the lowest possible Ra values. Response optimization for this model yields the settings of 93 µm and 100 W resulting in Ra = 17.25 µm. Given that the curvature of the model is not significant, follow-up experiments along the steepest descent would be needed to find a true minimum Ra. However, the decreasing VED in this direction would result in unacceptable porosity in the parts, as will be discussed further in Section 4.5.2. Therefore, this experimental model is sufficient for determining a minimal surface roughness while maintaining low porosity.

A second contour plot, shown in Figure 91, was generated from a model of the standard deviation of the mean of all angled downskin Ra (adjusted R^2 = 89.74 and predicted R^2 = 84.50). The plot shows that as the Ra of the 30° surface is reduced, the variability of the downskin surface roughness similarly decreases. Thus, the robustness of the downskin surface roughness to different angles is improved with the optimization of the 30° downskin surface roughness.

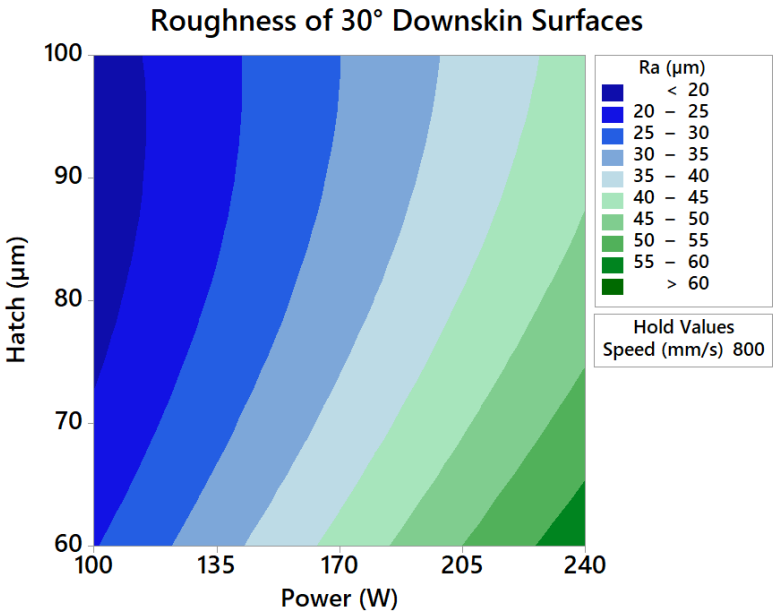

Figure 90: Response contours of 30° downskin Ra

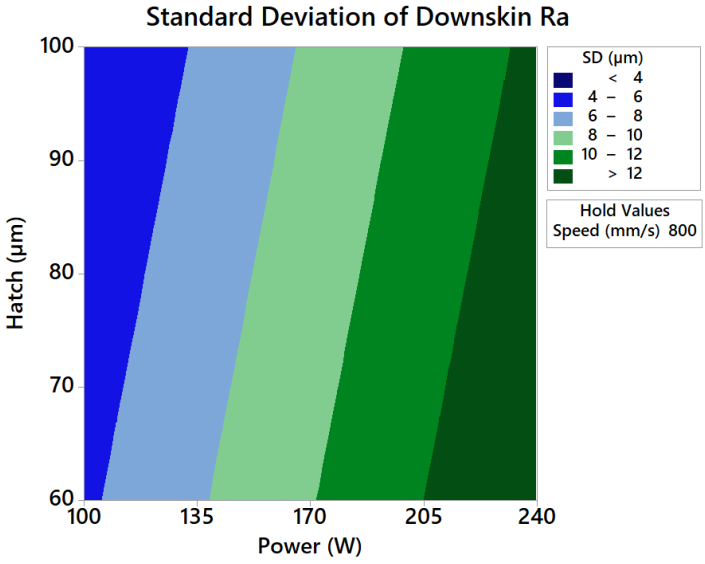

Figure 91: Response contours of the standard deviation (SD) of mean angled downskin Ra

The ANOVA table for the stepwise model of the average Ra of all angled upskins can be seen in Table 19. Hatch distance, P*P, h_d*h_d, and the interaction of P*v are significant terms, with $p \leq 0.05$. The model has adjusted R^2 and predicted R^2 values of 80.54% and 48.12%, respectively, and therefore has some over-fitting. Hatch distance is found to have

the highest F-value and, therefore, the largest effect on surface roughness. The regression equation is shown in equation (8). The curvature of the model is significant, so a minimum Ra for upskins can be determined within the experiment region.

$$Ra = -11.7 - 0.1577P + 0.1188v - 0.423h_d + 0.000268P * P - 0.0063v * v + 0.003519h_d * h_d + 0.000070P * v - 0.000210v * h_d \quad \textbf{(8)}$$

Table 19: ANOVA table for the average upskin Ra response surface regression

Source	DF	Adj SS	Adj MS	F-Value	P-Value
Power	1	0.5311	0.53107	1.33	0.274
Speed	1	0.0047	0.00466	0.01	0.916
Hatch	1	9.5072	9.50723	23.77	0.000
Power*Power	1	4.7337	4.73371	11.84	0.006
Speed*Speed	1	1.1058	1.10580	2.77	0.125
Hatch*Hatch	1	5.4489	5.44894	13.62	0.004
Power*Speed	1	1.9405	1.94050	4.85	0.050
Speed*Hatch	1	1.4134	1.41343	3.53	0.087
Lack-of-Fit	6	2.2320	0.37200	0.86	0.578
Pure Error	5	2.1672	0.43344		
Total	19	39.0540			

A contour plot for the power and hatch factors is shown in Figure 92; speed is held to 800 mm/s as v had the lowest effect on the response and 800 mm/s results in the lowest possible Ra values. Response optimization for this model yields the settings of 84 µm and 189.1 W resulting in Ra = 8.31 µm. These exposure parameters can, in theory, be used together with the resulting minimized downskin Ra settings, as the upskin layers can be set to have individual exposure parameters. The settings for minimal downskin Ra would be used for the main part stripes exposure, as the infill has been shown to affect downskin surface roughness, even with custom downskin exposures [182]. The h_d would be rounded to 0.08 mm in the exposure parameter settings.

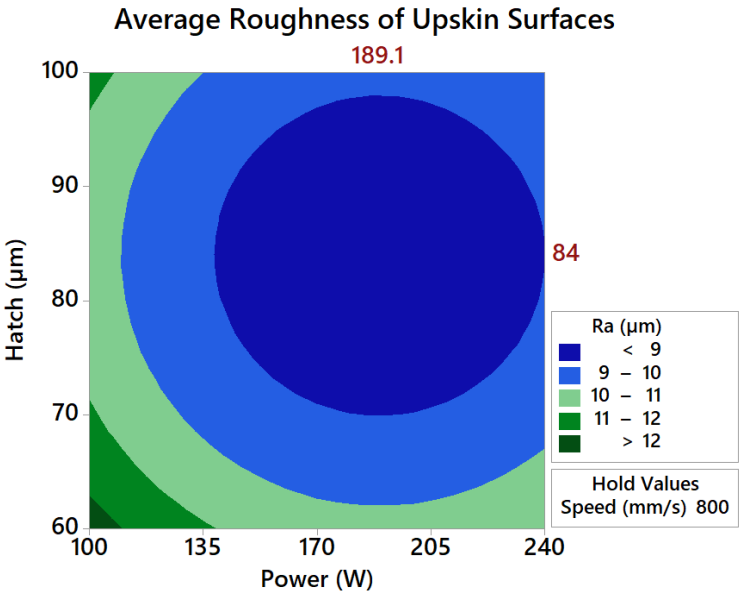

Figure 92: Response contours of average upskin Ra for the CCD DOE

A second contour plot (Figure 93) generated from a model of the standard deviation of the upskin Ra (adjusted R^2 = 80.86 and predicted R^2 = 67.19) shows that the variability of the upskin surface roughness (robustness to changing angle) decreases almost proportionally to the decrease in average upskin Ra.

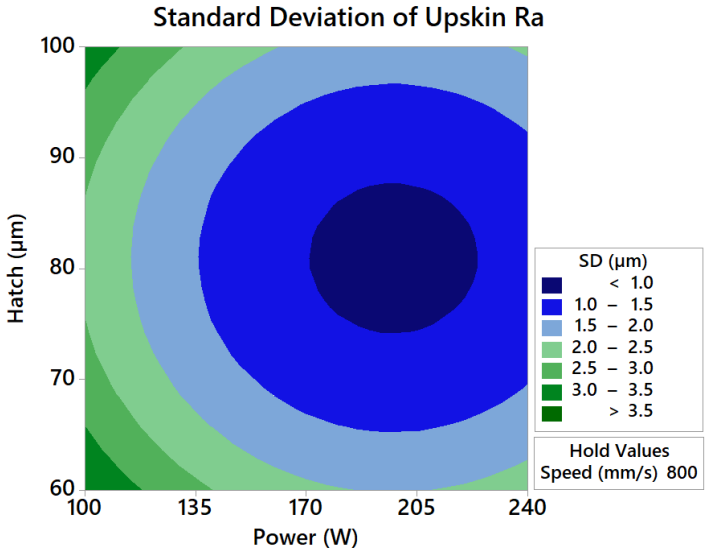

Figure 93: Response contours of the standard deviation (SD) of average upskin Ra

When a critical planar surface must be printed with the lowest possible roughness, the previously optimized upskin exposure parameter settings for angled upskins can be switched to a parameter set developed specifically for top surfaces. These surfaces benefit differently from adjusted exposures than angled upskins, as they are not subject to the staircase effect or adherence of surrounding powder.

The ANOVA table for the stepwise model of the top surface Ra can be seen in Table 20. P, v, and P*P are significant terms, with $p < 0.05$. The model has adjusted R^2 and predicted R^2 values of 82.40% and 66.52%, respectively, but has a lack-of-fit with $p < 0.05$. Therefore, the model may not accurately describe the relationship, despite fitting the data well. Power is found to have the highest F-value and, therefore, the largest effect on surface roughness. The regression equation is shown in equation (9).

$$Ra = 53.7 - 0.5101P + 0.01806v - 0.218h_d + 0.000933P * P + 0.001278P * h_d \quad \textbf{(9)}$$

Table 20: ANOVA table for the top surface Ra response surface regression

Source	DF	Adj SS	Adj MS	F-Value	P-Value
Power	1	402.854	402.854	66.92	0.000
Speed	1	32.632	32.632	5.42	0.035
Hatch	1	0.005	0.005	0.00	0.978
Power*Power	1	104.481	104.481	17.36	0.001
Power*Hatch	1	25.621	25.621	4.26	0.058
Lack-of-Fit	9	79.419	8.824	9.09	0.013
Pure Error	5	4.856	0.971		
Total	19	649.867			

A contour plot generated for the power and speed factors is shown in Figure 94; hatch is held to 60 µm as h_d had the lowest effect on the response, and 60 µm results in the lowest possible Ra values. Response optimization for this model yields the settings of 800 mm/s

and 232.9 W resulting in Ra = 4.74 µm, which is lower than the predicted Ra from the optimized upskin parameters (7.04 µm). Though not a true minimum since the experimental range was driven by downskin optimization, these settings yield the lowest possible as-built surface roughness for a planar part surface within the experimented parameter region.

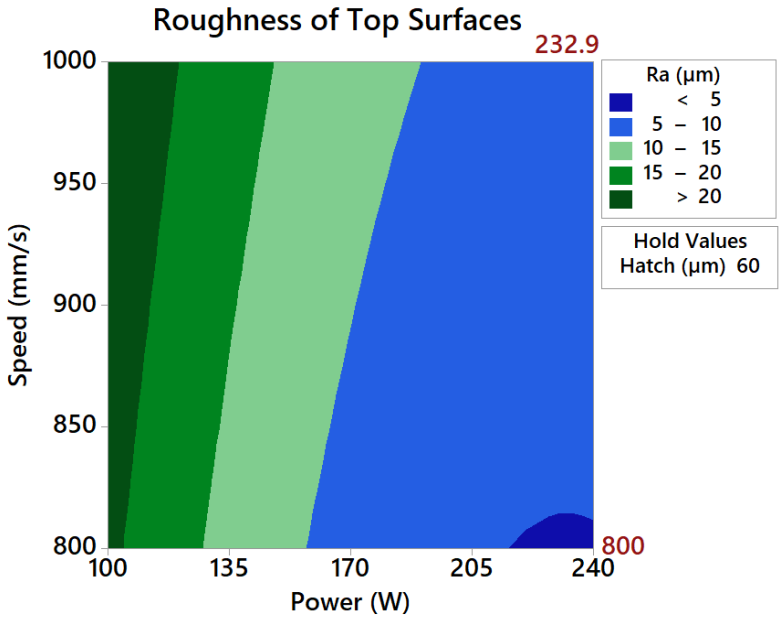

Figure 94: Response contours of top surface Ra

4.4.1 Density

The ANOVA table for the stepwise model of relative density can be seen in Table 21. P, v, P*P, and the interactions of P*v and v*h_d are significant terms, with $p < 0.05$. The model has adjusted R^2 and predicted R^2 values of 89.52% and 65.27%, respectively, but a lack-of-fit p-value < 0.05. Thus, the model may not accurately describe the relationship, despite fitting the data well. Power is found to have the largest effect on porosity. The regression equation is shown in equation (10).

$$RD = 117.46 + 0.0004P - 0.02794v - 0.1094h_d - 0.000190P * P + 0.000084P * v + 0.000122v * h_d \quad \textbf{(10)}$$

Table 21: ANOVA table for the relative density response surface regression

Source	DF	Adj SS	Adj MS	F-Value	P-Value
Power	1	6.9623	6.96229	73.03	0.000
Speed	1	1.4928	1.49275	15.66	0.002
Hatch	1	0.0000	0.00000	0.00	0.999
Power*Power	1	4.3167	4.31674	45.28	0.000
Power*Speed	1	2.7946	2.79461	29.31	0.000
Speed*Hatch	1	0.4729	0.47294	4.96	0.044
Lack-of-Fit	8	1.2052	0.15065	22.06	0.002
Pure Error	5	0.0341	0.00683		
Total	19	17.2787			

The contour plot for relative density can be seen in Figure 95; speed is kept as the unchanging variable at 800 mm/s to match the plot for the downskin Ra. The plot shows that as power is decreased to 100 W and below, the relative density drops lower than 99.4%. The highest porosity measured was for sample #18 (relative density = 96.47%), shown in Figure 96. A relative density of 99.4% is set as the lower limit to account for variability and ensure the confidence interval of the optimized response does not extend below 99% relative density. The optimal exposure settings found by minimizing the 30° downskin Ra, and any further parameter optimization in this direction, would result in unacceptable porosity levels for high-density printing. As such, the optimization includes relative density as a response objective.

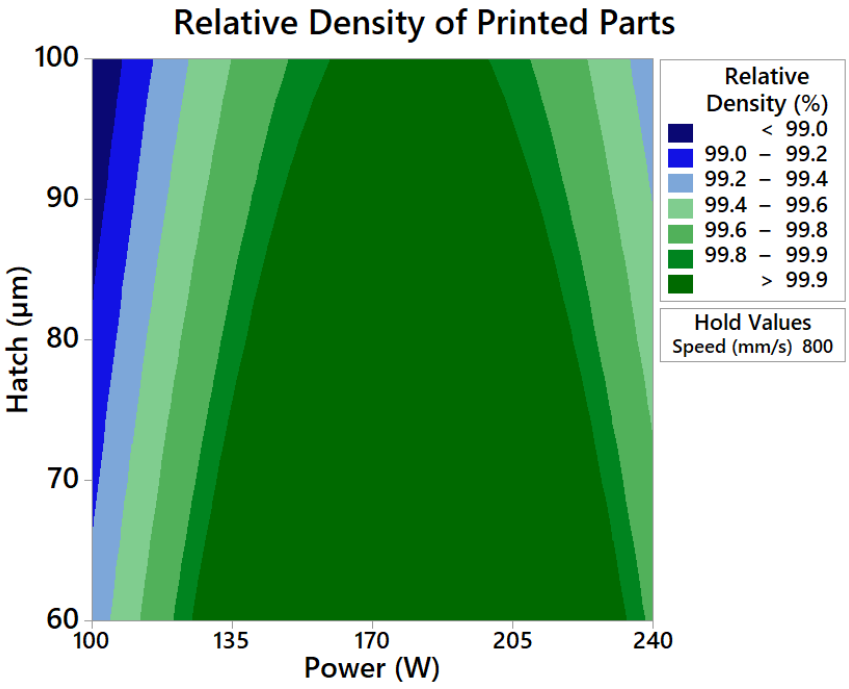

Figure 95: Response contours of relative density

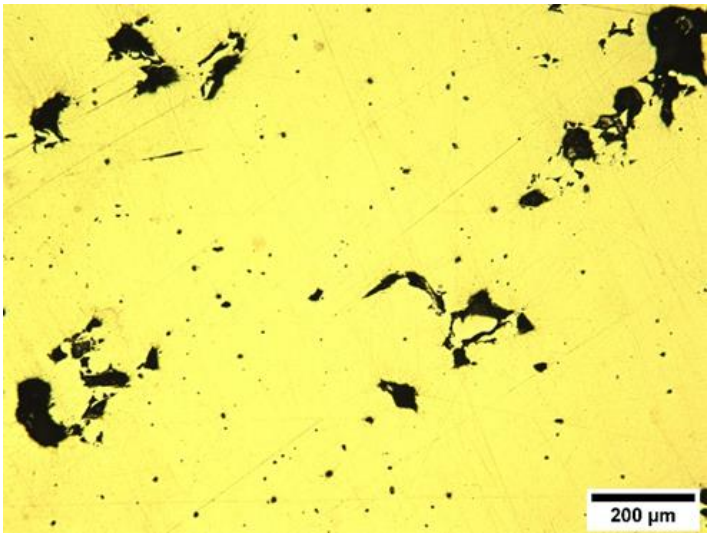

Figure 96: Polished cross-section of DOE part #18, showing small gas pores and large voids resulting in the lowest measured relative density

4.4.2 Downskin Optimization

Multi-objective response optimization of the downskin Ra and relative density models (Figure 97) yielded optimal exposure settings of P = 119.8 W, v = 800 mm/s, and h_d =

88 µm; Figure 97 shows the response optimization results as displayed in Minitab. The resulting predicted values for downskin Ra and relative density are 21.26 µm and 99.45%, respectively. The low end of the 95% confidence interval for relative density is 99.08%, so there is statistical confidence that a 99% density is ensured for the optimized parameters. An overlaid contour plot of the downskin Ra and relative density models is seen in Figure 98.

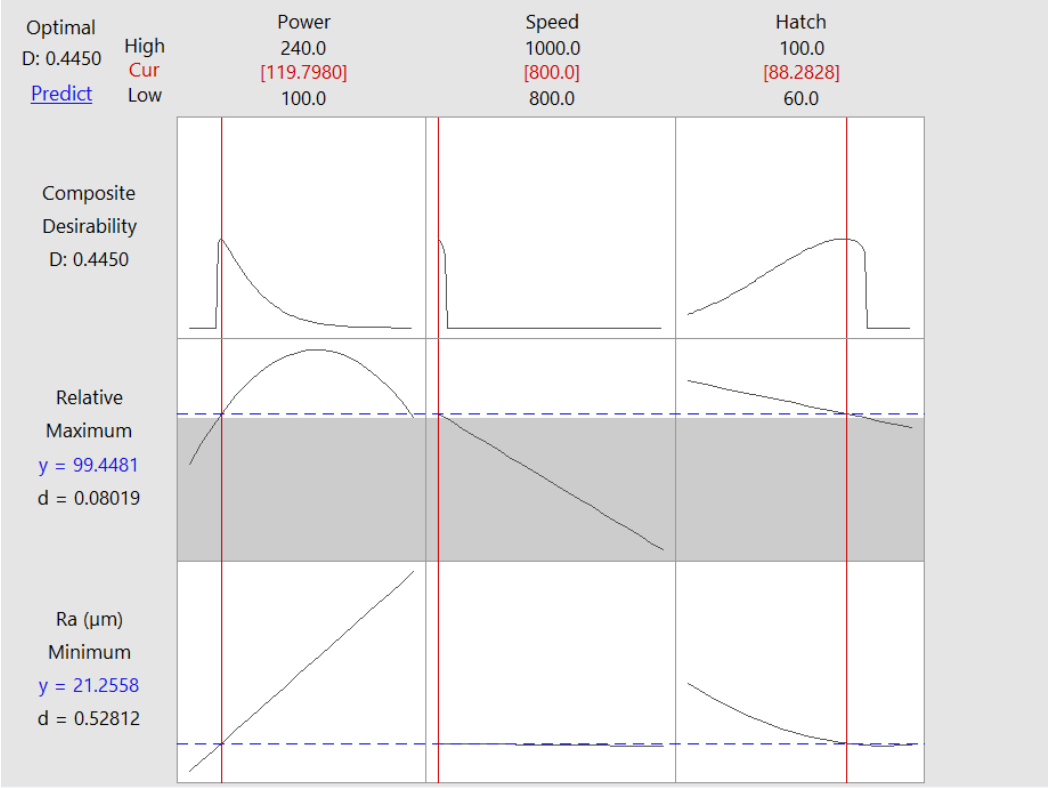

Figure 97: Response optimization of relative density and 30° downskin Ra in Minitab

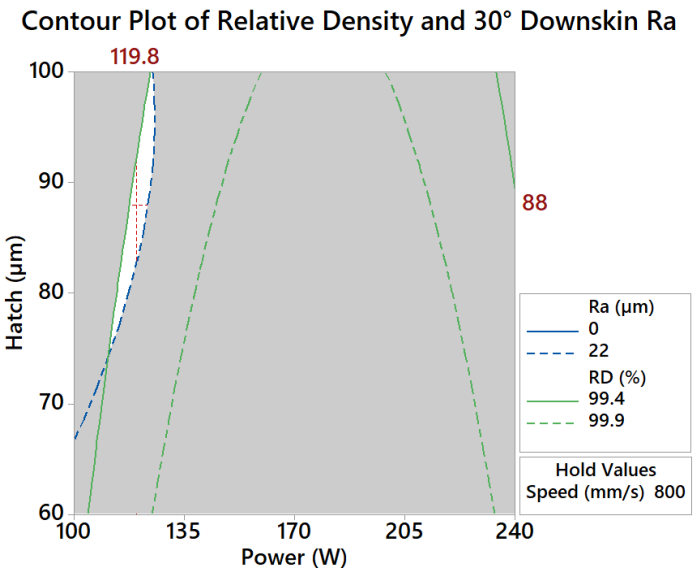

Figure 98: Overlaid response contours of relative density and 30° downskin Ra

4.4.3 Surface Deviations

To ensure the form of the surface does not exceed reasonable tolerance levels (± 0.3 mm), the minimum and maximum deviations were modelled statistically to compare with the multi-objective optimized parameter settings. The ANOVA tables for the stepwise model of min and max deviation are shown in Table 22 and Table 23, with the regressions shown in equations (11) and (12), respectively.

$$min = 1.077 + 0.00686P - 0.00179v - 0.02444h_d - 0.000019P * P + 0.000024v * h_d \quad \textbf{(11)}$$

Table 22: ANOVA table for the minimum deviation (min) response surface regression

Source	DF	Adj SS	Adj MS	F-Value	P-Value
Power	1	0.003610	0.003610	1.43	0.252
Speed	1	0.002560	0.002560	1.01	0.331
Hatch	1	0.025000	0.025000	9.89	0.007
Power*Power	1	0.045125	0.045125	17.85	0.001
Speed*Hatch	1	0.019013	0.019013	7.52	0.016
Lack-of-Fit	9	0.026254	0.002917	1.60	0.315
Pure Error	5	0.009133	0.001827		
Total	19	0.130695			

$$max = -0.203 + 0.002886P \quad \textbf{(12)}$$

Table 23: ANOVA table for the maximum deviation (max) response surface regression

Source	DF	Adj SS	Adj MS	F-Value	P-Value
Power	1	0.4080	0.408040	23.03	0.000
Lack-of-Fit	13	0.1185	0.009119	0.23	0.985
Pure Error	5	0.2003	0.040067		
Total	19	0.7269			

The minimum deviations for the downskins would be caused by defects such as warping and burning, causing surface irregularities. The significant terms for the minimum deviations are h_d, P*P, and the interaction of v*h_d, with $p < 0.05$. Power is found to have the highest F-value and effect on these defects. The model has adjusted R^2 and predicted R^2 values of 63.25% and 41.39%, respectively. The maximum deviations for the downskins would be caused by dross formation defects. Power is the only term in the stepwise model for maximum deviation and is significant, with $p < 0.001$. The model has adjusted R^2 and predicted R^2 values of 53.70% and 47.85%, respectively, so the linear fit with power is a good approximation for the experimental range.

Deviation predictions are found for the optimized exposure parameters of downskin Ra: max = 0.143 ± 0.089 mm and min = 0.246 ± 0.053 mm (95% confidence intervals). The optimized P, v, and h_d do not result in deviations outside ± 0.3 mm for 30° downskins.

4.4.4 Vickers Microhardness

The ANOVA table for the stepwise model of microhardness can be seen in Table 24. P, h_d, P*P, v*v, and the interaction of P*h_d are significant terms, with $p < 0.05$. The model has adjusted R^2 and predicted R^2 values of 75.99% and 36.64%, respectively, and lack-of-fit

p-value < 0.05, so it is not a very accurate model. Power and the square term of power have the highest F-values, so power has the largest effect on hardness. The contour plot generated of power vs. hatch distance can be seen in Figure 99. Hardness can be sparingly used as an indication of the tensile properties of a material [61]. The predicted microhardness for the optimized parameter settings is 215 HV1.

Table 24: ANOVA table for the Vickers microhardness response surface regression

Source	DF	Adj SS	Adj MS	F-Value	P-Value
Power	1	5752.3	5752.26	23.91	0.000
Speed	1	97.9	97.90	0.41	0.535
Hatch	1	1536.1	1536.10	6.39	0.027
Power*Power	1	6038.0	6037.95	25.10	0.000
Speed*Speed	1	1537.5	1537.52	6.39	0.027
Power*Speed	1	810.0	810.02	3.37	0.091
Speed*Hatch	1	1829.7	1829.73	7.61	0.017
Lack-of-Fit	7	2600.9	371.55	6.50	0.028
Pure Error	5	285.8	57.16		
Total	19	19036.4			

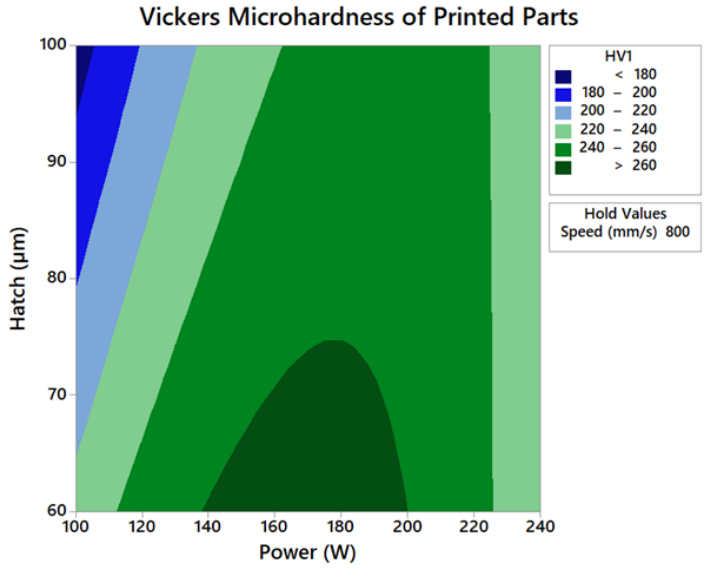

Figure 99: Response contours of Vickers microhardness

4.4.5 Residual Stress

The ANOVA table for the stepwise model of deflection can be seen in Table 25. P, h_d, P*P, h_d*h_d and all interaction terms are significant ($p < 0.05$). The model has high adjusted R^2 and predicted R^2 values of 93.20% and 85.51%, respectively; the regression equation is shown in equation (13). Power has the largest main effect on the deflection; however, both interaction terms with power also have high F-values. The contour plot generated of power vs. hatch distance can be seen in Figure 100. The predicted deflection for the optimized parameter settings is 29.7%.

$$\begin{aligned} deflection\ [\%] = {} & 15.7 - 0.0953 - 0.0012v + 0.597h_d - 0.000522P * P \\ & - 0.002623h_d * h_d + 0.000218P * v + 0.0012P * h_d \\ & - 0.000454v * h_d \end{aligned} \quad \textbf{(13)}$$

Table 25: ANOVA table for the deflection response surface regression

Source	DF	Adj SS	Adj MS	F-Value	P-Value
Power	1	18.073	18.0731	39.40	0.000
Speed	1	0.017	0.0174	0.04	0.849
Hatch	1	2.933	2.9330	6.39	0.028
Power*Power	1	20.960	20.9596	45.70	0.000
Hatch*Hatch	1	3.524	3.5237	7.68	0.018
Power*Speed	1	18.619	18.6189	40.59	0.000
Power*Hatch	1	22.572	22.5721	49.21	0.000
Speed*Hatch	1	6.583	6.5825	14.35	0.003
Lack-of-Fit	6	2.275	0.3792	0.68	0.674
Pure Error	5	2.770	0.5540		
Total	19	128.211			

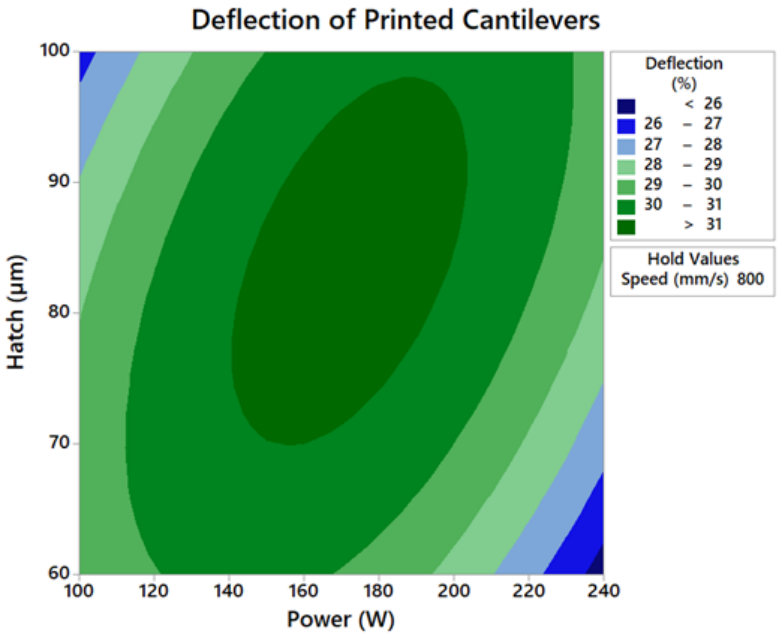

Figure 100: Response contours of percent deflection

4.5 Verification Prints

Settings for the 'new' exposure parameters for the model verification print were selected using the optimized downskin surface roughness from Section 4.4.2. The hatch distances for the new exposure parameter settings were rounded to the nearest 0.01 mm for the EOSPRINT settings. Selected settings for the print are listed in Table 26. Due to software issues for upskin issues detailed in Section 0 and to test model accuracy for different contour conditions, neither upskin nor contour exposures are included. Indirect verification of upskin regression models is completed for printed parameters. This adjustment does not affect the 30° and 45° downskins, as the contour power for low-angle overhangs is set to 0 W by default. The 60-90° surfaces did, however, have different contour exposures from the model, which is important to note when interpreting the results. The 30° and 45° surfaces are the most important to verify directly, as they have the greatest impact on reducing the overall surface roughness of a printed part.

Table 26: Exposure settings for the optimization verification print

Exposure	Type	Stripes			Upskin			Downskin		
		P [W]	v [mm/s]	h_d [mm]	P [W]	v [mm/s]	h_d [mm]	P [W]	v [mm/s]	h_d [mm]
Default	Infill	214.2	928.1	0.10	150.2	514.9	0.10	74.3	951.2	0.09
	Contour (x1)	136.1	446.9	--	127.9	447.1	--	0	4000	--
'New'	Infill	119.8	800	0.09	189.1	800	0.08	119.8	800	0.09
	Contour (x0)	--	--	--	--	--	--	--	--	--

4.5.1 Roughness

Resulting Ra and Rz values for all upskins are shown in Figure 101. The predicted average angled upskin Ra for the downskin-optimized parameters was 9.66 ± 0.44 µm, which would be comparable to the measured average for the default settings (10.55 ± 0.53 µm). However, since the contour exposures were not enabled for the 'new' prints, the measured angled upskin Ra values are consistently much higher than the default-printed samples ($\overline{Ra}$ = 16.73 ± 0.51 µm). The measured average upskin Ra for the default exposure (with default contour scans) agrees with the upskin Ra model prediction of 9.80 ± 0.41 µm. The difference in predicted and measured Ra for the 'new' upskins shows that using modified contour scans, different than the default contours used to model the regression, greatly affects the surface roughness of printed parts. The measured top surface Ra of the new exposure was 7.16 ± 0.80 µm, which agrees with the predicted value of 7.04 ± 1.09 µm from the top surface model and is comparable to the measured default top surface Ra 7.20 ± 0.73 µm. As such, the upskin parameters are shown to have similar top-surface roughness to default parameters (as predicted).

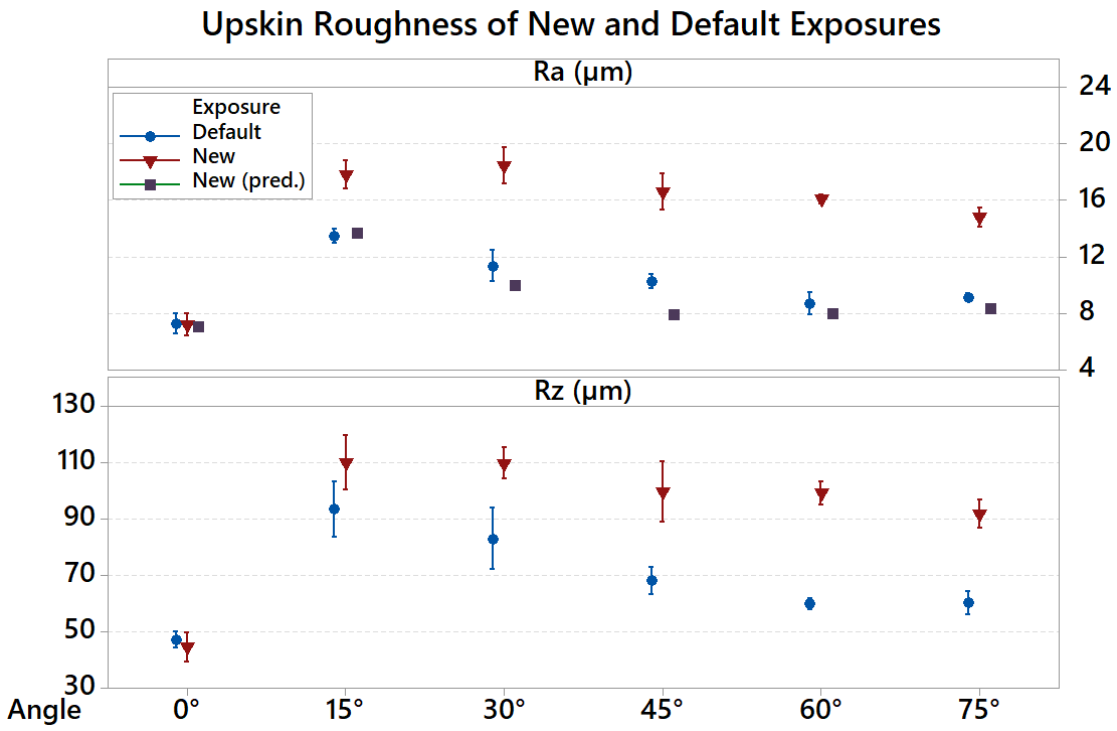

Figure 101: Upskin Ra and Rz of default and new test exposure parameters; also shown is the predicted Ra from regression models with the new parameters (with proper contour and upskin exposures)

Based on the measured default Ra values, the predicted improvements to average upskin Ra using the optimized upskin exposure parameters (with default contours) for proper upskin layer exposures would be 2.24 µm, a 21.2% decrease. Similarly, the predicted improvements to top surface Ra using the upskin exposure parameters optimized for top surfaces would be 2.47 µm, a 34.2% decrease.

As for the downskin and side surfaces, measured Ra and Rz are found in Figure 102. Both downskin exposures resulted in decreasing surface roughness with increased part angle. However, the optimized parameters resulted in a more levelled slope, with a lower maximum surface roughness than the default prints. Individual t-tests were conducted for each discrete angle. Significant differences were found for the 30° ($t(2) = 4.92$, $p = 0.039$),

45° (t(2) = 5.75, p = 0.029), and 90° comparisons (t(3) = -9.47, p = 0.002). The 30° mean Ra is improved by 7.99 µm ($\overline{Ra}$ = 28.88, SD = 0.91 to $\overline{Ra}$ = 20.89, SD = 2.66), the 45° surfaces are improved by 3.11 µm ($\overline{Ra}$ = 22.19, SD = 0.29 to $\overline{Ra}$= 19.08, SD = 0.89), and the 90° mean Ra is increased by 4.58 µm ($\overline{Ra}$ = 8.36, SD = 0.43 to $\overline{Ra}$ = 12.94, SD = 0.72). The increased roughness of the measured higher angle and side surfaces is again attributed to the lack of default contours. The measured 30° and 45° are in good agreement with the predicted values from the regression models (21.28 and 19.58 µm).

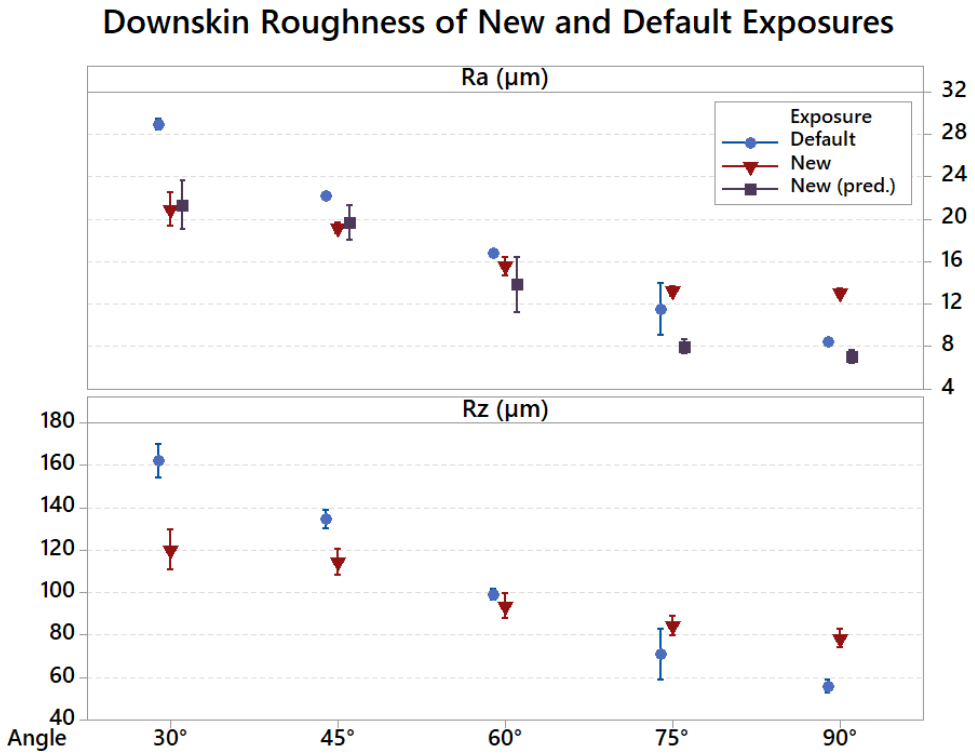

Figure 102: Downskin Ra and Rz of default and new test exposure parameters; also shown is the predicted Ra from regression models with the new parameters (includes contours for ≥ 60°)

Areal colour maps of the new and default 30° downskin surfaces are shown in Figure 103. The default surface is less uniform than the new exposure surface, with many more peak artifacts from dross formation and adhered powder. The Sa of the default and new

exposures are 44.5 µm and 33.5 µm, respectively, a similar improvement result as with the contact profilometer measurements.

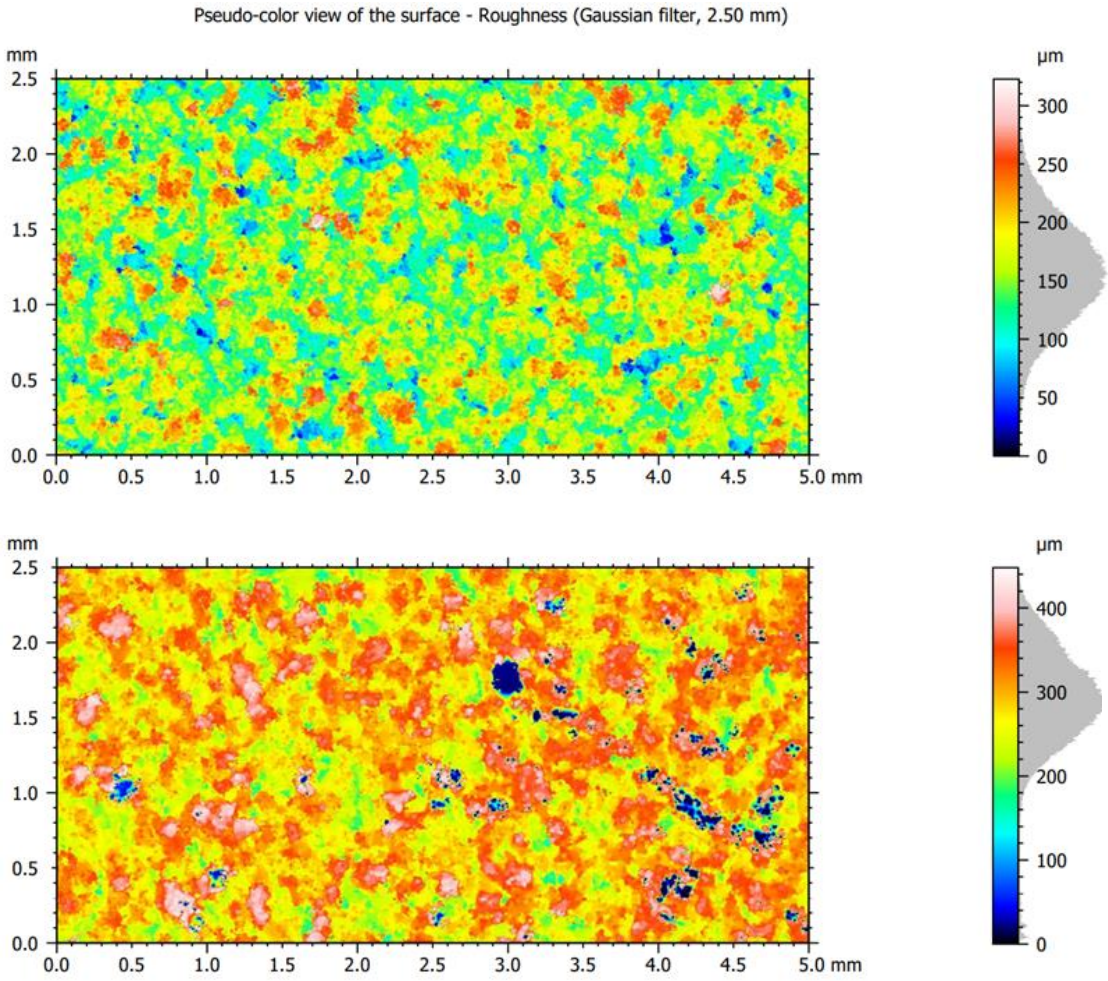

Figure 103: Color height maps for the surface roughness of 30° downskin surfaces for optimized (top) and default (bottom) exposures

4.5.2 Other Properties

The relative density of the new exposure-printed samples dropped slightly from 99.98% to 99.45%, though this is above the limit of 99%. The mean deflections of the residual stress specimens for the default and new exposures are listed in Table 27. A two-sample t-test found a significant difference between the default-printed and the new exposure-printed

parts: $t(2) = -11.90$, $p = 0.007$. However, the predicted deflection for the new exposures from the regression model (29.7%) is lower than the measured deflections. This result implies that the inclusion of contours has a large effect on the residual stress of the final part, which was also observed by Artzt [181]; moreover, the interaction of stripes and contour exposures on residual stress may be significant.

Table 27: Deflection results for default and new exposure parameters

Exposure	Deflection ± SD [%]
Default	27.4 ± 0.4
'New'	34.8 ± 1.0

The average Vickers microhardness values of the printed samples are listed in Table 28. A two-sample t-test did not determine any significant difference between the two exposures ($t(2) = 2.46$, $p = 0.133$), though the 'new' average was lower by 13 HV1. Measured hardness values for the new exposure parameter prints agree with the predicted 215 HV1.

Table 28: Vickers microhardness results for default and new exposure parameters

Exposure	Hardness ± SD [HV1]
Default	231 ± 2
'New'	218 ± 9

The resulting mean UTS values of the printed tensile specimens are shown in Figure 104. A two-sample t-test did yield a significant difference between the default ($\overline{\sigma_u}$ = 621, SD = 2 MPa) and new ($\overline{\sigma_u}$ = 526, SD = 27 MPa) exposures; $t(4) = 6.06$, $p = 0.004$. This large decrease results in UTS values at the lower end of the EOS value range while still within the given limits. The stress-strain curve in Figure 105 shows how the YS appears to be reduced with the new exposure, along with a much lower ductility.

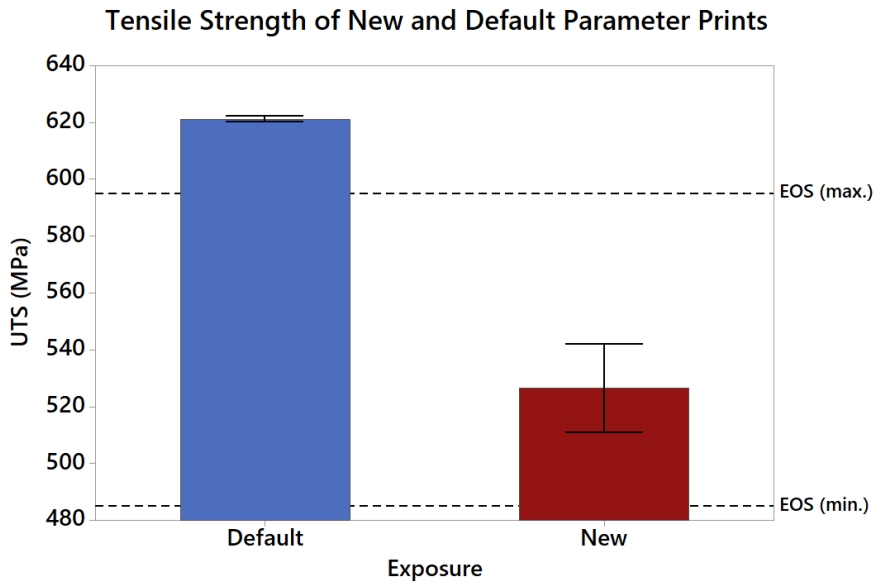

Figure 104: Tensile strength (UTS) for default and new exposure parameters

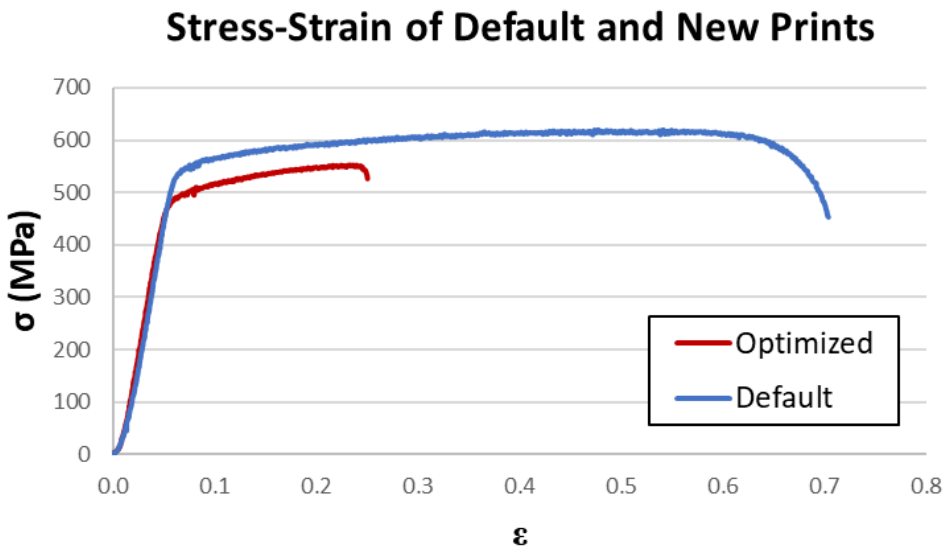

Figure 105: Stress-strain curve of default and new exposure parameter-printed tensile specimens

Microstructural inspection of the samples was completed for XY and XZ planes of a new exposure-printed part. Mean intercept lengths for grain size were measured following ASTM E112 [209], which yielded mean intercept lengths of 12.2 ± 0.4 µm in the XY plane, which is smaller than the 24.9 ± 0.5 µm length from the default parameters. However, a

similar grain structure was retained, with smaller grains along the centerlines of laser scan tracks, as shown in Figure 106. Increased voids in the new exposure part cross-section, which contribute to the lower relative density, are largely located along the edges of scan tracks as LOF defects. This void pattern of ~10 µm pores is due to the scan track width only being approximately 90 µm (110 µm for default exposures). This width is equal to the hatch distance, so any balling of the MP results in void formation. Although the porosity is still within the high-density range (>99%), the exposure settings can be adjusted to increase the MP width and close these gaps. As adjustments, the hatch distance could be lowered, or power could be incrementally increased, as power has a substantial impact on MP width [137]. In the XZ plane, the MP depth was measured as ~80 µm, compared to ~90 µm for default prints, and the grain elongation ratio for the Z-axis was measured as 2.1 as opposed to 2.6 in default prints.

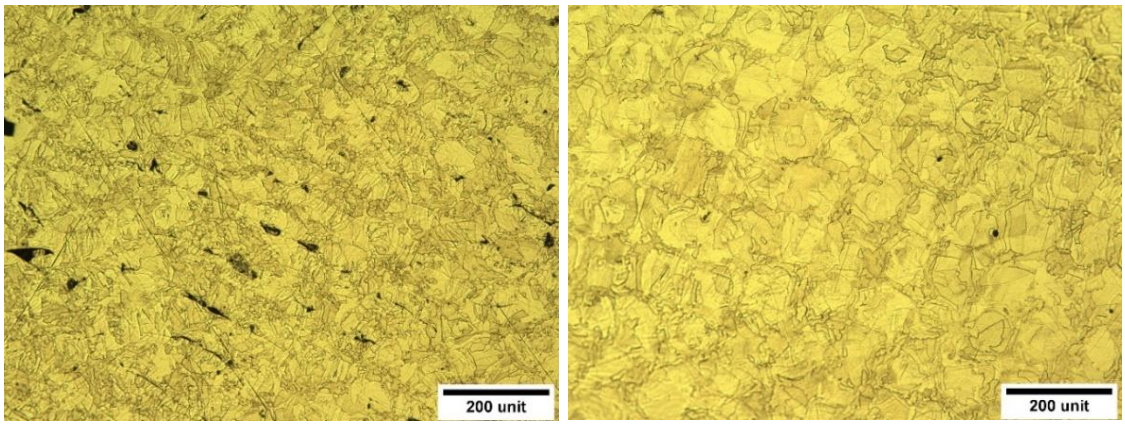

Figure 106: XY-plane microstructures of default (left) and new exposure (right) prints

4.5.3 Test Artifact

The test artifact printed with the new exposures was inspected following the same regime described in Section 2.1. Notable results included lower hardness for both PERP (179 HB) and PAR (169 HB) surfaces compared to the hardness measured in default printed artifacts:

203 ± 3 HB for PERP surfaces and 189 ± 3 HB for PAR surfaces. Deflection of the cantilever feature (31.4 %) was only slightly higher than the average from default test artifacts (28.1 ± 2.8 %), as the placement on the artifact contributes to the overall residual stress in the specimen.

Dimensionally, the overall error of the part was found to be slightly lower for XY and XZ planes compared to default artifacts, as shown in Figure 107. The printability of small features also differed, as shown in Table 29. The 'new' test artifact had better success with small holes and spaces but mostly worse success with boss features. All other features appeared to have similar print results as default exposures. These differences are likely attributed to the difference in contours between the prints. The new exposure parameters were equally successful in printing the 8:1 aspect ratio circular boss feature.

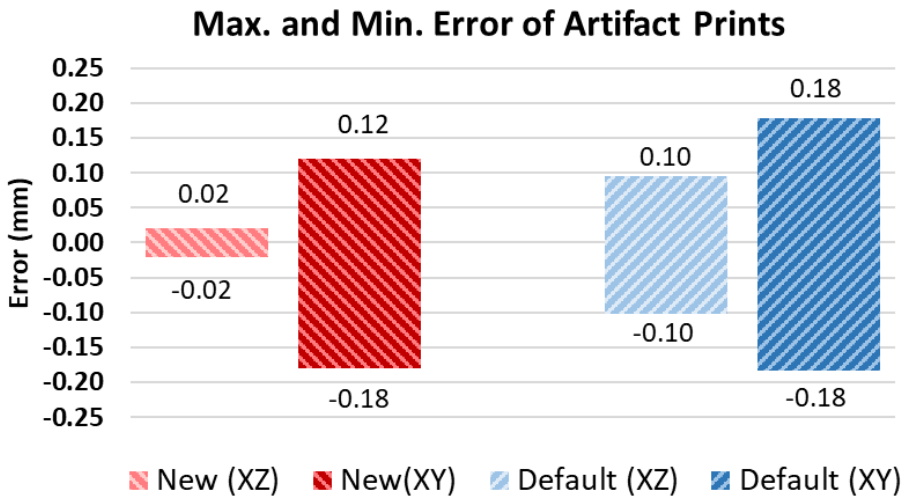

Figure 107: Maximum and minimum error of default and new exposure printed test artifact(s)

Table 29: Small feature print success of default and 'new' exposure-printed test artifact(s) (a: Partial, b: Failed, c: Success)

Feature (100 µm)	'New'	Default							
		1	*2*	*3*	*4*	*5*	*6*	*7*	*8*
Rectangular boss	P[a]	P	F[b]	F	F	P	P	P	F
Rectangular walls	F	P	S[c]	S	F	S	P	F	F
Rectangular hole	S	F	F	F	F	F	P	F	F
Rectangular spaces	S	P	P	P	P	P	P	P	P
Circular boss	F	S	S	S	S	S	S	S	S
Circular hole	S	F	F	F	F	F	F	F	F
PERP square holes (250 µm)	P	F	P	P	P	P	P	F	P
PERP circular holes (250 µm)	P	P	P	P	P	F	P	P	P

Overhang printability is generally improved for angle and arc overhang features; results are shown in Figure 108 and Figure 109.

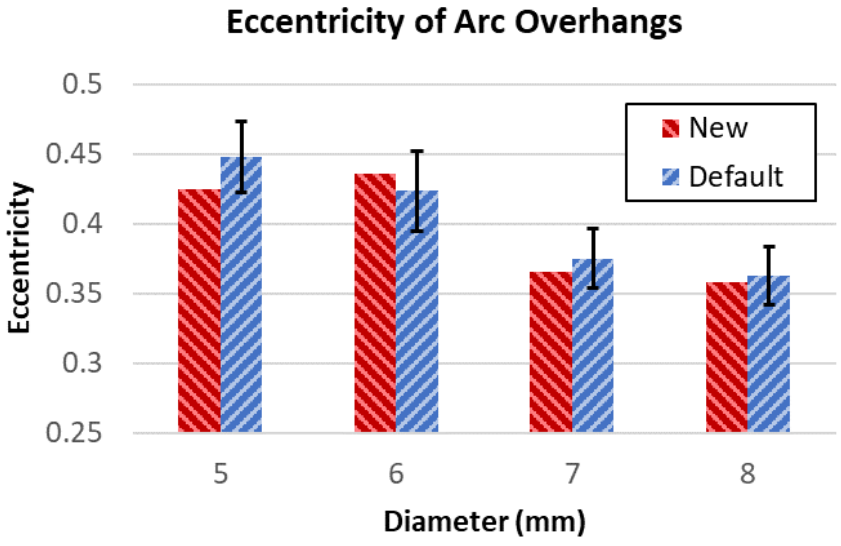

Figure 108: Arc overhang eccentricity of new and default prints

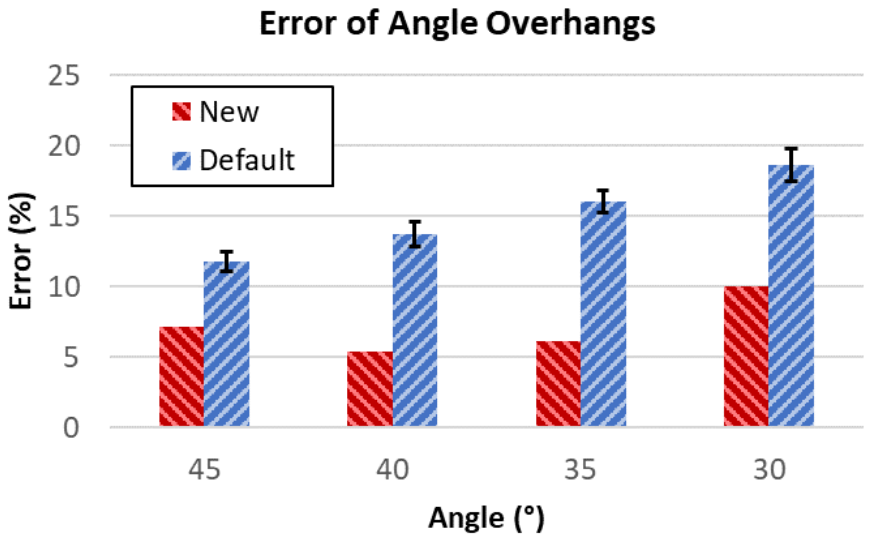

Figure 109: Angle overhang error of new and default prints

4.6 Discussion

4.6.1 Benchmarking

Procedures for benchmarking DMLS printers are important to allow transferrable investigations between machines. A benchmark study was conducted for default parameters using a novel test artifact to determine the equivalency of DMLS prints on an M100 and M290 printer. Two different M290 prints were included for opposing orientations and repeatability, whereas each M100-printed artifact required an individual build. The changes in orientations added robustness to part positioning as a source of variability. Procedures for comparisons of default parameters and similar energy density parameter prints were performed. This artifact can be used for future general benchmarking or extensive multi-objective optimization of all feature properties. However, given the large number of features and the relative part size to the M100 build platform, separate specimens are suggested for optimization objectives, as they are smaller and simpler to facilitate the production and inspection of large sample sizes. Characterization results from

the test artifact can inform the selection of areas for further investigation for future and more direct (smaller specimen) testing for a given study.

When set to default process parameters, there is no statistical difference observed in tensile strength, hardness, roughness, or overhang dross between the printers. UTS values were within EOS ranges. Surface roughness values were below EOS values. Both machines exhibited a similar increase in dross formation for decreasing overhang angles and increased burning for increasing overhang radii. Both printers yield highly dense parts (>99.7%), and the difference between printers is not significant. Residual stresses were similar for the printed samples, and the inclusion of the part volume had an increased deflection effect in both printers. Despite similar performance properties, microstructures were finer for the M100 and more columnar in the M290. Scan tracks in the M290 developed a wider region of refined grains along the centerlines.

Additionally, smaller test specimens were printed to assess and compare the effects of changing exposure parameters on both machines. Test print errors exemplified how, at the least, a full optimization experiment would need to be conducted with all input parameters (h_d, P, v) and a proper dosing cylinder to achieve equivalent performance at 40 µm. Increasing the programmable dosing factor alone does not compensate for increased layer thickness. Aside from the effects of power on hardness and top-surface roughness, as well as increased overheating with energy density. The printers appear to behave differently to changes in power and scan speed within the tested ranges of 200-360 W and 880-1000 mm/s for the M290 and 90-160 W and 650-950 mm/s for the M100. Interaction effects of the power and scan velocity vary for the printers and properties. For instance, the

different VED-hardness trends only partially resemble the results of Steinlechner [28], where the low-alloy steel prints in the M100 and M290 showed consistently similar decreasing hardness values for the same increasing VED. This further shows how the exact selection of parameters influences mechanical properties. Energy density appears to correlate qualitatively with overheating in both printers.

For the study of equivalence in M100 and M290 print performance, experiments of non-exposure-level-specific build strategies can have transferrable results. Other recommendations from the EOS printer benchmark study included a minimum feature size of 0.25 mm for transferrable print success and maintained VED exposure parameters for similar properties. Due to issues with dosing and surface roughness at 40-micron layer thickness, equivalent printing is only currently verified for the 20-micron default settings of the M100. Equivalent printing at 40-micron layer thickness on the M100 would require optimization of additional parameters such as hatch distance, as well as proper dosing.

The testing of the VED and $\beta \cdot$VED parameters is an example of using the designed test artifact in benchmarking newly selected process parameters. The artifact is, therefore, a meaningful tool for parameter development, in addition to benchmark qualification of different metal AM processes. With similar VED parameters as the M290 for the M100, MP depths are much larger with a finer grain structure. Despite producing a part with high density, M290-VED-equivalent scan tracks of a layer on the M100 do not overlap, as the MPs do not reach the same width as the M290. The microstructural effect on increased strength from this build is not only thought to be attributed to a smaller Z-axis grain size. Rather, the thermal gradient in the deep MPs is shown to promote XY-oriented grains

towards the midline that would preferably grow over any epitaxial growth in the Z-axis; this also results in the observed lack of centerline grains [65]. As such, the epitaxial growth in the build direction is limited, and the orientation of the cellular growth and the dislocation networks are inferred to be primarily XY-oriented, thus increasing the dislocation density in the Z-axis tensile direction [9]. Observed discoloration from overheating along the height of the PAR tensile specimen showed how this feature has a supplementary attribute for qualitative characterization of heat accumulation with increasing build height.

Given that the β·VED test print failed on the M100 from LOF, the β parameter does not properly compensate for the effect of the beam diameter. Instead, transferring a printable exposure between printers using β·VED yielded a power setting that is too low for scan track fusion. Oliveira et al. [20] noted the wide spread of high-density parameter VED and used that as motivation and the criteria for testing the β·VED equation. What they did not acknowledge, however, is that VED tends to do a good job of predicting the threshold of VED required for sufficient melting and to avoid print failure. By plotting the constituent VED parameters of P and BR, which is the product of v, h_d, and t, for the same sources for DMLS 316L as previously used, the threshold is clearly shown to be 30 J/mm^3 for this material. This plot, shown in Figure 110, distinguishes the exposure of the M100 β-print to be the sole point outside the distinct process zone. What is not extractable from this process map is a defined region for high-density printing.

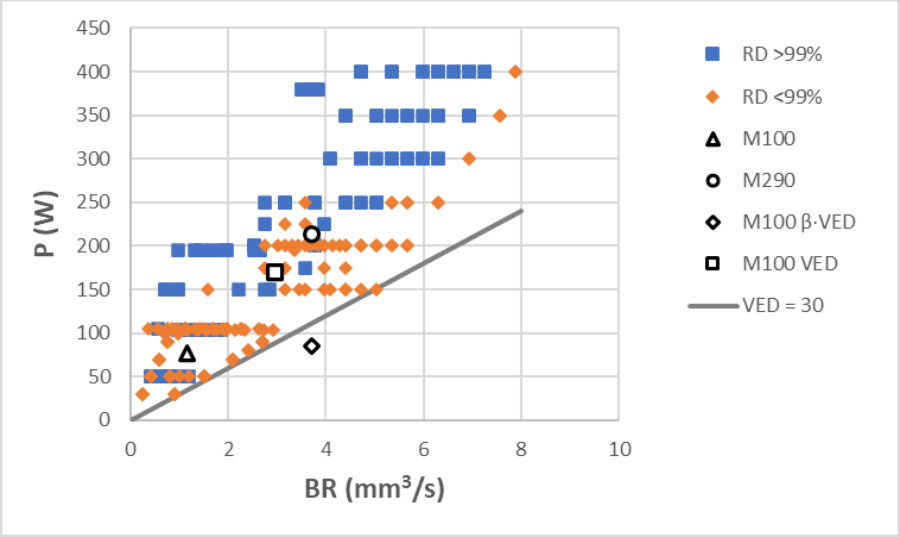

Figure 110: Power vs. build rate process map of high and low porosity DMLS 316L printing (using data from **[18, 21, 24, 69, 84, 119, 199-202]**)

On the other hand, the process map of β·P vs. BR in Figure 111 does appear to show that dimensionless parameter can reveal a definitive zone for high-density printing parameters above a β·VED threshold of 40 J/mm^3 for DMLS 316L. A secondary criterion of some relationship or combination of P and BR would account for scan track instability and define a zone where balling would be detrimental to relative density (roughly represented by the product of β·P and BR in this plot). However, there is a large region of mixed results between porous and high-density printing, and the threshold for successful printing is unclear. The default parameters of the M290 machine fall at the lower edge of this zone, thus realizing a significant difference in print success with the β·VED M100 build of the same point.

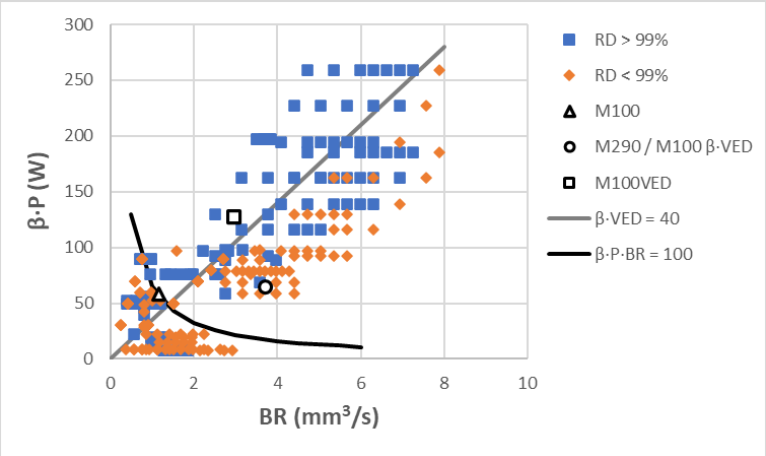

Figure 111: β·Power vs. build rate process map of high and low porosity DMLS 316L printing (using data from **[18, 21, 24, 69, 84, 119, 199-202]**)

Energy density parameters other than VED that have been used include the normalized energy density of Thomas et al. [212] and the similar normalized enthalpy used by King et al. [98]. Normalized energy density includes dimensionless process parameters for P, v, h_d, and t—all normalized with beam radius—, effective powder density, and thermal material properties (conductivity, diffusivity, absorptivity, heat capacity, and melting temperature). Normalized energy density process maps are used to classify the results of DMLS processes and streamline parameter development rather than directly predicting properties [212]. Normalized enthalpy has primarily been used to determine thresholds between keyhole, transition, and conduction mode melting, which is shown by Patel et al. [99] to be at a dimensionless temperature calculated for an MP using Rosenthal's equation. Estimated relationships for MP depth and width have been given by Metelkova et al. [101] and Tang et al. [213] using normalized enthalpy and Rosenthal's equation, where VED was incapable of continuous trends. Still, this method makes some simplification of the physics and only considers effective bulk properties [98]. Despite transition mode melting in

contours being shown to improve side surface roughness, these normalized parameters have not yet been shown to maintain useful overall predictions for realistic part geometries.

The addition of the dimensionless parameter does not accurately account for the complex interactions of exposure and other energy density parameters; perhaps other process parameters, such as build platform size, need to be considered. For other normalized energy density parameters, there may be potential for growth in this area with future research. However, optimization methods, such as response surface methodology, appear to still be a most effective method of obtaining desirable print quality and properties [214].

4.6.2 Surface Roughness Experiments

Surface roughness is one of the main limitations of as-built DMLS parts. Test specimens designed to measure the surface quality of a range of geometries through profilometry and 3D scanning, in addition to dogbone tensile testing, deflection specimens, and final characterization of the multi-feature test artifact, enabled quantitative assessment of strategies and optimization efforts.

Using multiple contours appears to have a detrimental effect on downskins. Multiple-contour exposure strategies, namely those with low hatch distance and higher VED, may produce better surface quality for higher angled downskin or side surfaces (60° - 90°). The observed effect of smoothed outer contours could be partially attributed to the denudation of the previous contour; the powder surrounding the scan tracks is dispersed, allowing the following scan to remelt and smooth the surface without excess adhered powder. However, this powder motion would negatively affect low-angle surfaces without sufficient part overlap and conduction. The disturbed powder bed would produce heightened surface

irregularities in subsequent contours. Surface cracks were also observed on side surfaces, likely caused by the increased residual stresses from these exposures. A contour strategy with decreasing laser scan power did not improve angled downskin accuracy but did result in improved quality of short ledge features (< 0.5 mm). However, these settings also resulted in prolific near-surface LOF defects and a related decrease in UTS.

Prints with nitrogen or argon as the shielding gas resulted in similar downskin and upskin surface roughness. Nitrogen as a shielding gas increased UTS by 33 MPa compared to argon. This strength could be partially explained by the higher cooling rates from the increased thermal conductivity of nitrogen, resulting in grains roughly half the size in the Z-axis as in argon. Another contributing mechanism is nitrogen strengthening by increased diffused N_2 in the 316L matrix. This change in shielding gas would result in cost savings, even for bottled nitrogen, as it is generally cheaper than argon. A nitrogen generator as the shielding gas could also be used so long as a suitably low oxygen level is achieved [147].

Prints with powder sieved to a finer PSD resulted in similar downskin surface roughness as prints with non-sieved powder. However, the fine-sieved powder improved upskin surface roughness, lowering Ra by up to 5.39 µm. The difference observed for the tested distributions is not significant enough to justify the additional higher-mesh-size sieving of the stock powder, but rather for a similar 15-30 µm PSD substitute powder supply. Other rheology characterizations are commonly conducted, which could have added a layer of insight to the powder size investigation. However, these untested characterizations are nonetheless influenced by the overall powder size for the standard spherical morphology powders used in this work [152].

The higher-than-wrought microhardness for all powder and gas prints is explained through dislocation cells, though this level of HV is not as high as the outlying reported values of 325 HV [43]. However, the measurements in this study were only taken in the Z direction; microhardness is mostly reported to be higher in the XY direction [23]. A source of error for the variability in HV would be the proximity variations to sub-surface pores, particularly in parts with higher porosity; clear correlations have been found between porosity and HV in lower-density parts (porosity > 1%) [23, 122]. Spatial relation to grain boundaries may also influence a Vickers hardness measurement [41]. As well, the relative location of indents to the MP solidification structure would affect the spread due to varied cell sizes [11]. Microstructure and sub-surface porosity were not visible for the polished test surface.

Well-fitted models presented for 30° downskin Ra and mean downskin Ra standard deviation, average upskin Ra and upskin Ra standard deviation, and top surface Ra were generated from a face-centred CCD response surface design. Models for relative density, surface geometric deviations, Vickers microhardness, and deflection were also presented. Some models exhibited an amount of over-fitting, but these models were not critical to the optimization objective. Multi-objective optimization for 30° downskin Ra with relative density as a constraint resulted in a 27.7% reduction of maximum downskin Ra to 21.28 µm, as measured through a validation print. Maximum overhang Ra from the optimized 30° downskins is lower than the default 45° surfaces. Given that 45° is generally the critical angle for support material use, 30° surfaces can effectively be printed without supports by using the optimized exposures, saving material and easing post-processing.

Using these optimized parameters as infill exposures results in a relative density of 99.45%. In comparison, sample #18 of the response surface print, which has the same calculated VED of 42 J/mm^3 and a similar downskin roughness, results in an unacceptably low density of 96.47%. These results demonstrate how the multi-objective DOE method enables minimizing downskin surface roughness while avoiding severe porosity. Still, the lowered density in the optimized prints results in a significantly lower as-built UTS of 526 MPa, with a more brittle fracture. Larger voids are predominantly located along scan track edges caused by the MPs being roughly the same width as the hatch distance. Hardness is also lowered.

Issues were identified with the EOSPRINT software in which the upskin layers of angled surfaces were not being exposed with the upskin parameters. This issue is shown in Figure 112a, along with an example of how the upskin exposures should look. A separate defect where chunks of the top surface upskin exposure layers were missing is shown in Figure 112b. For these reasons, the upskin surface regression optimization could not be directly verified. Instead, other exposures were used to verify the model's accuracy. Since the optimized parameters for angled upskins could not be tested due to this issue, the default contour exposures were removed for the ‘new’ exposure parameters tested. In removing the contours, their effect on the upskin surface roughness was investigated. The default contour exposures were necessary for accurate predictions of upskin Ra using the regression model. Improvements to the angled upskins are contingent on proper exposure of the upskin layers by the software.

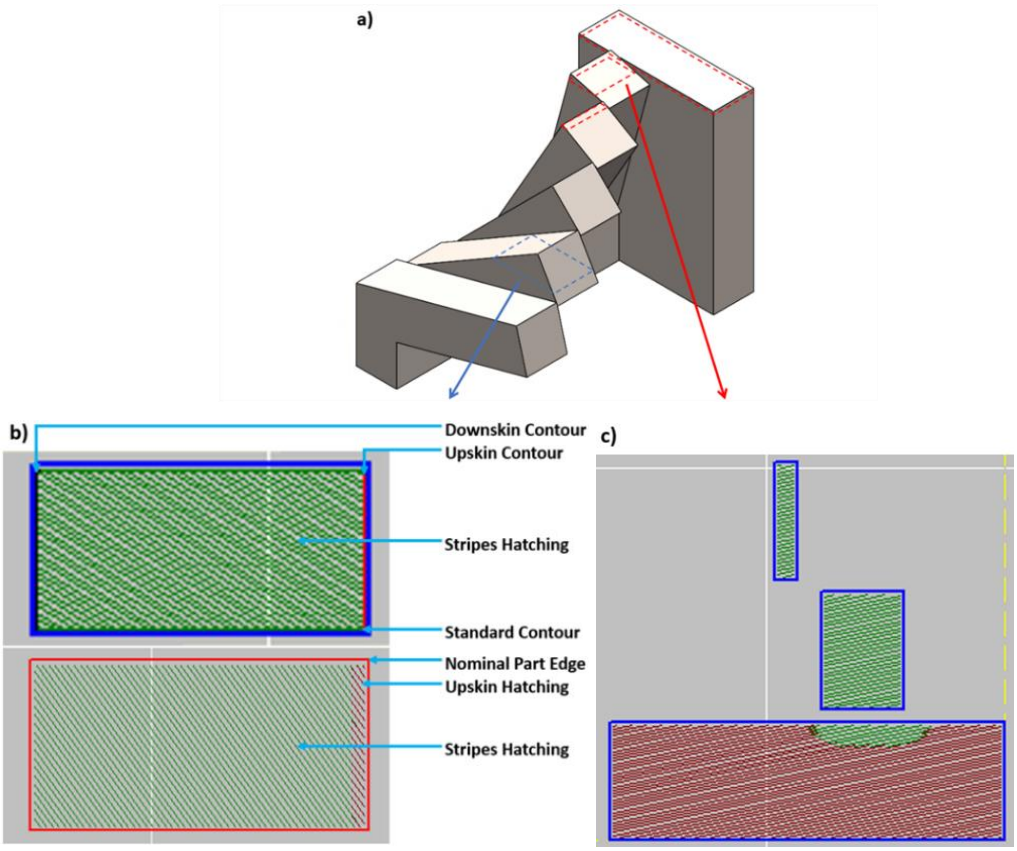

Figure 112: a) Layer sections of the angle specimen shown in (a) and (b); b) EOSPRINT scan lines for the M290 (top) and the M100 (bottom), showing how upskin exposures do not register for the M290 (contours turned off for the M100 image); c) M290 scan lines for the top surface, showing a missing patch of upskin exposure

4.6.3 Proposed Parameter Settings

The surface roughness DOE results, namely Section 4.5.1, demonstrated reduced overhang surface roughness from optimized exposure parameter settings. As a result, two possible parameter sets are proposed for reducing as-built surface roughness, depending on the upskin surface objective. The parameter sets have upskin parameters adjusted for optimized top-surface Ra (Set #1) or optimized average upskin Ra (Set #2). Cloots et al. [182] have shown that the infill exposure can affect the downskin surface roughness even with a 'shell' of multiple contours with adjusted exposures. As such, the minimized downskin Ra parameters are proposed for the infill stripes exposure of both sets, ensuring

an accurately improved downskin surface roughness. Each parameter set results in lowered Ra for all surface angles, as shown in Figure 113. The predicted Ra values shown are based on the models from the response surface DOE. The accuracy of the top surface and average upskin Ra regression models, and Ra predictions from 30° and 45° downskin models for optimized parameters, were verified in Section 4.5.1 for a maximum Ra reduction of 27.7% (to 21.28 µm). Predicted improvements from optimized upskin and top-surface exposure parameters are a 21.2% decrease in average angled upskin Ra to 8.31 µm and a 34.3% decrease in top surface Ra to 4.74 µm.

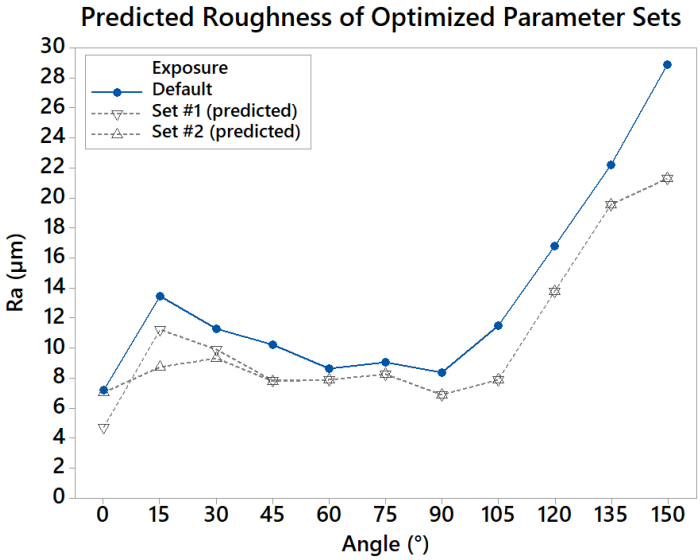

Figure 113: Predicted Ra for the proposed parameter sets, assuming proper upskin exposure

Using the optimized downskin parameters as the primary infill settings results in the reduced strength of the part, as shown in Figure 104. The porosity contributing to the low strength may be addressed through N_2 shielding gas and access to a HIPing process. However, the observed void formations along scan track edges are likely to be addressed by adjusting the hatch distance from 90 µm to 80 µm; the predicted 30° downskin Ra would change from 21.28 to 22.52 µm. Power could also be increased to improve relative

density according to the regression model (to approx. 125 W). However, adjusting power may not completely solve the characteristic void formations, as MP instability may increase with any increases in the MP width [19, 104]. Alternatively, changing the infill stripes settings of either set to default parameters, or selected parameters for a desired mechanical performance, could be tested, provided the downskin and upskin exposures are properly scanned, as shown in Figure 114. These exposures would still allow for improvements to most surfaces, though the optimal thickness and infill overlap of the downskin exposures would need testing.

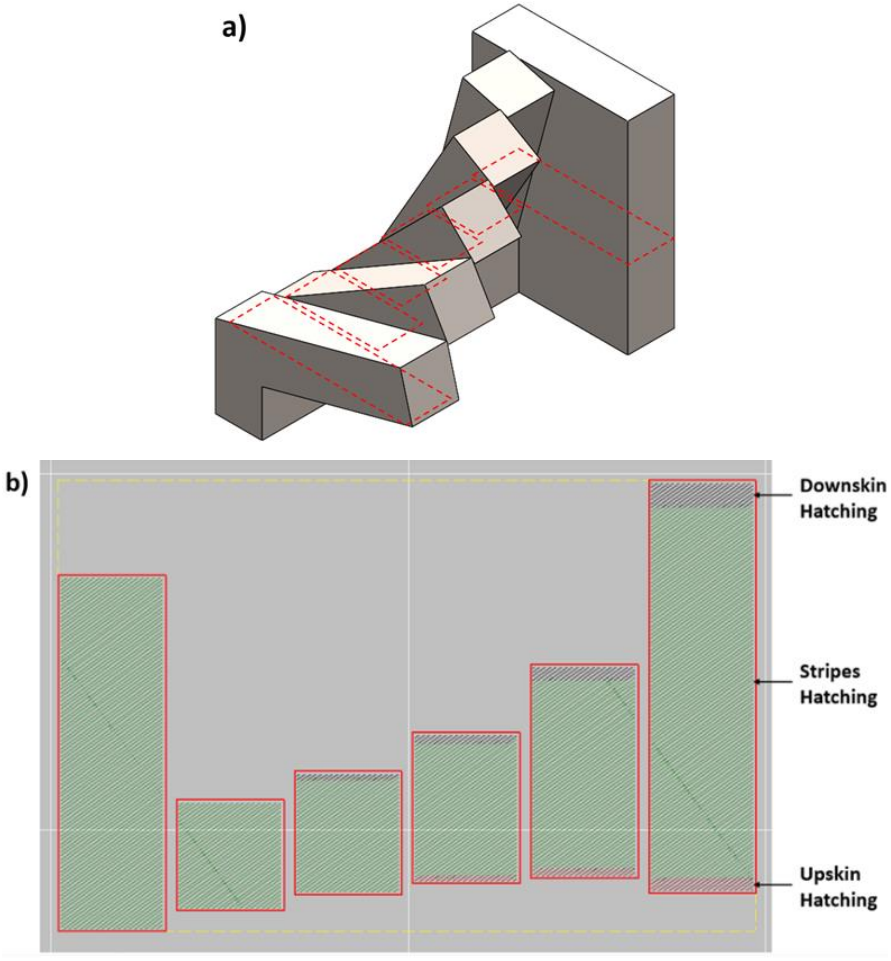

Figure 114: a) Layer section of the angle specimen shown in (b); b) Proper scan lines for the proposed parameter set upskin and downskin in EOSPRINT (contours not shown)

4.6.4 Process Mapping and Modelling

For a given exposure parameter set, Nguyen et al. [121] showed top surface Ra to reduce with decreasing t, demonstrating that it is an effective parameter for achieving the lowest possible roughness of a specific surface. Density, accuracy, hardness, and even the tensile properties of strength and elasticity in the XY direction were improved while maintaining ductility. However, this reduction is at the expense of build rate (BR), which can considerably lower the efficiency of the process.

Charles and other contributing authors have put forward many experimental works towards improving downskin dimensional error and surface roughness for SLM Ti-6Al-4V; they noted both surface metrics to be important for downskin quality. Through factorial experiments of P, v, and h_d, they found P to consistently increase error, v to have a large interaction with downskin angle for error, v to consistently increase roughness, and P to have minimal effects for low v or h_d [178, 215]. They then produced regression predictions for dimensional error using a CCD DOE at 45°, noting its promise for future dross prediction modelling; the main contributing effects for dross were P, t, v, and P*v [216, 217]. A subsequent CCD for error and surface roughness at lower angles (35° and 25°) revealed rough contrasting trends with VED. Interestingly, their trend for surface roughness was lessened at lower angles, whereas error was heightened. The phenomenon was explained by high VED allowing sunken MPs to attach for a flat, but largely inaccurate, surface [218]. This sunken MP smoothing effect was not observed for the DOE experiment, or any other experiment, in this thesis work.

The importance of cognizance of individual parameter contributions to the MP behaviour and parameter interactions is clear. As an example, Larimian et al. [67] showed that improved relative density could be achieved through higher scan speeds (lower VED), whereas Simchi [219] had opposite densification results for their scan speed settings.

Letenneur et al. [22] used a simplified analytical thermal field model to approximate MP width and depth and determine initial P and v ranges for the proper fusion of a given layer thickness; the model accounted for powder bed density for material properties. Acceptable width-to-hatch distance and depth-to-layer thickness ratios were set. Additionally, they experimentally found trends for increasing XY dimensional error and decreasing top-surface roughness for increasing VED. A VED range for porosity < 0.5% in iron prints was also found. In other published works, the same author used the numerical model to fit a regression of experimentally measured relative density for calculated depth-to-thickness and width-to-hatch, as well as to determine h_d/t constraints for low porosity. The result is a relative density process map of VED vs. BR that can be used to determine optimal high-density exposure parameters. First, t is selected, followed by an acceptable h_d based on a secondary process diagram. Then, the desired BR is selected within the high-density zone to determine the corresponding P and v values. However, they note that calibration is required for each different machine and t used due to varying unaccounted process parameters [220]. VED-BR process maps were similarly generated for grain size and aspect ratio using calculated MP thermal gradients and cooling rates. Moderately accurate estimates were achieved to show potential in selecting parameters for a more equiaxed structure, where high VED and low BR were found to produce larger elongated grains. For

this use, there is an added need to calibrate the model for each h_d, and no experimental relation to mechanical properties has been reported [221]. Thus, their model and tools offer a process to determine exposure parameters for high-density and fine-grained prints for any input material, but calibration procedures are required. Even then, the simplified model approach only accounts for cube geometries and would likely not reflect performance in more complex geometries, especially in overhangs where heat conduction varies and where surface quality is a key consideration.

CHAPTER 5

Heat Exchanger Application

The following design application work aims to put the results of downskin surface roughness reduction in DMLS towards a use case for validation. The optimized exposure parameter set from the exposure parameter DOE is applied to an AM design for performance enhancement. Specifically, downskin surface roughness improvements are applicable to designs with down-facing geometries that must not require support material, thus improving their surface printability and quality for the intended use.

Industrial applications of SS are typically for use in sanitary, corrosive, or thermally intensive environments: chemical and food processing, valves, cryogenic vessels, naval components, etc. [222]. This list of applications also tends to correlate well with areas sensitive to surface roughness, inhibiting the adoption of DMLS parts for design enhancements [125]. Despite alloyed steels having comparatively low thermal conductivity to certain materials, such as copper and aluminum, its robust strength and resilient surface

properties in harsh environments make it the material of choice for heat exchangers (HXs) in some industries [223].

One potential application that could greatly benefit from the increased complexity of suitably smooth DMLS 316L parts is HXs for dairy pasteurization, where the standard material is 316L. Biofouling is a primary issue in these processes and is enhanced by surface roughness [224]. HXs in this process are required to be cleaned every day due to a rapid accumulation of calcium phosphate and whey protein deposits that resists heat transfer, increases pressure loss, and can cause contamination [224-226]. This frequent pause in production for cleaning accounts for about 80% of production costs. Although the standard roughness requirements for use in dairy processing (Ra = 0.8 μm) are much below the achievable level for DMLS surfaces, material removal post-processing techniques such as HCAF or AFM have shown the capability of achieving these surfaces, as described in Section 1.5. The achievable Ra of these treatments depends on material removal allowances and as-built surface roughness, so it is crucial to apply in-process techniques to lower roughness for the realization of AM pasteurization HXs [166, 169]. Improved downskin surface roughness would have a higher attainable surface quality, reducing the surface defects for fouling nucleation.

5.1 Background

5.1.1 AM-Enabled Improvements to Heat Exchanger Designs

Heat exchanger design is one area greatly applicable for improvements from AM, with its ability to realize complex designs. Forms of HXs include heat sinks or solid-fluid HXs that can operate under natural or forced convection conditions, such as in electronics cooling

systems [227]. The other form of HX is for fluid-fluid heat transfer, where the goal is to either control or transfer maximum heat between fluids. Depending on the process application, a HX is mainly either parallel or counter flow; traditional HX types are forms of plate, coil, or shell-and-tube type similar to the diagram shown in Figure 115. As the heat is transferred primarily through convection, a main HX design parameter for thermal efficiency is the surface area-to-volume ratio (SA/V). Another main performance parameter is pressure drop, which governs the required pumping power [228]. The specific trade-off of overall heat transfer may depend on application-specific considerations.

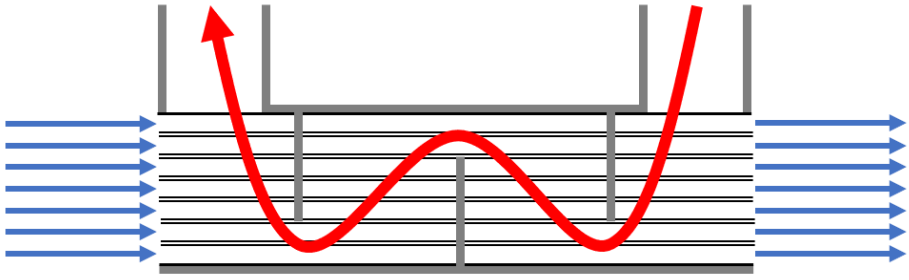

Figure 115: Diagram of a baffled shell-and-tube HX, similar to the one presented in **[228]**

In using DfAM methodology and DMLS to construct complex internal structures, designs with significantly higher maximum surface area-to-volume ratios are possible for heat transfer. Additionally, the designs can be built as a single part with no additional manufacturing procedures [205]. Re-designed HXs for DMLS have been shown to reduce pressure drop and increase heat transfer three-fold, all with reduced weight and size [205]. The capability of AM to produce heat exchangers with high surface area, compact scale, and improved flow makes it an attractive technology to produce a wide range of heat exchangers, including for high-performance engines in aerospace [229].

However, roughness in DMLS internal channels increases pressure drop, which in many cases has substantial importance [230]. Pressure losses from these rough channels are more significant at higher flow rates [231]. While the roughness of DMLS surfaces disrupts the boundary layer for improved flow characteristics for heat transfer, there is a concomitant increase in pressure drop [48]. The increase in pressure drop in microchannels may negate the augmented heat transfer, as it is influenced more severely by surface roughness [232]. In some cases, highly rough DMLS surfaces can also decrease heat transfer [233]. Rough surfaces also facilitate fouling (biological, particle, chemical, salts, or ice) deposit initiation, thus restricting designs from certain susceptible applications [234]. With limited wide-scale post-processing capabilities for the hard-to-access internal geometries, HXs that require lower surface roughness necessitate build optimization [227].

Moreover, the low printability of DMLS HX internal channel overhangs can cause poor form quality, further increasing friction factors and can be detrimental to heat transfer [233, 235]. Internal channels cannot be supported as the support material would not be removable. The generic recommendation is to avoid HX geometries with overhangs lower than the critical angle of 45° [223]. The need to tighten surface tolerances is heightened for smaller channel sizes, as the deviation to channel geometry has a more severe effect [236]. Leak-free thin walls are also demanded [227].

Some design innovations enabled by AM include compact microchannels, oscillating internal channels, and double-corrugated channel geometries [237-239]. In addition to the pressure drop from surface roughness, these small internal channel matrices often lead to undesirable inlet and outlet designs that contribute to large pressure drops [223].

Figure 116 shows a representation of the limited inlets. Designers can address the inlet/outlet problem by gradually increasing channel complexity. Scheithauer et al. [223] achieved this design feature through biomimetic furcating networks resembling organic plant structures, though their final design used fractal curve channels, starting with single fluid channels. A simple 2D representation of a bifurcating HX is shown in Figure 117; Gerstler et al. [240] used trifurcating unit cells in their complex HX design.

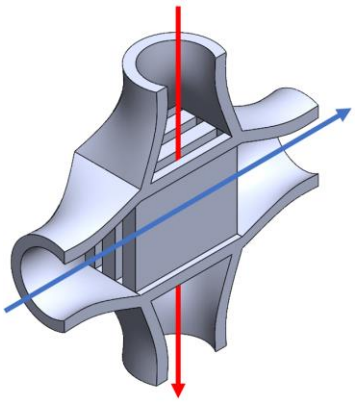

Figure 116: Representation of inlet designs for microchannel HXs (such as in **[237]**)

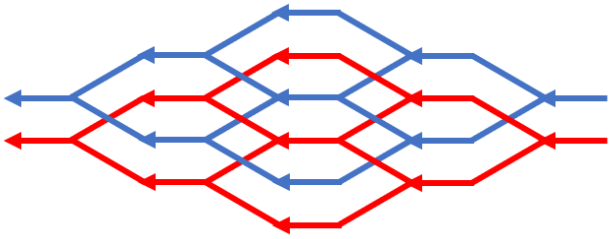

Figure 117: A 2D line diagram of flow channels for a bifurcating HX, inspired by **[240]**

5.1.2 Triply Periodic Minimal Surfaces for AM HXs

Minimal surfaces are surfaces that divide the volume between boundaries with minimal area, and they are desirable for heat transfer due to high surface area-to-volume ratios. Triply periodic minimal surfaces (TPMS) form repeatable unit cells to generate lattices in all directions. For example, the unit cell and lattice for Schoen's gyroid TPMS are shown

in Figure 118. TPMS are approximated by equations, such as equation (14) for gyroids, to allow for modelling and functional grading [241]:

$$cos(x)sin(y) + cos(y)sin(z) + cos(z)sin(x) = 0 \quad \textbf{(14)}$$

Printability of the gyroid is aided by a lowered frequency of angles approaching 0°; the most frequent angle is 55°. Still, the downskins of printed gyroids are observed by Yang et al. to be distinctly worse than upskins [242]. These biomimetic TPMS lattices are observed in nature as lightweight structures in insect bodies, in addition to the topology of soap films [243, 244].

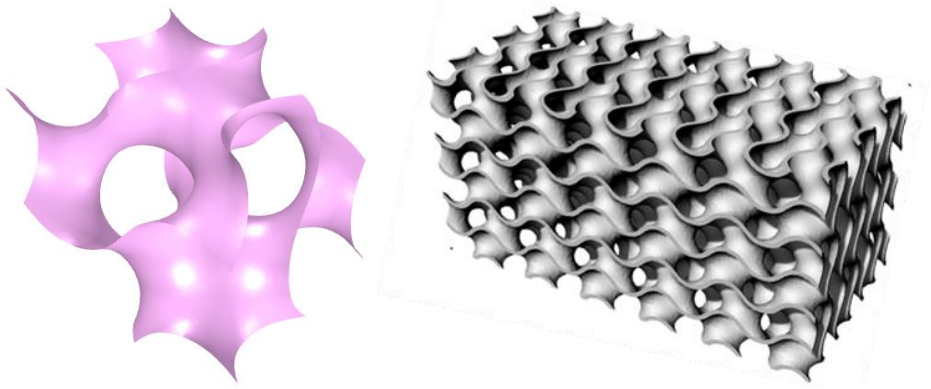

Figure 118: Unit cell (left) and lattice structure (right) for the gyroid TPMS

The high SA/V of TPMS cells allows for maximal heat transfer for the lowest amount of material [245]. TPMS heat exchangers can thus have the same heat transfer as a previous design but in a much smaller design space [205]. The lattice symmetry also allows for separate channels with equalized pressure on the walls [245]. However, the interfaces of the fluid domain inlets and outlets are currently a limitation to the achievable performance of these TPMS HXs. Designs of current TPMS HXs have manifold-type connections, where one channel is completely blocked and the other open, which would not be ideal for pressure drop [245]; an example is shown in Figure 119.

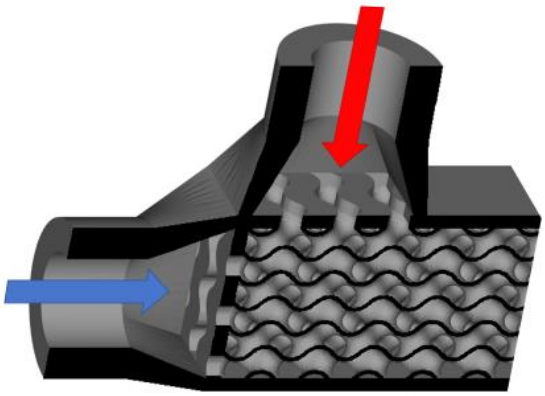

Figure 119: Manifold HX inlet design for a uniform gyroid HX, similar to **[245]**

The gyroid structure was selected for this design case. The other commonly explored TPMS lattice for heat exchangers is the Schwarz-D; Schwarz-P and IWP surfaces have consistently less desirable heat exchange properties [246, 247]. Comparisons of the HX performance of these structures in the literature were reviewed to inform the gyroid selection. Li et al. [243] calculated large turbulent kinetic energy for high shear stress in gyroid and D channels, favouring anti-fouling. The energy in the gyroid flow was substantially higher than D for cold channels, and thermal performance was better for higher flow velocity. Experiments with low flow velocity have shown D channels to have better heat transfer and lower pressure drop than the gyroid [246, 247]. However, the CFD simulation of TPMS flow channels by Rathore et al. [248] showed the gyroid to exhibit lower viscous resistance than D for a lower pressure drop with increased flow rates and a more tortuous flow than the D surface. Overall, the performances of the two lattices are similar for a range of conditions [243, 246, 247]. Although, gyroid sheet structures have a unique helical flow pattern, which improves the fluid mixing for heat transfer and has potential anti-fouling behaviour [245]. Gyroid HXs are thus an especially fitting design application for lowered as-built DMLS surface roughness, as smooth final surfaces would

realize the anti-fouling design potential of these printable geometries. The selection between D and gyroid lattices for HX efficiency would vary for specific applications.

Dixit et al. [249] attributed their experimentally improved gyroid HX effectiveness to the smooth topology of the resin-printed design, which was superior to AM and non-AM HX designs. A gyroid HX was similarly designed and analyzed by Peng et al. [245], who found it to have an increase in heat transfer coefficient of almost 90% for the tested conditions compared to a benchmark plate-type design, though the pressure drop was also greatly increased. These reference benchmark comparisons allow this work to focus on comparing the different gyroid lattice geometries with the knowledge of heat exchange improvements compared to a traditional design. The benchmark for this study uses the inlet/outlet design shown in Figure 121b, which serves as a simplified reference for a common gyroid HX [245].

5.2 Design and Modelling

While AM enables the production of complex gyroid channels, desirable for their heat transfer efficiency in HXs, these internal geometries are susceptible to issues with downskin printability and related surface roughness. In terms of HX performance, this high roughness increases pressure drop. Since the issues with inlet/outlet designs concern the same performance metric of pressure drop, a novel design modification is developed, to which the downskin roughness-optimized parameters would be applied. The objective of this design was to address the pressure drop induced by gyroid heat exchanger inlet and outlet designs, thus complementing the roughness reduction for minimal pressure loss in these complex AM HXs.

With inspiration from fractal and furcating HX designs, a graded cell-size gyroid HX is proposed in this use case to improve pressure drop by replacing manifold inlets/outlets for single-channel interfaces. General fluid dynamics principles tell us that the gradual contraction of the flow paths from cell size grading should result in a much-improved pressure drop than the sudden change from blocked channels [243]. A more uniform flow with fewer flow disruptions yields a reduced pressure drop [223]. Functional grading of lattices is commonly used for achieving desirable mechanical performance for various design structures [241]. A review of the available literature did not, however, show any use of functional grading in fluid-fluid heat exchangers.

The graded cell size structure for the HX model was generated using the free software MSLattice [250]. This software allows for linear cell-size grading of STL lattices, as described by Liu et al. [251]. Two symmetrical graded gyroid lattices were combined to form the HX core geometry. Figure 120 shows one half-structure: a 30 x 30 x 60 mm^3 lattice with cell sizes that transition from 10 to 30 mm along its principal direction so that the inlet interface is of a single unit cell. The lattice density is set to 20% for acceptable wall thickness. The combined graded structures were imported into Rhino 3D to model the external design. Figure 121a shows the final concept model; each fluid channel is connected to a single inlet and outlet using the major openings of the gyroid unit cell. Limitations of this conceptual model for analysis include the cuboid shape of the shell and that it is generated as an STL file, so the channel accuracy is limited by the STL facet coarseness.

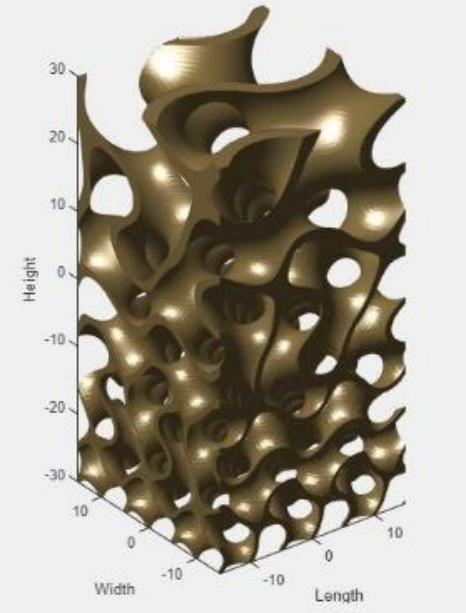

Figure 120: Graded cell-size gyroid structure in MSLattice (30 x 30 x 60 mm^3)

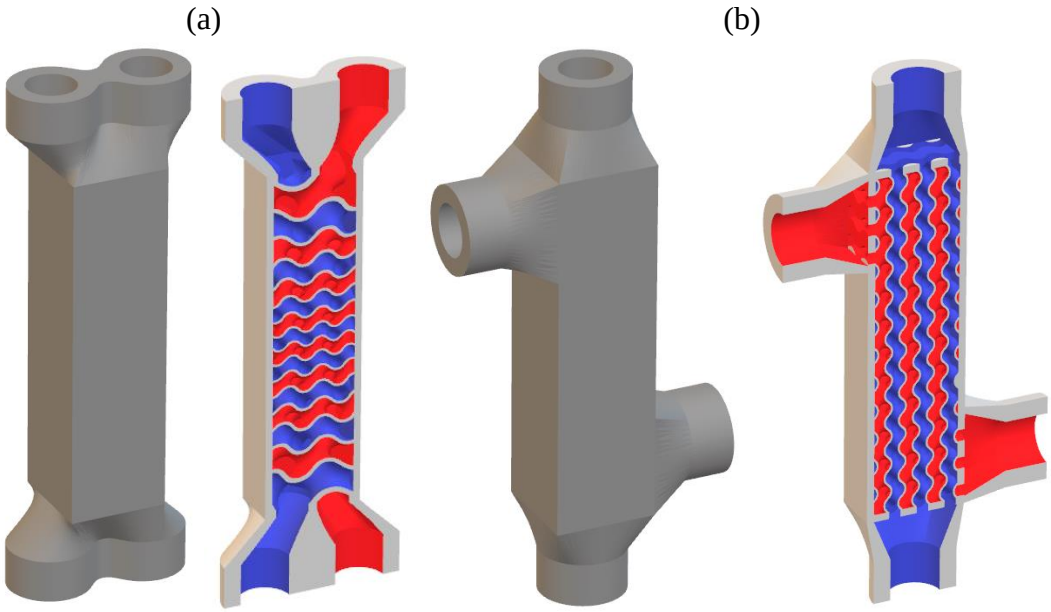

Figure 121: Gyroid HX models with sectioned views of hot and cold fluid channels: a) Graded Design b) Uniform Design

Only the gyroid TPMS was analyzed, though the takeaways are assumed to apply to a Schwarz-D or other type HX. Differences in the exterior design of the two gyroid HX designs mean that results do not accurately represent the effects of cell-size grading of the

core performance alone. Instead, this study compares the improved design from the novel application of cellular gyroid structure modification. The inlet pipe diameter and inlet length were consistent between designs, along with cell density for a similar gyroid channel hydraulic diameter, so the connections of the inlets in the graded design are considered a valid design advantage to be included in the analysis.

A ‘shrinkwrap’ was applied in ANSYS SpaceClaim to homogenize the STL facets to 0.9 mm; this resolution is limited by system and software capability. A mesh independence study determined a mesh size of 0.5 mm; the resultant output trends used for this selection are shown in Figure 122. Figure 123 shows the fluid channels for the graded and 10-mm-cell uniform designs in ANSYS Fluent. The fluent studies used the realizable k-epsilon turbulence model and inlet temperatures of 20 and 100 °C. Based on the work of Simmons et al. [204], the thermal conductivity of the DMLS 316L is reasonably estimated as 14.1 W/m-K for both exposure sets, with a specific heat capacity of 500 J/kg-K. Inlet velocities of 20 mm/s, 200 mm/s, and 2 m/s were run to span a general range of liquid heat exchanger flows.

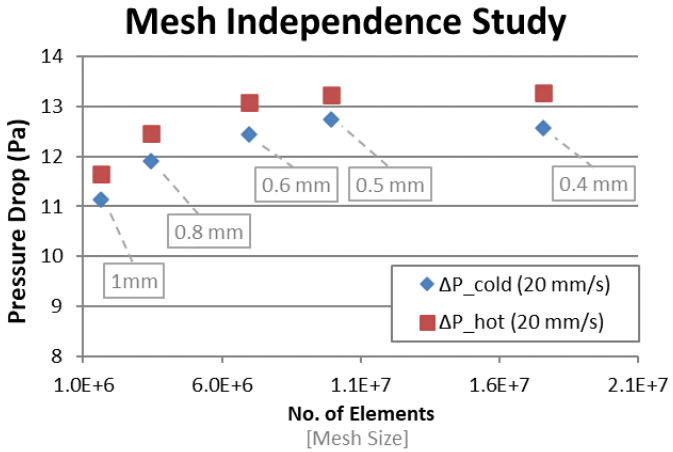

Figure 122: Pressure drop vs. mesh elements from the mesh independency study

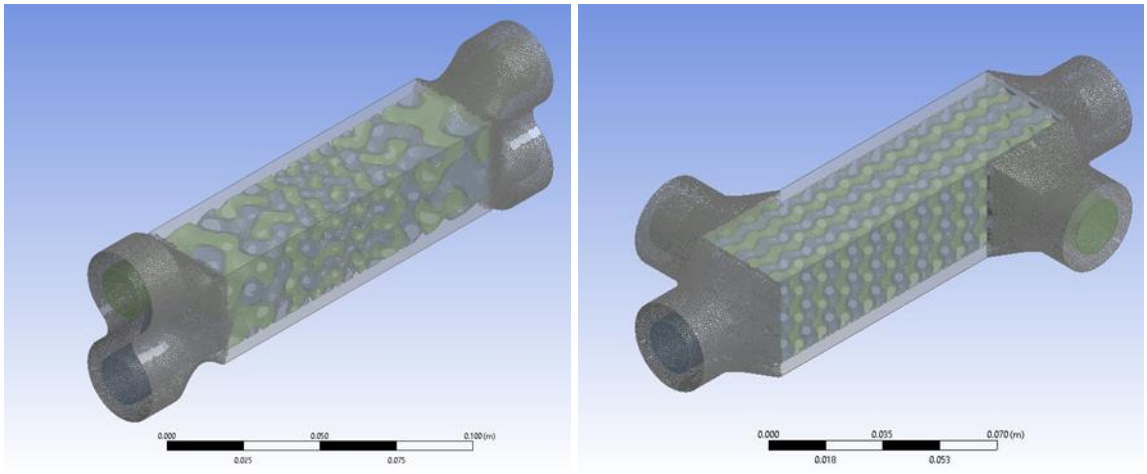

Figure 123: Colored fluid channels of the graded (left) and uniform (right) gyroid HXs

The performance of the graded heat exchanger is compared to a regular uniform design for pressure drop and heat transfer using computational fluid dynamics. The effects of the graded inlet and outlet are assessed, as well as the effect of different measured roughness values of the designs using downskin-optimized and default laser exposures. Other characterization includes a measurement of relative density. A full factorial DOE layout was used for graded and uniform design combinations to determine the effects of the outlet and inlet; the four different runs used combined models, as shown in Figure 124. Performance comparison of parallel and counterflow graded models is also assessed, as well as results from the inlet velocities of 0.02 – 2 m/s.

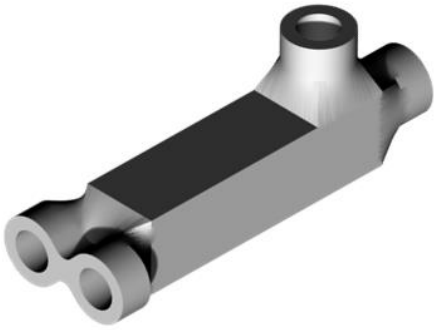

Figure 124: A combined graded and uniform gyroid HX model for the factorial DOE

5.3 Comparisons

The overall heat transfer coefficient (U) is calculated as a parameter of the thermal performance of the HX. The calculation of this parameter is shown in equation (15), where $\dot{Q}$ is the rate of heat transfer (equation (16)) of the HX flow, and ΔT_{lm} is the log-mean temperature difference.

$$U = \frac{\dot{Q}}{SA \cdot \Delta T_{lm}} \quad \textbf{(15)}$$

$$\dot{Q} = \dot{m} \cdot c_p \cdot \Delta T \quad \textbf{(16)}$$

Temperature contour results for the graded and uniform HX designs at parallel inlet velocities of 200 mm/s can be seen in Figure 125. The overall heat transfer is decreased for the graded design. The difference in outlet bulk temperatures is 37.20 °C for the uniform model and 47.02 °C for the graded model. The uniform design allows for more heat transfer, which is expected from the higher area and flow disruptions of the uniform design. This reduced heat exchange is found to be more affected by the graded inlet than the graded outlet, where the effects on U are calculated to be -55.80 W/m^2-K and -52.29 W/m^2-K, respectively.

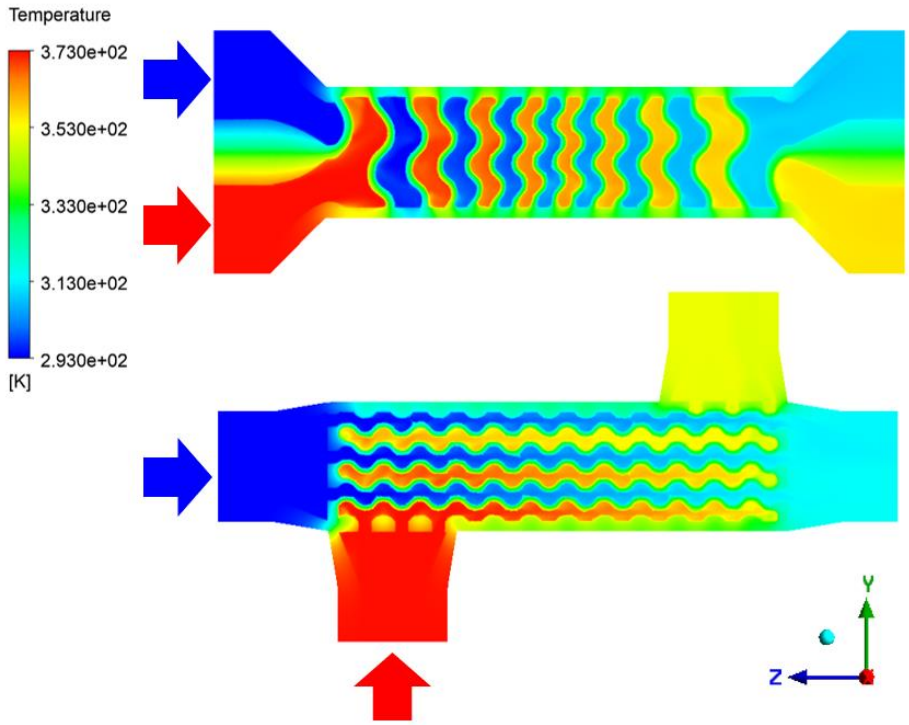

Figure 125: Temperature contours for the graded (top) and uniform (bottom) HXs at an inlet velocity of 200 mm/s

Comparing the full models at different flow rates, the bar graph in Figure 126 shows the graded heat exchanger in counterflow and parallel flow to perform similarly for all tests, especially at 200 mm/s. However, the parallel heat exchanger does perform better at higher inlet velocities, and the opposite is true for the lower velocity. Compared to the uniform heat exchanger, the difference in U increases with velocity. This increase is shown in Figure 127 to be exponential (power of 1.15) for an increasing rate of change.

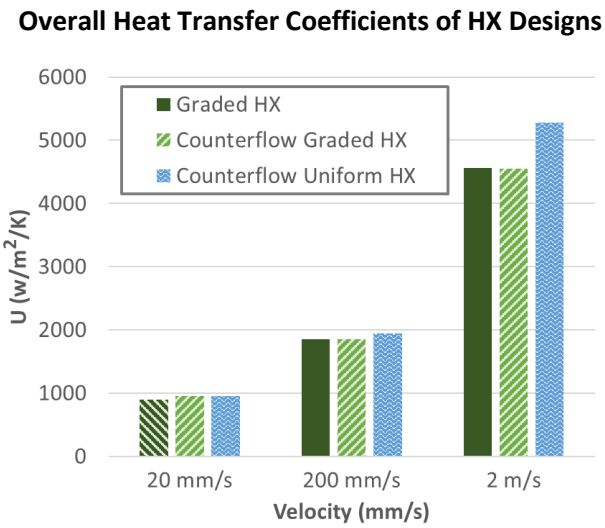

Figure 126: Heat transfer coefficients (U) for HXs in counterflow and parallel flow for different inlet velocities

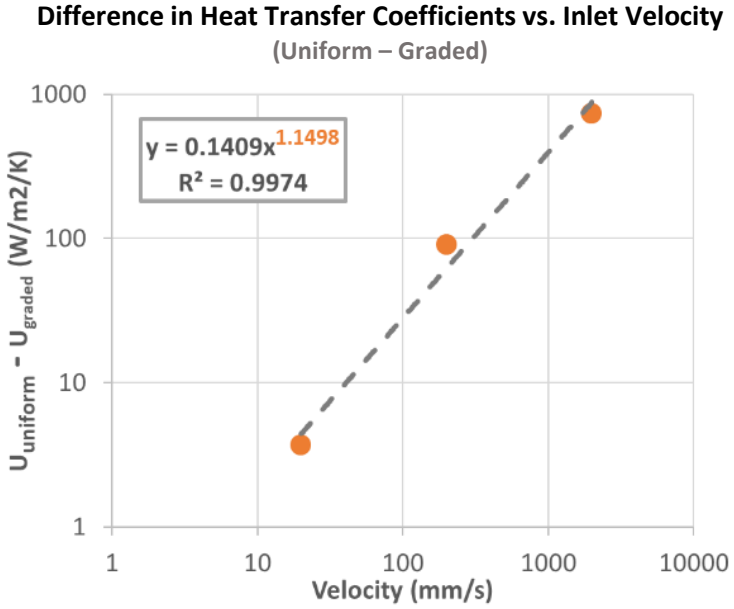

Figure 127: Increasing difference in heat transfer coefficients between HXs for increasing inlet velocities

The pressure drop is decreased for the graded design: 800 Pa for the 200 mm/s cold fluid flow of the uniform model (the straight channel) and 560 Pa for the cold fluid of the graded model. Thus, the graded design does facilitate the fluid flow for a reduced entry and exit pressure drop of a gyroid heat exchanger, which was the objective. This reduction in

pressure drop is found to be slightly more affected by the graded outlet than the graded inlet, where the effects on pressure drops are calculated to be -124.03 Pa and -112.12 Pa, respectively. The pressure contours for both designs are visualized in Figure 128, where the rapid drops in pressure can be seen at both the inlet manifold and outlet manifold/nozzle.

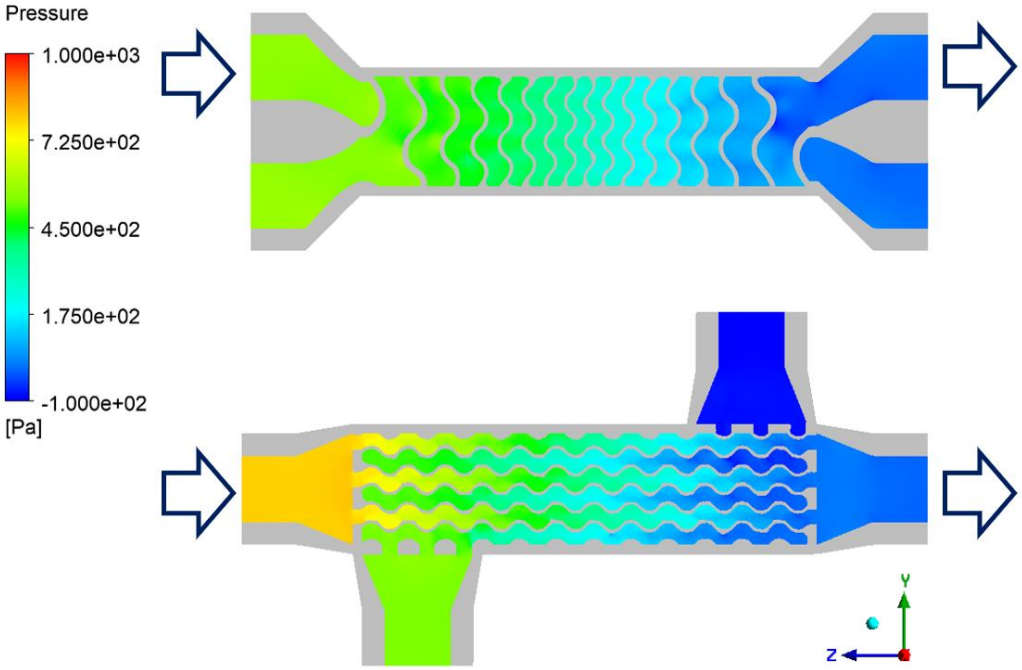

Figure 128: Pressure contours for the graded (top) and uniform (bottom) HXs at an inlet velocity of 200 mm/s

Corresponding velocity contours along the longitudinal flow are shown in Figure 129a. Clear non-uniform velocity distributions and stagnant or reverse flow regions are visible at the inlet and outlet manifolds of the uniform design, unlike the less disrupted flow of the graded design. As previously mentioned, the limited resolution of the STL results in discontinuous small channels along HX edges; these appear to have a greater effect on the graded design, which would be a source of negative error for pressure drop improvement. The eccentric velocity profile and helical flow of gyroid lattices observed by others, and

for the uniform design in this study, are maintained in the graded channels, as shown in Figure 129b and **Appendix E** [245]. However, the gradual reduction in cell size forms more distinct vortices, though the flow is mostly developed to resemble the uniform channels upon reaching the 10-mm cell size.

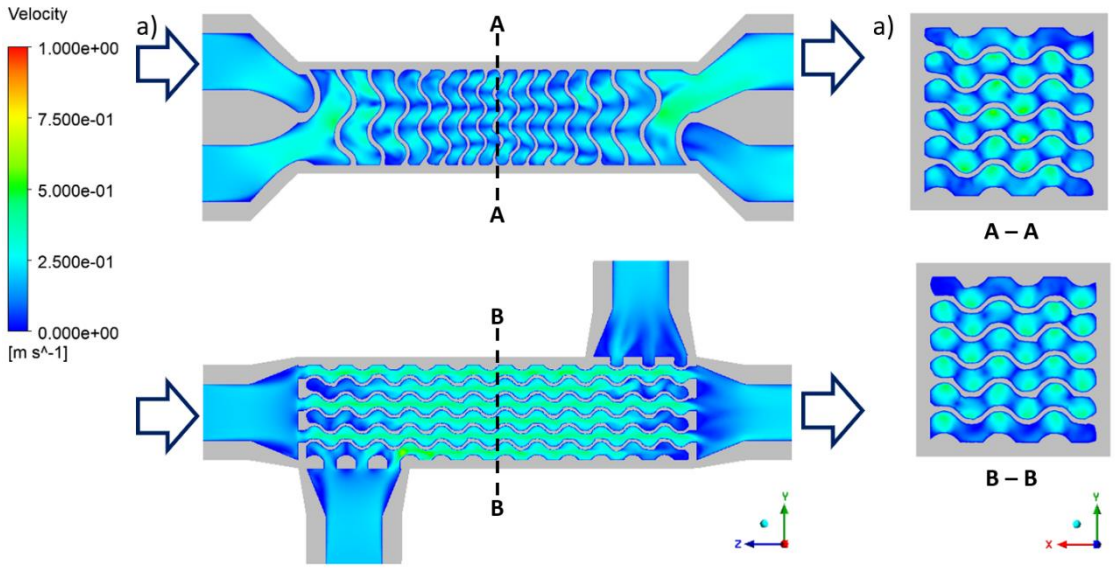

Figure 129: a) Velocity contours for the graded (top) and uniform (bottom) HXs at an inlet velocity of 200 mm/s, and b) corresponding cross-sectional velocity contour views

Comparisons of pressure drops for the full models at different flow rates are shown in Figure 130. The counterflow and parallel flow graded models naturally have similar pressure drops. The log-plot bar graph also shows that the graded design outperforms the uniform design at all tested velocities, where the pressure drop rapidly increases in magnitude with velocity. This improvement is shown in Figure 131 to be exponential to the power of 1.72, which is greater than the 1.15 determined for U, so this relative increase is more rapid for pressure drop. For a higher-flow, low-pressure-drop application, cell-size grading would thus yield a significantly better-suited design.

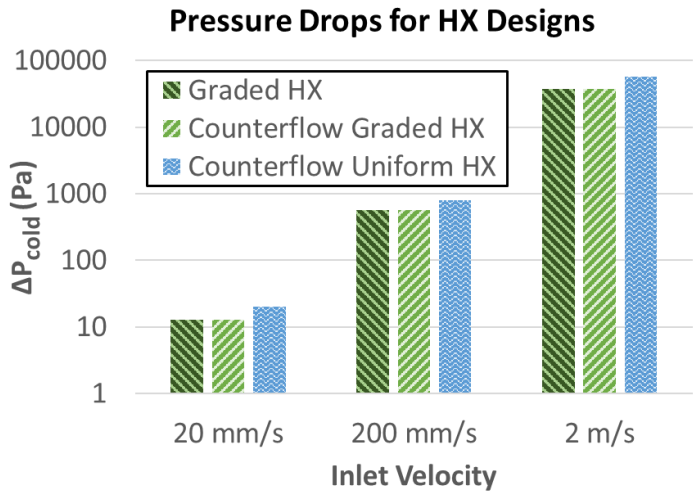

Figure 130: Pressure drops of HXs in counterflow and parallel flow for different inlet velocities

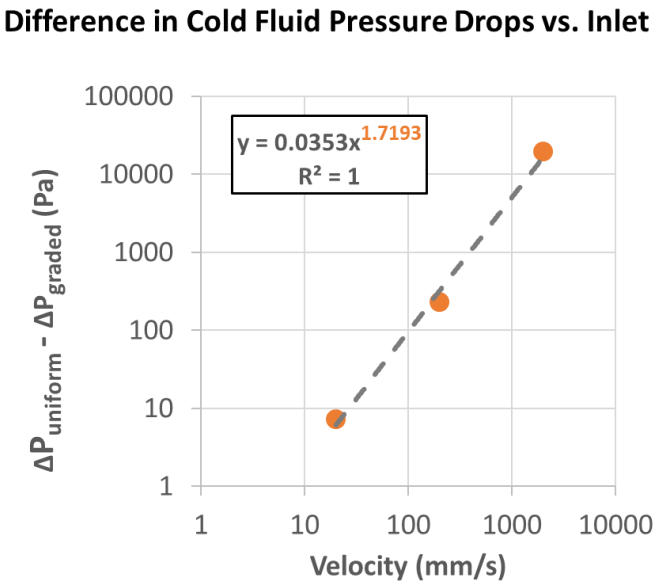

Figure 131: Increasing difference in pressure drop between HXs for increasing inlet velocities

5.4 Print Characterization

The printability of the gyroid lattices was first tested with open-shell parts on the M100 printer with default settings. The minimum thickness of the lattices was ~0.6 mm. Both gyroid lattice parts printed successfully, as shown in Figure 132, and passed a sealed static leak test, though the overhang surfaces did have observable roughness and discoloration.

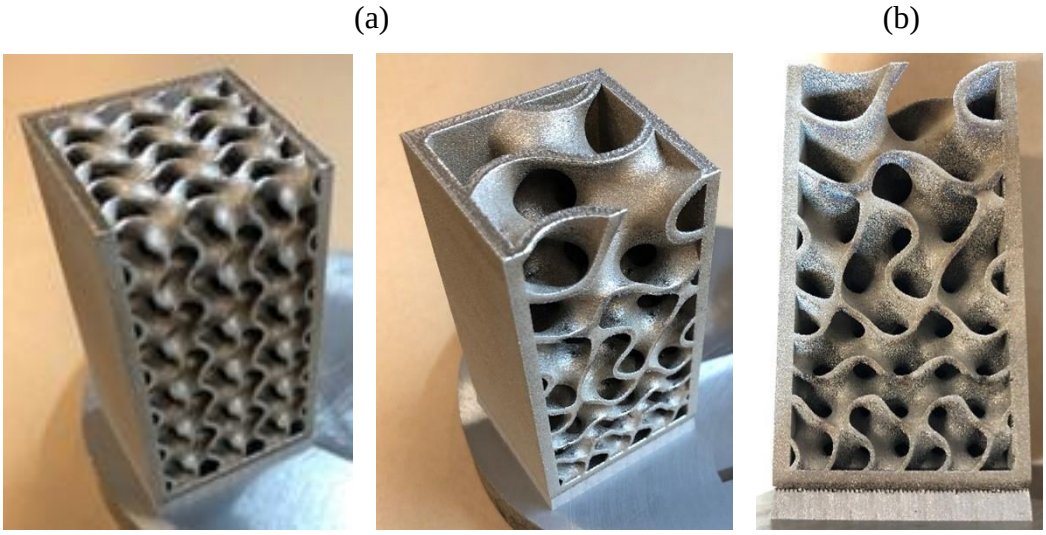

Figure 132: a) Test prints of uniform (left) and graded (right) internal structures, and b) Image of rough downskin areas of the as-built graded gyroid structure

Two heat exchanger models were printed to collect actual roughness values and use them in subsequent ANSYS CFD models. The parts were built in an upright orientation on the M290 printer—one with default exposures and one with downskin-optimized exposures. As seen in the sectioned parts, discoloration from overheating is pronounced for the default parameters with increasing build height but not for the optimized part. The overhang surface roughness of each printed model was destructively measured by sectioning and polishing the parts. Then, images of the overhanging regions at 100X magnification were stitched together as shown in Figure 133, and Ra was calculated using data from boundary tracing in MATLAB and utilizing the filtering methods described in ISO 4288, 16610-21, and 16610-28 [190, 252, 253]. The average Ra of the downskins was determined to be 46.5 µm for the optimized print and 65.4 µm for the default; the Ra of default surfaces also has a higher variability. The calculated Ra values are likely to include some overestimation due to the limited accuracy of the polynomial form removal, as the downskin of the sectioned HX overhang has a sinusoidal-type profile.

The printed lattice walls were all printed successfully, with no porous walls. The part density of both parameters is above 99.4%. Improvement of the as-built downskin surface roughness is not only beneficial to the as-built condition. Post-processing is limited for poor and heterogeneous surface quality. As such, lowering as-built surface roughness eases post-processing and results in an overall lower final part roughness, potentially in the range of 0.5 µm [166].

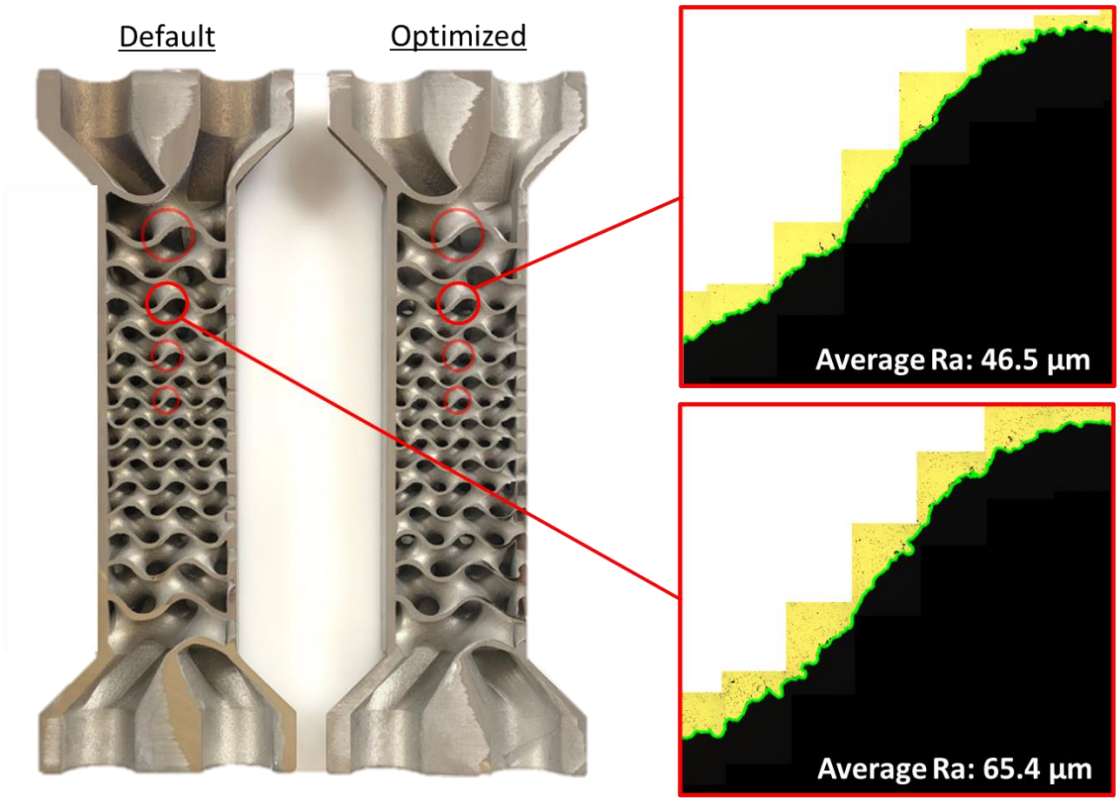

Figure 133: Sectioned and polished HX prints (left), with red circles showing the captured areas for Ra calculation, and corresponding stitched OM images of the downskins (right), with the traced boundaries in green

5.5 Effect of As-Built Roughness

The calculated Ra values were applied to the ANSYS model by converting the average Ra to sand-grain roughness (K_s) by using the common conversion in equation (17) and then applying them as constants for all walls as a reasonable over-estimate of the channel

roughness [254]. As shown in Figure 134 and Figure 135, the calculated U at 200 mm/s was reduced by 366 W/m^2-K for the optimized-surface heat exchanger. The pressure drop was reduced as well, by 69 Pa. Though the pressure drop difference is low at this velocity, it increases more rapidly with velocity. Based on this simplified analysis, the consideration for this surface modification for general HX design would be how critical the pressure drop is and whether the flow rate is high enough for a substantial effect. However, Ascione et al. [231] showed flow in rough DMLS channels to behave differently than classical models for flow in rough piping. The Reynolds number for turbulent flow in rough DMLS channels is lower than in rough pipes, and friction factors increase with increasing Reynolds number. Therefore, the real effect of roughness is likely much greater and would require experimental correlation. This exposure will also be preferred if the fouling is significantly affected or if new post-processed roughness is lowered to acceptable levels for sanitary applications, i.e., dairy pasteurization.

$$K_s = 11.03 \cdot Ra \tag{17}$$

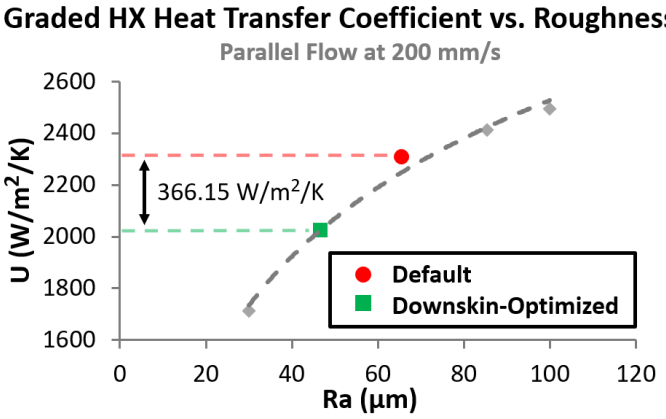

Figure 134: Heat transfer coefficients from applying the calculated Ra of printed HXs, with additional data points to show the trend

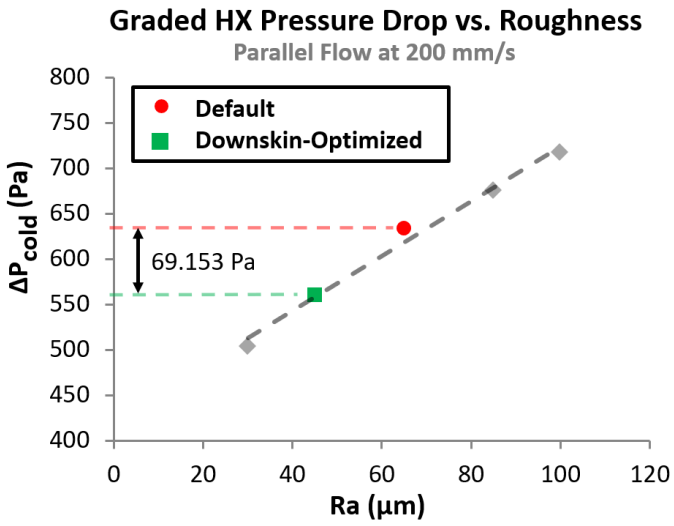

Figure 135: Pressure drops from applying the calculated Ra of printed HXs, with additional data points to show the trend

Where applicable, this design modification of grading TPMS HX lattice cell size improves channel inlets and outlets for lower pressure drop. The cell size grading could be combined with topology-conforming operations for optimally performing in-line HXs with respect to pressure drop [247]. Applying exposure parameters for optimized downskin roughness to these TPMS HXs results in an additional decrease in pressure drop. Altogether, this enables the production of high-performance AM HXs with diminished pressure losses incurred from channel design complexity and the DMLS process.

CHAPTER 6

Conclusions & Future Work

6.1 Summary

Metal L-PBF remains a field of research with an increasingly large body of contributions. Still, there is a need for further knowledge of process performance as well as a sustained potential for improvement. This thesis experimentally investigated the properties of 316L SS DMLS prints toward process parameter optimization of as-built surface roughness for complex and overhanging designs while ensuring acceptably high relative density. Toward this objective, a benchmark methodology was developed and tested to compare DMLS print performances with a test artifact that includes an assortment of features for streamlined characterizations of major performance properties. Then, investigations were conducted to understand the effects and potential surface roughness reduction for the use of multiple contours, fine-sieved powder, and nitrogen shielding gas while also testing the consequent relative density, residual stress, and mechanical properties of DMLS 316L. Next, a response surface design DOE was implemented to optimize exposure parameters for minimal downskin surface roughness with a density constraint to limit porosity to below 1%. Finally, the exposure parameters for optimized downskin surface roughness were applied to a secondary HX design improvement study to validate the improvement and use of the determined print conditions.

By assessing the results of the benchmarking test prints and analyses conducted with the M100 and M290 printers, the following conclusions are drawn. The designed test artifact is useful for testing multiple main performance properties of DMLS prints. The example

is given for testing for the statistically similar performance of different printers for desired ranges, as well as for newly selected exposure parameters. Similar mechanical properties and constraints for similar small feature printability were determined for default parameters, and VED was shown to be unfitting for exposure selection. A derivative small specimen design illustrated one example of possible next-step investigations, where specific parameter effects are studied using DOE.

Through experimentation with contour exposure strategies, shielding gas, and powder size on the M100 printer, and DOE response surface optimization methods on the M290, parameters for improved surface roughness and knowledge of the effects of process adjustments on roughness and other part properties were gained. As a result, the following recommendations are proposed for the build parameters of the EOS M290 printer. First, although the use of multiple contours is shown to have some potential for certain contour scan strategy-geometry combinations, the detrimental effects observed for downskins and surface cracking on side surfaces for all strategies are sufficient to conclude that these exposures are not useful for the overall improvement of part roughness; no immediate investigation efforts in this area are recommended. Secondly, nitrogen can be used in place of argon as a shielding gas without negative impacts to print performance for the tested part properties. The change in shielding gas from argon to nitrogen resulted in similar upskin and downskin surface roughness, with improved tensile strength. Third, a finer powder PSD (15-30 μm) can be beneficial for incremental improvement to upskin surface roughness. It should be noted that this recommendation is limited, as a further increase in fine powder particles will eventually lead to issues with powder cohesion and vaporization

[79, 152]. Lastly, the parameter sets presented in Section 4.6.3 offer roughness improvements of 28% lower as-built downskin surface roughness (Ra < 22 µm) and either 21% lower average upskin Ra or 34% lower top surface Ra (< 5 µm).

As a modification for the inlet and outlets of gyroid heat exchangers, the use of cell-size grading is determined through CFD to reduce pressure drop by 30% at 200 mm/s, with a negative effect on the overall heat transfer coefficient of 5%. The difference in pressure drop was also found to increase more rapidly with increasing flow rate. The relative effect of the graded inlet and outlets would be lower for a longer uniform midsection, but the absolute differences in pressure drop stay the same. Optimized parameters that reduce downskin Ra in the graded gyroid HX by 19 µm result in an additional 11% reduction in pressure drop. Overall, these results open a design capability to lower the pressure drop of gyroid heat exchangers with minimal relative impact on the heat transfer. As well, roughness can be minimized to further reduce pressure drop when critical and contribute to reduced fouling in gyroid channels.

The density-constrained reduction of downskin roughness using exposure parameter optimization was suitable for the complex heat exchanger geometry. The roughness of the internal gyroid channels was improved while maintaining the proper fusion of walls for strength and seal. Simplified ANSYS CFD results indicate that pressure drop is reduced at an increasingly greater degree than heat transfer for higher flow rates. Additionally, the improved surfaces facilitate the potential for post-processing applicability using methods such as HCAF or AFM to achieve smooth surfaces, suitable to implement the advanced DMLS HX design in the prospective application of heat exchange in dairy pasteurization.

6.2 Contribution and Impact

The current body of research lacks studies of as-built downskin roughness and methods for holistic roughness improvement. Experimental efforts in this work for benchmarking, build parameter effects, multiple contour strategies, and DOE optimization contribute to the improvement and understanding of DMLS surface quality. A novel benchmark test artifact and methodology was developed for DMLS prints. The benchmarking study built on the understood limits of relating published VED and exposure parameter effects. Multiple-contour scan strategies were assessed for downskin quality, providing insight into issues not previously discussed in the literature. Discussions of contour scanning and benchmarking results also improve the understanding of dross and warping interactions for varying downskin overhang geometries. Experiments for powder size and shielding gas included an examination for downskins and consideration of other properties, while previous studies focused on upskins. A response surface optimization study proved the viability of exposure parameter DOE to achieve minimal downskin surface roughness without low relative density. This thesis also explores the benefits and opportunities for cell-size grading and roughness optimization as it applies to complex HX design, demonstrating pressure drop characteristics and trade-offs with heat transfer. Other sustainability impacts from the demonstrated roughness reduction include less support material waste and improved post-processing: lower final roughness, shorter post-processing time, labour and materials cost savings, and less use of consumables. Though exact parameters are specific to the EOS M290, they can be used as a reference for optimizations of 316L prints in similar machines.

6.3 Recommendations for Future Work

Given that the reduction in the mechanical performance of strength and ductility from the optimized downskin exposure is attributed to a characteristic issue with MP overlap, the exposure parameter adjustment of hatch distance to 0.08 mm should be tested to remove the characteristic LOF porosity. With no software issues preventing upskin and downskin exposures, default parameters can also be tested as the bulk stripes exposure, with optimized skin exposures, to see if downskin and upskin surface roughness improvements are maintained along with default mechanical properties. Any optimal downskin thickness should also be determined for this exposure parameter set.

Future work relating to the novel heat exchanger design and characterization includes improving the graded model by enhancing the modelled features for more accurate simulation results of the graded design. Potential improvements include a higher resolution to remove closed channels along the walls and the filling or smoothing stagnant areas from the graded connection. A parametric study could also be conducted using ANSYS CFD for optimal graded gyroid lattice sizing, which could include varying the grading length, cell size, and unit cell aspect ratio. This study may require additional advanced modelling software such as nTopology or Gen3D [229, 255]. Experimental testing of these results using a functional DMLS-printed graded-gyroid HX would also be required for validation and correlations, especially for the improved accuracy of surface roughness effects. Testing could also include determining the optimal minimum wall thickness of the printed lattice.

Another method of improving the CFD analysis would involve attaining a true mesh of the printed part to include a proper model for the irregular surfaces of the internal structure.

Because of the complexity of the gyroid geometry and the resulting roughness limiting the ability to apply a suitable surface function, this would be done using imaging techniques. X-ray computed tomography (XCT) is commonly used in metal AM to measure the dimensions and porosity defects in printed samples [256]. XCT has been used to accurately measure the roughness of internal geometries, even with thick outer shells (~20 mm) [257]. This method is proven to provide accurate measures of Ra even for low-resolution voxel size (even 20 μm), so long as it does not exceed the Ra value [258, 259]. Provided sufficient computational power and an XCT device capable of supporting the full design for multiple section scans, actual design models from XCT data could be input into ANSYS Fluent for a CFD analysis of heat transfer and pressure drop performance of true surfaces. Experimental model validation would follow, which would then allow the mesh to be used for simulating flow regimes not easily attainable in-lab.

Testing post-processes for the surfacing capability of the internal gyroid channels using AFM or HCAF would give a direct knowledge of the scope of application for both the HX and the density-controlled downskin optimization. Resultant fouling and pressure drop effects could be studied. The relative influence of the graded cells would decrease with an increasing channel length, but the absolute impact of removing the large pressure drop of the manifolds would remain [223].

Though there is further potential in improving as-built part roughness, the relevant techniques, such as improved shielding gas flow control or pre-processing of the exposure, are often not retrofittable to all manufacturer machines due to software and hardware constraints [260]. Regardless, the characteristic high surface roughness of DMLS parts

generally cannot be avoided, as is the case with the optimized Ra values in this work. Thus, the apparent area for the most potential in improving the surface roughness of DMLS parts is the advancement of post-processing technologies in tandem with optimized parameters. Some highlighted processes with good applicability to complex geometries include AFM, chemical polishing, dry electropolishing, and stream finishing. Further research efforts in this area will help achieve smooth final part surfaces, and innovative process parameter capabilities—such as dynamic exposure settings—will increase treatment efficiency to unlock a wider range of applications of the DMLS process.

REFERENCES

[1] M. Schmidt, M. Merklein, D. Bourell, D. Dimitrov, T. Hausotte, K. Wegener, L. Overmeyer, F. Vollertsen and G. N. Levy, "Laser based additive manufacturing in industry and academia," *CIRP Annals*, vol. 66, no. 2, pp. 561-583, 2017.

[2] M. K. Thompson, G. Moroni, T. Vaneker, G. Fadel, R. I. Campbell, I. Gibson, A. Bernard, J. Schulz, P. Graf, B. Ahuja and F. Martina, "Design for additive manufacturing: Trends, opportunities, considerations, and constraints," *CIRP Annals*, vol. 65, no. 2, pp. 737-760, 2016.

[3] M. Shellabear and O. Nyrhilä, "DMLS - development history and state of the art," *Proceedings of the 4th LANE Conference*, 2004.

[4] M. Anand and A. K. Das, "Issues in fabrication of 3D components through DMLS technique: A review," *Optics & Laser Technology*, vol. 139, pp. 106914, 2021.

[5] S. Bagherifard, J. Kondas, S. Monti, J. Cizek, F. Perego, O. Kovarik, F. Lukac, F. Gaertner and M. Guagliano, "Tailoring cold spray additive manufacturing of steel 316 L for static and cyclic load-bearing applications," *Materials & Design*, vol. 203, pp. 109575, 2021.

[6] M. Gabilondo, X. Cearsolo, M. Arrue and F. Castro, "Influence of build orientation, chamber temperature and infill pattern on mechanical properties of 316L parts manufactured by bound metal deposition," *Materials*, vol. 15, no. 3, 2022.

[7] D. Gu and Y. Shen, "Balling phenomena in direct laser sintering of stainless steel powder: Metallurgical mechanisms and control methods," *Materials in Engineering*, vol. 30, no. 8, pp. 2903-2910, 2009.

[8] J. P. Kruth, G. Levy, F. Klocke and T. H. C. Childs, "Consolidation phenomena in laser and powder-bed based layered manufacturing," *CIRP Annals*, vol. 56, no. 2, pp. 730-759, 2007.

[9] T. DebRoy, H. L. Wei, J. S. Zuback, T. Mukherjee, J. W. Elmer, J. O. Milewski, A. M. Beese, A. Wilson-Heid, A. De and W. Zhang, "Additive manufacturing of metallic components – process, structure and properties," *Progress in Materials Science*, vol. 92, pp. 112-224, 2018.

[10] B. Dovgyy and M. Pham, "Epitaxial growth in 316L steel and CoCrFeMnNi high entropy alloy made by powder-bed laser melting," *Proceedings of the 21st International ESAFORM Conference on Material Forming*, 2018.

[11] P. Krakhmalev, G. Fredriksson, K. Svensson, I. Yadroitsev, I. Yadroitsava, M. Thuvander and R. Peng, "Microstructure, solidification texture, and thermal stability of 316 L stainless steel manufactured by laser powder bed fusion," *Metals*, vol. 8, no. 8, 2018.

[12] S. Sarafan, P. Wanjara, J. Gholipour, F. Bernier, M. Osman, F. Sikan, J. Soost, R. Amos, P. Patnaik and M. Brochu, "Benchmarking of 316L stainless steel manufactured by a hybrid additive/subtractive technology," *Journal of Manufacturing and Materials Processing*, vol. 6, no. 2, 2022.

[13] S. Moylan, J. Slotwinski, A. Cooke, K. Jurrens and M. A. Donmez, "Proposal for a standardized test artifact for additive manufacturing machines and processes," *International Solid Freeform Fabrication Symposium*, pp. 902-920, 2012.

[14] K. Kellens, R. Mertens, D. Paraskevas, W. Dewulf and J. R. Duflou, "Environmental impact of additive manufacturing processes: Does AM contribute to a more sustainable way of part manufacturing?" *Procedia CIRP 61,* vol. 61, pp. 582-587, 2017.

[15] O. Abdulhameed, A. Al-Ahmari, W. Ameen and S. H. Mian, "Additive manufacturing: Challenges, trends, and applications," *Advances in Mechanical Engineering*, vol. 11, no. 2, pp. 1-27, 2019.

[16] J. Faludi, M. Baumers, I. Maskery and R. Hague, "Environmental impacts of selective laser melting: Do printer, powder, or power dominate?" *Journal of Industrial Ecology*, vol. 21, no. S1, pp. S144-S156, 2017.

[17] K. Kellens, M. Baumers, T. G. Gutowski, W. Flanagan, R. Lifset and J. R. Duflou, "Environmental dimensions of additive manufacturing: Mapping application domains and their environmental implications," *Journal of Industrial Ecology*, vol. 21, no. S1, pp. S49-S68, 2017.

[18] E. Yasa, T. Craeghs, M. Badrossamay and J. Kruth, "Rapid manufacturing research at the catholic university of leuven," *US - Turkey Workshop on Rapid Technologies*, pp. 63-73, 2009.

[19] E. Ramirez-Cedillo, M. J. Uddin, J. A. Sandoval-Robles, R. A. Mirshams, L. Ruiz-Huerta, C. A. Rodriguez and H. R. Siller, "Process planning of L-PBF of AISI 316L for improving surface quality and relating part integrity with microstructural characteristics," *Surface & Coatings Technology*, vol. 396, pp. 125956, 2020.

[20] J. P. Oliveira, T. G. Santos and R. M. Miranda, "Revisiting fundamental welding concepts to improve additive manufacturing: From theory to practice," *Progress in Materials Science*, vol. 107, 2020.

[21] A. Leicht, M. Rashidi, U. Klement and E. Hryha, "Effect of process parameters on the microstructure, tensile strength and productivity of 316L parts produced by laser powder bed fusion," *Materials Characterization,* vol. 159, no. 110016, pp. 110016, 2020.

[22] M. Letenneur, V. Brailovski, A. Kreitcberg, V. Paserin and I. Bailon-Poujol, "Laser powder bed fusion of water-atomized iron-based powders: Process optimization," *Journal of Manufacturing and Materials Processing,* vol. 1, no. 2, 2017.

[23] W. M. Tucho, V. H. Lysne, H. Austbø, A. Sjolyst-Kverneland and V. Hansen, "Investigation of effects of process parameters on microstructure and hardness of SLM manufactured SS316L," *Journal of Alloys and Compounds,* vol. 740, pp. 910-925, 2018.

[24] Y. Parikh, J. Carter and M. Kuttolamadom, "Investigation of porosity and microstructure-induced property variations in additive manufactured stainless steel 316L," *Proceedings of the ASME 2020 15th International Manufacturing Science and Engineering Conference,* vol. 84256, 2020.

[25] Y. M. Wang, T. Voisin, J. T. McKeown, J. Ye, N. P. Calta, Z. Li, Z. Zeng, Y. Zhang, W. Chen, T. T. Roehling, R. T. Ott, M. K. Santala, P. J. Depond, M. J. Matthews, A. V. Hamza and T. Zhu, "Additively manufactured hierarchical stainless steels with high strength and ductility," *Nature Materials,* vol. 17, no. 1, pp. 63-71, 2018.

[26] U. Scipioni Bertoli, A. J. Wolfer, M. J. Matthews, J. R. Delplanque and J. M. Schoenung, "On the limitations of volumetric energy density as a design parameter for selective laser melting," *Materials & Design,* vol. 113, pp. 331-340, 2017.

[27] T. Kurzynowski, K. Gruber, W. Stopyra, B. Kuźnicka and E. Chlebus, "Correlation between process parameters, microstructure and properties of 316 L stainless steel processed by selective laser melting," *Materials Science & Engineering: A,* vol. 718, pp. 64-73, 2018.

[28] R. Steinlechner, "Development of laser powder bed fusion parameters and their effect on microstructure formation in low alloyed steels," *Techische Universität Wien,* 2020.

[29] T. H. J. Vaneker, "The role of design for additive manufacturing in the successful economical introduction of AM," *Procedia CIRP,* vol. 60, pp. 181-186, 2017.

[30] J. Richter and P. Jacobs, "Accuracy," *Rapid Prototyping & Manufacturing, P. Jacobs, Society of Manufacturing Engineers,* pp. 287-315, 1992.

[31] D. Scaravetti, P. Dubois and R. Duchamp, "Qualification of rapid prototyping tools: Proposition of a procedure and a test part," *International Journal of Advanced Manufacturing Technology,* vol. 38, no. 7, pp. 683-690, 2007.

[32] L. Castillo, "Study about the rapid manufacturing of complex parts of stainless steel and titanium," *TNO Report with the Collaboration of AIMME,* pp. 1-31, 2005.

[33] J. Kruth, B. Vandenbroucke, J. Van Vaerenbergh and P. Mercelis, "Benchmarking of different SLS/SLM processes as rapid manufacturing techniques," 2005.

[34] E. Yasa, F. Demir, G. Akbulut, N. Cızıoğlu and S. Pilatin, "Benchmarking of different powder-bed metal fusion processes for machine selection in additive manufacturing," 2014.

[35] E. Atzeni and A. Salmi, "Study on unsupported overhangs of AlSi10Mg parts processed by direct metal laser sintering (DMLS)," *Journal of Manufacturing Processes,* vol. 20, pp. 500-506, 2015.

[36] ISO/ASTM 52902:2019, *Additive manufacturing - Test artifacts - Geometric capability assessment of additive manufacturing systems,* ISO/ASTM International, Switzerland, 2019.

[37] D. Thomas, "The development of design rules for selective laser melting," *University of Wales Institute,* 2010.

[38] ASTM A276-06, *Standard Specification for Stainless Steel Bars and Shapes,* ASTM International, West Conshohocken, PA, USA, 2006.

[39] L. Liu, Q. Ding, Y. Zhong, J. Zou, J. Wu, Y. Chiu, J. Li, Z. Zhang, Q. Yu and Z. Shen, "Dislocation network in additive manufactured steel breaks strength–ductility trade-off," *Materials Today,* vol. 21, no. 4, pp. 354-361, 2018.

[40] D. Wang, Y. Yang, Z. Yi and X. Su, "Research on the fabricating quality optimization of the overhanging surface in SLM process," *International Journal of Advanced Manufacturing Technology,* vol. 65, no. 9-12, pp. 1471-1484, 2012.

[41] J. S. Zuback and T. DebRoy, "The hardness of additively manufactured alloys," *Materials,* vol. 11, no. 11, 2018.

[42] K. Dávid Miklós, P. Dávid and K. Dorina, "Microstructure examination of additive manufactured 316L steel," *IOP Conference Series. Materials Science and Engineering,* vol. 903, no. 1, 2020.

[43] K. Saeidi, X. Gao, F. Lofaj, L. Kvetková and Z. J. Shen, "Transformation of austenite to duplex austenite-ferrite assembly in annealed stainless steel 316L

consolidated by laser melting," *Journal of Alloys and Compounds,* vol. 633, pp. 463-469, 2015.

[44] M. Ghasri-Khouzani, H. Peng, R. Attardo, P. Ostiguy, J. Neidig, R. Billo, D. Hoelzle and M. R. Shankar, "Direct metal laser-sintered stainless steel: Comparison of microstructure and hardness between different planes," *International Journal of Advanced Manufacturing Technology,* vol. 95, no. 9-12, pp. 4031-4037, 2018.

[45] D. Wang, C. Song, Y. Yang and Y. Bai, "Investigation of crystal growth mechanism during selective laser melting and mechanical property characterization of 316L stainless steel parts," *Materials & Design,* vol. 100, pp. 291-299, 2016.

[46] C. Qiu, M. A. Kindi, A. S. Aladawi and I. A. Hatmi, "A comprehensive study on microstructure and tensile behaviour of a selectively laser melted stainless steel," *Scientific Reports,* vol. 8, no. 1, 2018.

[47] P. Mercelis and J. Kruth, "Residual stresses in selective laser sintering and selective laser melting," *Rapid Prototyping Journal,* vol. 12, no. 5, pp. 254-265, 2006.

[48] Mele, Bergmann, Campana and Pilz, "Experimental investigation into the effect of supports and overhangs on accuracy and roughness in laser powder bed fusion," *Optics and Laser Technology,* vol. 140, pp. 107024, 2021.

[49] Z. Fang, Z. Wu, C. Huang and C. Wu, "Review on residual stress in selective laser melting additive manufacturing of alloy parts," *Optics and Laser Technology,* vol. 129, pp. 106283, 2020.

[50] M. Yakout, M. A. Elbestawi and S. C. Veldhuis, "Density and mechanical properties in selective laser melting of invar 36 and stainless steel 316L," *Journal of Materials Processing Technology,* vol. 266, pp. 397-420, 2019.

[51] I. Yadroitsava and I. Yadroitsev, "Residual stress in metal specimens produced by direct metal laser sintering," *International Solid Freeform Fabrication Symposium,* pp. 614-625, 2015.

[52] J. Kruth, J. Deckers, E. Yasa and R. Wauthlé, "Assessing and comparing influencing factors of residual stresses in selective laser melting using a novel analysis method," *Proceedings of the Institution of Mechanical Engineers. Part B, Journal of Engineering Manufacture,* vol. 226, no. 6, pp. 980-991, 2012.

[53] C. Li, Z. Y. Liu, X. Y. Fang and Y. B. Guo, "Residual stress in metal additive manufacturing," *Procedia CIRP,* vol. 71, pp. 348-353, 2018.

[54] M. Godec, S. Zaefferer, B. Podgornik, M. Šinko and E. Tchernychova, "Quantitative multiscale correlative microstructure analysis of additive manufacturing of stainless

steel 316L processed by selective laser melting," *Materials Characterization,* vol. 160, 2020.

[55] A. Röttger, K. Geenen, M. Windmann, F. Binner and W. Theisen, "Comparison of microstructure and mechanical properties of 316 L austenitic steel processed by selective laser melting with hot-isostatic pressed and cast material," *Materials Science & Engineering: A,* vol. 678, pp. 365-376, 2016.

[56] D. Herzog, V. Seyda, E. Wycisk and C. Emmelmann, "Additive manufacturing of metals," *Acta Materialia,* vol. 117, pp. 371-392, 2016.

[57] E. Liverani, A. H. A. Lutey, A. Ascari and A. Fortunato, "The effects of hot isostatic pressing (HIP) and solubilization heat treatment on the density, mechanical properties, and microstructure of austenitic stainless steel parts produced by selective laser melting (SLM)," *International Journal of Advanced Manufacturing Technology,* vol. 107, no. 1-2, pp. 109-122, 2020.

[58] Q. Yu, X. Yang, C. Lai and Z. Tong, "Study on MnS inclusion aggregation along continuous casting slab thickness of medium carbon structural steel," *Metals,* vol. 12, no. 1, 2021.

[59] A. F. Padilha, R. L. Plaut and P. R. Rios, "Stainless steels heat treatment," *Steel Heat Treatment Handbook,* vol. 2, pp. 695-739, 2007.

[60] D. A. Arvola, S. N. Lekakh, R. J. O'Malley and L. N. Bartlett, "Two inoculation methods for refining as-cast grain structure in austenitic 316L steel," *International Journal of Metalcasting,* vol. 13, no. 3, pp. 504-518, 2018.

[61] W. D. Callister and D. G. Rethwisch, "Materials science and engineering: An introduction, 9th edition," John Wiley and Sons, 2013.

[62] D. Riabov, A. Leicht, J. Ahlström and E. Hryha, "Investigation of the strengthening mechanism in 316L stainless steel produced with laser powder bed fusion," *Materials Science & Engineering: A,* vol. 822, 2021.

[63] S. Kou, "Welding metallurgy," Wiley, 2003.

[64] X. Lin, Y. Li, M. Wang, L. Chen and W. Huang, "Columnar to equiaxed transition during alloy solidification," *Science in China. Series E, Technological Sciences,* vol. 46, no. 5, pp. 475-489, 2003.

[65] P. Liu, Z. Wang, Y. Xiao, M. F. Horstemeyer, X. Cui and L. Chen, "Insight into the mechanisms of columnar to equiaxed grain transition during metallic additive manufacturing," *Additive Manufacturing,* vol. 26, pp. 22-29, 2019.

[66] G. Zimmermann, L. Sturz, B. Billia, N. Mangelinck-Noël, H. N. Thi, C. A. Gandin, D. J. Browne and W. U. Mirihanage, "Investigation of columnar-to-equiaxed transition in solidification processing of AlSi alloys in microgravity – the CETSOL project," *Journal of Physics. Conference Series,* vol. 327, no. 1, pp. 12003-12, 2011.

[67] T. Larimian, M. Kannan, D. Grzesiak, B. AlMangour and T. Borkar, "Effect of energy density and scanning strategy on densification, microstructure and mechanical properties of 316L stainless steel processed via selective laser melting," *Materials Science & Engineering: A,* vol. 770, 2020.

[68] K. Saeidi, X. Gao, Y. Zhong and Z. J. Shen, "Hardened austenite steel with columnar sub-grain structure formed by laser melting," *Materials Science & Engineering: A,* vol. 625, pp. 221-229, 2015.

[69] Z. Sun, X. Tan, S. B. Tor and W. Y. Yeong, "Selective laser melting of stainless steel 316L with low porosity and high build rates," *Materials & Design,* vol. 104, pp. 197-204, 2016.

[70] S. Gorsse, C. R. Hutchinson, M. Gouné and R. Banerjee, "Additive manufacturing of metals: A brief review of the characteristic microstructures and properties of steels, ti-6Al-4V and high-entropy alloys," *Science and Technology of Advanced Materials,* vol. 18, no. 1, 2017.

[71] K. G. Prashanth and J. Eckert, "Formation of metastable cellular microstructures in selective laser melted alloys," *Journal of Alloys and Compounds,* vol. 707, pp. 27-34, 2017.

[72] Y. Zhong, L. Liu, S. Wikman, D. Cui and Z. Shen, "Intragranular cellular segregation network structure strengthening 316L stainless steel prepared by selective laser melting," *Journal of Nuclear Materials,* vol. 470, pp. 170-178, 2016.

[73] M. Laleh, A. E. Hughes, W. Xu, N. Haghdadi, K. Wang, P. Cizek, I. Gibson and M. Y. Tan, "On the unusual intergranular corrosion resistance of 316L stainless steel additively manufactured by selective laser melting," *Corrosion Science,* vol. 161, pp. 108189, 2019.

[74] A. J. Birnbaum, J. C. Steuben, E. J. Barrick, A. P. Iliopoulos and J. G. Michopoulos, "Intrinsic strain aging, Σ3 boundaries, and origins of cellular substructure in additively manufactured 316L," *Additive Manufacturing,* vol. 29, pp. 100784, 2019.

[75] L. Rännar, A. Koptyug, J. Olsén, K. Saeidi and Z. Shen, "Hierarchical structures of stainless steel 316L manufactured by electron beam melting,"

[76] U. Scipioni Bertoli, B. E. MacDonald and J. M. Schoenung, "Stability of cellular microstructure in laser powder bed fusion of 316L stainless steel," *Materials Science & Engineering: A,* vol. 739, pp. 109-117, 2019.

[77] T. Mukherjee, J. S. Zuback, A. De and T. DebRoy, "Printability of alloys for additive manufacturing," *Scientific Reports,* vol. 6, no. 1, pp. 19717, 2016.

[78] R. Casati, J. Lemke and M. Vedani, "Microstructure and fracture behavior of 316L austenitic stainless steel produced by selective laser melting," *Journal of Materials Science & Technology,* vol. 32, no. 8, pp. 738-744, 2016.

[79] P. W. Liu, Y. Z. Ji, Z. Wang, C. L. Qiu, A. A. Antonysamy, L. -. Chen, X. Y. Cui and L. Chen, "Investigation on evolution mechanisms of site-specific grain structures during metal additive manufacturing," *Journal of Materials Processing Technology,* vol. 257, pp. 191-202, 2018.

[80] K. M. Bertsch, G. Meric de Bellefon, B. Kuehl and D. J. Thoma, "Origin of dislocation structures in an additively manufactured austenitic stainless steel 316L," *Acta Materialia,* vol. 199, no. C, pp. 19-33, 2020.

[81] Z. Liu, D. Zhao, P. Wang, M. Yan, C. Yang, Z. Chen, J. Lu and Z. Lu, "Additive manufacturing of metals: Microstructure evolution and multistage control," *Journal of Materials Science & Technology,* vol. 100, pp. 224-236, 2022.

[82] Z. Sun, X. Tan, S. B. Tor and C. K. Chua, "Simultaneously enhanced strength and ductility for 3D-printed stainless steel 316L by selective laser melting," *NPG Asia Materials,* vol. 10, no. 4, pp. 127-136, 2018.

[83] B. Ahuja, A. Schaub, D. Junker, M. Karg, F. Tenner, R. Plettke, M. Merklein and M. Schmidt, "A round robin study for laser beam melting in metal powder bed," *South African Journal of Industrial Engineering,* vol. 27, no. 2, pp. 30-42, 2016.

[84] E. Liverani, S. Toschi, L. Ceschini and A. Fortunato, "Effect of selective laser melting (SLM) process parameters on microstructure and mechanical properties of 316L austenitic stainless steel," *Journal of Materials Processing Technology,* vol. 249, pp. 255-263, 2017.

[85] E. Koc, M. Coskun and Z. Cagatay Oter, "Anisotropic mechanical behavior of direct metal laser sintering (DMLS) parts," 2017.

[86] O. Andreau, I. Koutiri, P. Peyre, J. Penot, N. Saintier, E. Pessard, T. De Terris, C. Dupuy and T. Baudin, "Texture control of 316L parts by modulation of the melt pool morphology in selective laser melting," *Journal of Materials Processing Technology,* vol. 264, pp. 21-31, 2019.

[87] A. Leicht, C. H. Yu, V. Luzin, U. Klement and E. Hryha, "Effect of scan rotation on the microstructure development and mechanical properties of 316L parts produced by laser powder bed fusion," *Materials Characterization,* vol. 163, 2020.

[88] T. Niendorf, S. Leuders, A. Riemer, H. A. Richard, T. Tröster and D. Schwarze, "Highly anisotropic steel processed by selective laser melting," *Metallurgical and Materials Transactions. B, Process Metallurgy and Materials Processing Science,* vol. 44, no. 4, pp. 794-796, 2013.

[89] M. S. Pham, B. Dovgyy and P. A. Hooper, "Twinning induced plasticity in austenitic stainless steel 316L made by additive manufacturing," *Materials Science & Engineering: A,* vol. 704, pp. 102-111, 2017.

[90] I. Yadroitsev, P. Krakhmalev, I. Yadroitsava, S. Johansson and I. Smurov, "Energy input effect on morphology and microstructure of selective laser melting single track from metallic powder," *Journal of Materials Processing Technology,* vol. 213, no. 4, pp. 606-613, 2013.

[91] U. Scipioni Bertoli, G. Guss, S. Wu, M. J. Matthews and J. M. Schoenung, "In-situ characterization of laser-powder interaction and cooling rates through high-speed imaging of powder bed fusion additive manufacturing," *Materials & Design,* vol. 135, no. C, pp. 385-396, 2017.

[92] G. Mohr, S. J. Altenburg and K. Hilgenberg, "Effects of inter layer time and build height on resulting properties of 316L stainless steel processed by laser powder bed fusion," *Additive Manufacturing,* vol. 32, pp. 101080, 2020.

[93] A. F. Padilha, R. L. Plaut and P. R. Rios, "Annealing of cold-worked austenitic stainless steels," *ISIJ International,* vol. 43, no. 2, pp. 135-143, 2003.

[94] M. L. Montero-Sistiaga, M. Godino-Martinez, K. Boschmans, J. Kruth, J. Van Humbeeck and K. Vanmeensel, "Microstructure evolution of 316L produced by HP-SLM (high power selective laser melting)," *Additive Manufacturing,* vol. 23, pp. 402-410, 2018.

[95] L. Cui, S. Jiang, J. Xu, R. L. Peng, R. T. Mousavian and J. Moverare, "Revealing relationships between microstructure and hardening nature of additively manufactured 316L stainless steel," *Materials & Design,* vol. 198, 2021.

[96] M. Benedetti, M. Cazzolli, V. Fontanari and M. Leoni, "Fatigue limit of Ti6Al4V alloy produced by selective laser sintering," *Procedia Structural Integrity,* vol. 2, pp. 3158-3167, 2016.

[97] V. Gunenthiram, P. Peyre, M. Schneider, M. Dal, F. Coste, I. Koutiri and R. Fabbro, "Experimental analysis of spatter generation and melt-pool behavior during the

powder bed laser beam melting process," *Journal of Materials Processing Technology,* vol. 251, pp. 376-386, 2018.

[98] W. E. King, H. D. Barth, V. M. Castillo, G. F. Gallegos, J. W. Gibbs, D. E. Hahn, C. Kamath and A. M. Rubenchik, "Observation of keyhole-mode laser melting in laser powder-bed fusion additive manufacturing," *Journal of Materials Processing Technology,* vol. 214, no. 12, pp. 2915-2925, 2014.

[99] S. Patel and M. Vlasea, "Melting modes in laser powder bed fusion," *Materialia,* vol. 9, 2020.

[100] S. M. H. Hojjatzadeh, N. D. Parab, W. Yan, Q. Guo, L. Xiong, C. Zhao, M. Qu, L. I. Escano, X. Xiao, K. Fezzaa, W. Everhart, T. Sun and L. L. Chen, "Pore elimination mechanisms during 3D printing of metals," *Nature Communications,* vol. 10, no. 1, 2019.

[101] J. Metelkova, Y. Kinds, K. Kempen, C. de Formanoir, A. Witvrouw and B. Van Hooreweder, "On the influence of laser defocusing in selective laser melting of 316L," *Additive Manufacturing,* vol. 23, pp. 161-169, 2018.

[102] P. Bidare, I. Bitharas, R. M. Ward, M. M. Attallah and A. J. Moore, "Fluid and particle dynamics in laser powder bed fusion," *Acta Materialia,* vol. 142, pp. 107-120, 2018.

[103] P. Bidare, R. R. J. Maier, R. J. Beck, J. D. Shephard and A. J. Moore, "An open-architecture metal powder bed fusion system for in-situ process measurements," *Additive Manufacturing,* vol. 16, pp. 177-185, 2017.

[104] M. J. Matthews, G. Guss, S. A. Khairallah, A. M. Rubenchik, P. J. Depond and W. E. King, "Denudation of metal powder layers in laser powder bed fusion processes," *Acta Materialia,* vol. 114, no. C, pp. 33-42, 2016.

[105] H. J. Niu and I. T. H. Chang, "Instability of scan tracks of selective laser sintering of high speed steel powder," *Scripta Materialia,* vol. 41, no. 11, pp. 1229-1234, 1999.

[106] R. Li, J. Liu, Y. Shi, L. Wang and W. Jiang, "Balling behavior of stainless steel and nickel powder during selective laser melting process," *International Journal of Advanced Manufacturing Technology,* vol. 59, no. 9-12, pp. 1025-1035, 2011.

[107] M. Rombouts, J. P. Kruth, L. Froyen and P. Mercelis, "Fundamentals of selective laser melting of alloyed steel powders," *CIRP Annals,* vol. 55, no. 1, pp. 187, 2006.

[108] Z. C. Oter, M. Coskun, Y. Akca, O. Surmen, M. S. Yilmaz, G. Ozer, G. Tarakci, H. M. Khan and E. Koc, "Support optimization for overhanging parts in direct metal laser sintering," *Optik,* vol. 181, pp. 575-581, 2019.

[109] Z. Xiang, L. Wang, C. Yang, M. Yin and G. Yin, "Analysis of the quality of slope surface in selective laser melting process by simulation and experiments," *Optik,* vol. 176, pp. 68-77, 2019.

[110] U. Paggi, R. Ranjan, L. Thijs, C. Ayas, M. Langelaar, F. van Keulen and B. van Hooreweder, "New support structures for reduced overheating on downfacing regions of direct metal printed parts," *International Solid Freeform Fabrication Symposium,* 2019.

[111] P. J. DePond, G. Guss, S. Ly, N. P. Calta, D. Deane, S. Khairallah and M. J. Matthews, "In situ measurements of layer roughness during laser powder bed fusion additive manufacturing using low coherence scanning interferometry," *Materials & Design,* vol. 154, pp. 347-359, 2018.

[112] S. Feng, A. M. Kamat, S. Sabooni and Y. Pei, "Experimental and numerical investigation of the origin of surface roughness in laser powder bed fused overhang regions," *Virtual and Physical Prototyping,* vol. 16, no. S1, 2021.

[113] A. Charles, M. Bayat, A. Elkaseer, L. Thijs, J. H. Hattel and S. Scholz, "Elucidation of dross formation in laser powder bed fusion at down-facing surfaces: Phenomenon-oriented multiphysics simulation and experimental validation," *Additive Manufacturing,* vol. 50, 2022.

[114] K. Q. Le, C. H. Wong, K. H. G. Chua, C. Tang and H. Du, "Discontinuity of overhanging melt track in selective laser melting process," *International Journal of Heat and Mass Transfer,* vol. 162, 2020.

[115] C. J. Montgomery, "The effect of alloys, powder, and overhanging geometries in laser powder bed additive manufacturing," *Carnegie Mellon University,* 2017.

[116] I. Koutiri, E. Pessard, P. Peyre, O. Amlou and T. De Terris, "Influence of SLM process parameters on the surface finish, porosity rate and fatigue behavior of as-built inconel 625 parts," *Journal of Materials Processing Technology,* vol. 255, pp. 536-546, 2018.

[117] D. Wang, S. Mai, D. Xiao and Y. Yang, "Surface quality of the curved overhanging structure manufactured from 316-L stainless steel by SLM," *International Journal of Advanced Manufacturing Technology,* vol. 86, no. 1-4, pp. 781-792, 2015.

[118] P. Fathi, M. Rafieazad, X. Duan, M. Mohammadi and A. M. Nasiri, "On microstructure and corrosion behaviour of AlSi10Mg alloy with low surface

roughness fabricated by direct metal laser sintering," *Corrosion Science,* vol. 157, pp. 126-145, 2019.

[119] S. Greco, K. Gutzeit, H. Hotz, B. Kirsch and J. C. Aurich, "Selective laser melting (SLM) of AISI 316L—impact of laser power, layer thickness, and hatch spacing on roughness, density, and microhardness at constant input energy density," *International Journal of Advanced Manufacturing Technology,* vol. 108, no. 5-6, pp. 1551-1562, 2020.

[120] S. Romano, P. D. Nezhadfar, N. Shamsaei, M. Seifi and S. Beretta, "High cycle fatigue behavior and life prediction for additively manufactured 17-4 PH stainless steel: Effect of sub-surface porosity and surface roughness," *Theoretical and Applied Fracture Mechanics,* vol. 106, 2020.

[121] Q. B. Nguyen, D. N. Luu, S. M. L. Nai, Z. Zhu, Z. Chen and J. Wei, "The role of powder layer thickness on the quality of SLM printed parts," *Archives of Civil and Mechanical Engineering,* vol. 18, no. 3, pp. 948-955, 2018.

[122] J. A. Cherry, H. M. Davies, S. Mehmood, N. P. Lavery, S. G. R. Brown and J. Sienz, "Investigation into the effect of process parameters on microstructural and physical properties of 316L stainless steel parts by selective laser melting," *International Journal of Advanced Manufacturing Technology,* vol. 76, no. 5-8, pp. 869-879, 2014.

[123] A. Ilie, H. Ali and K. Mumtaz, "In-built customised mechanical failure of 316L components fabricated using selective laser melting," *Technologies,* vol. 5, no. 1, 2017.

[124] W. Di, Y. Yongqiang, S. Xubin and C. Yonghua, "Study on energy input and its influences on single-track, multi-track, and multi-layer in SLM," *The International Journal of Advanced Manufacturing Technology,* vol. 58, no. 9, pp. 1189-1199, 2012.

[125] M. A. Melia, J. G. Duran, J. R. Koepke, D. J. Saiz, B. H. Jared and E. J. Schindelholz, "How build angle and post-processing impact roughness and corrosion of additively manufactured 316L stainless steel," *Npj Materials Degradation,* vol. 4, no. 1, 2020.

[126] "EOS StainlessSteel 316L," Electro Optical Systems GmbH, 2014.

[127] J. Metelkova, L. Vanmunster, H. Haitjema and B. Van Hooreweder, "Texture of inclined up-facing surfaces in laser powder bed fusion of metals," *Additive Manufacturing,* vol. 42, 2021.

[128] J. Pakkanen, F. Calignano, F. Trevisan, M. Lorusso, E. P. Ambrosio, D. Manfredi and P. Fino, "Study of internal channel surface roughnesses manufactured by selective laser melting in aluminum and titanium alloys," *Metallurgical and Materials Transactions. A, Physical Metallurgy and Materials Science,* vol. 47, no. 8, pp. 3837-3844, 2016.

[129] M. Jamshidinia and R. Kovacevic, "The influence of heat accumulation on the surface roughness in powder-bed additive manufacturing," *Surface Topography Metrology and Properties,* vol. 3, no. 1, 2015.

[130] A. Sarker, N. Tran, A. Rifai, M. Brandt, P. A. Tran, M. Leary, K. Fox and R. Williams, "Rational design of additively manufactured Ti6Al4V implants to control staphylococcus aureus biofilm formation," *Materialia,* vol. 5, 2019.

[131] G. S. Sharma, M. Sugavaneswaran, U. Vijayalakshmi and R. Prakash, "Influence of γ-alumina coating on surface properties of direct metal laser sintered 316L stainless steel," *Ceramics International,* vol. 45, no. 10, pp. 13456-13463, 2019.

[132] M. Cabrini, S. Lorenzi, T. Pastore, S. Pellegrini, D. Manfredi, P. Fino, S. Biamino and C. Badini, "Evaluation of corrosion resistance of Al–10Si–Mg alloy obtained by means of direct metal laser sintering," *Journal of Materials Processing Technology,* vol. 231, pp. 326-335, 2016.

[133] Y. Deng, Z. Mao, N. Yang, X. Niu and X. Lu, "Collaborative optimization of density and surface roughness of 316L stainless steel in selective laser melting," *Materials,* vol. 13, no. 7, 2020.

[134] H. Chen, D. Gu, J. Xiong and M. Xia, "Improving additive manufacturing processability of hard-to-process overhanging structure by selective laser melting," *Journal of Materials Processing Technology,* vol. 250, pp. 99-108, 2017.

[135] F. Attarzadeh, B. Fotovvati, M. Fitzmire and E. Asadi, "Surface roughness and densification correlation for direct metal laser sintering," *International Journal of Advanced Manufacturing Technology,* vol. 107, no. 5-6, pp. 2833-2842, 2020.

[136] F. Calignano, D. Manfredi, E. P. Ambrosio, L. Iuliano and P. Fino, "Influence of process parameters on surface roughness of aluminum parts produced by DMLS," *International Journal of Advanced Manufacturing Technology,* vol. 67, no. 9-12, pp. 2743-2751, 2012.

[137] G. Dursun, S. Ibekwe, G. Li, P. Mensah, G. Joshi and D. Jerro, "Influence of laser processing parameters on the surface characteristics of 316L stainless steel manufactured by selective laser melting," *Materials Today: Proceedings,* vol. 26, pp. 387-393, 2020.

[138] Y. Tian, D. Tomus, P. Rometsch and X. Wu, "Influences of processing parameters on surface roughness of hastelloy X produced by selective laser melting," *Additive Manufacturing,* vol. 13, pp. 103-112, 2017.

[139] A. H. Maamoun, Y. F. Xue, M. A. Elbestawi and S. C. Veldhuis, "Effect of selective laser melting process parameters on the quality of al alloy parts: Powder characterization, density, surface roughness, and dimensional accuracy," *Materials,* vol. 11, no. 12, 2018.

[140] A. Charles, A. Elkaseer, L. Thijs, V. Hagenmeyer and S. Scholz, "Effect of process parameters on the generated surface roughness of down-facing surfaces in selective laser melting," *Applied Sciences,* vol. 9, no. 6, 2019.

[141] G. Piscopo, A. Salmi and E. Atzeni, "On the quality of unsupported overhangs produced by laser powder bed fusion," *International Journal of Manufacturing Research,* vol. 15, no. 2, 2020.

[142] B. Ferrar, L. Mullen, E. Jones, R. Stamp and C. J. Sutcliffe, "Gas flow effects on selective laser melting (SLM) manufacturing performance," *Journal of Materials Processing Technology,* vol. 212, no. 2, pp. 355-364, 2012.

[143] J. Reijonen, A. Revuelta, T. Riipinen, K. Ruusuvuori and P. Puukko, "On the effect of shielding gas flow on porosity and melt pool geometry in laser powder bed fusion additive manufacturing," *Additive Manufacturing,* vol. 32, 2020.

[144] L. C. Wei, L. E. Ehrlich, M. J. Powell-Palm, C. Montgomery, J. Beuth and J. A. Malen, "Thermal conductivity of metal powders for powder bed additive manufacturing," *Additive Manufacturing,* vol. 21, pp. 201-208, 2018.

[145] C. Montgomery, C. Farnin, G. Mellos, M. Brand, R. Pacheco and J. Carpenter, "Effect of shield gas on surface finish of laser powder bed produced parts," *Proceedings of the 29th Annual International Solid Freeform Fabrication Symposium,* 2018.

[146] P. Dastranjy Nezhadfar, M. Masoomi, S. Thompson, N. Phan and N. Shamsaei, "Mechanical properties of 17-4 PH stainless steel additively manufactured under ar and N2 shielding gas," pp. 13-15, 2018.

[147] C. Pauzon, E. Hryha, P. Forêt and L. Nyborg, "Effect of argon and nitrogen atmospheres on the properties of stainless steel 316 L parts produced by laser-powder bed fusion," *Materials & Design,* vol. 179, 2019.

[148] D. Dai and D. Gu, "Effect of metal vaporization behavior on keyhole-mode surface morphology of selective laser melted composites using different protective atmospheres," *Applied Surface Science,* vol. 355, pp. 310-319, 2015.

[149] H. Mendoza, "Effects of a binary argon-helium shielding gas mixture on ultra-thin features produced by laser-powder bed fusion additive manufacturing," *The Ohio State University,* 2021.

[150] P. Quinn, S. O'halloran, J. Lawlor and R. Raghavendra, "The effect of metal EOS 316L stainless steel additive manufacturing powder recycling on part characteristics and powder reusability," *Advances in Materials and Processing Technologies,* vol. 5, no. 2, 2019.

[151] C. Abel, R. Dorantes and A. Czekanski, "Effect in thermal conductivity due to compaction of powdered stainless-steel 316L used in additive manufacturing," *Proceedings of the Canadian Society for Mechanical Engineering International Congress,* 2020.

[152] A. T. Sutton, C. S. Kriewall, M. C. Leu and J. W. Newkirk, "Powder characterisation techniques and effects of powder characteristics on part properties in powder-bed fusion processes," *Virtual and Physical Prototyping,* vol. 12, no. 1, pp. 3-29, 2017.

[153] A. B. Spierings, M. Schneider and R. Eggenberger, "Comparison of density measurement techniques for additive manufactured metallic parts," *Rapid Prototyping Journal,* vol. 17, no. 5, pp. 380-386, 2011.

[154] A. B. Spierings, N. Herres and G. Levy, "Influence of the particle size distribution on surface quality and mechanical properties in AM steel parts," *Rapid Prototyping Journal,* vol. 17, no. 3, pp. 195-202, 2011.

[155] A. Simchi, "The role of particle size on the laser sintering of iron powder," *Metallurgical and Materials Transactions. B,* vol. 35, no. 5, pp. 937-948, 2004.

[156] L. P. Lefebvre, J. Dai, Y. Thomas and Y. Martinez-Rubi, "Metal powder flowability: Effect of humidity and impact on the reproducibility of the measurements," *Proceeding of the Additive Manufacturing with Powder Metallurgy Conference,* 2019.

[157] K. Cooper, P. Steele, B. Cheng and K. Chou, "Contact-free support structures for part overhangs in powder-bed metal additive manufacturing," *Inventions,* vol. 3, no. 1, 2017.

[158] C. S. Lefky, B. Zucker, D. Wright, A. R. Nassar, T. W. Simpson and O. J. Hildreth, "Dissolvable supports in powder bed fusion-printed stainless steel," *3D Printing and Additive Manufacturing,* vol. 4, no. 1, 2017.

[159] Q. Cao, Y. Bai, J. Zhang, Z. Shi, J. Y. H. Fuh and H. Wang, "Removability of 316L stainless steel cone and block support structures fabricated by selective laser melting (SLM)," *Materials & Design,* vol. 191, 2020.

[160] K. Alrbaey, D. Wimpenny, R. Tosi, W. Manning and A. Moroz, "On optimization of surface roughness of selective laser melted stainless steel parts: A statistical study," *Journal of Materials Engineering and Performance,* vol. 23, no. 6, pp. 2139-2148, 2014.

[161] P. Tyagi, T. Goulet, C. Riso, R. Stephenson, N. Chuenprateep, J. Schlitzer, C. Benton and F. Garcia-Moreno, "Reducing the roughness of internal surface of an additive manufacturing produced 316 steel component by chempolishing and electropolishing," *Additive Manufacturing,* vol. 25, pp. 32-38, 2019.

[162] H. Woo, J. Kim, J. Ryu, J. Lee and S. Lee, "Dry electropolishing of an additively manufactured spacer grid," Jul 2020.

[163] N. Mohammadian, S. Turenne and V. Brailovski, "Surface finish control of additively-manufactured inconel 625 components using combined chemical-abrasive flow polishing," *Journal of Materials Processing Technology,* vol. 252, pp. 728-738, 2018.

[164] A. P. Nagalingam, J. Lee and S. H. Yeo, "Multi-jet hydrodynamic surface finishing and X-ray computed tomography (X-CT) inspection of laser powder bed fused inconel 625 fuel injection/spray nozzles," *Journal of Materials Processing Technology,* vol. 291, 2021.

[165] A. Ribezzo, F. Calignano, A. Salmi, E. Atzeni, F. Pietrobono, F. Trovalusci and G. Rubino, "Finishing of metal additive manufactured parts by abrasive fluidized bed machining," *Euspen's 18th International Conference and Exhibition,* 2018.

[166] C. Bouland, V. Urlea, K. Beaubier, M. Samoilenko and V. Brailovski, "Abrasive flow machining of laser powder bed-fused parts: Numerical modeling and experimental validation," *Journal of Materials Processing Technology,* vol. 273, pp. 116262, 2019.

[167] M. Jamal and M. Morgan, "Design process control for improved surface finish of metal additive manufactured parts of complex build geometry," *Inventions,* vol. 2, no. 4, 2017.

[168] A. P. Nagalingam and S. H. Yeo, "Controlled hydrodynamic cavitation erosion with abrasive particles for internal surface modification of additive manufactured components," *Wear,* vol. 414-415, pp. 89-100, 2018.

[169] A. P. Nagalingam, V. Chinnaiyan, H. K. Thiruchelvam, Z. C. Yuvaraj, D. Yeo, W. Toh and S. H. Yeo, "Effect of internal surface finishing using hydrodynamic cavitation abrasive finishing (HCAF) process on the mechanical properties of additively manufactured components," pp. 122-131, 2019.

[170] A. P. Nagalingam, H. K. Yuvaraj, V. Santhanam and S. H. Yeo, "Multiphase hydrodynamic flow finishing for surface integrity enhancement of additive manufactured internal channels," *Journal of Materials Processing Technology,* vol. 283, 2020.

[171] Y. Bai, C. Zhao, J. Yang, J. Y. H. Fuh, W. F. Lu, C. Weng and H. Wang, "Dry mechanical-electrochemical polishing of selective laser melted 316L stainless steel," *Materials & Design,* vol. 193, 2020.

[172] M. Leary, "4 - surface roughness optimisation for selective laser melting (SLM): Accommodating relevant and irrelevant surfaces," *Laser Additive Manufacturing,* Elsevier Ltd, pp. 99-118, 2017.

[173] S. Rott, A. Ladewig, K. Friedberger, J. Casper, M. Full and J. H. Schleifenbaum, "Surface roughness in laser powder bed fusion – interdependency of surface orientation and laser incidence," *Additive Manufacturing,* vol. 36, 2020.

[174] S. Kleszczynski, A. Ladewig, K. Friedberger, J. Zur Jacobsmühlen, D. Merhof and G. Witt, "Position dependency of surface roughness in parts from laser beam melting systems," *International Solid Freeform Fabrication Symposium,* 2015.

[175] H. Yeung, B. Lane and J. Fox, "Part geometry and conduction-based laser power control for powder bed fusion additive manufacturing," *Additive Manufacturing,* vol. 30, 2019.

[176] A. M. Kamat and Y. Pei, "An analytical method to predict and compensate for residual stress-induced deformation in overhanging regions of internal channels fabricated using powder bed fusion," *Additive Manufacturing,* vol. 29, pp. 100796, 2019.

[177] C. Wang, X. Qian, W. D. Gerstler and J. Shubrooks, "Boundary slope control in topology optimization for additive manufacturing: For self-support and surface roughness," *Journal of Manufacturing Science and Engineering,* vol. 141, no. 9, 2019.

[178] A. Charles, A. Elkaseer, T. Müller, L. Thijs, M. Torge, V. Hagenmeyer and S. Scholz, "A study of the factors influencing generated surface roughness of down-facing surfaces in selective laser melting," *Proceedings of the World Congress on Micro and Nano Manufacturing,* 2018.

[179] S. Patel, A. Rogalsky and M. Vlasea, "Towards understanding side-skin surface characteristics in laser powder bed fusion," *Journal of Materials Research,* vol. 35, no. 15, pp. 2055-2064, 2020.

[180] T. Yang, T. Liu, W. Liao, H. Wei, C. Zhang, X. Chen and K. Zhang, "Effect of processing parameters on overhanging surface roughness during laser powder bed fusion of AlSi10Mg," *Journal of Manufacturing Processes,* vol. 61, pp. 440-453, 2021.

[181] K. Artzt, T. Mishurova, P. Bauer, J. Gussone, P. Barriobero-Vila, S. Evsevleev, G. Bruno, G. Requena and J. Haubrich, "Pandora's Box–Influence of contour parameters on roughness and subsurface residual stresses in laser powder bed fusion of ti-6Al-4V," *Materials,* vol. 13, no. 15, 2020.

[182] M. Cloots, L. Zumofen, A. B. Spierings, A. Kirchheim and K. Wegener, "Approaches to minimize overhang angles of SLM parts," *Rapid Prototyping Journal,* 2017.

[183] S. Moylan, J. Slotwinski, A. Cooke, K. Jurrens and M. A. Donmez, "Lessons learned in establishing the NIST metal additive manufacturing laboratory," *National Institute of Standards and Technology,* 2013.

[184] Ö Poyraz, E. Yasa, G. Akbulut, A. Orhangül and S. Pilatin, "Investigation of support structures for direct metal laser sintering (DMLS) of IN625 parts," *International Solid Freeform Fabrication Symposium,* 2015.

[185] ASTM E10-15, *Standard Test Method for Brinell Hardness of Metallic Materials,* ASTM International, West Conshohocken, PA, USA, 2015.

[186] F. Calignano, "Design optimization of supports for overhanging structures in aluminum and titanium alloys by selective laser melting," *Materials in Engineering,* vol. 64, pp. 203-213, 2014.

[187] "Design for additive metal manufacturing," Additive Metal Manufacturing Inc., 2016.

[188] Z. Sun, G. Vladimirov, E. Nikolaev and L. F. Velasquez-Garcia, "Exploration of metal 3-D printing technologies for the microfabrication of freeform, finely featured, mesoscaled structures," *Journal of Microelectromechanical Systems,* vol. 27, no. 6, pp. 1171-1185, 2018.

[189] W. S. Tan, S. R. Suwarno, J. An, C. K. Chua, A. G. Fane and T. H. Chong, "Comparison of solid, liquid and powder forms of 3D printing techniques in membrane spacer fabrication," *Journal of Membrane Science,* vol. 537, pp. 283-296, 2017.

[190] ISO 4288:1996, *Geometrical Product Specifications (GPS) — Surface texture: Profile method — Rules and procedures for the assessment of surface texture,* International Organization for Standardization, 1996.

[191] A. Triantaphyllou, C. L. Giusca, G. D. Macaulay, F. Roerig, M. Hoebel, R. K. Leach, B. Tomita and K. A. Milne, "Surface texture measurement for additive manufacturing," *Surface Topography: Metrology and Properties,* vol. 3, no. 2, pp. 024002, 2015.

[192] J. C. Fox, S. P. Moylan and B. M. Lane, "Effect of process parameters on the surface roughness of overhanging structures in laser powder bed fusion additive manufacturing," *Procedia CIRP,* vol. 45, pp. 131-134, 2016.

[193] L. Pagani, A. Townsend, W. Zeng, S. Lou, L. Blunt, X. Q. Jiang and P. J. Scott, "Towards a new definition of areal surface texture parameters on freeform surface: Re-entrant features and functional parameters," *Measurement: Journal of the International Measurement Confederation,* vol. 141, pp. 442-459, 2019.

[194] D. Buchbinder, W. Meiners, N. Pirch, K. Wissenbach and J. Schrage, "Investigation on reducing distortion by preheating during manufacture of aluminum components using selective laser melting," *Journal of Laser Applications,* vol. 26, no. 1, pp. 012004, 2014.

[195] ASTM B962-08, *Standard Test Methods for Density of Compacted or Sintered Powder Metallurgy (PM) Products Using Archimedes' Principle,* ASTM International, West Conshohocken, PA, USA, 2008.

[196] ASTM E92-17, *Standard Test Methods for Vickers Hardness and Knoop Hardness of Metallic Materials,* ASTM International, West Conshohocken, PA, USA, 2017.

[197] "CT PowderRange 316L F," Carpenter Additive, 2019.

[198] D. Riabov and S. Bengtsson, "Factors affecting printability of 316L powders using the DMLS process," *World Congress on Powder Metallurgy,* pp. 1-12, 2018.

[199] B. Liu, R. Wildman, C. Tuck, I. Ashcroft and R. Hague, "Investigation the effect of particle size distribution on processing parameters optimisation in selective laser melting process," *International Solid Freeform Fabrication Symposium,* 2011.

[200] J. Kruth, M. Badrossamay, E. Yasa, J. Deckers, L. Thijs and J. Van Humbeeck, "Part and material properties in selective laser melting of metals," *Proceedings of the 16th International Symposium on Electromachining,* pp. 3-14, 2010.

[201] A. B. Spierings and G. Levy, "Comparison of density of stainless steel 316L parts produced with selective laser melting using different powder grades," *International Solid Freeform Fabrication Symposium,* 2009.

[202] C. Kamath, B. El-dasher, G. F. Gallegos, W. E. King and A. Sisto, "Density of additively-manufactured, 316L SS parts using laser powder-bed fusion at powers up to 400 W," *International Journal of Advanced Manufacturing Technology,* vol. 74, no. 1-4, pp. 65-78, 2014.

[203] B. Whip, L. Sheridan and J. Gockel, "The effect of primary processing parameters on surface roughness in laser powder bed additive manufacturing," *International Journal of Advanced Manufacturing Technology,* vol. 103, no. 9-12, pp. 4411-4422, 2019.

[204] J. C. Simmons, X. Chen, A. Azizi, M. A. Daeumer, P. Y. Zavalij, G. Zhou and S. N. Schiffres, "Influence of processing and microstructure on the local and bulk thermal conductivity of selective laser melted 316L stainless steel," *Additive Manufacturing,* vol. 32, no. C, pp. 100996, 2020.

[205] "Leverage the full potential of a heat exchanger with additive manufacturing," *Electro Optical Systems GmbH,* 2018.

[206] "Basic training EOS M100," Electro Optical Systems GmbH,

[207] "Getting started with metal additive manufacturing," *Proto Labs,* 2022.[Online]. Available: protolabs.com/resources/design-tips/how-to-design-and-manufacture-metal-3d-printed-parts/

[208] C. T. Wang, "Process parameter optimization for additively manufactured stainless steel 316L parts by selective electron beam melting," *Pro-AM,* 2018.

[209] ASTM E112-10, *Standard Test Methods for Determining Average Grain Size,* ASTM International, West Conshohocken, PA, USA, 2010.

[210] V. Ganesan, M. D. Mathew and K. B. Sankara Rao, "Influence of nitrogen on tensile properties of 316LN SS," *Materials Science and Technology,* vol. 25, no. 5, pp. 614-618, 2009.

[211] E. H. Valente, V. K. Nadimpalli, S. A. Andersen, D. B. Pedersen, T. L. Christiansen and M. A. Somers, "Influence of atmosphere on microstructure and nitrogen content in AISI 316L fabricated by laser-based powder bed fusion," *Euspen's 19th International Conference & Exhibition,* pp. 244-247, 2019.

[212] M. Thomas, G. J. Baxter and I. Todd, "Normalised model-based processing diagrams for additive layer manufacture of engineering alloys," *Acta Materialia,* vol. 108, pp. 26-35, 2016.

[213] M. Tang and P. C. Pistorius, "Oxides, porosity and fatigue performance of AlSi10Mg parts produced by selective laser melting," *International Journal of Fatigue,* vol. 94, pp. 192-201, 2017.

[214] G. Miranda, S. Faria, F. Bartolomeu, E. Pinto, S. Madeira, A. Mateus, P. Carreira, N. Alves, F. S. Silva and O. Carvalho, "Predictive models for physical and mechanical properties of 316L stainless steel produced by selective laser melting," *Materials Science & Engineering: A,* vol. 657, pp. 43-56, 2016.

[215] A. Charles, A. Elkaseer, T. Mueller, L. Thijs, V. Hagenmeyer and S. Scholz, "Effect of process parameters on dimensional accuracy of down-facing surfaces in selective laser melting of Ti6Al4V," *Additive Manufacturing,* vol. 10, no. 250, pp. 850, 2018.

[216] A. Charles, A. Elkaseer, L. Thijs, V. Hagenmeyer and S. Scholz, "Prediction of dimensional error in down-facing surfaces for laser powder bed fusion parts," *Proceedings of the World Congress on Micro and Nano Manufacturing,* pp. 10-12, 2019.

[217] A. Charles, A. Elkaseer, L. Thijs and S. G. Scholz, "Dimensional errors due to overhanging features in laser powder bed fusion parts made of ti-6Al-4V," *Applied Sciences,* vol. 10, no. 7, 2020.

[218] A. Charles, A. Elkaseer, U. Paggi, L. Thijs, V. Hagenmeyer and S. Scholz, "Down-facing surfaces in laser powder bed fusion of Ti6Al4V: Effect of dross formation on dimensional accuracy and surface texture," *Additive Manufacturing,* vol. 46, 2021.

[219] A. Simchi, "Direct laser sintering of metal powders: Mechanism, kinetics and microstructural features," *Materials Science & Engineering: A,* vol. 428, no. 1, pp. 148-158, 2006.

[220] M. Letenneur, A. Kreitcberg and V. Brailovski, "Optimization of laser powder bed fusion processing using a combination of melt pool modeling and design of experiment approaches: Density control," *Journal of Manufacturing and Materials Processing,* vol. 3, no. 1, pp. 21, 2019.

[221] M. Letenneur, A. Kreitcberg and V. Brailovski, "The average grain size and grain aspect ratio in metal laser powder bed fusion: Modeling and experiment," *Journal of Manufacturing and Materials Processing,* vol. 4, no. 1, pp. 25, 2020.

[222] A. Adeyemi, E. T. Akinlabi and R. M. Mahamood, "Powder bed based laser additive manufacturing process of stainless steel: A review," *Materials Today: Proceedings,* vol. 5, no. 9, pp. 18510-18517, 2018.

[223] U. Scheithauer, R. Kordaß, K. Noack, M. F. Eichenauer, M. Hartmann, J. Abel, G. Ganzer and D. Lordick, "Potentials and challenges of additive manufacturing technologies for heat exchanger," *Advances in heat exchangers,* IntechOpen, pp. 61, 2018.

[224] B. Bansal and X. D. Chen, "A critical review of milk fouling in heat exchangers," *Comprehensive Reviews in Food Science and Food Safety,* vol. 5, no. 2, pp. 27-33, 2006.

[225] S. Chekurov, J. Kajaste, K. Saari, H. Kauranne, M. Pietola and J. Partanen, "Additively manufactured high-performance counterflow heat exchanger," *Progress in Additive Manufacturing,* vol. 4, no. 1, pp. 55-61, 2018.

[226] E. Sadeghinezhad, S. N. Kazi, M. Dahari, M. R. Safaei, R. Sadri and A. Badarudin, "A comprehensive review of milk fouling on heated surfaces," *Critical Reviews in Food Science and Nutrition,* vol. 55, no. 12, pp. 1724-1743, 2015.

[227] J. R. McDonough, "A perspective on the current and future roles of additive manufacturing in process engineering, with an emphasis on heat transfer," *Thermal Science and Engineering Progress,* vol. 19, 2020.

[228] D. A. Bartlett, "The fundamentals of heat exchangers," *The Industrial Physicist,* vol. 2, no. 4, pp. 18-21, 1996.

[229] A. Vlahinos and R. O'Hara, "Unlocking advanced heat exchanger design and simulation with nTop platform and ANSYS CFX," nTopology Inc., 2020.

[230] C. K. Stimpson, J. C. Snyder, K. A. Thole and D. Mongillo, "Roughness effects on flow and heat transfer for additively manufactured channels," *Journal of Turbomachinery,* vol. 138, no. 5, 2016.

[231] F. Ascione, A. Conrozier, A. Sakly, P. Planquart, J. M. Hugo and D. Laboureur, "Aerothermal characterization of a compact heat exchanger element by additive manufacturing," *Proceedings of the AerospaceEurope Conference,* pp. 25-28, 2020.

[232] Kaur and Singh, "State-of-the-art in heat exchanger additive manufacturing," *International Journal of Heat and Mass Transfer,* vol. 178, pp. 121600, 2021.

[233] J. C. Snyder and K. A. Thole, "Tailoring surface roughness using additive manufacturing to improve internal cooling," *Journal of Turbomachinery,* vol. 142, no. 7, 2020.

[234] B. Thonon, "Fouling of heat transfer equipment in the food industry," *Handbook of Water and Energy Management in Food Processing,* Elsevier, pp. 570-584, 2008.

[235] Y. Zhu, L. Zhou, S. Wang, C. Zhang, C. Zhao, L. Zhang and H. Yang, "On friction factor of fluid channels fabricated using selective laser melting," *Virtual and Physical Prototyping,* vol. 15, no. 4, 2020.

[236] T. Parent-Simard, A. Landry-Blais, P. K. Dubois, M. Picard and V. Brailovski, "Effect of surface roughness induced by laser powder bed fusion additive manufacturing in a mini-channel heat exchanger," *Proceedings of ASME Turbo Expo: Turbomachinery Technical Conference and Exposition,* 2019.

[237] R. P. P. da Silva, M. V. V. Mortean, K. V. de Paiva, L. E. Beckedorff, J. L. G. Oliveira, F. G. Brandão, A. S. Monteiro, C. S. Carvalho, H. R. Oliveira, D. G. Borges and V. L. Chastinet, "Thermal and hydrodynamic analysis of a compact heat exchanger produced by additive manufacturing," *Applied Thermal Engineering,* vol. 193, 2021.

[238] O. T. Ibrahim, J. G. Monroe, S. M. Thompson, N. Shamsaei, H. Bilheux, A. Elwany and L. Bian, "An investigation of a multi-layered oscillating heat pipe additively manufactured from ti-6Al-4V powder," *International Journal of Heat and Mass Transfer,* vol. 108, pp. 1036-1047, 2017.

[239] K. Navickaitė, A. Mocerino, L. Cattani, F. Bozzoli, C. Bahl, K. Liltrop, X. Zhang and K. Engelbrecht, "Enhanced heat transfer in tubes based on vascular heat exchangers in fish: Experimental investigation," *International Journal of Heat and Mass Transfer,* vol. 137, pp. 192-203, 2019.

[240] W. D. Gerstler and D. Erno, "Introduction of an additively manufactured multi-furcating heat exchanger," *16th IEEE Intersociety Conference on Thermal and Thermomechanical Phenomena in Electronic Systems,* pp. 624-633, 2017.

[241] S. Yu, J. Sun and J. Bai, "Investigation of functionally graded TPMS structures fabricated by additive manufacturing," *Materials & Design,* vol. 182, 2019.

[242] E. Yang, M. Leary, B. Lozanovski, D. Downing, M. Mazur, A. Sarker, A. Khorasani, A. Jones, T. Maconachie, S. Bateman, M. Easton, M. Qian, P. Choong and M. Brandt, "Effect of geometry on the mechanical properties of ti-6Al-4V gyroid structures fabricated via SLM: A numerical study," *Materials & Design,* vol. 184, 2019.

[243] W. Li, G. Yu and Z. Yu, "Bioinspired heat exchangers based on triply periodic minimal surfaces for supercritical CO2 cycles," *Applied Thermal Engineering,* vol. 179, 2020.

[244] A. H. Schoen, "Infinite periodic minimal surfaces without self-intersections," NASA, 1970.

[245] H. Peng, F. Gao and W. Hu, "Design, modeling and characterization on triply periodic minimal surface heat exchangers with additive manufacturing," *International Solid Freeform Fabrication Symposium*, 2019.

[246] T. Femmer, A. J. C. Kuehne and M. Wessling, "Estimation of the structure dependent performance of 3-D rapid prototyped membranes," *Chemical Engineering Journal*, vol. 273, pp. 438-445, 2015.

[247] J. Kim and D. Yoo, "3D printed compact heat exchangers with mathematically defined core structures," *Journal of Computational Design and Engineering*, vol. 7, no. 4, pp. 527-550, 2020.

[248] S. Singh Rathore, B. Mehta, P. Kumar and M. Asfer, "Flow characterization in triply-periodic-minimal-surface (TPMS) based porous geometries: Part 1 - hydrodynamics," *arXiv E-Prints*, 2022.

[249] T. Dixit, E. Al-Hajri, M. C. Paul, P. Nithiarasu and S. Kumar, "High performance, microarchitected, compact heat exchanger enabled by 3D printing," *Applied Thermal Engineering*, vol. 210, 2022.

[250] O. Al-ketan and R. K. Abu Al-rub, "MSLattice: A free software for generating uniform and graded lattices based on triply periodic minimal surfaces," *Material Design & Processing Communications*, vol. 3, no. 6, 2020.

[251] F. Liu, Z. Mao, P. Zhang, D. Z. Zhang, J. Jiang and Z. Ma, "Functionally graded porous scaffolds in multiple patterns: New design method, physical and mechanical properties," *Materials & Design*, vol. 160, pp. 849-860, 2018.

[252] ISO 16610-21:2011, *Geometrical product specifications (GPS) — Filtration — Part 21: Linear profile filters: Gaussian filters*, International Organization for Standardization, 2011.

[253] ISO 16610-28:2010, *Geometrical product specifications (GPS) — Filtration — Part 28: Profile filters: End effects*, International Organization for Standardization, 2010.

[254] T. Adams, C. Grant and H. Watson, "A simple algorithm to relate measured surface roughness to equivalent sand-grain roughness," *International Journal of Mechanical Engineering and Mechatronics*, vol. 1, no. 1, 2012.

[255] "Sulis lattice - user-friendly lattice generation software," *Gen3D*, 2022.[Online]. Available: gen3d.com/sulis-lattice/

[256] H. Villarraga-Gómez, C. M. Peitsch, A. Ramsey and S. T. Smith, "The role of computed tomography in additive manufacturing," *ASPE and Euspen Summer Topical Meeting: Advancing Precision in Additive Manufacturing,* vol. 69, pp. 201-209, 2018.

[257] J. J. Lifton, Y. Liu, Z. J. Tan, B. Mutiargo, X. Q. Goh and A. A. Malcolm, "Internal surface roughness measurement of metal additively manufactured samples via x-ray CT: The influence of surrounding material thickness," *Surface Topography Metrology and Properties,* vol. 9, no. 3, 2021.

[258] A. Townsend, L. Blunt and P. J. Bills, "Investigating the capability of microfocus x-ray computed tomography for areal surface analysis of additively manufactured parts," *American Society for Precision Engineering Summer Topical Meeting: Dimensional Accuracy and Surface Finish in Additive Manufacturing,* 2016.

[259] Y. Quinsat, J. B. Guyon and C. Lartigue, "Qualification of CT data for areal surface texture analysis," *International Journal of Advanced Manufacturing Technology,* vol. 100, no. 9-12, pp. 3025-3035, 2018.

[260] "Free float: The support-free printing revolution," *SLM Solutions,* 2021.[Online]. Available: freefloat.slm-solutions.com/

Appendix A: Supplementary Small Specimen Results

M100 40 µm Prints:

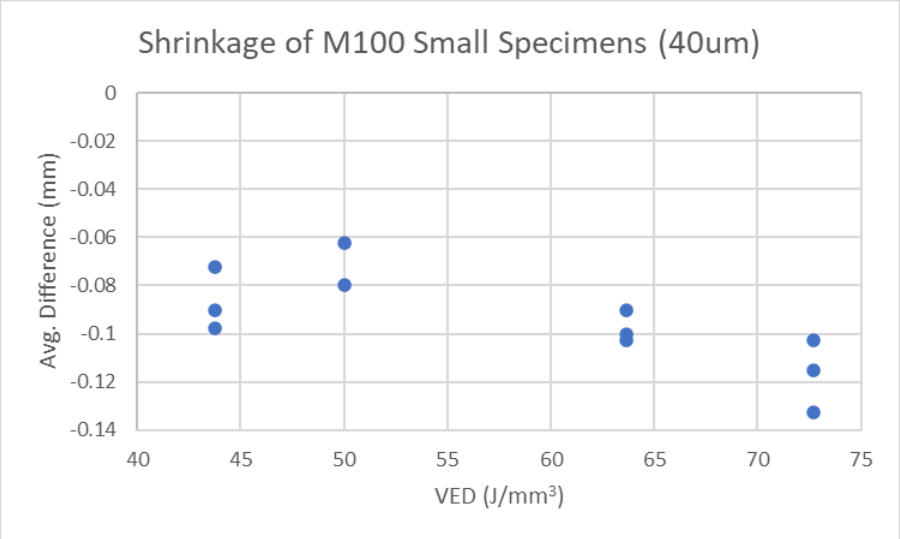

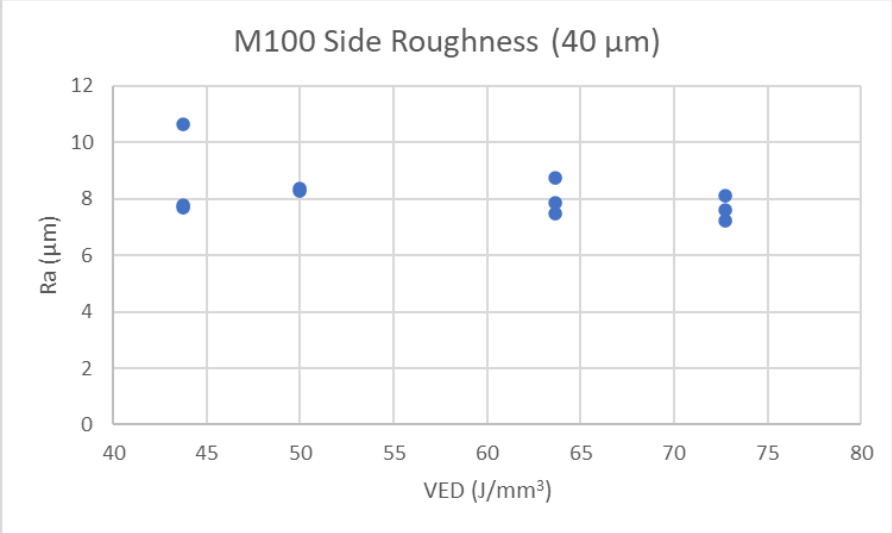

Small feature print success for 40-micron M100 small specimens

Feature (100um)	***M100 (40 µm)***											
	1a	***1b***	***1c***	***2b***	***2c***	***2d***	***3a***	***3c***	***3d***	***4a***	***4b***	***4c***
Rectangular boss	F	P	F	P	F	F	P	P	F	F	F	F
Rectangular walls	P	P	S	P	S	S	P	P	P	P	P	P
Rectangular hole	P	P	P	P	P	P	P	P	F	P	P	P
Rectangular spaces	P	P	P	P	P	P	P	P	S	S	S	P
Circular boss	S	F	S	S	S	S	S	S	S	S	S	S
Circular hole	F	F	F	F	F	F	F	F	F	F	F	F

M290 & M100 Rz Roughness:

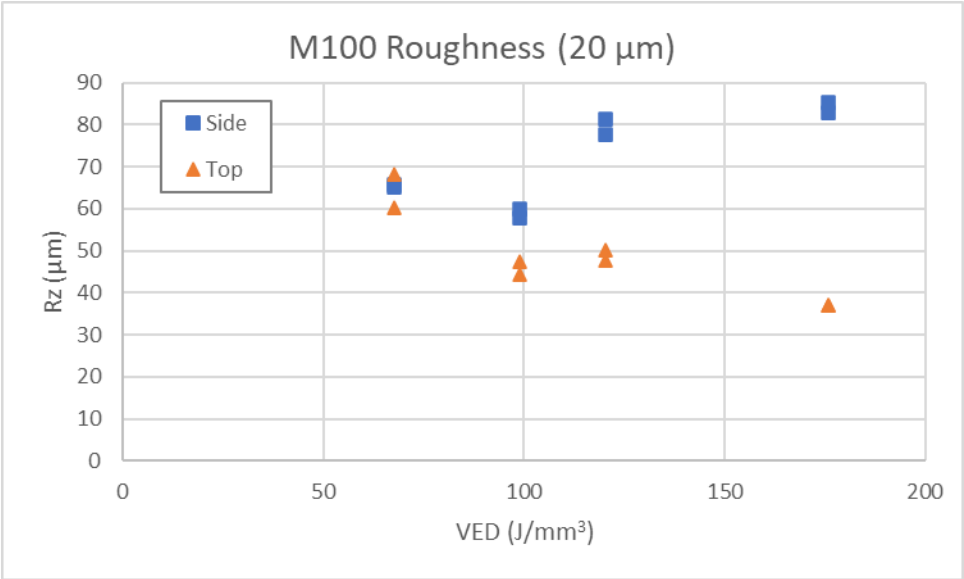

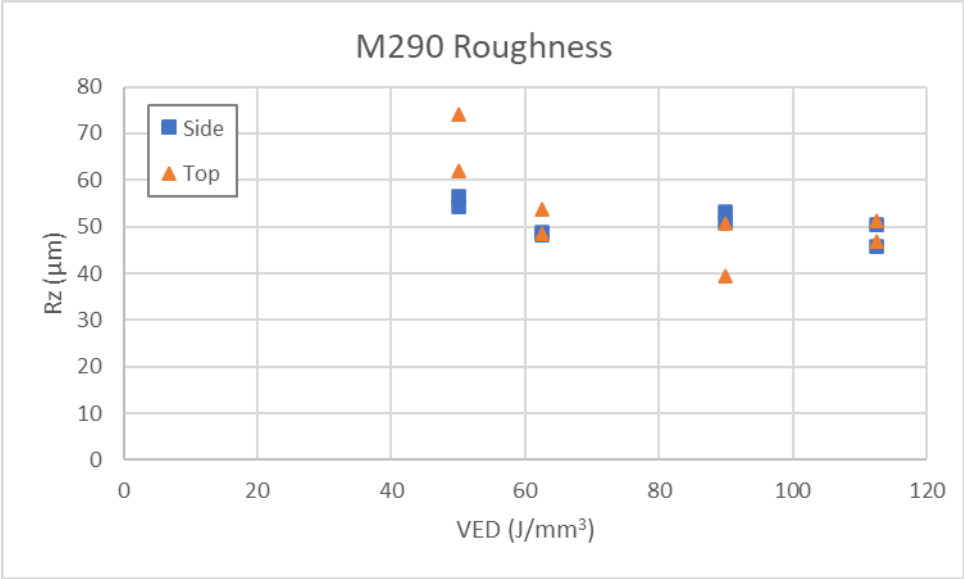

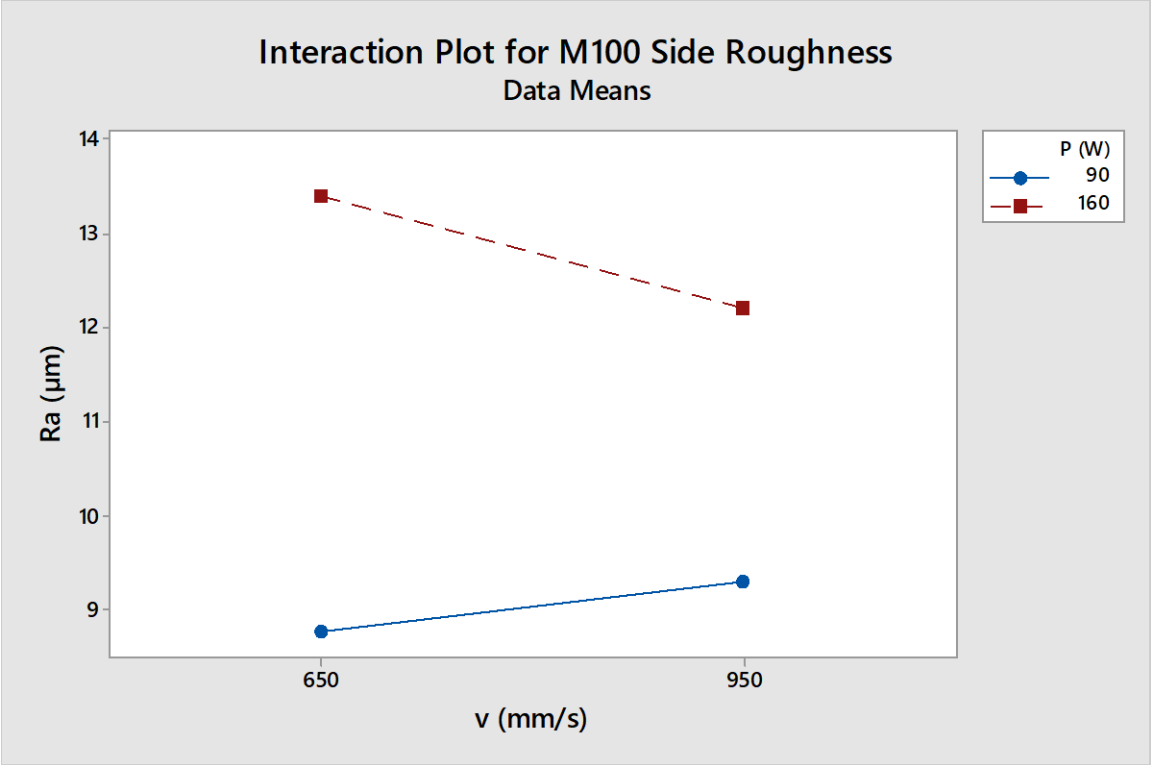
Interaction Plot for M100 Side Roughness
Data Means
Ra (µm)
14
13
12
11
10
9
650
950
v (mm/s)
P (W)
90
160

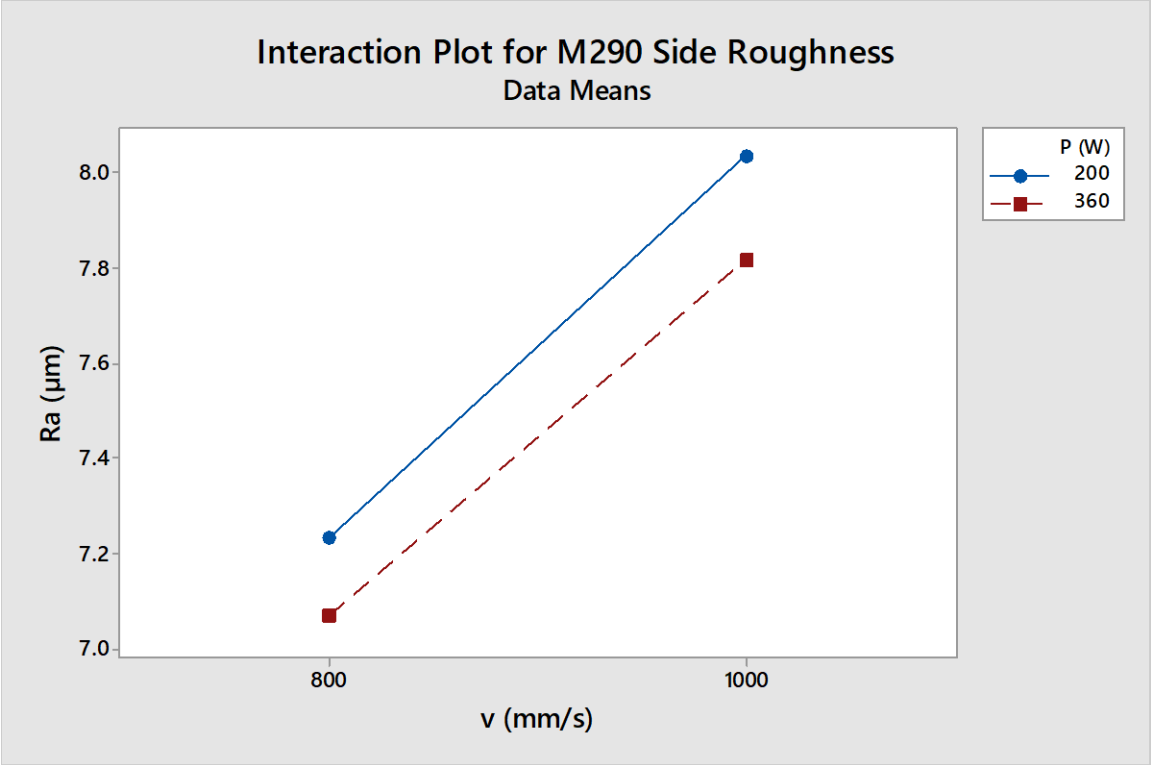
Interaction Plot for M290 Side Roughness
Data Means
Ra (µm)
8.0
7.8
7.6
7.4
7.2
7.0
800
1000
v (mm/s)
P (W)
200
360

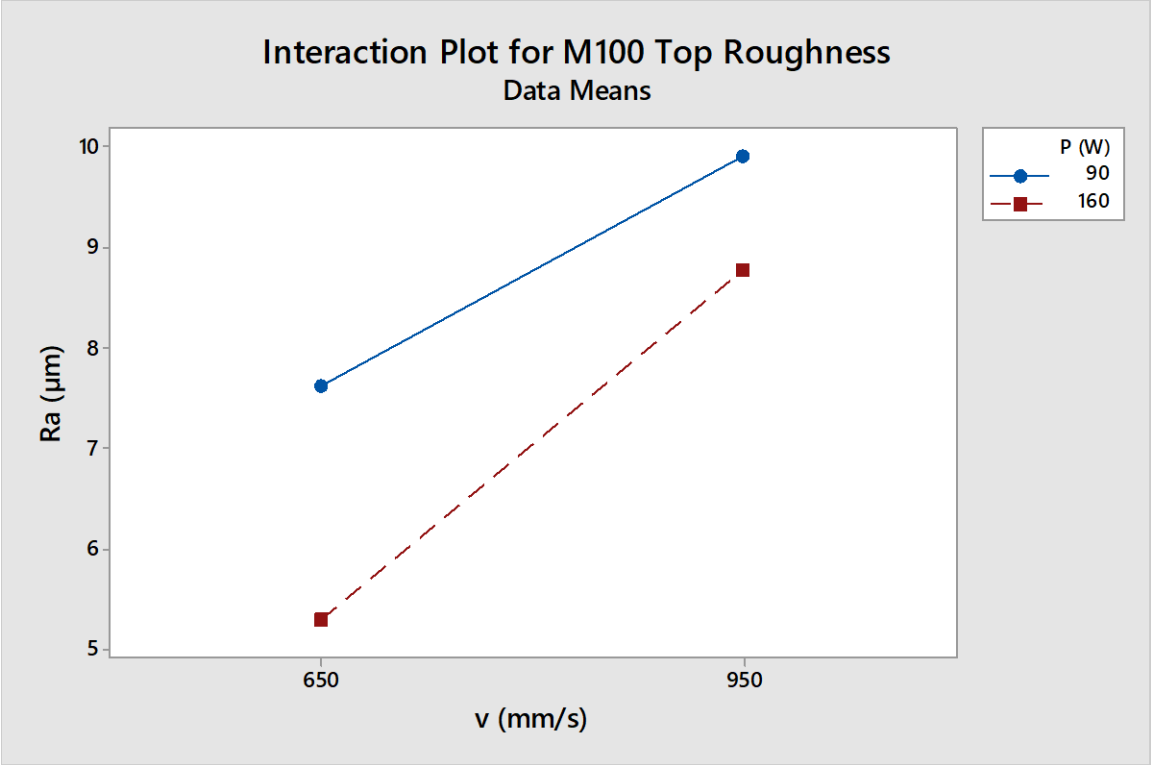
Interaction Plot for M100 Top Roughness
Data Means
Ra (µm)
10
9
8
7
6
5
650
950
v (mm/s)
P (W)
90
160

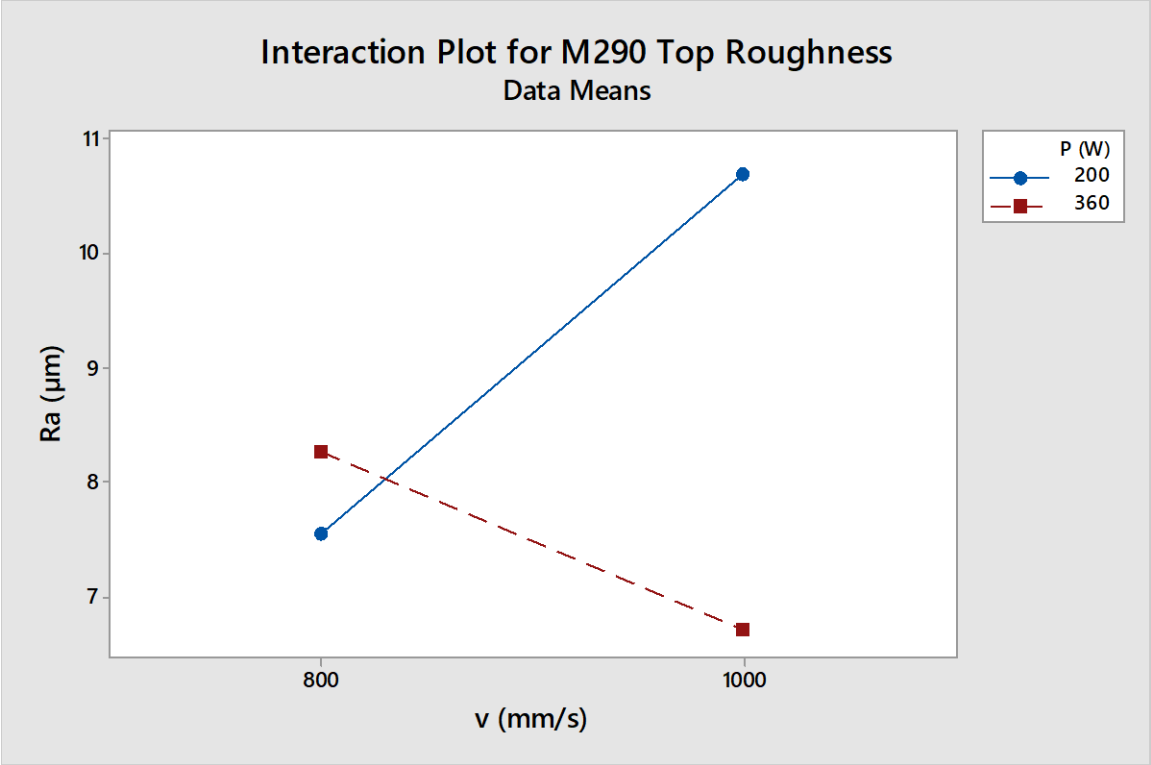
Interaction Plot for M290 Top Roughness
Data Means
Ra (µm)
11
10
9
8
7
800
1000
v (mm/s)
P (W)
200
360

M290 & M100 Shrinkage:

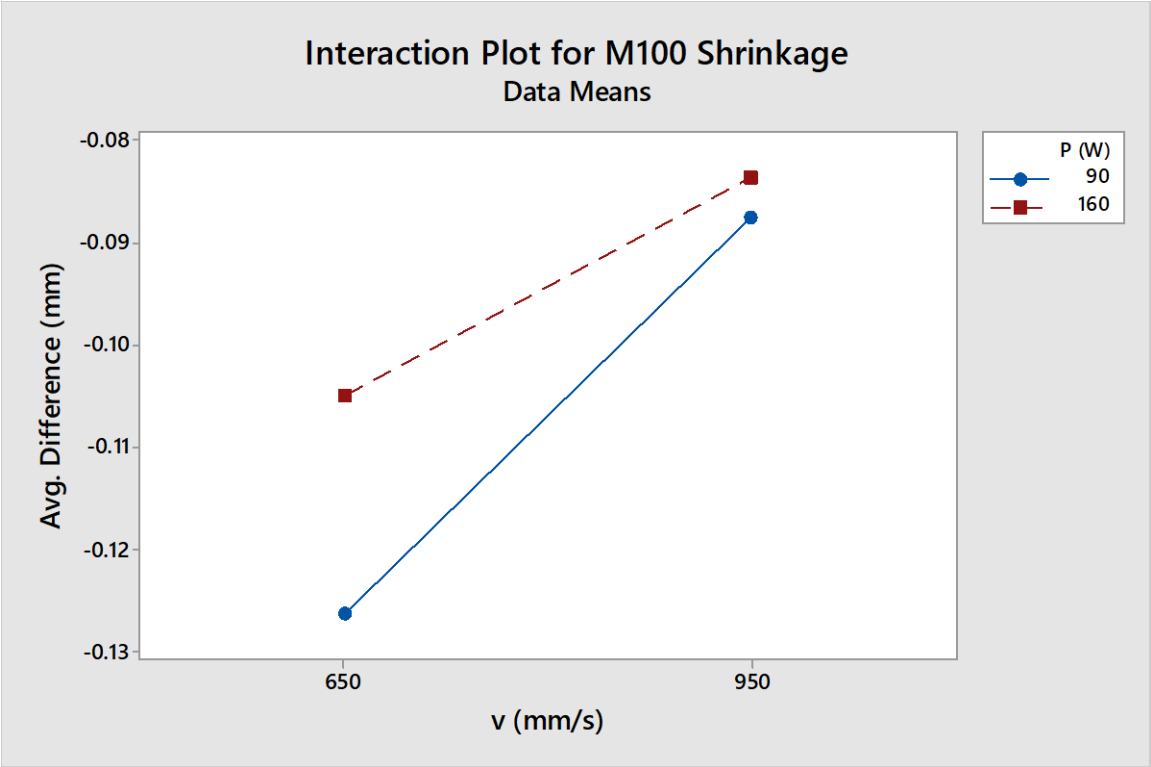

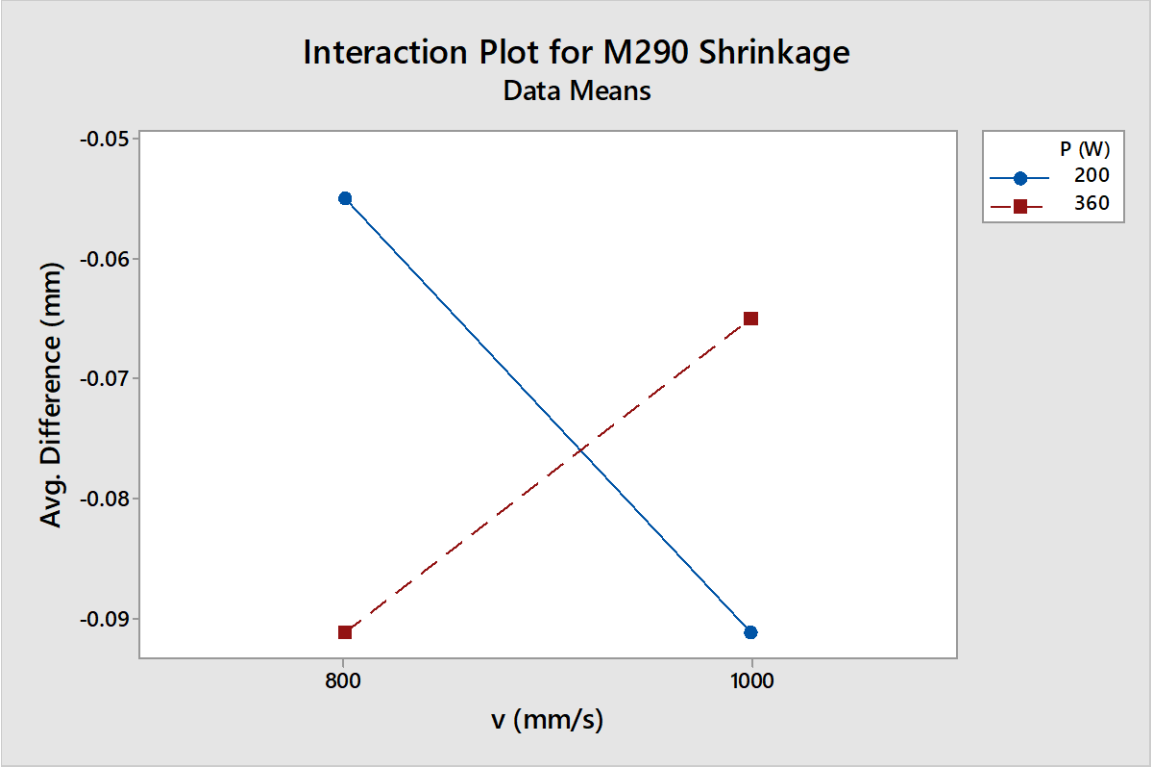

M290 & M100 Relative Density:

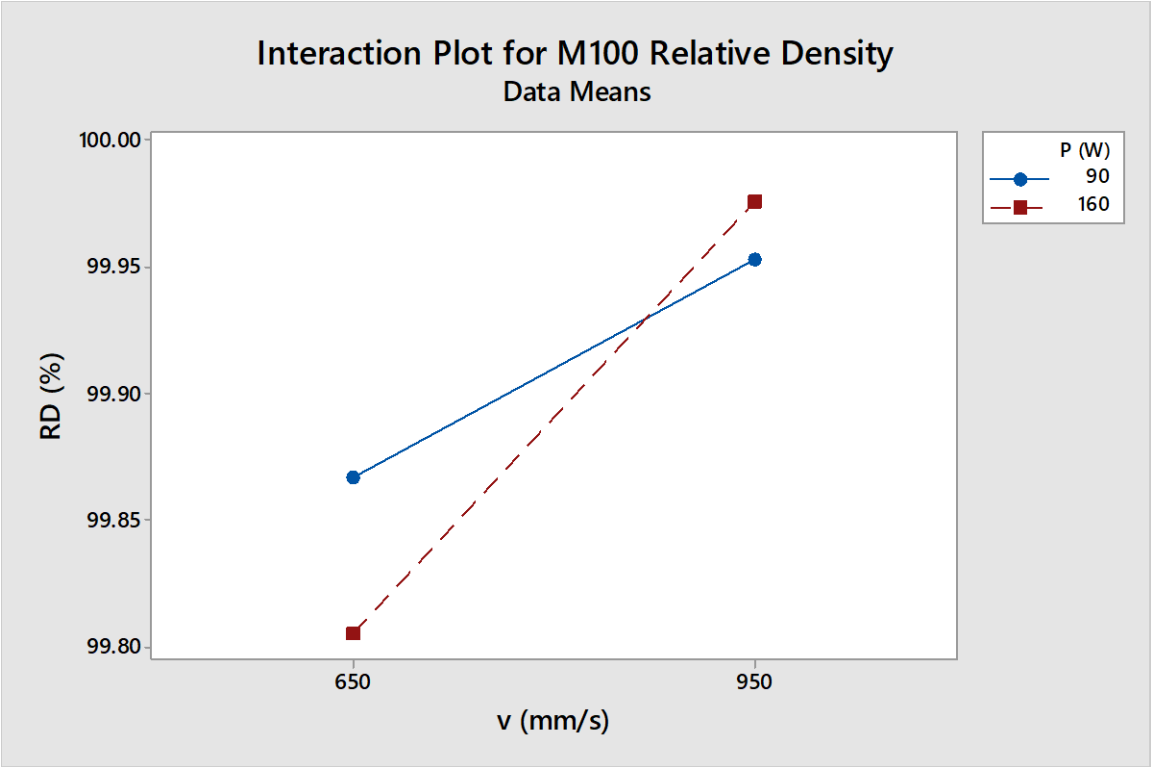

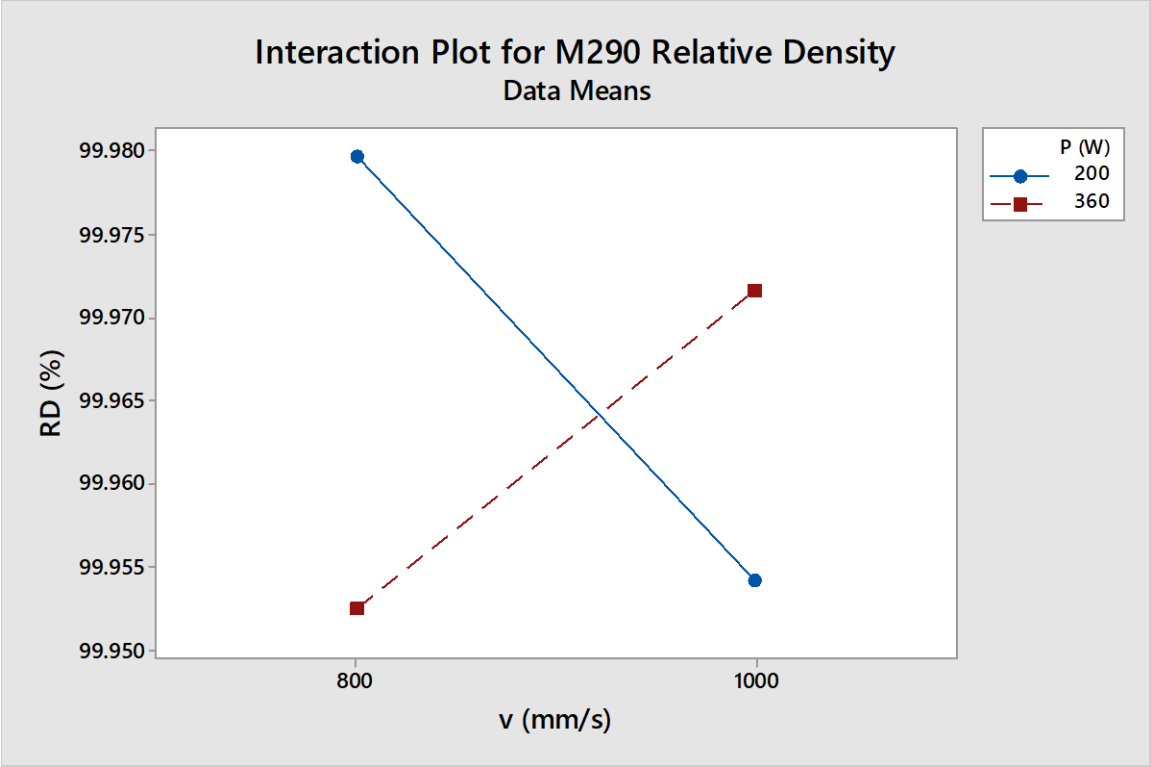

M290 & M100 Hardness:

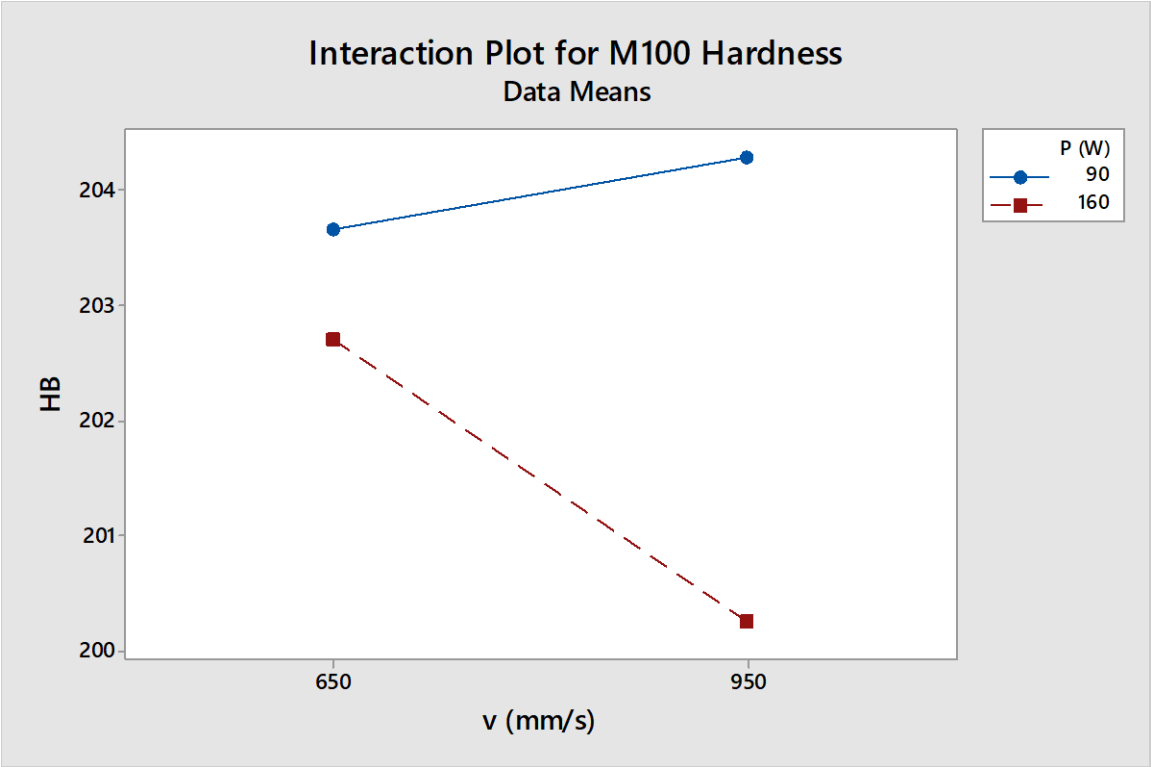

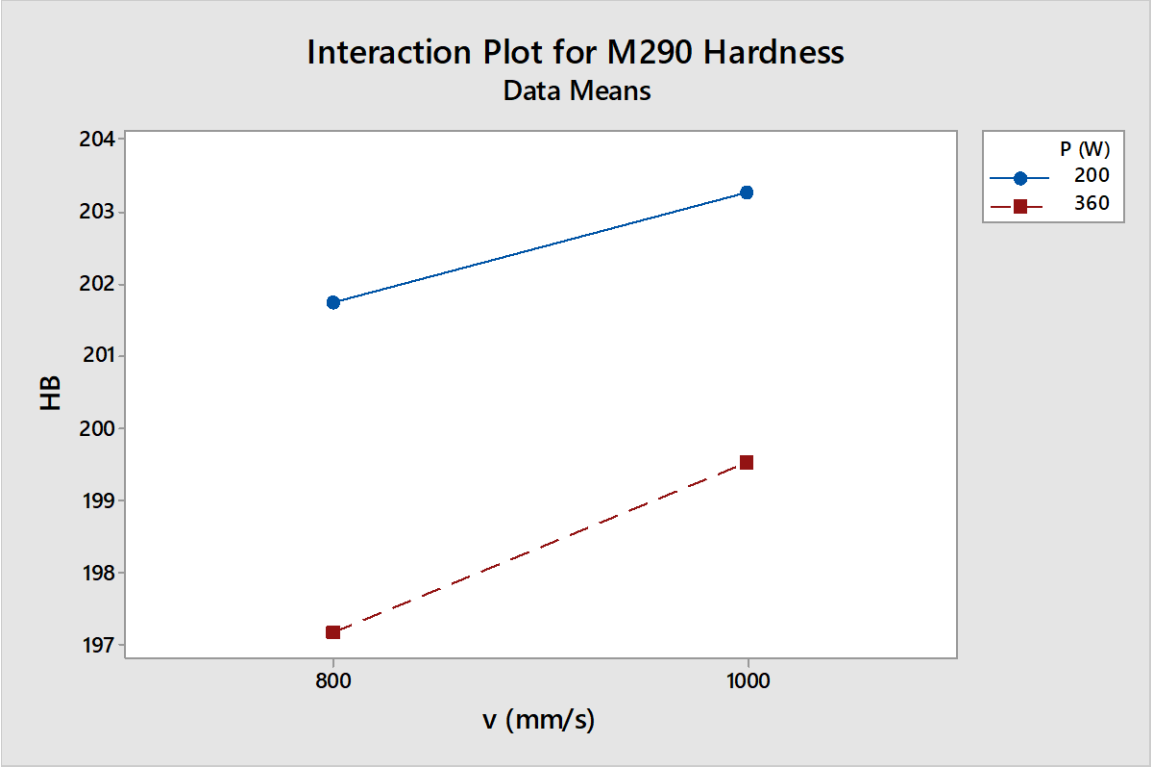

Appendix B: Microstructural OM Images

M100 Default Test Artifact

XZ plane (100X) ***XY plane (100X)***

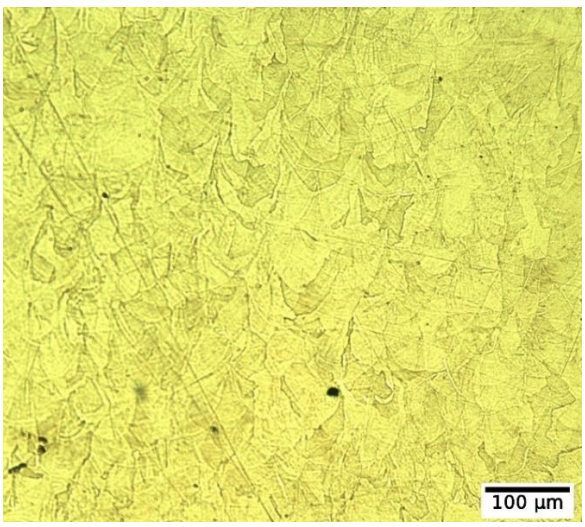

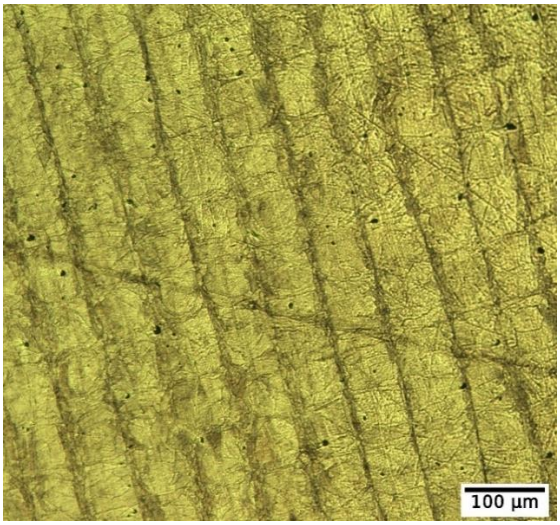

M290 Default Test Artifact

XZ plane (100X) ***XY plane (100X)***

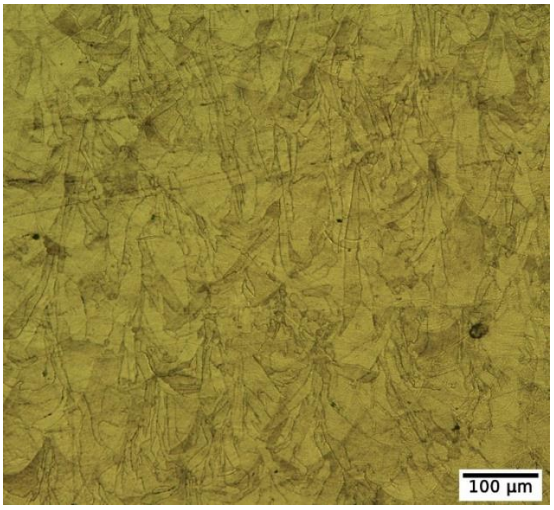

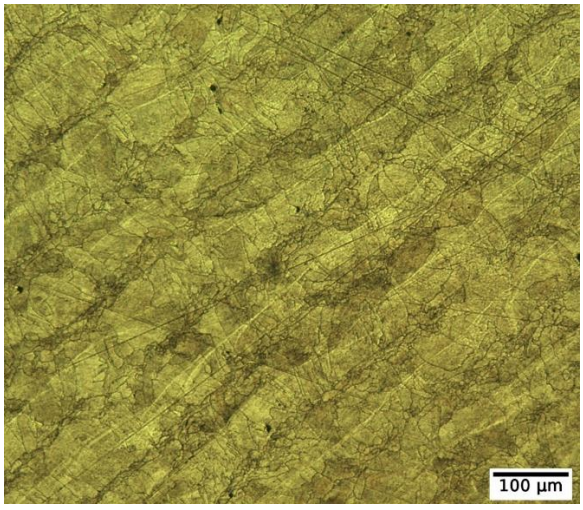

XZ plane (500X) ***XY plane (100X)***

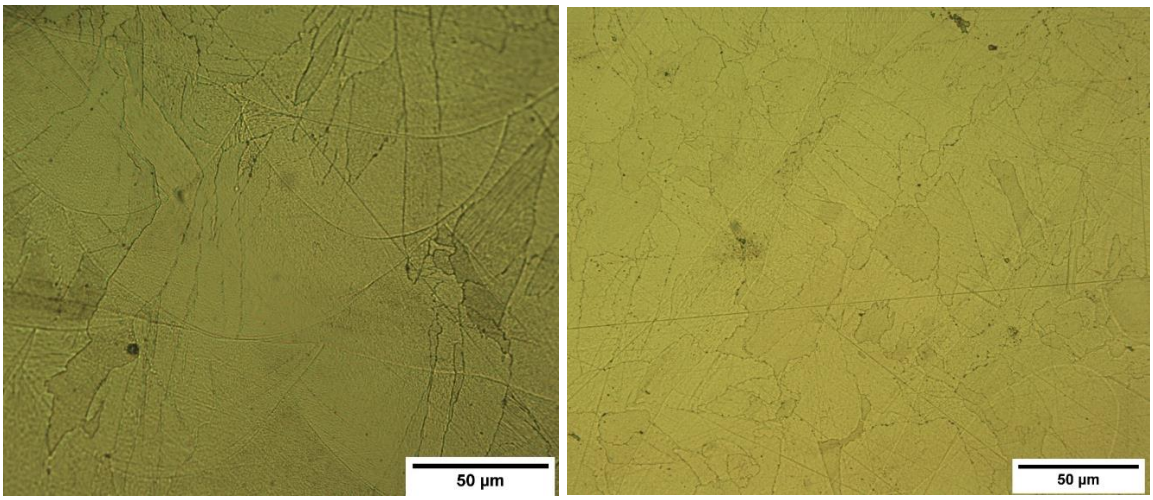

M100 Equalized VED Test Artifact

XZ plane (100X)

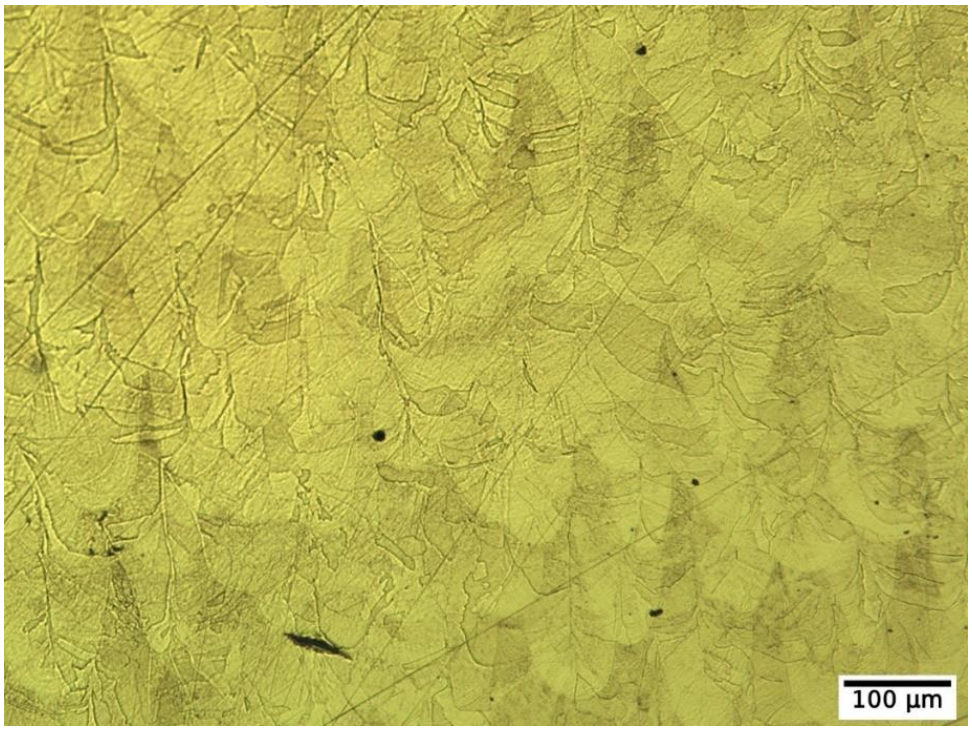

M290 'New' Exposure Parameter

XY plane (100X):

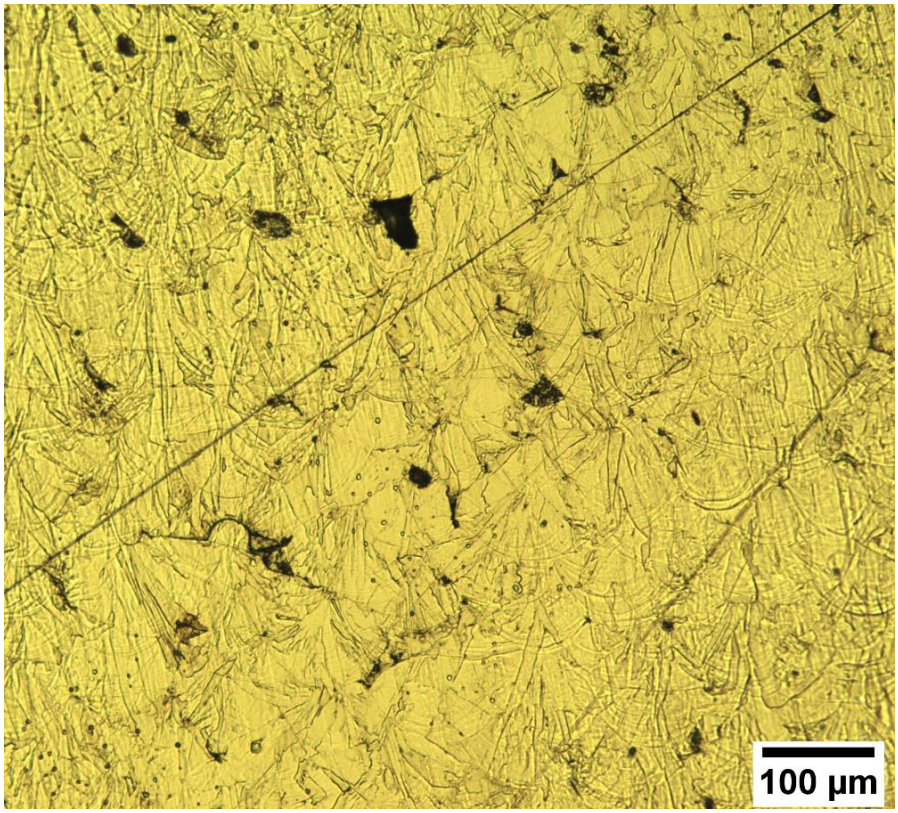

XY plane (500X)

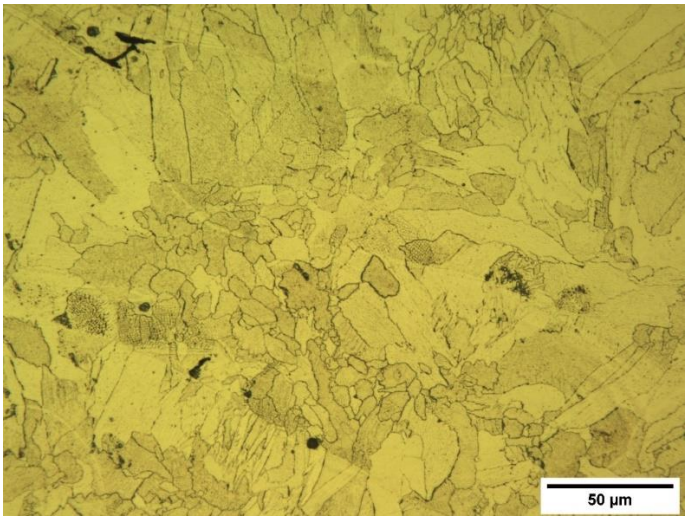

XZ plane (500X):

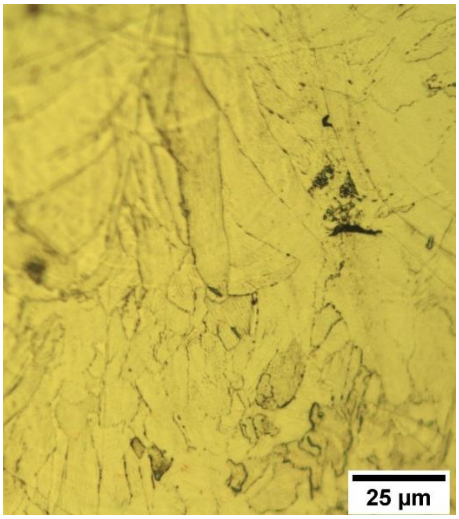

M100 Default Surface Roughness Print:

XY plane (100X)

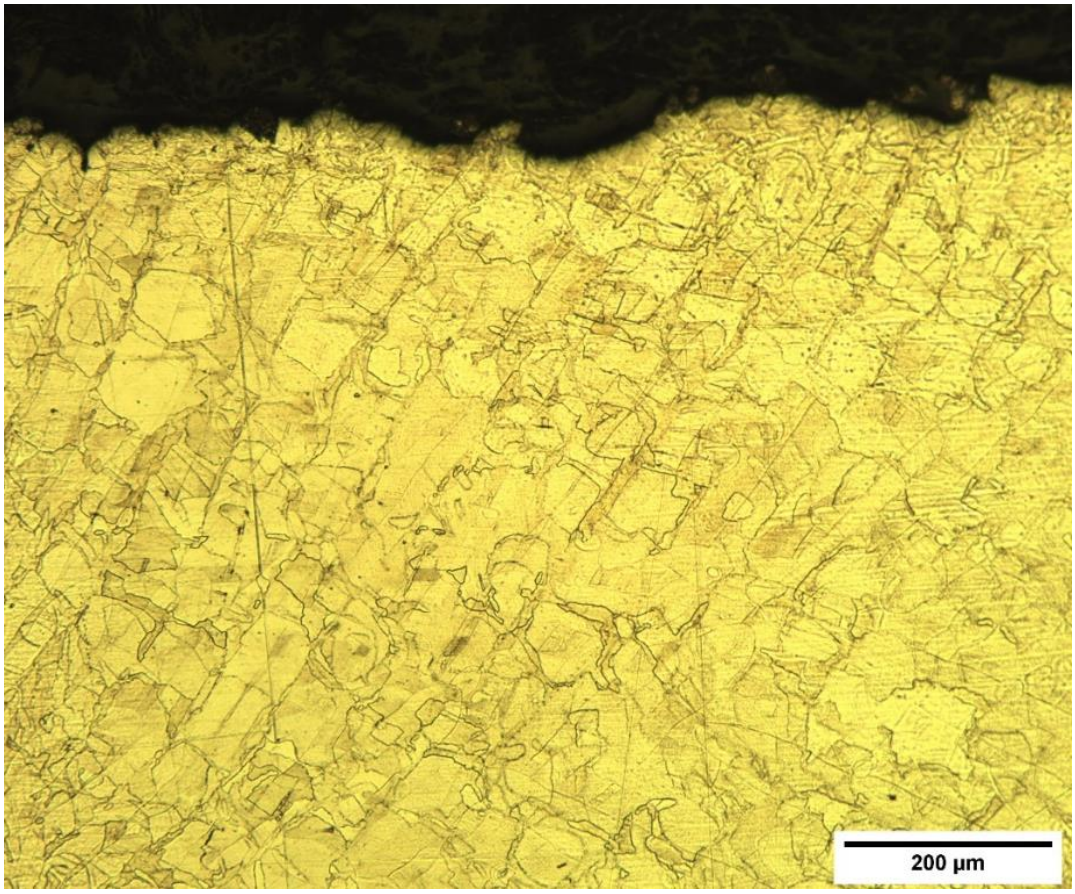

XY plane (500X)

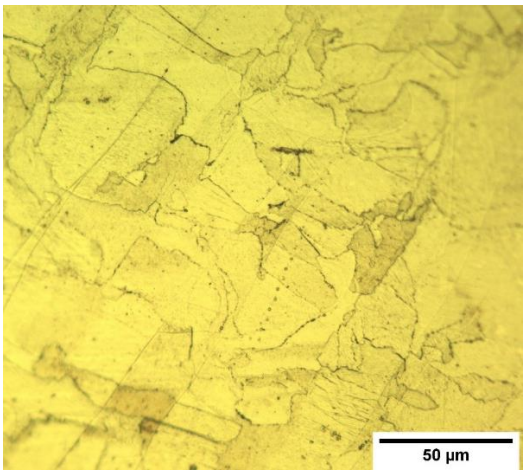

XZ plane (500X)

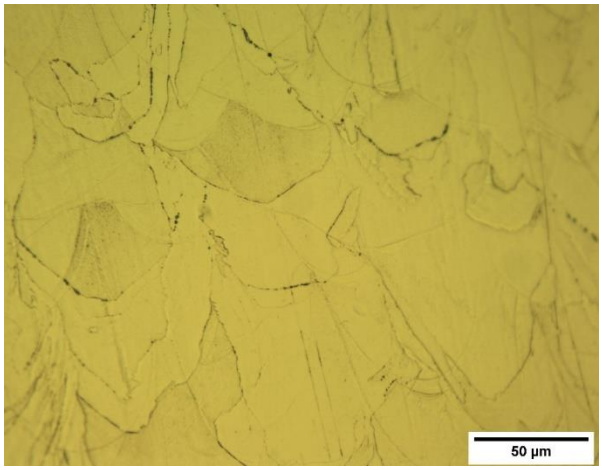

M100 Nitrogen Surface Roughness Print

XY plane (100X):

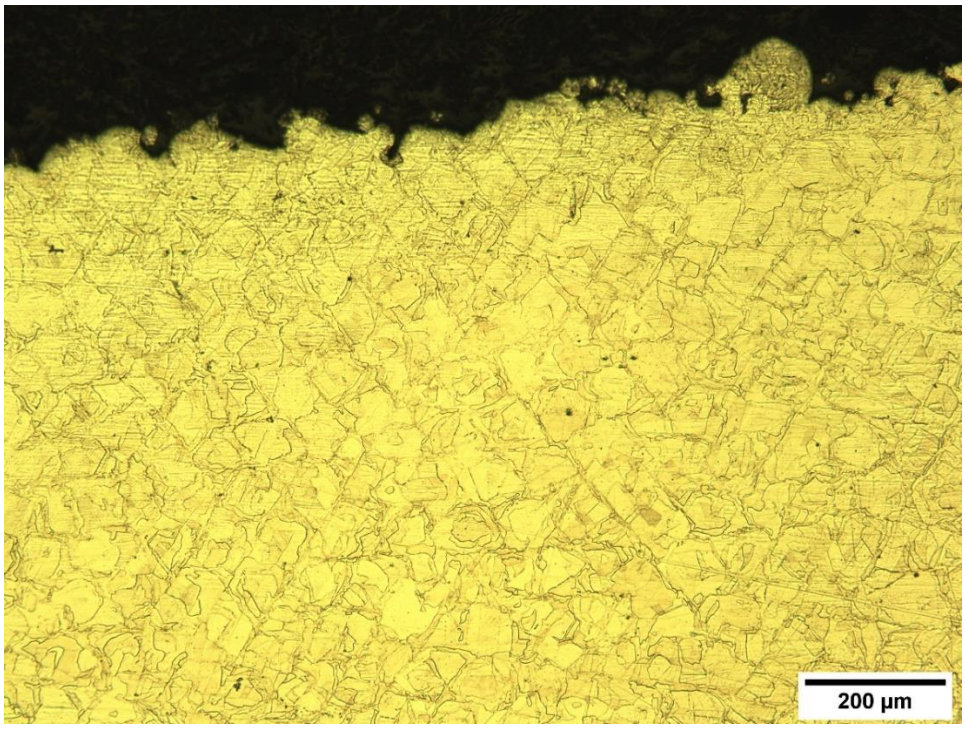

XY plane (500X)

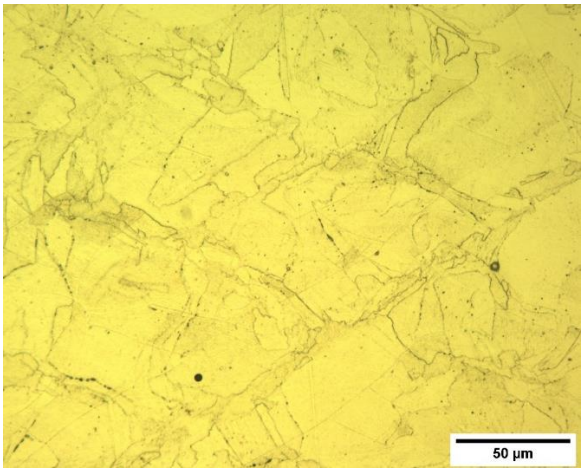

XZ plane (500X):

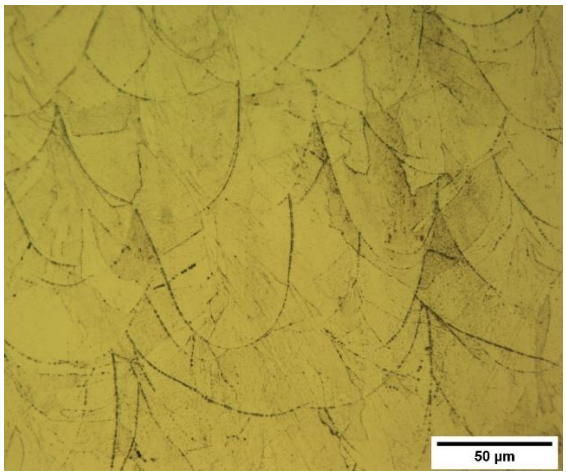

Appendix C: Main Effects and Residuals of Roughness DOE

30° Downskin Ra:

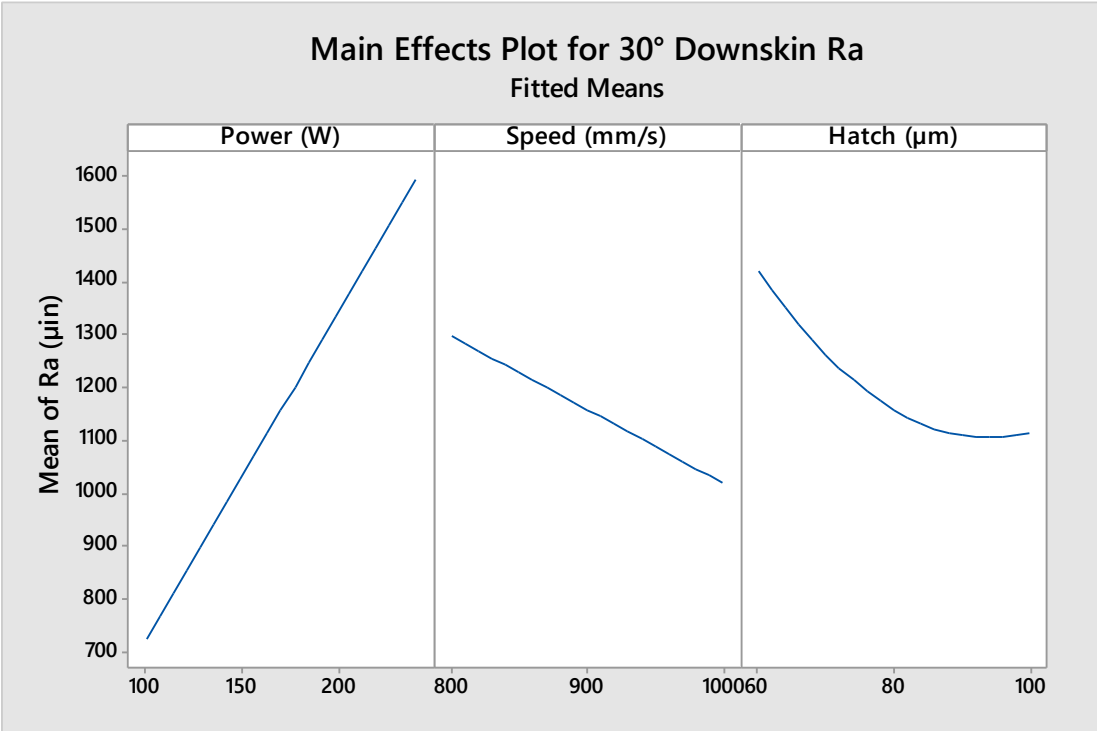

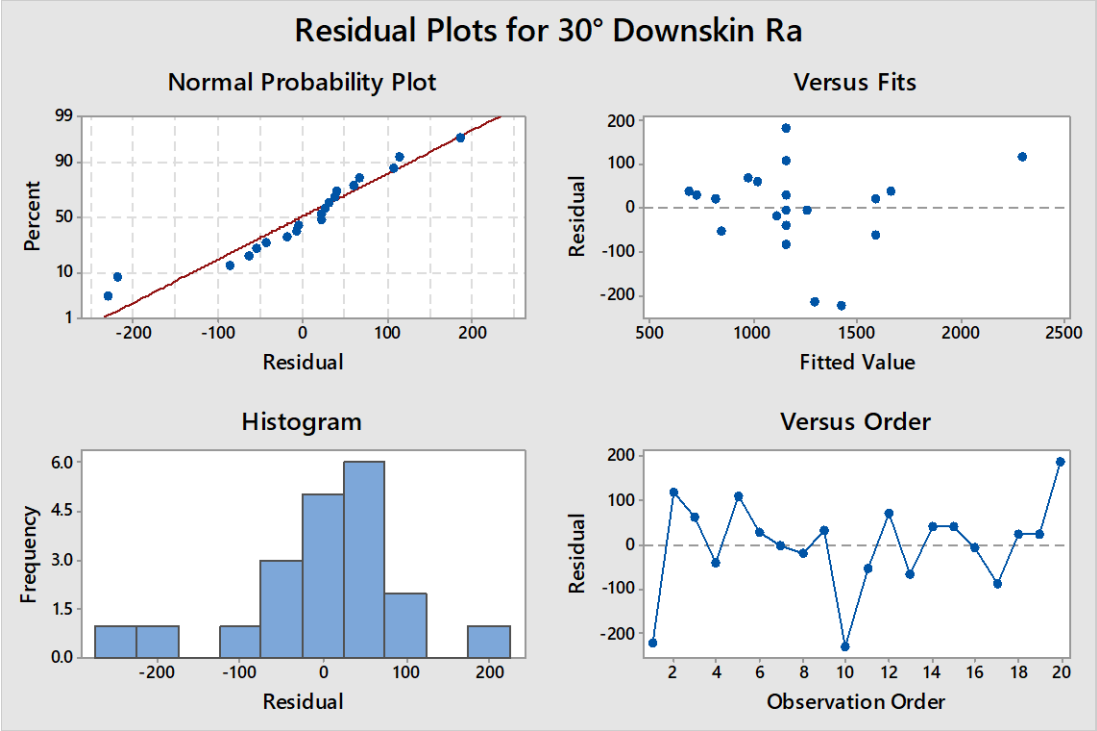

Average Upskin Ra:

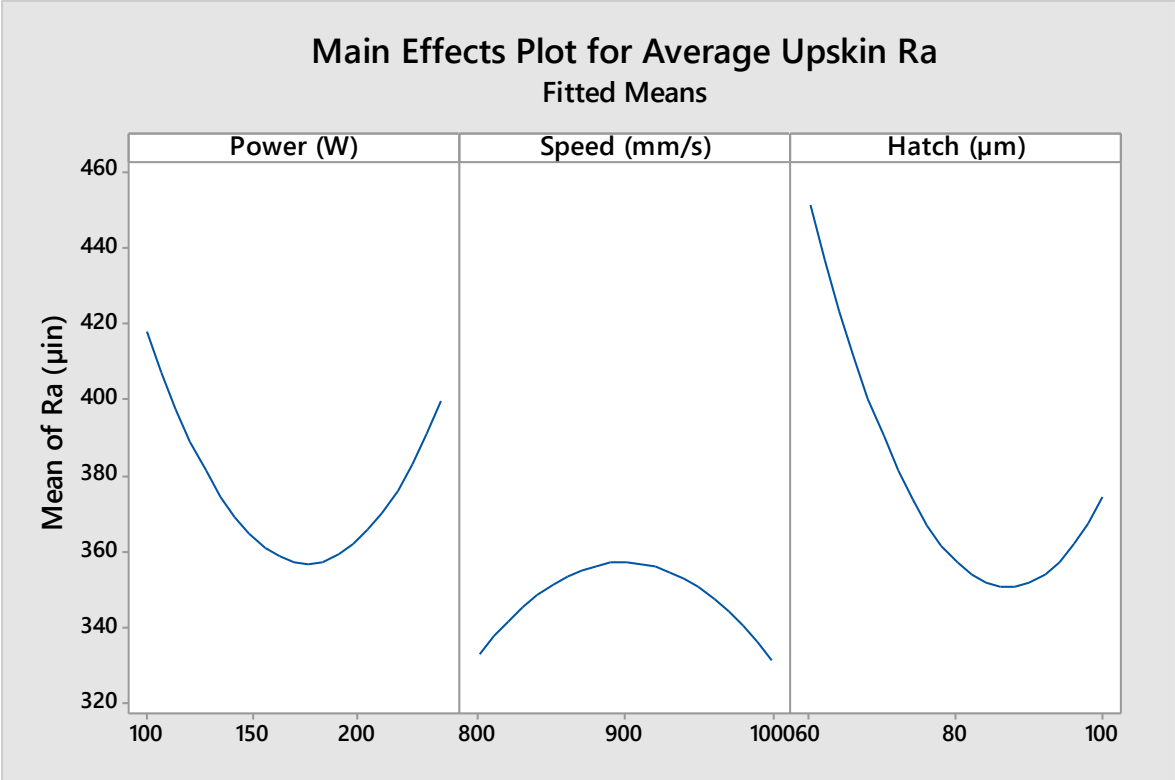

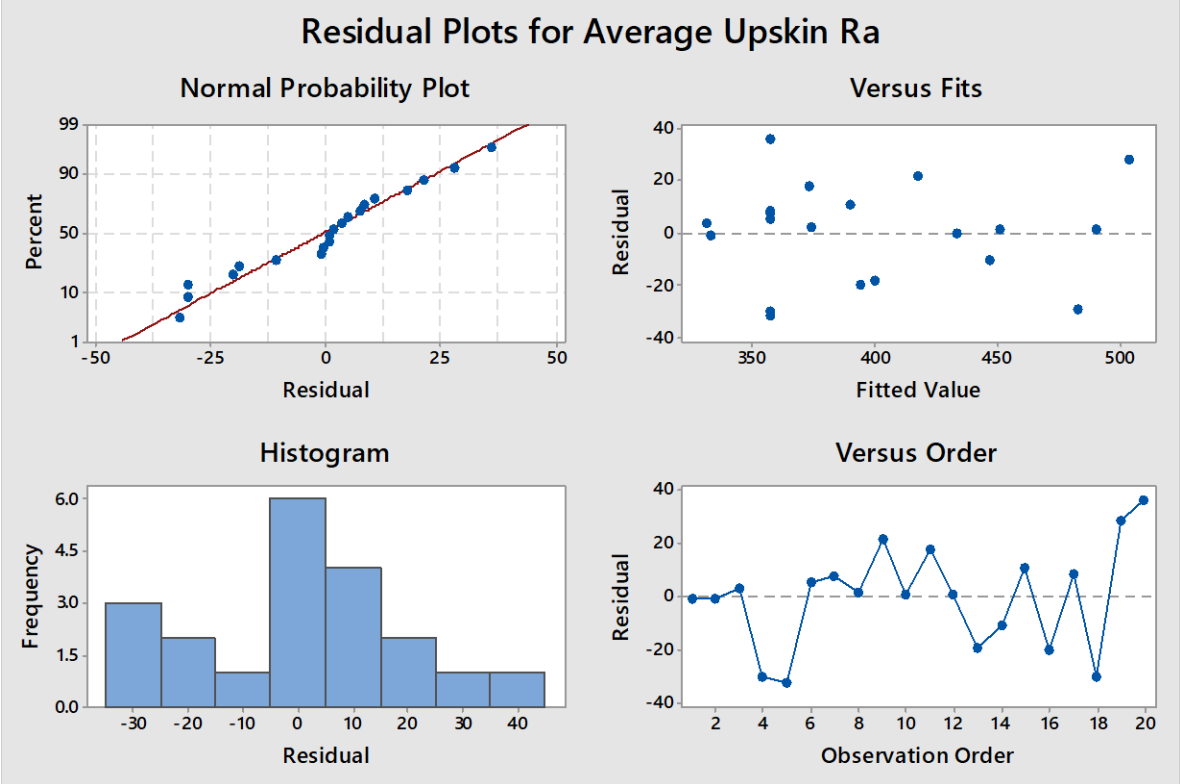

Top Surface Ra:

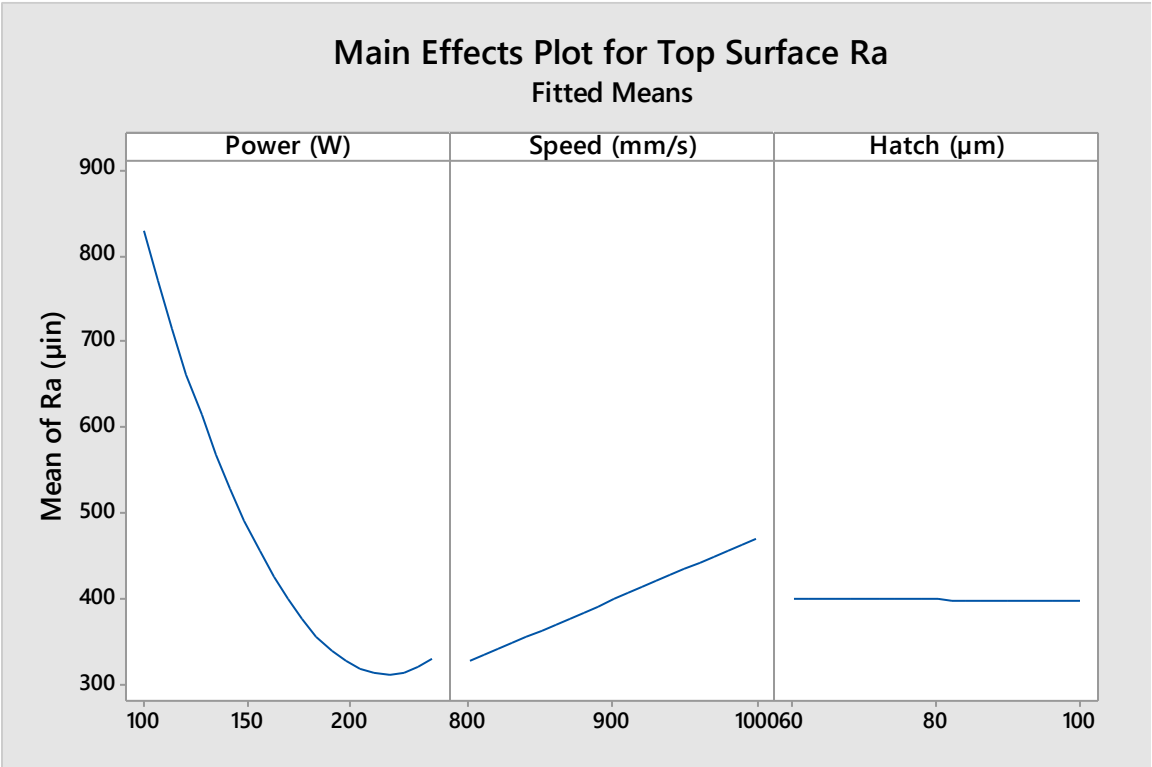

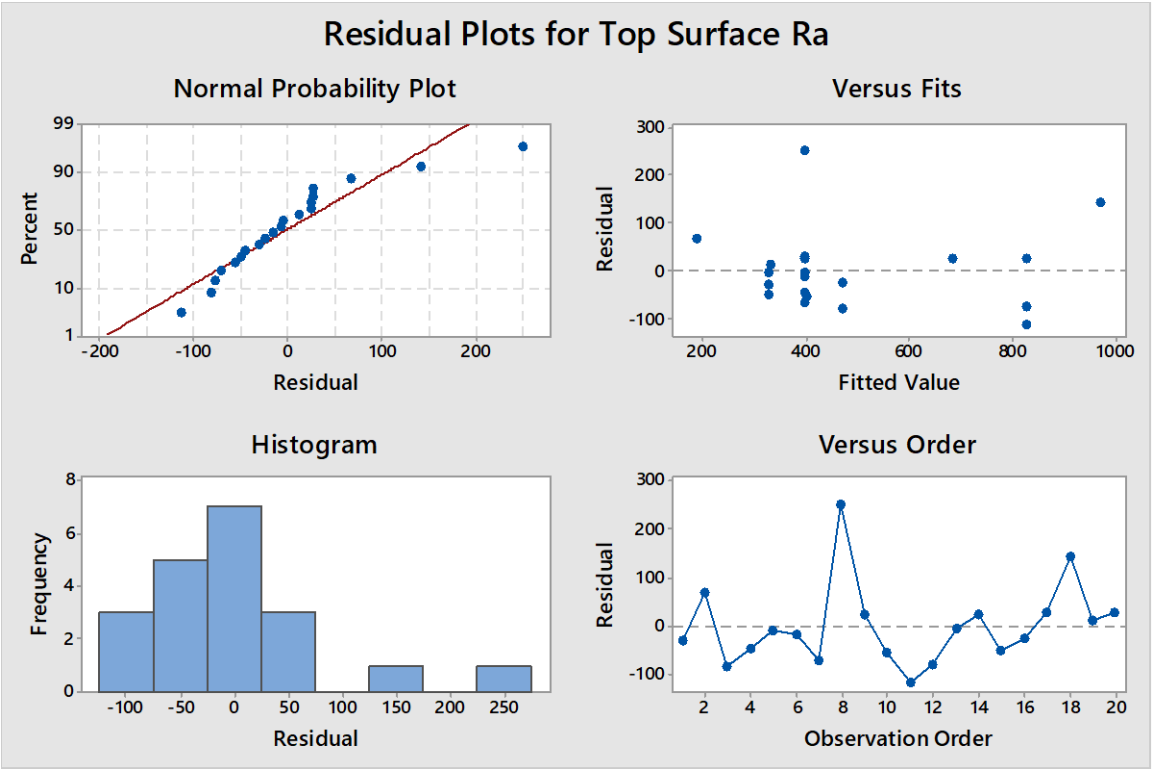

Relative Density:

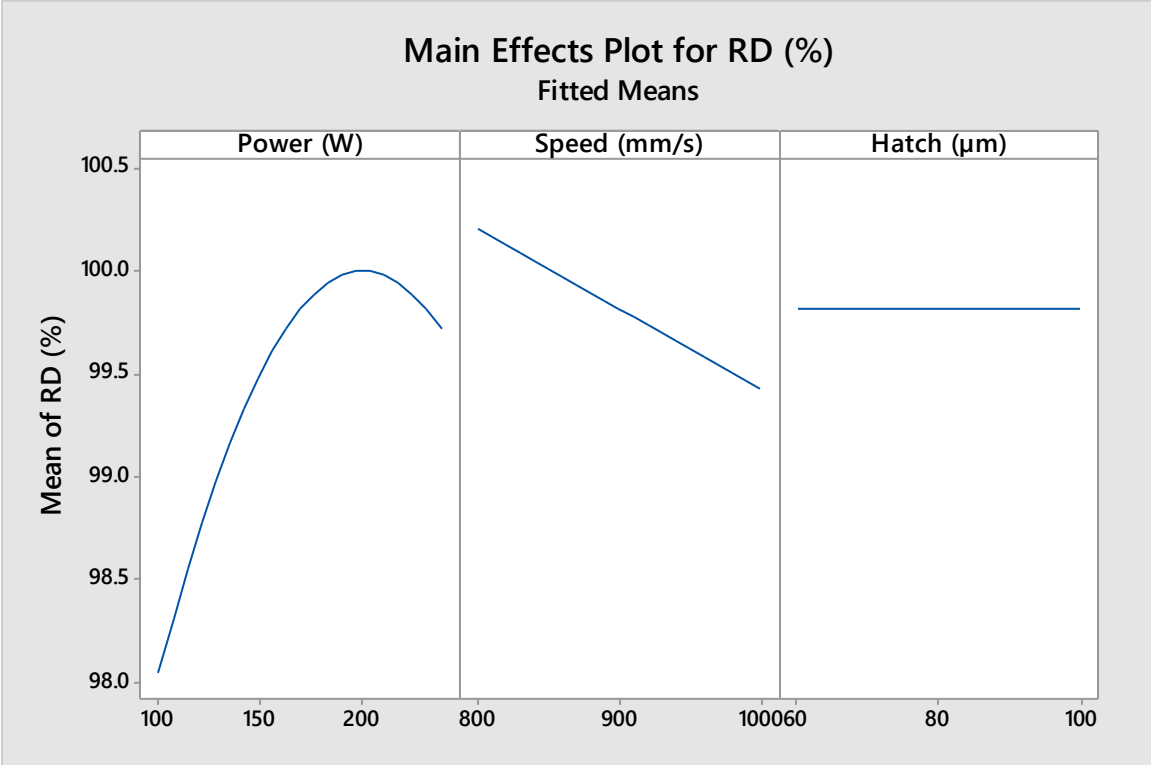

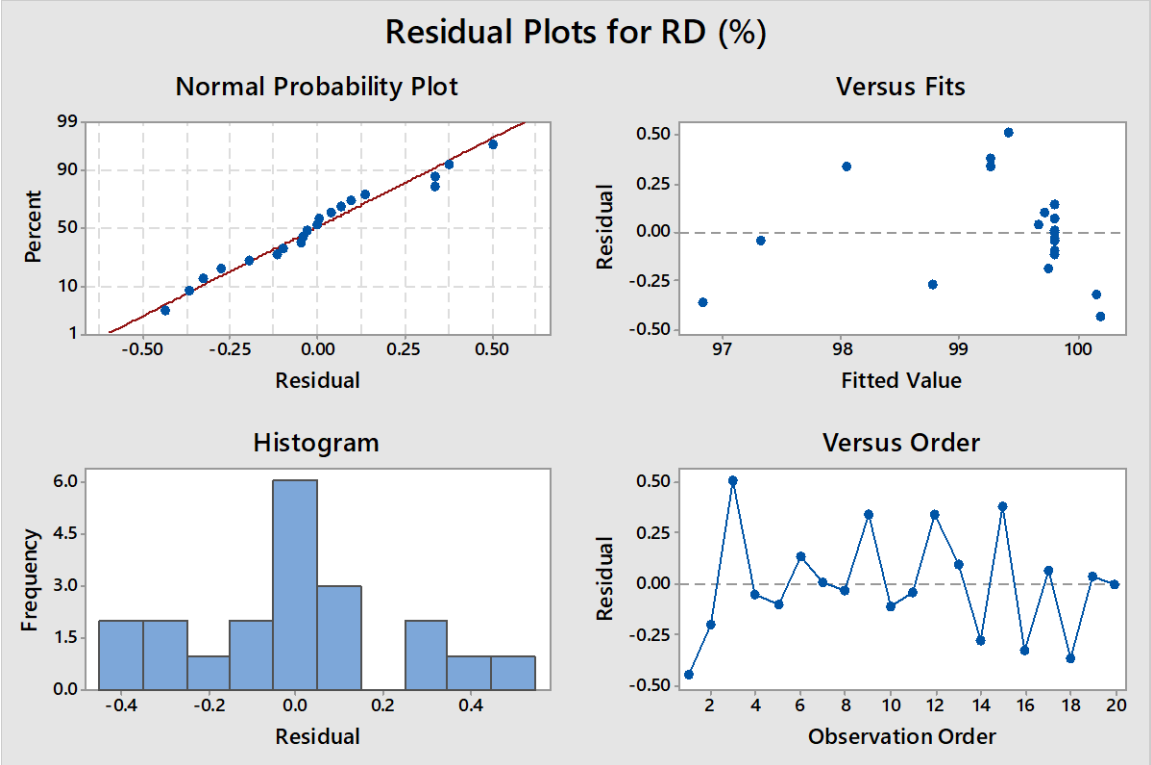

Vickers Microhardness:

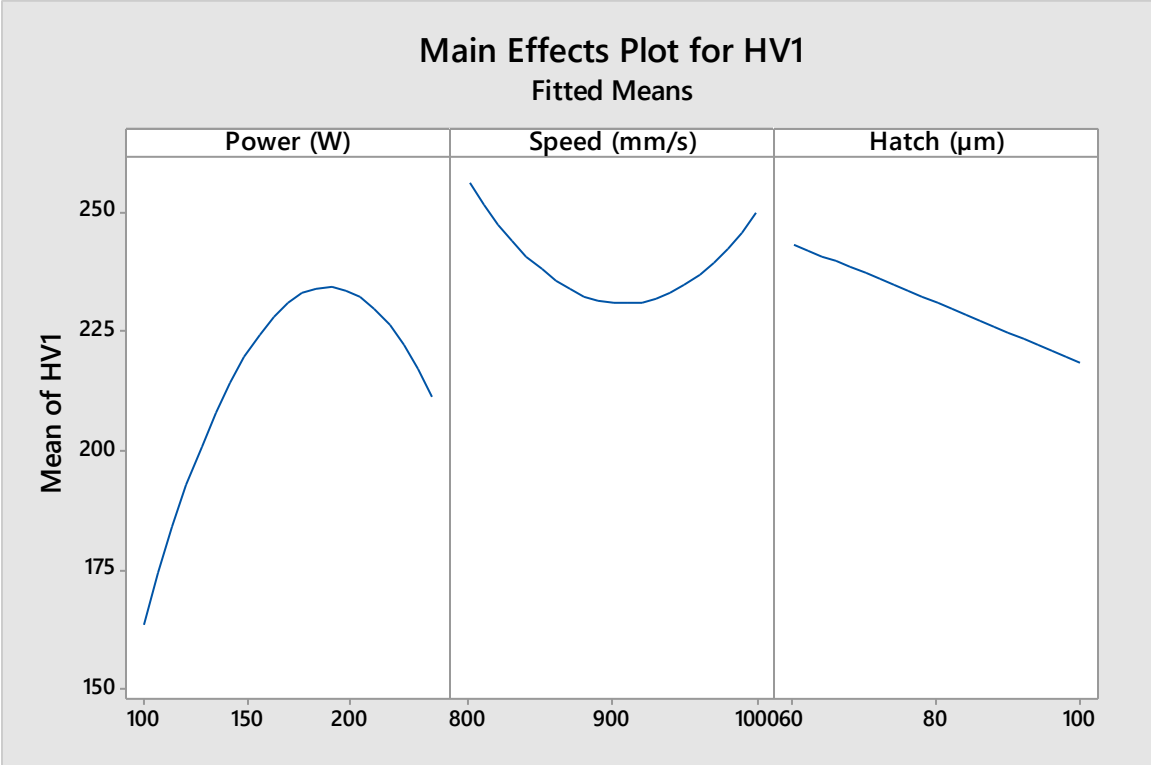

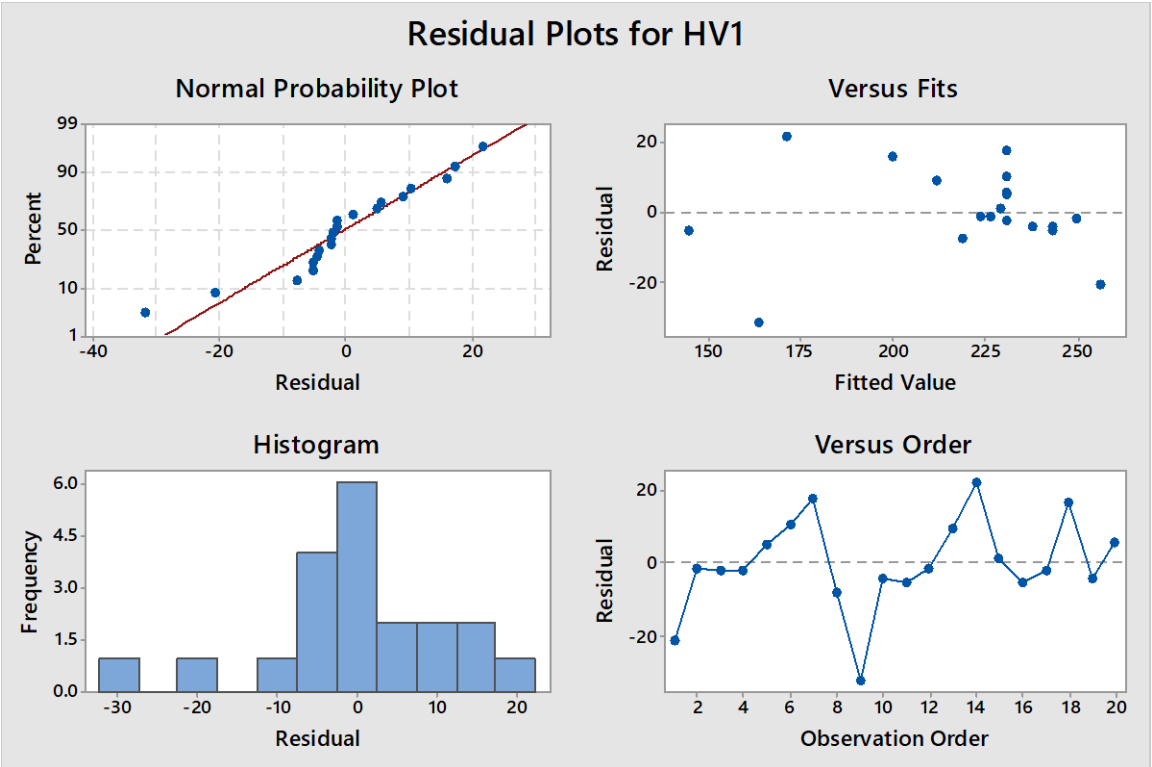

Residual Stress Deflections:

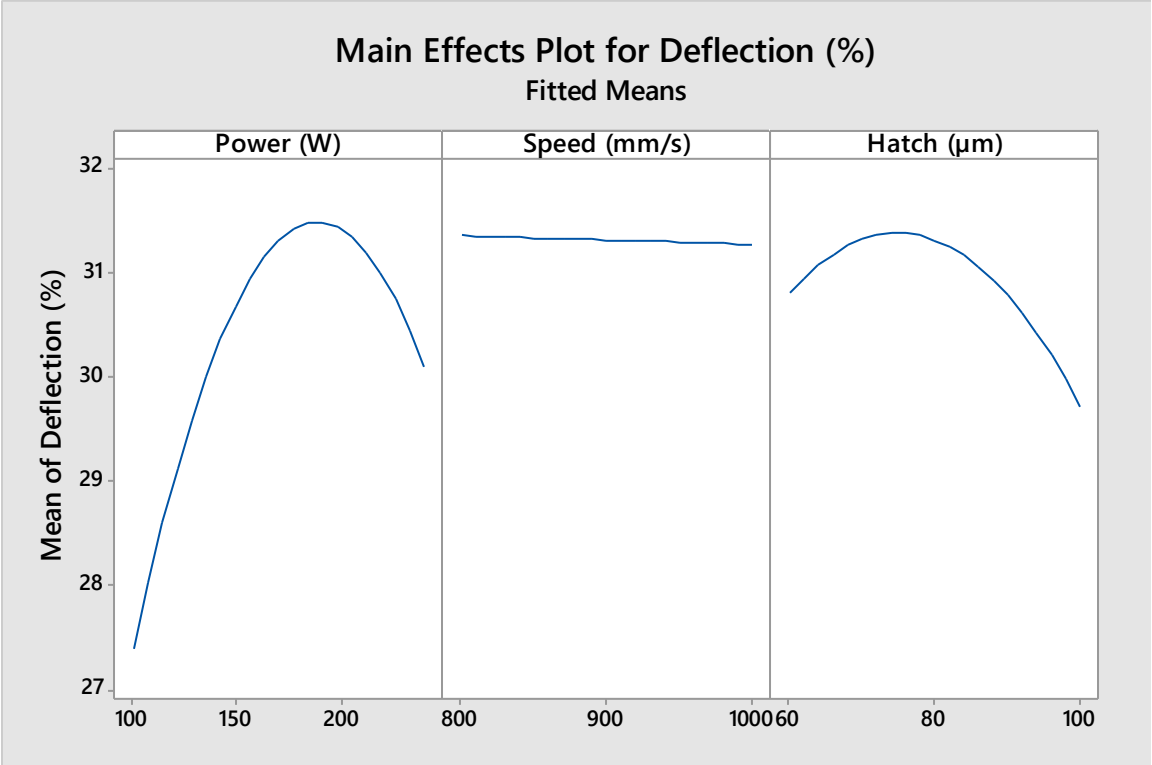

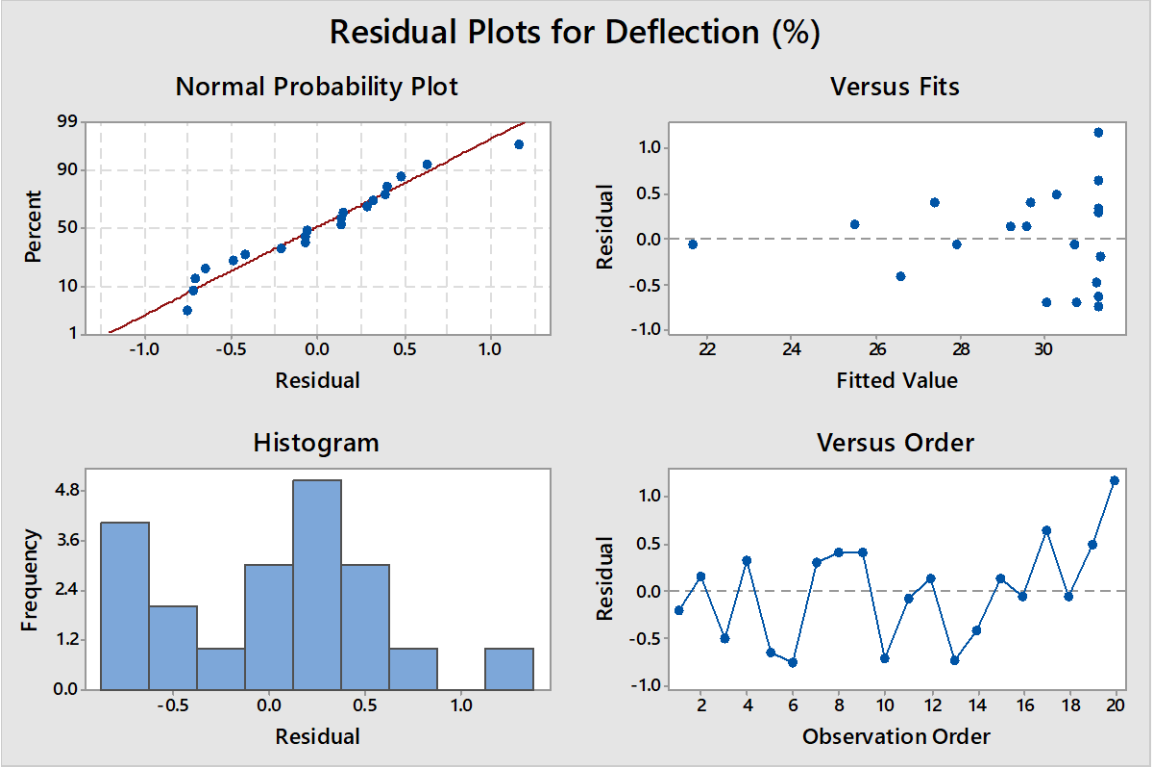

Appendix D: Supplementary Roughness Parameter Plots

Contour Strategy Prints:

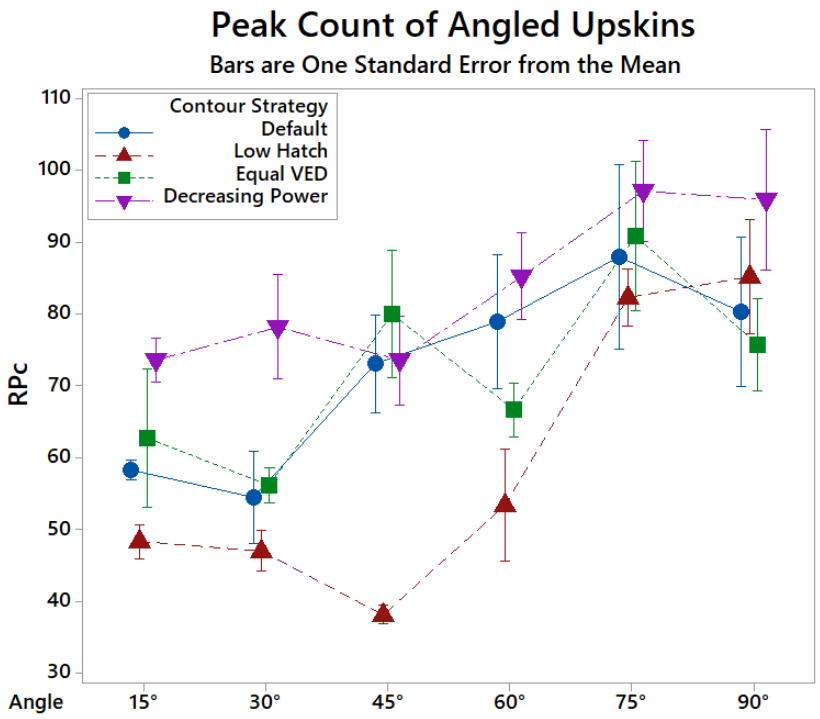

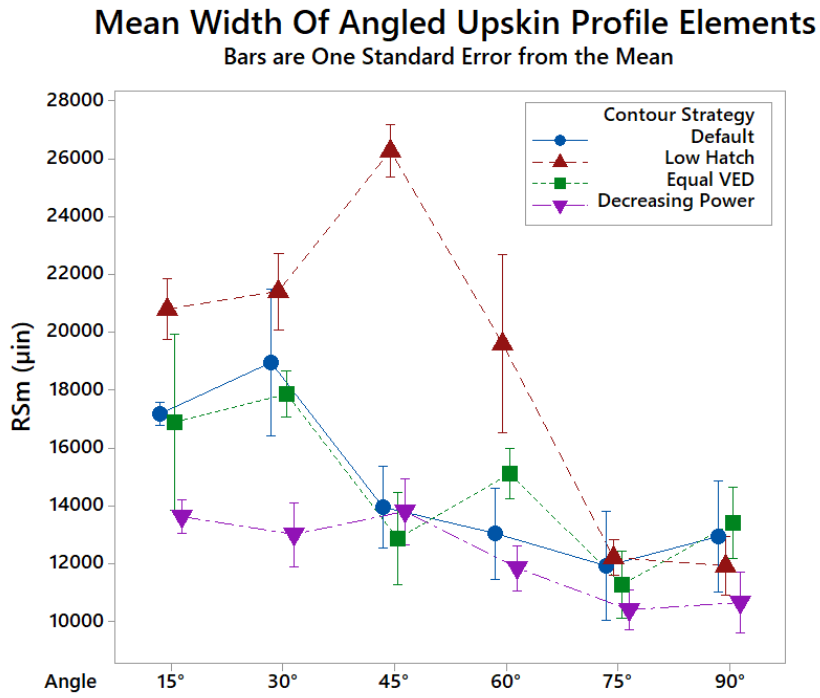

Powder Size and Shielding Gas Prints:

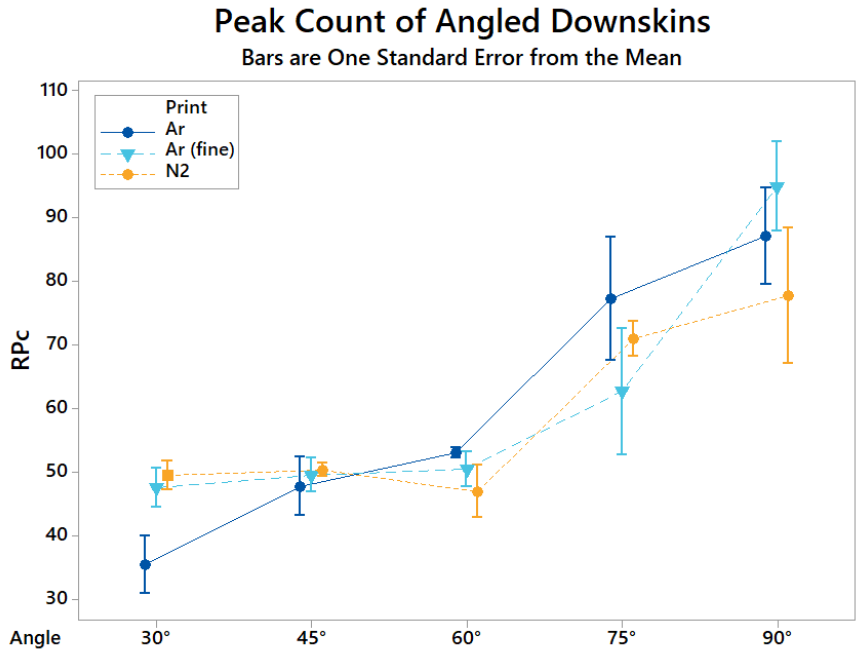

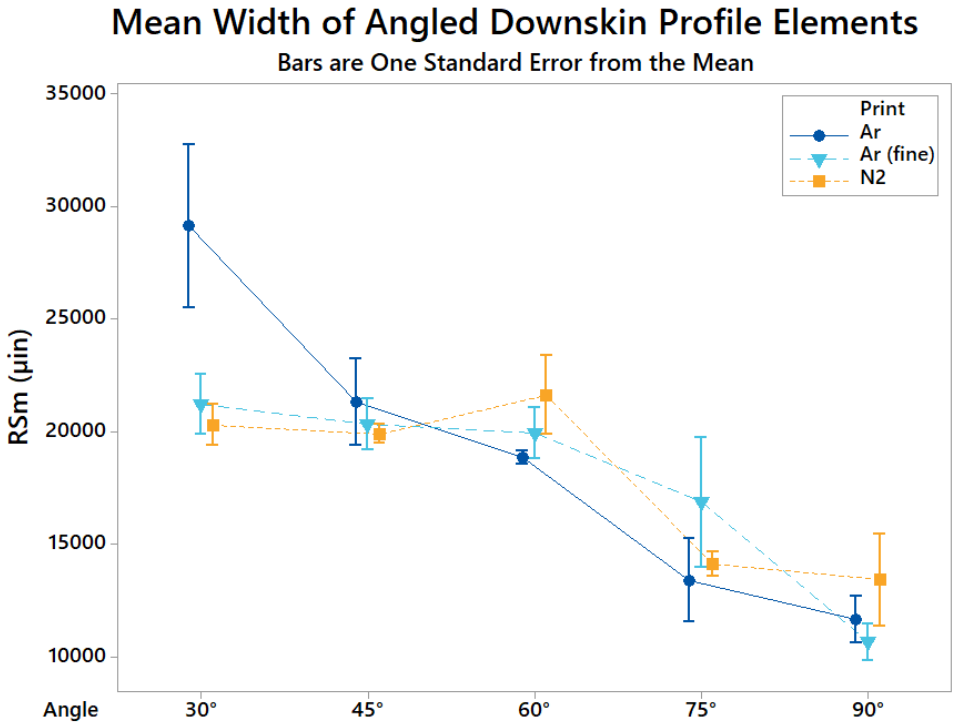

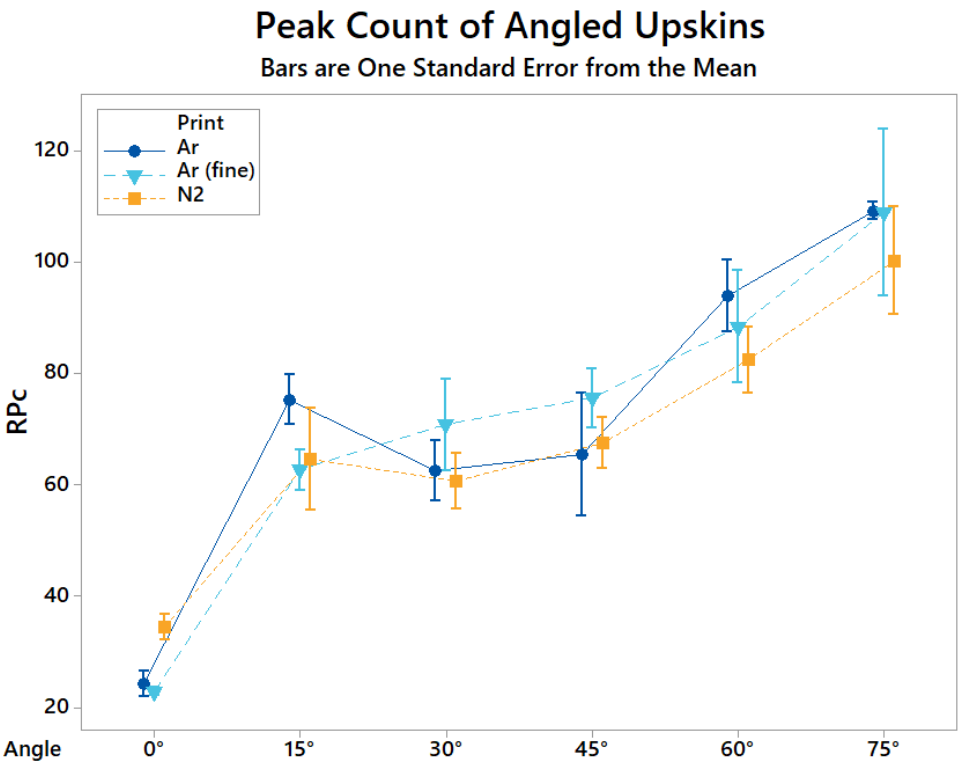
Peak Count of Angled Upskins
Bars are One Standard Error from the Mean
Print
Ar
Ar (fine)
N2
RPc
120
100
80
60
40
20
Angle
0°
15°
30°
45°
60°
75°

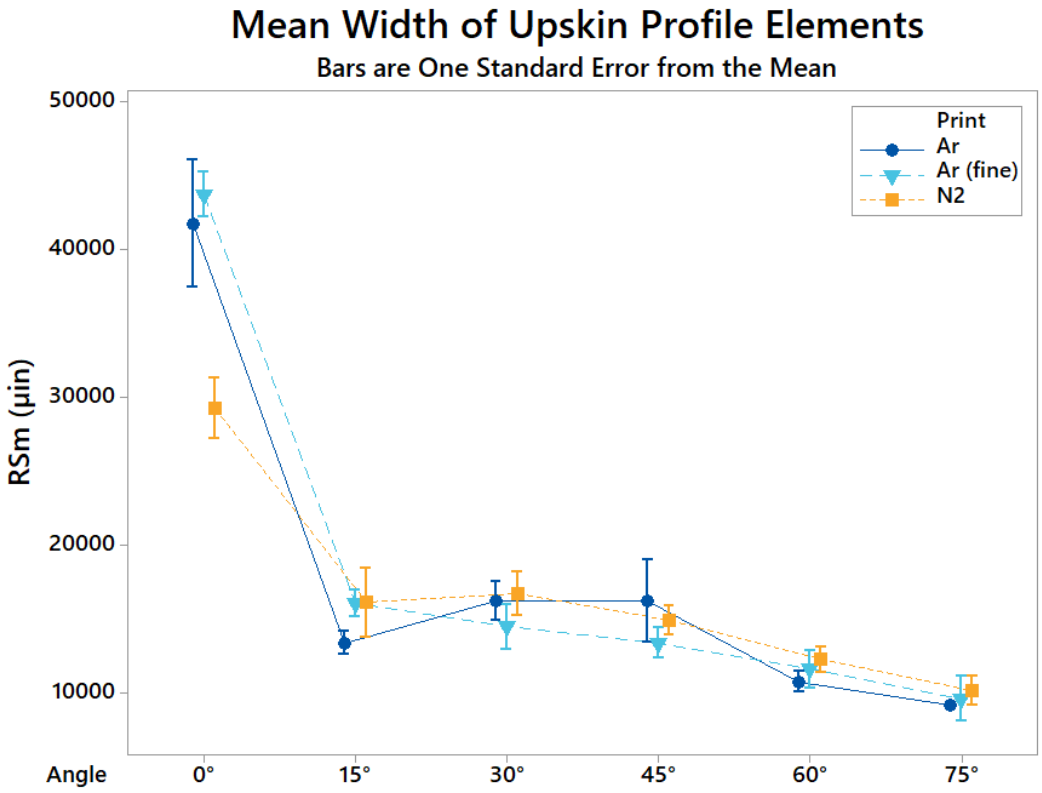
Mean Width of Upskin Profile Elements
Bars are One Standard Error from the Mean
Print
Ar
Ar (fine)
N2
RSm (µin)
50000
40000
30000
20000
10000
Angle
0°
15°
30°
45°
60°
75°

30° Downskin Models:

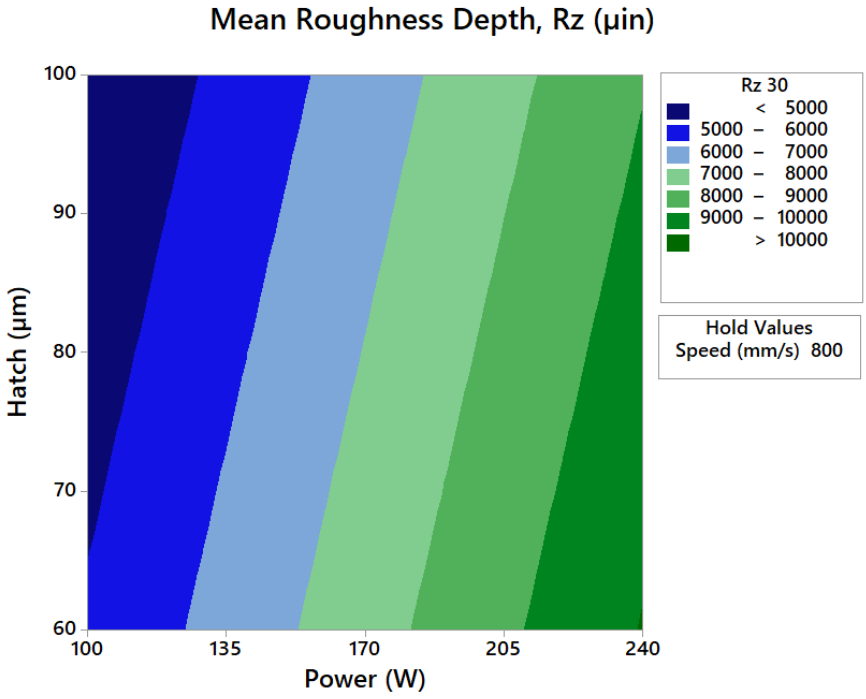

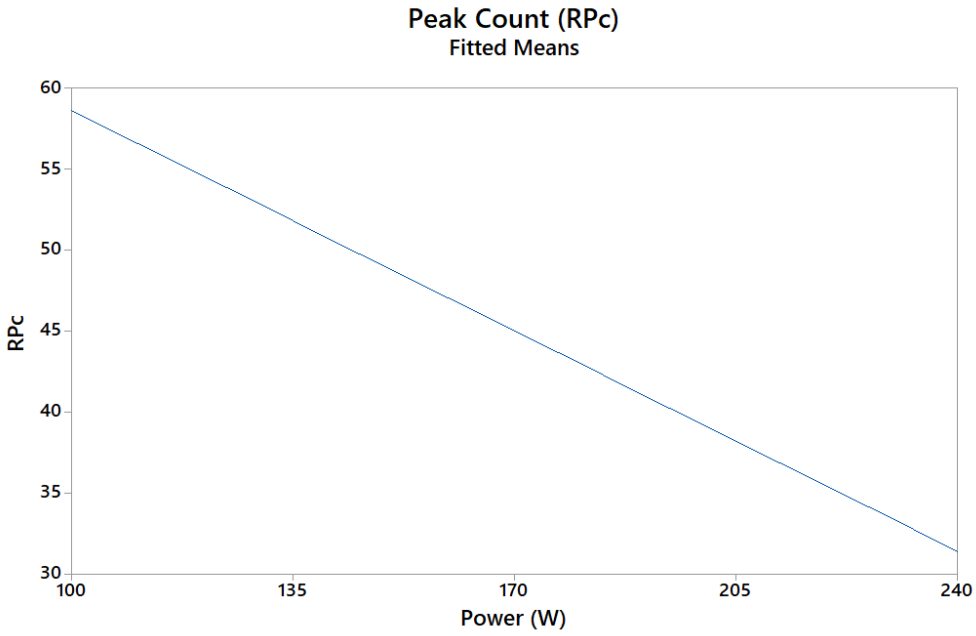

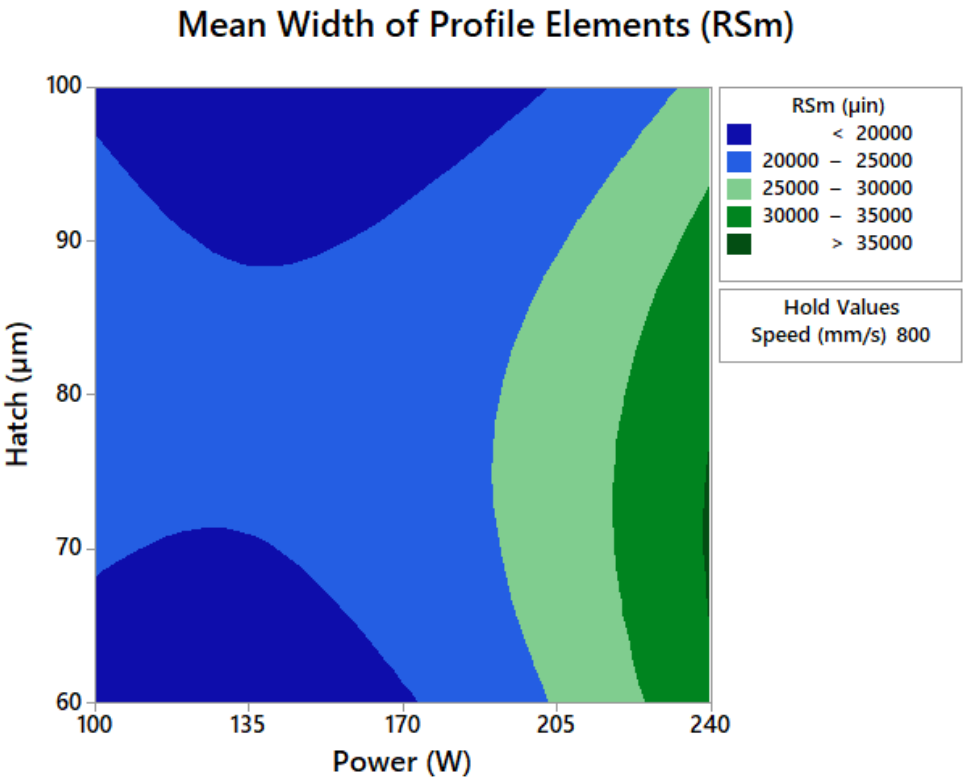
Mean Width of Profile Elements (RSm)
RSm (µin)
< 20000
20000 – 25000
25000 – 30000
30000 – 35000
> 35000
Hold Values
Speed (mm/s) 800
Hatch (µm)
100
90
80
70
60
100
135
170
205
240
Power (W)

Average Upskin Models:

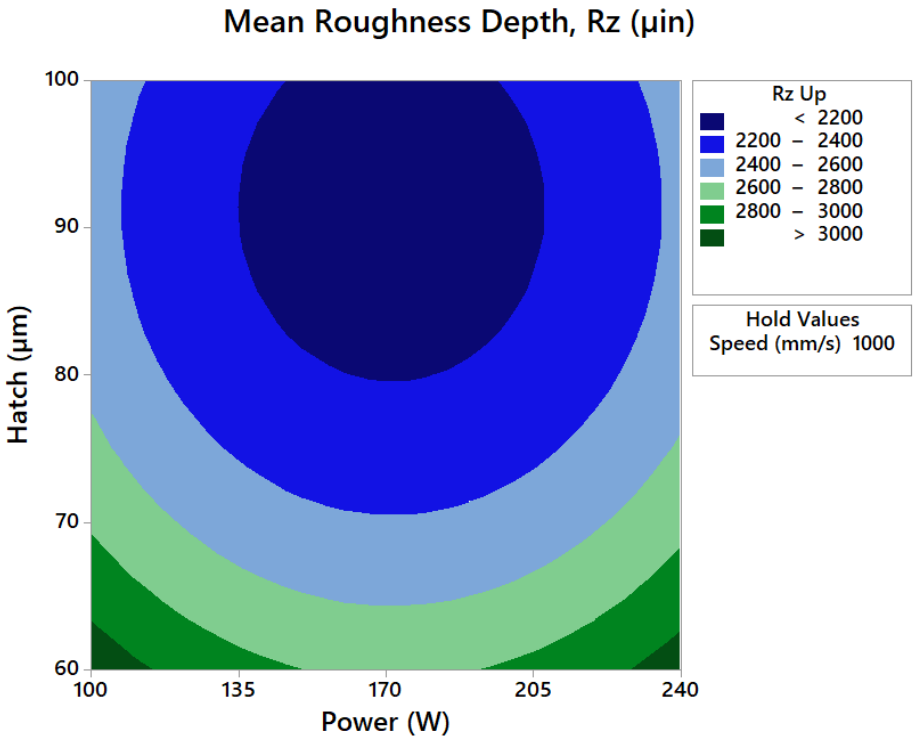

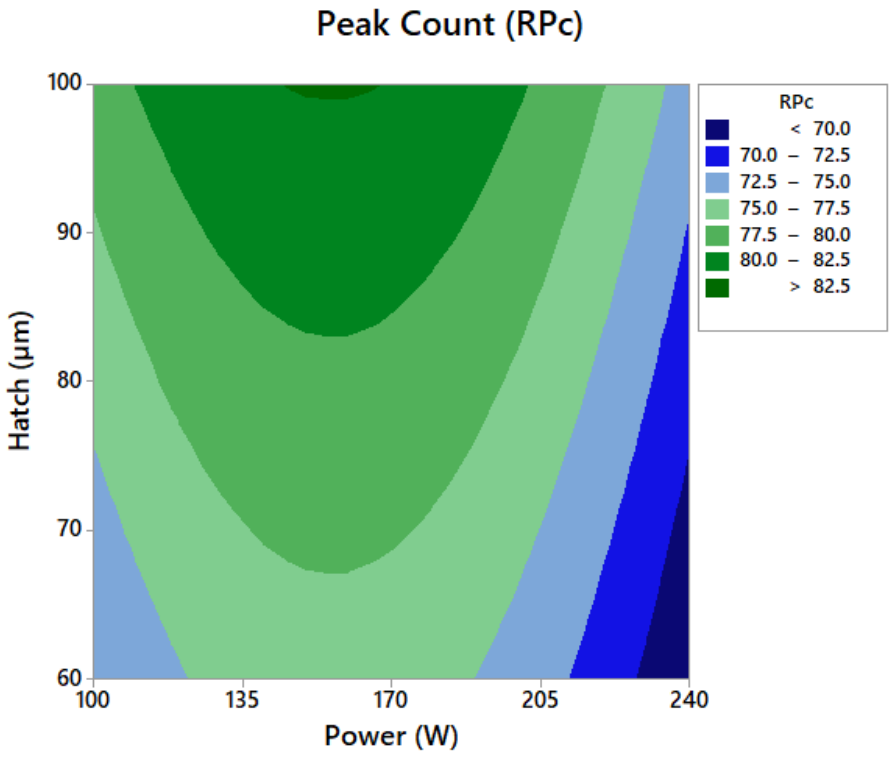

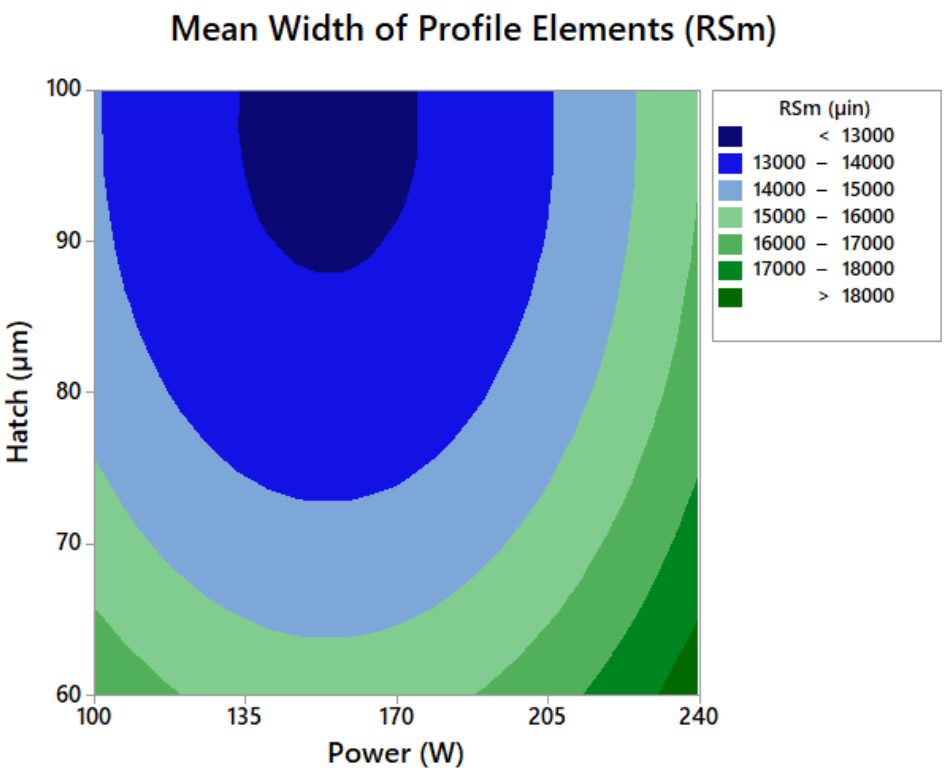
Mean Width of Profile Elements (RSm)
RSm (µin)
< 13000
13000 – 14000
14000 – 15000
15000 – 16000
16000 – 17000
17000 – 18000
> 18000
Hatch (µm)
100
90
80
70
60
100
135
170
205
240
Power (W)

Top Surface Models:

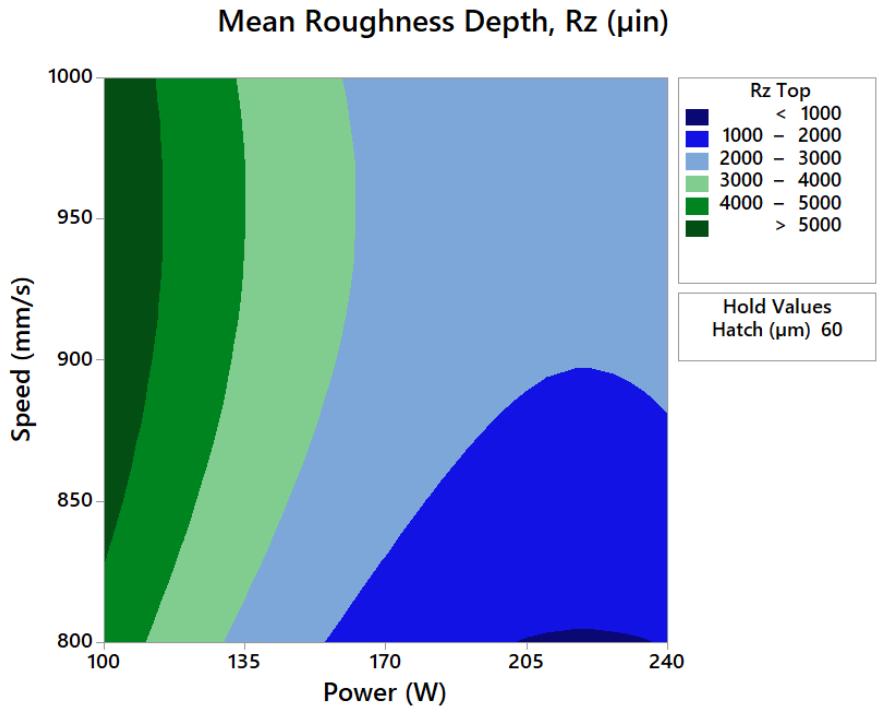

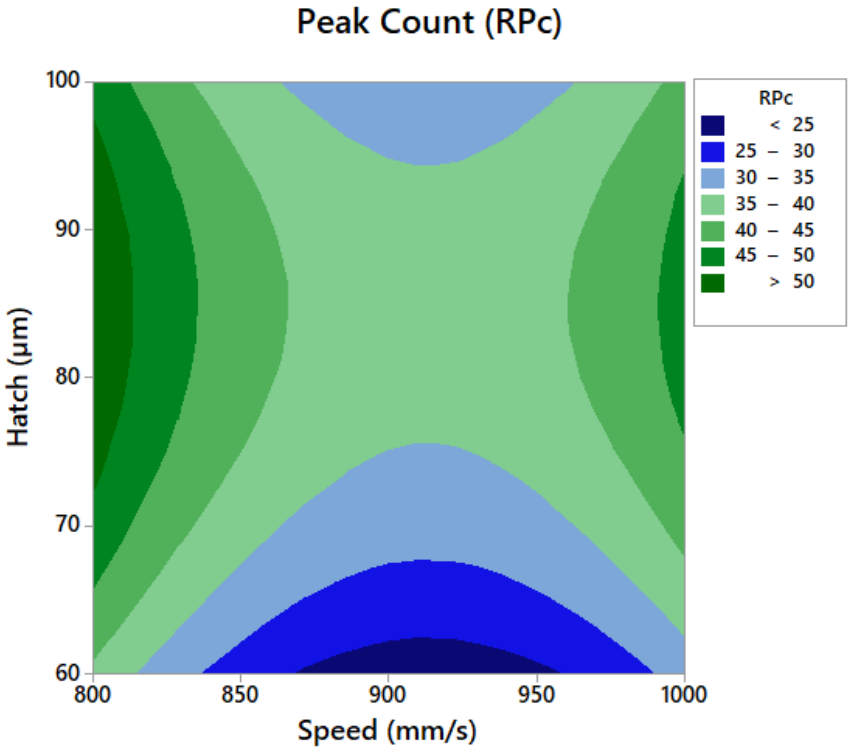

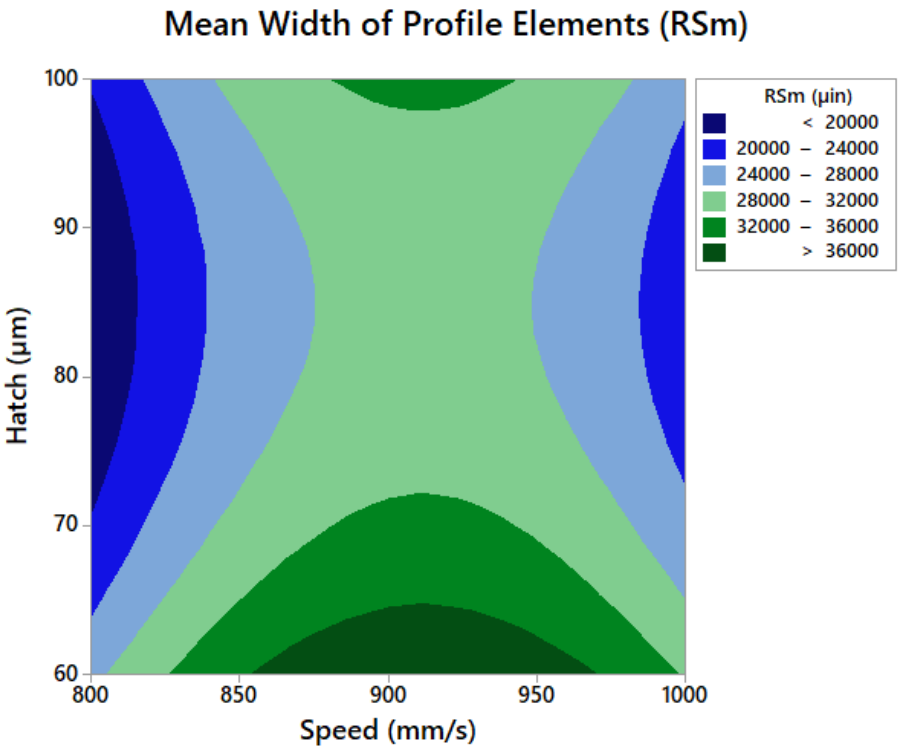
Mean Width of Profile Elements (RSm)
RSm (µin)
< 20000
20000 – 24000
24000 – 28000
28000 – 32000
32000 – 36000
> 36000
Hatch (µm)
100
90
80
70
60
800
850
900
950
1000
Speed (mm/s)

New & Default Prints:

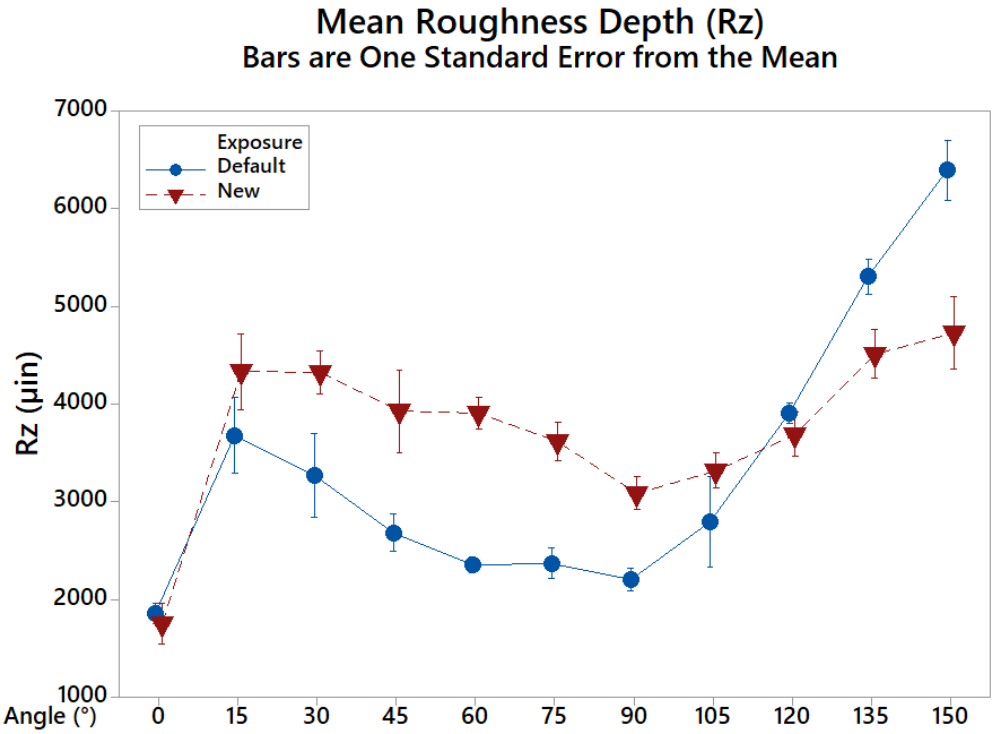

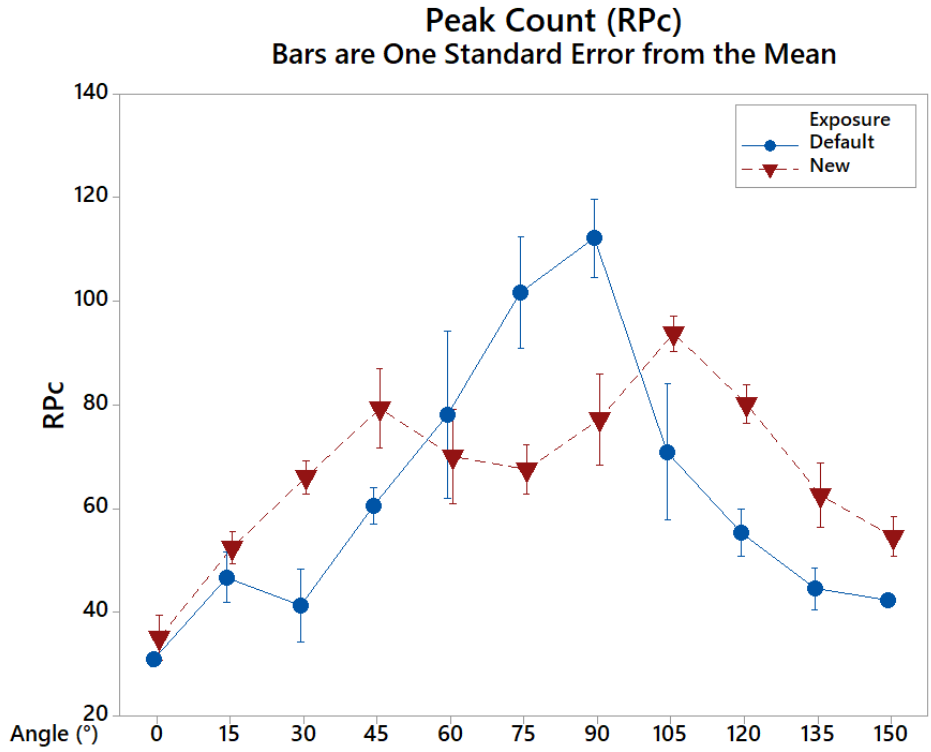

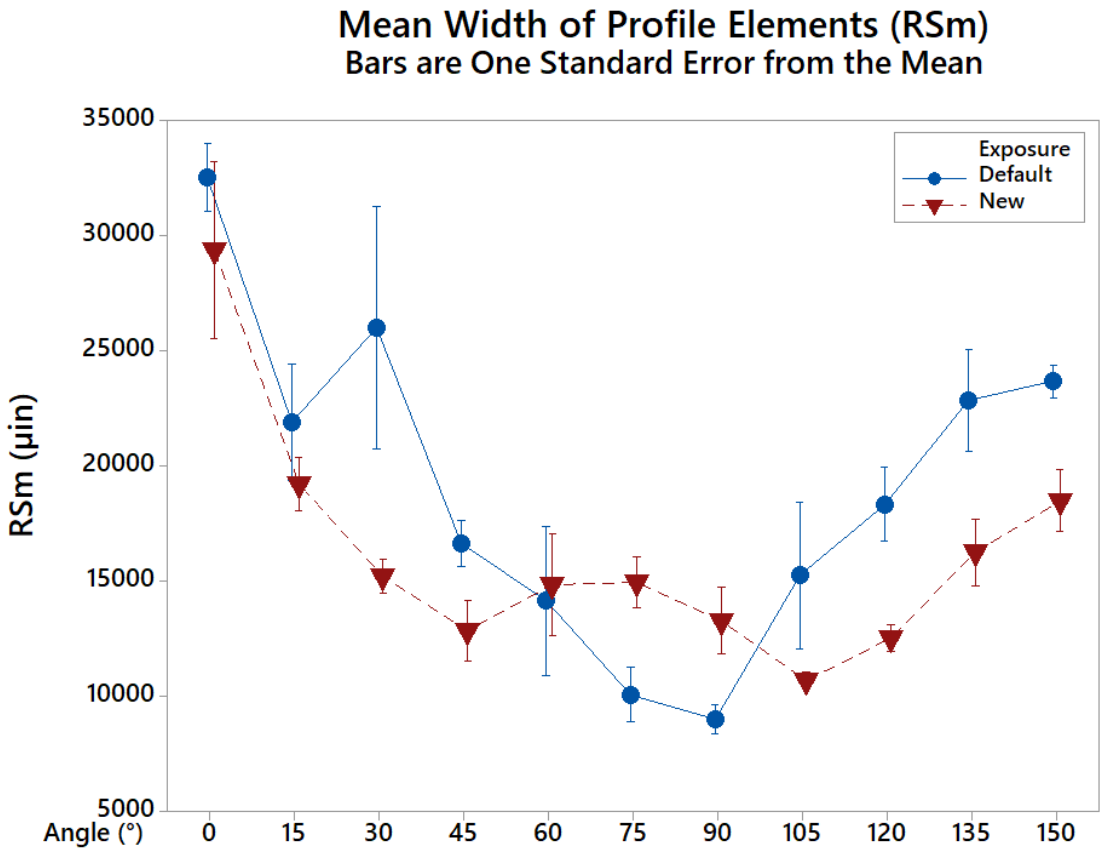
Mean Width of Profile Elements (RSm)
Bars are One Standard Error from the Mean
RSm (µin)
35000
30000
25000
20000
15000
10000
5000
Angle (°)
0
15
30
45
60
75
90
105
120
135
150
Exposure
Default
New

Appendix E: Heat Exchanger Streamlines